Technische Universität
Kaiserslautern

Fachbereich
Physik

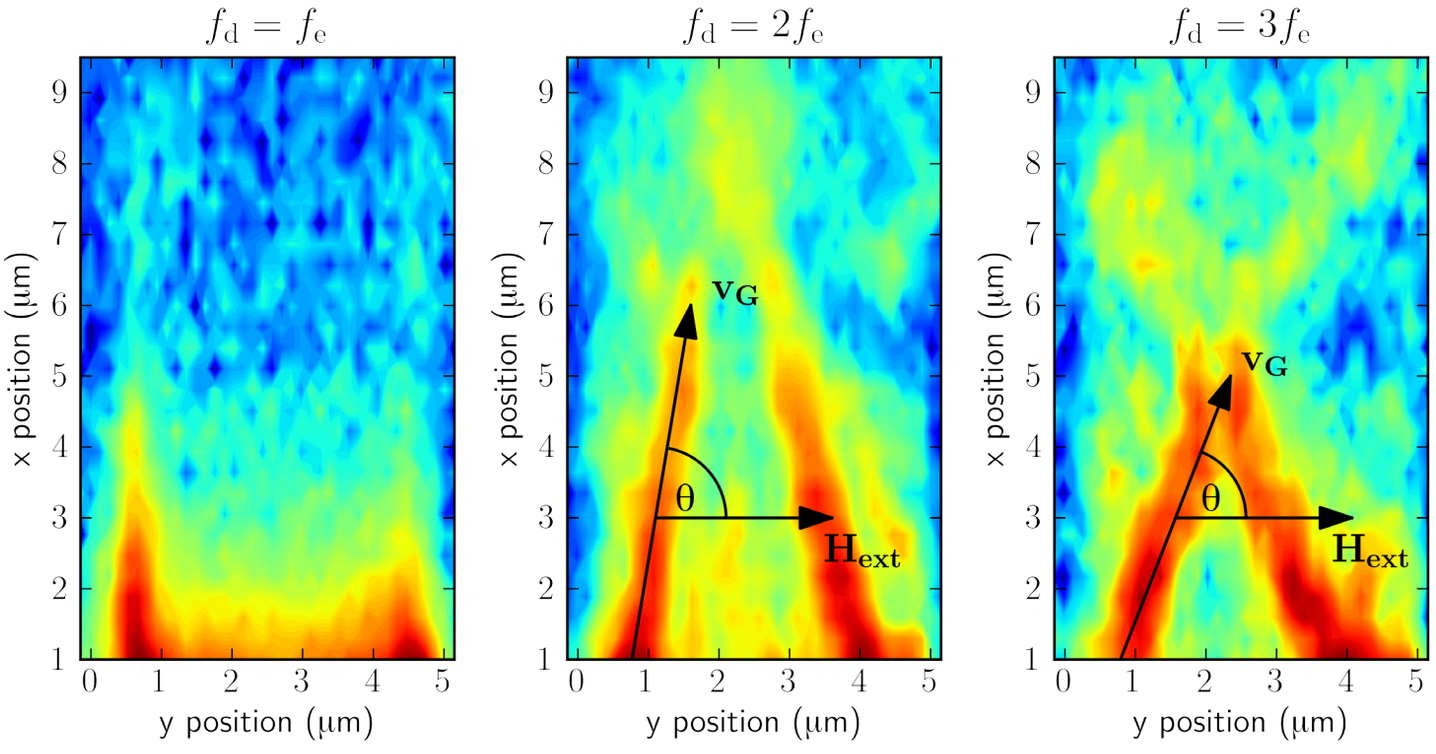

AG Magnetismus
Annual Report 2012

OPTIMAS

AG MAGNETISMUS
TU KAISERSLAUTERN

Front page: Nonlinear emission of spin-wave caustics at twice and three times the excitation frequency f_e from a directly excited spin-wave edge mode in a micro-structured $Co_2Mn_{0.6}Fe_{0.4}Si$ Heusler waveguide. The graphs show the intensity distributions at the detection frequency $f_\mathrm{d} = f_\mathrm{e}$ and of the higher harmonics at $f_\mathrm{d} = 2f_\mathrm{e}$ and $f_\mathrm{d} = 3f_\mathrm{e}$, respectively. The data was recorded via Brillouin light scattering microscopy. The demagnetizing field near the edges of the transversely magnetized waveguide allows for the existence of a localized edge mode with a frequency far below the cut-off frequency for propagating modes and results in the intensity distribution shown on the left side. The higher harmonic generation leads to propagating and strongly directed spin-wave beams or caustics. The caustic formation and the observed propagation angles $\theta = \angle(\mathbf{H_{ext}}, \mathbf{v_G})$ between the external field $\mathbf{H_{ext}}$ and the group velocity $\mathbf{v_G}$ can be described by the anisotropic dispersion relation for magnetic thin films. Our analytical calculations yield an excellent agreement with our experimental findings. For more details about this phenomenon see Section 4.15 of the Report.

Annual Report 2012

Address:	Prof. Dr. Burkard Hillebrands Fachbereich Physik Landesforschungszentrum OPTIMAS Technische Universität Kaiserslautern Erwin-Schrödinger-Straße 56 67663 Kaiserslautern, Germany Tel.: +49-(0)631-205-4228 Fax.: +49-(0)631-205-4095
Postal address:	Postfach 3049 67653 Kaiserslautern, Germany
Internet:	http://www.physik.uni-kl.de/hillebrands/
E-Mail:	hilleb@physik.uni-kl.de

This Annual Report can be downloaded from:
http://www.physik.uni-kl.de/hillebrands/publications/annual-reports/

Our Group

From left to right:

Philipp Pirro, Thomas Brächer, Milan Agrawal, Frank Heussner,
Ana Ruiz Calaforra, Benjamin Jungfleisch, Dr. Evangelos Papaioannou,
Jochen Greser, Dr. Vitaliy Vasyuchka, Dr. Tomohiro Koyama, Björn Obry,
Philipp Fuhrmann, Thomas Langner, Viktor Lauer, Dr. Andrés Conca Parra,
Dr. Alexander Serga, Dr. Andrii Chumak, Peter Clausen, Thomas Sebastian,
Katrin Vogt, Prof. Dr. Burkard Hillebrands, Thomas Meyer

Contents

Chapter 1: Preface

Dear Colleagues and Friends,

we present our Annual Report 2012 covering the period November 2011 to October 2012 - this year with slightly modified front and back cover incorporating the new university corporate design.

A few highlights of our research in this period: The research topic "magnon gases" remains extremely exciting. We progressed in investigating the evaporating cooling process and we found a new phonon-mediated pathway to Bose Einstein condensation of a magnon gas. Highlights in the field of magnon spintronics are the observation of parametrically generated magnons in Permalloy microstructures, the transport of magnons in curved spin-wave waveguides, and the direct detection of magnon transport by the inverse spin Hall effect. In the field of magnonic crystals an important milestone is the observation of the storage-recovery phenomenon. In the field of spin caloric transport we succeeded to measure the magnon temperature in the ferrimagnetic insulator yttrium iron garnet. We continued our work on Heusler compounds and showed nonlinear magnon instability and the formation of caustics in $Co_2Mn_{0.6}Fe_{0.4}Si$ spin-wave waveguides. In the field of applied spintronics, we introduced a new concept for patterned storage media by ion beam irradiation.

An important event was the successful prolongation of the Graduate School of Excellence "Materials Science in Mainz (MAINZ)". We currently participate with two stipendiates and two collegiates. In the field of applied magnetism we started a new project to establish a spintronics technology platform in Rhineland-Palatinate (STeP), cooperating partner is the Johannes Gutenberg University Mainz. Jointly with partners at the Université de la Lorraine and Saar Universität Saarbrücken a Magnetism Network of the Greater Region (Réseau de Magnétisme pour la Grande Région (GRMN)/Magnetismus-Netzwerk der Großregion (GRMN)) was started. Aim is to create a magnetism center across the French/German border to coordinate activities in the fields of research, training and technology transfer.

In August we have hosted the IEEE International Conference on Microwave Magnetics 2012. More than 120 participants discussed physical and technological aspects of magnetic phenomena in the microwave frequency range.

Again, there have been several changes in our group. We are happy to welcome (in alphabetical order) Philipp Fuhrmann, Dr. Tomohiro Koyama, Viktor Lauer, and Dr. Evangelos Papaioannou. Tomohiro Koyama will stay with us for one year as a Humboldt Research Fellowship postdoctoral researcher addressing dynamics of domain walls, and Evangelos Papaioannou holds a post-doctoral position devoted to our molecular beam epitaxy work. Thomas Meyer started his Ph.D. research work. Florin Ciubotaru and Georg Wolf finished their Ph.D., and Jan Westermann completed his diploma thesis.

Our work would not have been possible without valuable collaborations with people all over the world. They are too many to list them here all. In particular we would like to thank, in alphabetical order, Johan Åkerman, Toshu An, Kazuya Ando, Yasuo Ando, Christian Back, Gerrit Bauer, Arne Brataas, Giovanni Carlotti, Frederick Casper, Claude Chappert, Russell Cowburn, Sergei Demokritov, Bernard Dieny, Ursula Ebels, Hajo Elmers, Jürgen Fassbender, Gerhard Fecher, Claudia Felser, Albert Fert, Suzanna and Paulo Freitas, Yasuhiro Fukuma, John Gregg, Hartmut Grützediek, Dirk Grundler, Gianluca Gubbiotti, Konstantin Gusliyenko, Jarsolav Hamrle, Uwe Hartmann, Axel Hoffmann, Koichiro Innomata, Gerhard Jakob, Xiaofeng Jin, Martin Jourdan, Gleb Kakazei, Boris Kalinikos, Alexy Karenowska, Sang-Koog Kim, Mathias Kläui, Peter

Kopietz, Mikhail Kostylev, Andreas Kreisel, Jürgen Kübler, Takahide Kubota, Luis Lopez Diaz, Wolfram Maaß, Roland Mattheis, Gennadiy Melkov, Claudia and Tim Mewes, Hiroshi Naganuma, Hans Nembach, Mikihiko Oogane, Yoshichika Otani, Johannes Paul, Dorothée Petit, Günter Reiss, Bernhard Reuscher, Karsten Rott, Jürgen Rühl, Manfred Rührig, Eiji Saitoh, John R. Sandercock, Rudi Schäfer, Gerd Schönhense, Justin Shaw, Andrei Slavin, Bob Stamps, Yoshishige Suzuki, Koki Takanashi, Vasyl Tiberkevich, Simon Trudel, Ken-ichi Uchida, and Bert van Wees for their interactions with us and their strong input to our work.

Collaborations within the Fachbereich Physik at the University of Kaiserslautern (in particular Martin Aeschlimann, James Anglin, Sebastian Eggert, Michael Fleischhauer, Georg von Freymann, Herwig Ott, Hans-Christian Schneider, Volker Schünemann, and Arthur Widera and their groups), the Institut für Oberflächen- und Schichtanalytik, as well as Sandra Wolff and the Nano Structuring Center have been very stimulating. We are very grateful to be a member of the State Research Center for Optics and Material Sciences OPTIMAS.

I would also like to thank all our sponsors, which are the Deutsche Forschungsgemeinschaft (DFG), the Bundesministerium für Bildung und Forschung (BMBF), the Deutscher Akademischer Austauschdienst (DAAD), the European Community, INTAS, the Carl Zeiss Foundation, the State of Rhineland Palatinate and the University of Kaiserslautern. Concerning our projects in applied research, I would like to express my gratitude to Prema GmbH, Sensitec GmbH, Siemens AG, and Singulus Technologies AG as our strong partners in R&D on spintronic sensors.

My special thanks go to Benjamin Jungfleisch, Isabel Sattler, and Sibylle Müller for their help in preparing this report and to Hubert Gerber from Photo-Repro-Druck, TU Kaiserslautern.

It is my special pleasure to greet all former group members. May this report help to stay in touch. If you are interested in our work I would be happy to hear from you. If you have any questions, comments or suggestions please contact us.

With all my best wishes for Christmas, and a Happy New Year,

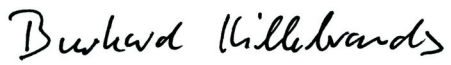

Kaiserslautern, November 2012

Vorwort

Liebe Kolleginnen und Kollegen und Freunde unserer Arbeitsgruppe,

wir freuen uns, Ihnen unseren Jahresbericht 2012 in diesem Jahr mit einem leicht veränderten Umschlag zu präsentieren, welcher im neuen *Corporate* Design unserer Universität erscheint.

Der Bericht deckt den Zeitraum von November 2011 bis Oktober 2012 ab. Einige Höhepunkte unserer Forschung in diesem Zeitfenster: Das Forschungsfeld "Magnonengase" bleibt extrem aufregend. Wir haben die Untersuchung eines evaporativen Kühlprozesses vorangetrieben und einen neuen, phonon-vermittelten Weg zur Bose-Einstein Kondensation eines Magnonengases gefunden. Darüber hinaus ist es uns gelungen, parametrische Magnonen in Mikrostrukturen superkritisch anzuregen. Höhepunkte im Bereich Magnon-Spintronik sind der Transport von Magnonen in gekrümmten Spinwellen-Wellenleitern und der direkte Nachweis von Magnontransport mittels des inversen Spin-Hall-Effektes. Ein wichtiger Meilenstein im Feld der Magnonischen Kristalle ist die Beobachtung des *storage-recovery* Phänomens. Im Feld Spinkalorischer Transport ist es uns gelungen die Magnonentemperatur im ferrimagnetischen Isolator Yttrium-Eisen-Granat zu messen. Wir haben unsere Arbeiten mit Heusler-Verbindungen fortgesetzt und stellen eine nichtlineare Magnoneninstabilität und die Ausbildung von Spinwellen-Kaustiken in $Co_2Mn_{0.6}Fe_{0.4}Si$ Spinwellen-Wellenleitern vor. Im Bereich der angewandten Spintronik stellen wir ein neues Konzept eines *Patterned Storage Mediums* durch Ionenbestrahlung vor.

Ein wichtiges Ereignis war die erfolgreiche Verlängerung der Graduiertenschule der Exzellenz "Material Science in Mainz (MAINZ)", an der wir zur Zeit mit zwei Stipendiaten und zwei Kollegiaten teilnehmen. Im Feld angewandter Magnetismus haben wir in Kooperation mit der Johannes Gutenberg Universität Mainz ein neues Projekt gestartet, welches eine Spintronik-Technologie-Plattform in Rheinland-Pfalz (STeP) etabliert. Zusammen mit der Université de la Lorraine und der Universität des Saarlandes, Saarbrücken wurde das Magnetismus Netzwerk der Großregion (GRMN) ins Leben gerufen. Sein Ziel es ist, ein Zentrum für Magnetismus, welches die deutsch-französische Grenze überspannt, zu schaffen, um die Aktivitäten in Forschung, Ausbildung und Technologietransfer zu koordinieren.

Im August waren wir Gastgeber der IEEE International Conference on Microwave Magnetics 2012. Mehr als 120 Teilnehmer haben physikalische und technologische Aspekte von magnetischen Phänomenen auf der Mikrowellenfrequenzskala diskutiert.

Erneut gab es einige Veränderungen in unserer Gruppe. Wir freuen uns, (in alphabetischer Reihenfolge) Philipp Fuhrmann, Dr. Tomohiro Koyama, Viktor Lauer und Dr. Evangelos Papaioannou in unserer Gruppe zu begrüßen. Tomohiro Koyama wird ein Jahr als Humboldt-Forschungsstipendiat für Postdoktoranden an der Dynamik von Domänenwänden forschen und Evangelos Papaioannou arbeitet als Post-Doc an unserer Molekularstrahlepitaxie-Anlage. Thomas Meyer hat mit seiner Doktorarbeit begonnen. Florin Ciubotaru und Georg Wolf haben ihre Doktorarbeit abgeschlossen und Jan Westermann hat seine Diplomarbeit vollendet.

Unsere Arbeit wäre nicht ohne wertvolle Kooperationen mit Partnern aus der ganzen Welt möglich gewesen. Es sind zu viele um sie alle an dieser Stelle aufzulisten. Insbesondere möchten wir, in alphabetischer Reihenfolge, Johan Åkerman, Toshu An, Kazuya Ando, Yasuo Ando, Christian Back, Gerrit Bauer, Arne Brataas, Giovanni Carlotti, Frederick Casper, Claude Chappert, Russell Cowburn, Sergei Demokritov, Bernard Dieny, Ursula Ebels, Hajo Elmers, Jürgen Fassbender, Gerhard Fecher, Claudia Felser, Albert Fert, Suzanna and Paulo Freitas, Yasuhiro Fukuma, John Gregg, Hartmut Grützediek, Dirk Grundler, Gianluca Gubbiotti, Konstantin Gusliyenko, Jarsolav Hamrle,

Uwe Hartmann, Axel Hoffmann, Koichiro Innomata, Gerhard Jakob, Xiaofeng Jin, Martin Jourdan, Gleb Kakazei, Boris Kalinikos, Alexy Karenowska, Sang-Koog Kim, Mathias Kläui, Peter Kopietz, Mikhail Kostylev, Andreas Kreisel, Jürgen Kübler, Takahide Kubota, Luis Lopez Diaz, Wolfram Maaß, Roland Mattheis, Gennadiy Melkov, Claudia and Tim Mewes, Hiroshi Naganuma, Hans Nembach, Mikihiko Oogane, Yoshichika Otani, Johannes Paul, Dorothée Petit, Günter Reiss, Bernhard Reuscher, Karsten Rott, Jürgen Rühl, Manfred Rührig, Eiji Saitoh, John R. Sandercock, Rudi Schäfer, Gerd Schönhense, Justin Shaw, Andrei Slavin, Bob Stamps, Yoshishige Suzuki, Koki Takanashi, Vasyl Tiberkevich, Simon Trudel, Ken-ichi Uchida und Bert van Wees für eine gute Zusammenarbeit und ihren großen Beitrag zu unserer Arbeit danken.

Die Zusammenarbeit mit dem Fachbereich Physik der Technischen Universität Kaiserslautern (insbesondere mit Martin Aeschlimann, James Anglin, Sebastian Eggert, Michael Fleischhauer, Georg von Freymann, Herwig Ott, Hans-Christian Schneider, Volker Schünemann und Arthur Widera und ihren Arbeitsgruppen), dem Institut für Oberflächen- und Schichtanalytik und Sandra Wolff und dem Nano Structuring Center waren sehr stimulierend. Wir sind sehr dankbar, Mitglied des Landesforschungszentrum für Optik und Materialwissenschaften (OPTIMAS) zu sein.

Ich möchte außerdem unseren Geldgebern danken: Der Deutschen Forschungsgemeinschaft (DFG), dem Bundesministerium für Bildung und Forschung (BMBF), dem Deutschen Akademischen Austauschdienst (DAAD), der Europäischen Gemeinschaft, INTAS, der Carl Zeiss Stiftung, dem Land Rheinland-Pfalz und der Technischen Universität Kaiserslautern. In Bezug auf unsere Projekte in der angewandten Forschung möchte ich meine Dankbarkeit gegenüber der Prema GmbH, der Sensitec GmbH, der Siemens AG und der Singulus Technologies AG, unseren starken Partnern in R&D von spintronischen Sensoren, zum Ausdruck bringen.

Mein besonderer Dank geht an Benjamin Jungfleisch, Isabel Sattler und Sibylle Müller für ihre Hilfe beim Erstellen dieses Berichtes und an Hubert Gerber von Photo-Repro-Druck, TU Kaiserslautern.

Es ist mir eine besondere Freude, hiermit auch alle ehemaligen Gruppenmitgliedern einen Gruß zu senden. Möge dieser Bericht uns helfen, im Kontakt zu bleiben. Wenn Sie an unserer Arbeit interessiert sind, würde ich mich freuen, von Ihnen zu hören. Wenn Sie irgendwelche Fragen, Kommentare oder Anregungen haben, kontaktieren Sie uns bitte.

Mit den besten Wünschen für ein frohes Weihnachtsfest und ein gutes Neues Jahr

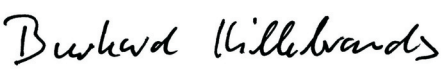

Kaiserslautern, im November 2012

Chapter 2: Personnel

2.1 Members of the group

Group leader:

Prof. Dr. Burkard Hillebrands

Senior scientists:

Dr. Andrii Chumak
Dr. Andrés Conca Parra
Dr. Britta Leven, Akad. Oberrätin
Dr. habil. Alexander Serga
Dr. Vitaliy Vasyuchka

Postdocs and long-term guest scientists:

Dr. Florin Ciubotaru	since 04/12
Dr. Evangelos Papaioannou	since 06/12
Dr. Tomohiro Koyama	since 09/12

Ph.D. students:

Dipl.-Phys. Milan Agrawal	
Dipl.-Phys. Thomas Brächer	
Dipl.-Phys. Florin Ciubotaru	until 04/12
Dipl.-Phys. Peter Clausen	
Dipl.-Phys. Benjamin Jungfleisch	
Dipl.-Phys. Thomas Langner	
Dipl.-Phys. Thomas Meyer	since 09/12
Dipl.-Phys. Roland Neb	
Dipl.-Phys. Björn Obry	
Dipl.-Phys. Philipp Pirro	
Dipl.-Phys. Ana Ruiz Calaforra	
Dipl.-Phys. Thomas Sebastian	
Dipl.-Phys. Georg Wolf	until 11/12
Dipl.-Phys. Katrin Vogt	

Diploma Students:

Philipp Fuhrmann	since 09/12
Viktor Lauer	since 12/11
Thomas Meyer	until 04/12
Jan Westermann	until 07/12

Engineers and Technicians

Dipl.-Ing. (FH) Dieter Weller

Administration:

Sibylle Müller
Dr. Isabel Sattler

2.2 Visiting scientists, postdoctoral fellows and exchange students

(sorted by date of first arrival in our group)

Alexandr Talalaevsky, National Taras Shevchenko University, University of Kyiv, Ukraine — 12.01. - 09.03.2012

Oleksandr Talalayevskyy obtained his MS degree from the Department of Radiophysics of Taras Shevchenko National University of Kyiv in 2011, and afterwards performed his research work in the group of Prof. G. A. Melkov. His scientific interests are mainly connected with the investigations of nonlinear interactions and spectral properties of spin waves in metal magnetic films and dots arrays. In 2011 he joined us for two months to improve his experience in the modern methods of microwave and optical spectroscopy of magnetic materials. The main aim of his work was to study the dynamical and spectral characteristics of spin-waves in layered Pt-YIG structures and to understand the influence of the spin-Hall- and spin-Seebeck-effects on relaxation properties of dipolar-exchange spin waves.

Dr. Koji Sekiguchi, Keio University, Yokohama, Japan — 08.03. - 11.03.2012

Dr. Koji Sekiguchi stayed with us for an exchange of knowhow on Brillouin light scattering spectroscopy. In particular, he was interested in our methods for setting up and aligning the Brillouin light scattering microscope. In addition, we discussed our software tools TFPDAS4 and TFPDAS4-Micro.

Prof. Andrei Slavin, Oakland University, USA — 20.08. - 30.08.2012

The visit of Prof. Slavin was supported by the Deutsche Forschungsgemeinschaft in the frame of the SFB/Transregio 49 “Condensed Matters Systems with Variable Many-Body Interactions”. The results of joint work on theoretical study of energy distribution of magnon gas in parametrically pumped magnetic insulator and thermalization processes in strongly overheated magnon gases have been discussed and prepared for publication.

Dmytro Bozhko, National Taras Shevchenko University of Kyiv, Ukraine — 01.06. - 01.09.2012

Dmytro Bozhko is a graduate student working in the magnetism group of Prof. G. Melkov at the National University of Kyiv. After his short visit in 2011 he visited us this year for 3 months to investigate the temporal dynamics of parametrically controlled magnon gases and condensates. Dmytro significantly improved the adjustment procedure of the wavevector resolved BLS setup and obtained new interesting results on the density distribution of dipolar-exchange magnons in the low-energy spectral area.

Yuki Kawada, Graduate School of Engineering, Tohoku University, Japan — 08.08. - 06.09.2012

Yuki Kawada visited our group in the framework of the DFG-JST-project *Advanced spintronic materials and transport phenomena, ASPIMATT.* In the subproject *Novel devices based on Heusler films with GMR and TMR nanocontacts*, he is responsible for the fabrication of spin-torque nano-oscillators. During his stay, we jointly performed Brillouin light scattering experiments.

Prof. Gennadii Melkov, National Taras Shevchenko University of Kyiv, Ukraine — 20.08. - 09.09.2012

This year the regular visit of Prof. Melkov to our group was supported by the Deutsche Forschungsgemeinschaft in the frame of the SFB/Transregio 49 “Condensed Matter Systems with Variable Many-Body Interactions”. During his stay Prof. Melkov was mainly working on different aspects of phonon-magnon interactions in parametrically and thermally driven magnetic insulators. The recent results of our joint work have been presented on the IEEE 2012 International Conference on Microwave Magnetics, which was held in Kaiserslautern this year and where Prof. Melkov was honored for his life-time achievements in nonlinear spin-wave physics.

Dr. Yevgen Pogoryelov, University of Gothenburg, Sweden — 30.08. - 19.09.2012

During the stay of Dr. Yevgen Pogoryelov in our group, we jointly worked on the observation of spin waves radiated from spin-torque nano-oscillators via Brillouin light scattering microscopy. The devices based on perpendicular magnetized $Ni_{81}Fe_{19}$ free layers were prepared in the group of Prof. Åkerman in Gothenburg.

2.3 Guest seminars

Prof.Dr. Hubert Ebert	LMU München, Germany
14.11.2011	*Ab-initio studies on orbit induced properties of magnetic solids*
	Physics colloquium
Prof. Dr. Gernot Güntherodt	RWTH Aachen, Germany
	Spin currents in nanostructures
16.01.2012	Physics colloquium

2.4 Visits of group members at other laboratories

Andrii Chumak	Faculdade de Ciencias da Universidade do Porto, Portugal 09.11. - 17.11.2011 Host: Dr. Gleb Kakazei
Vitaliy Vasyuchka	Faculdade de Ciencias da Universidade do Porto, Portugal 09.11. - 17.11.2011 Host: Dr. Gleb Kakazei
Thomas Langner	Faculdade de Ciencias da Universidade do Porto, Portugal 09.11. - 17.11.2011 Host: Dr. Gleb Kakazei
Alexander Serga	Faculdade de Ciencias da Universidade do Porto, Portugal 06.02. - 16.02.2011 Host: Dr. Gleb Kakazei
Benjamin Jungfleisch	Institute for Materials Research, Tohoku University, Sendai, Japan 02.04. - 07.06.2012 Host: Prof. Dr. Eiji Saitoh
Thomas Sebastian	Tohoku University, Sendai, Japan 01.04. - 15.05.2012 Host: Prof. Dr. Yasuo Ando
Frank Heussner	University of Alabama, Tuscaloosa, USA 22.05. - 22.08.2012 Host: Prof. Dr. Tim Mewes
Milan Agrawal	Quantum Nano-Scale Magnetics Laboratory, Advanced Science Institute, RIKEN, Hirosawa Wako, Japan 15.01. - 30.03.2012 Host: Prof. Yoshichika Otani
Katrin Vogt	Materials Science Division, Argonne National Laboratory, Argonne, Illinois, USA 11.05. - 09.07.2012 Host: Dr. Axel Hoffmann
Katrin Vogt	University of Hawaii, HI, USA 20.05. - 24.05.2012 Host: Prof. Dr. Murli Manghnani

2.5 Group member photo gallery

Milan Agrawal
Ph.D. student

Thomas Brächer
Ph.D. student

Dr. Andrii Chumak
Senior scientist

Florin Ciubotaru
Ph.D. student

Peter Clausen
Ph.D. student

Dr. Andrés Conca Parra
Senior scientist

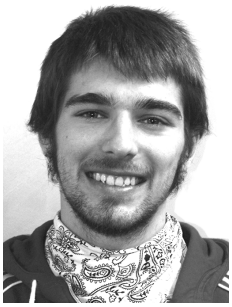

Philipp Fuhrmann
Diploma student

Prof. Dr. Burkard Hillebrands
Group leader

Benjamin Jungfleisch
Ph.D. student

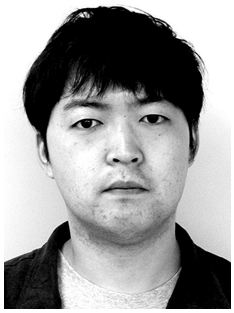

Dr. Tomohiro Koyama
Postdoc

Thomas Langner
Ph.D. student

Viktor Lauer
Diploma student

Dr. Britta Leven
Senior scientist

Thomas Meyer
Ph.D. student

Sibylle Müller
Secretary

Roland Neb
Ph.D. student

Björn Obry
Ph.D. student

Dr. Evangelos Papaioannou
Postdoc

Philipp Pirro
Ph.D. student

Ana Ruiz Calaforra
Ph.D. student

Dr. Isabel Sattler
Administration

Thomas Sebastian
Ph.D. student

Dr. Alexander Serga
Senior scientist

Dr. Vitaliy Vasyuchka
Senior scientist

Katrin Vogt
Ph.D. student

Dieter Weller
Mechanical engineer

Jan Westermann
Diploma student

Georg Wolf
Ph.D. student

Chapter 3: Methods

3.1 Brillouin light scattering spectroscopy (BLS)

Brillouin light scattering (BLS) spectroscopy is one of the key techniques in our laboratory to investigate the dynamic properties of magnetic materials and devices. It is based on the interaction of photons with the fundamental excitations of a solid such as magnons, the quanta of magnetic excitations. The interaction can be understood as an inelastic scattering process of the incident photons with magnons, taking into account energy and momentum conservation as indicated in Fig. 1.

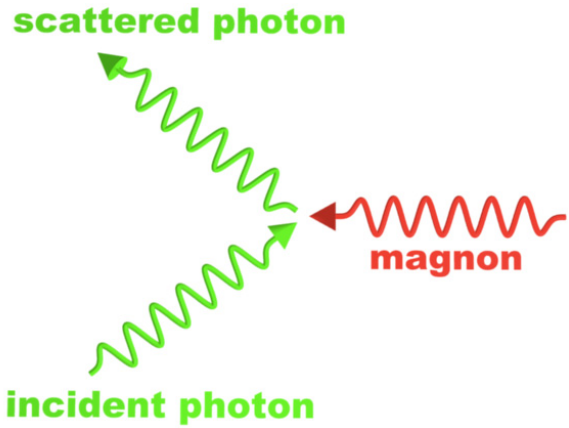

Fig. 1: Scheme of inelastic scattering of an incident photon by a magnon.

The detection of the inelastically scattered photons, i.e. the separation from the elastically scattered photons and the determination of the transferred energy, requires an interferometry technique with extremely high contrast and sensitivity. In our laboratory we implemented the (3+3) Tandem-Fabry-Perot-Interferometer, designed by John R. Sandercock and schematically shown in Fig. 2. It consists of two Fabry-Perot interferometers (FPI), each one passed three times by the inelastically scattered light. This approach results in a contrast better than 10^{10} for the separation of the elastically and inelastically scattered photons in a frequency range from 500 MHz up to 1 THz.

In the last decade we made significant progress in the improvement of BLS spectroscopy. The spatial resolution was pushed to the fundamental limit of classical optics by constructing a BLS-microscope (Fig. 3) with sophisticated active stabilization methods. Spin-wave transport phenomena can be investigated by time, phase- and wave-vector resolution. The following list gives an overview of the different BLS setups available in our group:

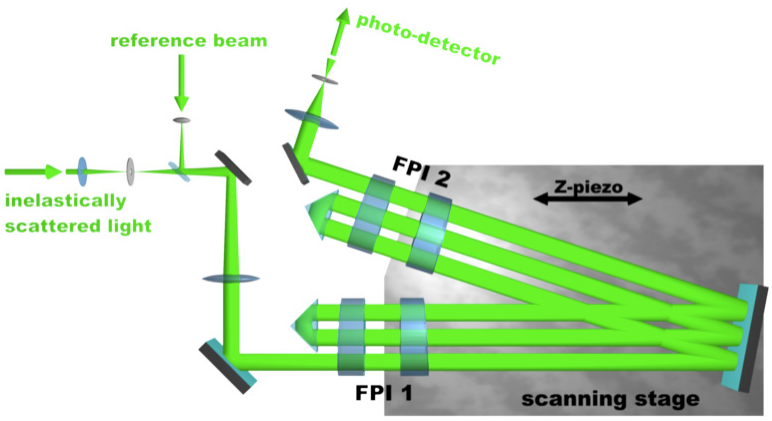

Fig. 2: Scheme of a (3+3) tandem Fabry-Perot interferometer, designed and build by John R. Sandercock (JRS Scientific Instruments, Zürich)

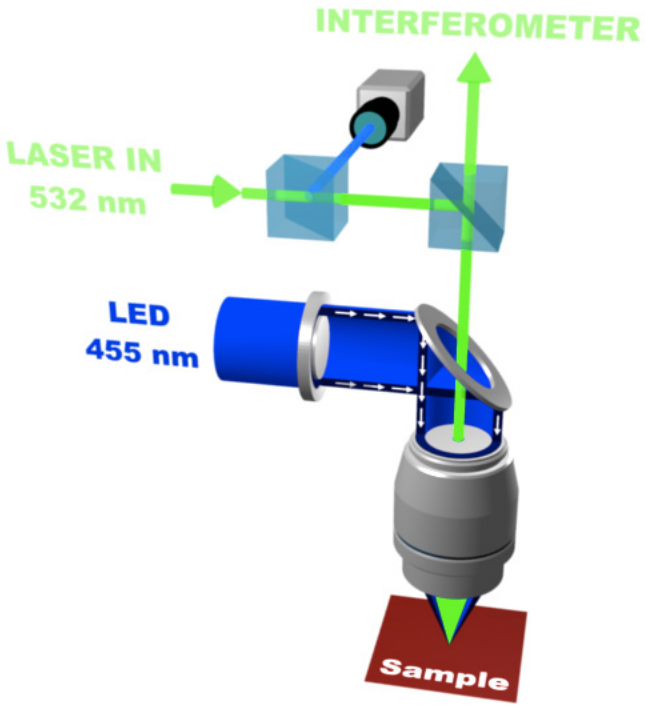

Fig. 3: Schematic setup of a BLS-microscope. The LED light is used to monitor the position of the laser focus on the sample by a CCD camera and to apply active position control to the sample stage.

BLS1: High-field electromagnet (1.2 T), standard BLS spectroscopy equipment. Time resolution, phase resolution, space resolution (50 µm), wave-vector resolution.

BLS2: High-field electromagnet (1.2 T), standard BLS spectroscopy equipment. Microscope stage with 200 nm spatial resolution and build-in time and phase resolution.

BLS3: High-field electromagnet (1.2 T), standard BLS spectroscopy equipment. Microscope stage with 200 nm spatial resolution and build-in time and phase resolution.

BLS4: Electromagnet (0.1 T), standard BLS spectroscopy equipment. Microscope stage with 200 nm spatial resolution and build-in time and phase resolution.

3.2 Microwave techniques

The Brillouin Light Scattering (BLS) spectroscopy described in the previous section is indeed a powerful tool for the detection of spin waves and measurement of their characteristics. Nevertheless, it allows no spin-wave excitation. Thus, in many of our experiments BLS spectroscopy is combined with microwave techniques which ensures high-efficient generation of spin waves in magnetic structures. Spin waves are emitted by nano- and micro-sized microstip antennas placed on the surface of magnetic thin films and is driven by a microwave signal in the GHz frequency range [1]. Microwave sources in our laboratories generate the signals up to 67 GHz providing access to spin-waves in a very wide range of frequencies and wavenumbers. Furthermore, large powers (up to 100 W) provided by microwave amplifiers allow the study of strongly nonlinear spin-wave dynamics as well as quantum effects in parametrically-driven magnon gases. The microwave technique allows the excitation of both, continuous spin waves as well as short spin-wave packets. Among the others advantages, the pulsed technique allows the realization of time resolved (resolution down to 250 ps) BLS spectroscopy [2] shown in Fig. 1. The continuous microwave excitation, by-turn, allows realization of phase-resolved BLS spectroscopy [3, 4].

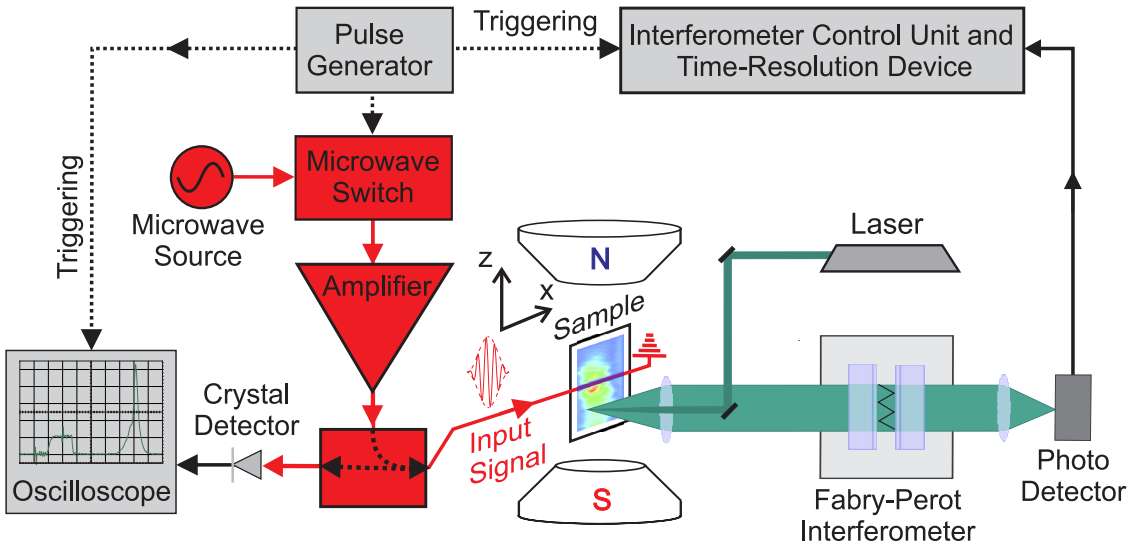

Fig. 1: Scheme of the microwave-assisted time- and space-resolved BLS setup

Besides the excitation of spin waves, the microwave technique is intensively used for high-sensitive (10^{-13} W) detection. Using the same antennas the magnetization precession is converted into microwave currents. These currents are amplified by low-noise amplifiers and analyzed using wide-band oscilloscopes, vector network analyzers or a spectrum analyzer [1]. A vector network analyzer is also used for the ferromagnetic resonance (FMR) measurements allowing determination of such characteristics of the magnetic thin films as magnetization saturation, exchange constant, and damping.

References

[1] A.A. Serga, A.V. Chumak, B. Hillebrands, *YIG magnonics*, J. Phys. D **43**, 264002 (2010).
[2] O. Büttner, M. Bauer, S.O. Demokritov, B. Hillebrands, Yu.S. Kivshar, V. Grimalsky, Yu. Rapoport, A.N. Slavin, *Linear and nonlinear diffraction of dipolar spin waves in yttrium iron garnet films observed by space- and time-resolved Brillouin light scattering*, Phys. Rev. B **61**, 11576 (2000).
[3] A.A. Serga, T. Schneider, B. Hillebrands, S.O. Demokritov, M.P. Kostylev, *Phase-sensitive Brillouin light scattering spectroscopy from spin-wave packets*, Appl. Phys. Lett. **89**, 063506 (2006).
[4] K. Vogt, H. Schultheiss , S.J. Hermsdoerfer, P. Pirro , A.A. Serga, B. Hillebrands *All-optical detection of phase fronts of propagating spin waves in a $Ni_{81}Fe_{19}$ microstripe* Appl. Phys. Lett. **95**, 182508 (2009).

3.3 Magneto-optic Kerr effect magnetometry and microscopy (MOKE)

The magneto-optical Kerr effect (MOKE) is a well established technique to study magnetization properties. The effect is based on the fact, that the plane of polarization of light is rotated when the light is reflected from a magnetic material [1]. The physical origin of MOKE is the magnetic circular dichroism effect: exchange and spin-orbit coupling in a magnetic material lead to different absorption spectra for left- and right-circularly polarized light. Measuring the change of the polarization of the reflected beam (often referred to as Kerr angle Θ_{Kerr}) gives access to the magnetization state of the sample.

With MOKE it is possible to study quasi-static magnetization reversal properties and magnetic anisotropies. When using a pulsed laser system it is also possible to study the time dependence of

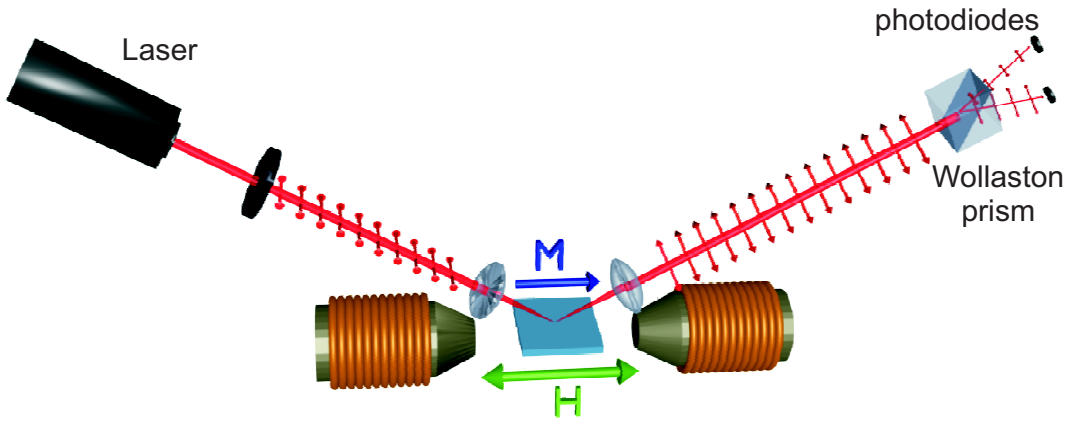

Fig. 1: Schematic setup of a longitudinal Kerr magnetometer.

the magnetization under the influence of, e.g., a pulsed magnetic field or a microwave field. Since it is an optical technique it is non invasive, and the spatial resolution is only limited by the optical resolution. Thus, we are able to study the static and dynamic properties of magnetic thin films and magnetic structures with lateral dimension down to 1 µm.

Our group uses four different MOKE setups, all of them using the same principle. The light of a laser source is s-polarized through a thin-film polarizer. The beam is focused onto the sample. The polarization of the reflected light is analyzed by a detector unit that was developed and is built in our laboratory. A Wollaston prism divides the beam into two orthogonally polarized beams, which are monitored by a pair of photodiodes. The detector works as an opto-electrical bridge circuit to increase the signal-to-noise ratio. The obtained normalized differential signal $(I_1 - I_2)/(I_1 + I_2)$ is directly proportional to the Kerr angle Θ_{Kerr}.

Four experimental setups are available to investigate different scientific aspects:

Longitudinal Kerr magnetometer: Longitudinal MOKE geometry to probe quasi-static properties of magnetic thin films. Optical resolution $\sim 100\,\mu\text{m}$, magnetic field up to 2 T, automated sample positioning and rotation.

Microfocus Kerr microscope with rotation unit: Longitudinal MOKE geometry to probe quasi-static properties of micro-structured magnetic elements. Optical resolution $< 1\,\mu\text{m}$, magnetic field up to 0.6 T, automated sample positioning, rotation and stabilization.

Dual MOKE magnetometer: Two combined MOKE magnetometers working in parallel, one in longitudinal and one in polar geometry to study the quadratic MOKE effects on magnetic thin films. Optical resolution $\sim 100\,\mu\text{m}$, two orthogonal pairs of magnet coils to provide any in-plane field direction up to 0.25 T, automated sample positioning and rotation.

Time resolved scanning Kerr microscope: Longitudinal or polar MOKE geometry to study dynamic magnetization reversal properties of micro-structured elements. Optical resolution $< 500\,\text{nm}$, time resolution $\sim 60\,\text{ps}$, magnetic field up to 150 mT, automated sample positioning and stabilization.

References

[1] J. Kerr, *On rotation of the plane of polarization by reflection from the pole of a magnet*, Phil. Mag. **4**(5), 321 (1877).

3.4 Molecular beam epitaxy (MBE)

The Molecular Beam Epitaxy (MBE) technique involves highly controlled evaporation of materials in an ultra-high vacuum chamber ($\sim$ low 10^{-11} mbar). This deposition from the vapor phase can lead to single crystal film growth. For this reason MBE possesses a dominant role in the world of nanotechnology in fabrication of materials for high performance applications. Our group operates two MBE clusters. One of them is displayed in Fig.1. Both systems are equipped with tools for cleaning the substrates, for controlling the evaporation from the sources and the film deposition, for in-situ structural and chemical characterization, as well as for sample storage.

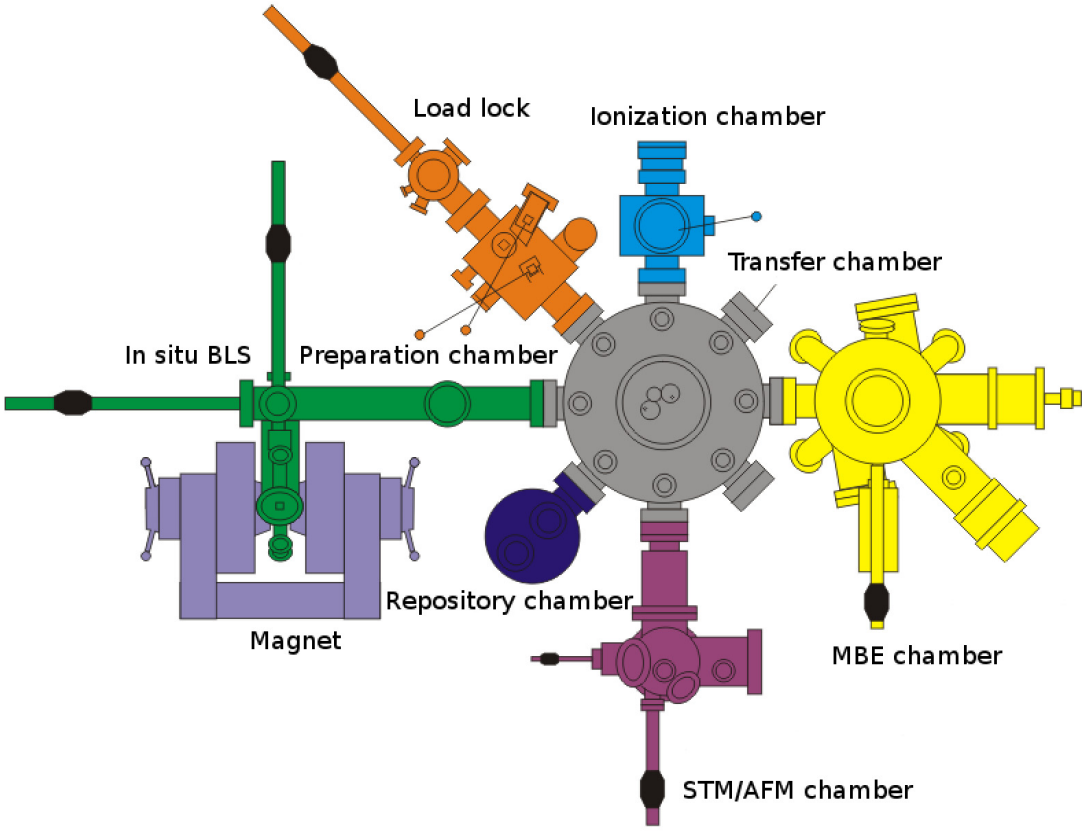

Fig. 1: Schematic diagram of the MBE growth cluster.

In more details, the heart of the cluster of Fig. 1 constitutes an ultra-high vacuum (UHV) Molecular Beam Epitaxy (MBE) growth chamber. It contains two Knudsen cells, and one electron gun with 4 crucibles that are used to heat and evaporate the materials. The growth procedure is controlled in situ by a quartz crystal. One of the great advantages of our MBE system is the capability to control the in situ growth by means of Reflection of High-Energy Electron Diffraction (RHEED) and of Low-Energy Electron Diffraction (LEED) and Auger analytics. A RHEED pattern of a Pt/Fe film deposited on MgO is shown in Fig. 2. The characteristics of the RHEED technique is not to interfere with the deposition. This renders it as a unique tool for real-time structural characterization of the sample.

In addition to the aforementioned techniques and linked to the MBE, an AFM-STM set-up is used for in-situ atomic probing. The cluster includes furthermore a load chamber for inserting samples in vacuum and preparation chamber. The latter is used for cleaning the samples since there is the

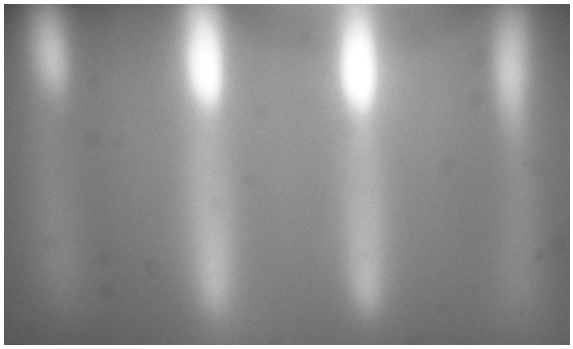

Fig. 2: An example of a RHEED pattern: a few monolayers of Pt grown on Fe on a MgO substrate. The appearance of spots superimposed on the streaks indicate the nucleation of islands on a flat surface. RHEED is a powerful tool in our hands, suitable for the study of dynamical processes during film growth.

possibility to heat up to 2300° the samples. Furthermore, there is an option for optical coatings. The ion beam chamber is equipped with a fine-focus noble gas keV ion source, with the module of ion beam oxidation. A transfer chamber connects all the parts of the growth cluster while a repository chamber is also available.

The cluster of Fig. 1 has another unique feature: that of in-situ magnetic characterization with Brillouin light scattering spectroscopy and Kerr effect magnetometry. The applied magnetic field can reach 1.2 T. There is an option for implementation of a cryostat.

The MBE evaporation technique offers unique advantages for the fabrication of patterned samples. The good control of the film growth and the directionality of the beam renders MBE suitable to grow materials on patterned masks. Patterned samples of extreme quality can be produced either with pre- or post treatment techniques, see i.e. Fig. 3.

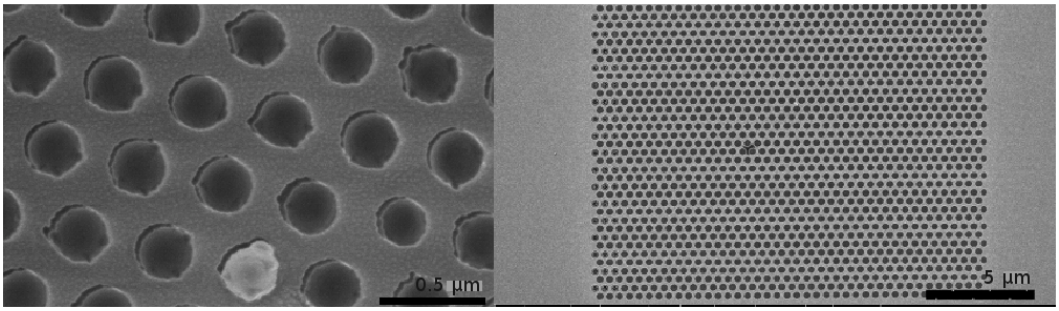

Fig. 3: Scanning electron microscopy surface images of two anti-dot samples prepared in the MBE. The samples are composed of a Au/Py/Au trilayer. To the left the sample was directly prepared on a mask composed of polystyrene spheres. To the right the anti-dot lattice was fabricated ex-situ, after the deposition of the trilayer, with the help of the Focus Ion Beam (FIB) technique. The MBE offers unique advantages in preparing high quality patterned samples.

Chapter 4: Reports on Experimental Results

A. Magnon Gases and Condensates

In ferromagnetic materials atoms having unpaired electrons act as individual magnets. Their magnetism is mostly caused by the magnetic moments of the uncompensated electron spins. Since these atomic magnets tend to be oriented in the same direction due to quantum-mechanical exchange interaction, a macroscopic magnetic moment appears. As the atoms strongly interact a reversal of a single atomic magnetic moment is not spatially localized but spreads through the solid as a wave of discrete magnetic momentum transfer. This wave is known as a spin wave, and in frame of the second quantization it is associated with a quasi-particle called magnon. Weakly interacting magnons can be considered as a gas of magnetic bosonic quasi-particles, and therefore this is called a magnon gas. It is remarkable that the character of magnon-magnon interactions within magnon gases as well as their static and dynamic spectral properties can be effectively controlled using a combination of static and microwave frequency external magnetic fields. For example, the dispersion branch of a magnon gas can be frequency shifted or even drastically modified by change of strength or orientation of a bias magnetic field.

Recently magnon gases have been recognized as an excellent model environment for the experimental investigation of collective classical and quantum macroscopic properties of bosonic systems. The phenomenon of high-temperature Bose-Einstein condensation (BEC) of magnons in a magnetically ordered medium first reported by our group (Nature **443**, 430 (2006)) is one demonstration of this. It is known that BEC can be achieved either by decreasing the temperature of the ideal gas of bosons or by increasing its density. The most effective mechanism to increase the magnon density above the thermally equilibrated level is microwave parametric pumping (see Gurevich and Melkov, Magnetization Oscillation and Waves, CRC, Cleveland, 1996). In the simplest case one photon of the pumping electromagnetic field excites two magnons with half the energy/frequency that propagate in opposite directions. Such a mechanism creates a huge quantity of phase correlated magnons, called condensate of photon-coupled magnon pairs. Among others, such magnon pairs serve as an energy source and as a strong disturbing factor for the entire spin-wave system. Formation, thermalization and disintegration of this condensate as well as its interaction with the other magnonic states and especially with the magnon BEC constitutes a hot topic of research. The main goal of our work is to study the phase transition processes resulting in the formation of quantum macroscopic states of a magnon gas and to understand the role of multi-magnon interactions in the properties of these correlated states of matter in comparison with the dynamics of ultra-cold quantum gases and quantum spin systems. The main experimental method is space-, time- and wavevector-resolved Brillouin light scattering (BLS) spectroscopy in combination with microwave pumping techniques.

In Report 4.1 “Dynamics of hot magnon Bose-Einstein condensate in wavevector-space” we show that the growth of the magnon gas temperature with increase of the pumping power leads to the pronounced spectral redistribution of gaseous magnons, and thus to the disappearance of the magnon BEC. At the same time the magnon condensation at the energy minimum of the magnon spectrum caused by cooling of a magnon gas after the pumping pulse is clear observed. In Report 4.2 “Phonon mediated Bose-Einstein condensation of magnons” we present the observation of a magneto-elastic magnon mode in the parametrically driven magnon gas and discuss its possible influence on the magnon BEC formation. This experiment gives us first experimental evidence of a phonon contribution to the magnon gas thermalization and magnon condensation. In Re-

port 4.3 we demonstrate how an inhomogeneous magnetization leads to a change of the generated mode in the supercritical regime of parametric amplification.

A. Magnonengase und -kondensate

In ferromagnetischen Materialien treten Atome, die ungepaarte Elektronen haben, als einzelne Magnete auf. Ihr Magnetismus wird in der Regel durch die magnetischen Momente des nicht kompensierten Elektronenspins verursacht. Diese atomaren Magnete richten sich aufgrund der quantenmechanischen Austauschwechselwirkung in einem Ferromagneten parallel zueinander aus. Daher beobachtet man ein makroskopisches magnetisches Moment. Da die Atome stark miteinander wechselwirken, wird das Umklappen eines einzelnen atomaren Moments nicht räumlich lokalisiert sein, sondern breitet sich als Welle mit einem diskreten magnetischen Moment über den gesamten Festkörper aus. Diese Welle wird als Spinwelle bezeichnet und ist im Rahmen der zweiten Quantisierung mit einem Quasiteilchen, dem so genannten Magnon, verbunden. Schwach miteinander wechselwirkende Magnonen können als Gas von magnetischen bosonischen Quasiteilchen angesehen werden. Daher werden sie auch als Magnonengas bezeichnet. Ihr Potenzial liegt dabei in der guten Kontrollierbarkeit der Magnonendichte und den Eigenschaften des Spektrums, welche die Magnon-Magnon-Wechselwirkung beeinflusst und wirksam mit statischen und dynamischen Magnetfeldern im Mikrowellenfrequenzbereich kontrolliert werden können. Zum Beispiel kann nur durch eine Änderung der Richtung oder der Stärke eines externen Magnetfelds das Spektrum des Magnonengases leicht in der Frequenz verschoben oder stark verändert werden.

Magnonengase sind unlängst als hervorragendes Modellsystem erkannt worden und dienen zur Untersuchung von korrelierten bosonischen Systemen mit sowohl klassischen Eigenschaften als auch mit makroskopischen Quanteneigenschaften. Die Beobachtung der Bose-Einstein-Kondensation (BEC) von Magnonen bei Raumtemperatur in einem magnetisch geordneten System in unserer Arbeitsgruppe (Nature **443**, 430 (2006)) zeigt dies deutlich. Es ist bekannt, dass ein BEC entweder durch Absenken der Temperatur des idealen Bosonengases oder durch Erhöhung der Bosonendichte erreicht werden kann. Der wirkungsvollste Mechanismus, Magnonen in ein Magnonengas einzufüllen, ist parametrisches Pumpen mittels Mikrowellen (s. Gurevich and Melkov, Magnetization Oscillation and Waves, CRC, Cleveland, 1996). Im einfachsten Fall erzeugt ein Photon des elektromagnetischen Pumpfeldes zwei Magnonen mit je der Hälfte der Energie des Photons, die sich in entgegengesetzte Richtungen ausbreiten. Dieser Mechanismus erzeugt eine große Anzahl von phasenkorrelierten Magnonen, ein Kondensat von photonengekoppelten Magnonenpaaren. Unter anderem dienen solche Magnonenpaare als Energiequelle und als starke Störung des gesamten Spinwellensystems. Erzeugung, Thermalisierung und Zerfall dieses Kondensats sowie seine Wechselwirkung mit anderen Magnonenzuständen und besonders mit dem Bose-Einstein-Kondensat von Magnonen sind ein aktuelles Thema unserer Forschung. Das Hauptziel der aktuellen Forschung ist die Untersuchung der Phasenübergänge, die zu der Bildung von Zuständen mit makroskopischen Quanteneigenschaften in Magnonengasen führen, und das Verständnis der Funktion der Viel-Magnonen-Wechselwirkungen in diesen korrelierten Zuständen der Materie im Vergleich mit der Dynamik von ultrakalten Quantengasen und Quanten-Spinsystemen. Zur Untersuchung dieser Prozesse verwenden wir zeit- und wellenvektoraufgelöste Brillouin-Lichtstreuspektroskopie in Verbindung mit konventioneller Mikrowellentechnik.

In Bericht 4.1 “Dynamics of hot magnon Bose-Einstein condensate in wavevector-space” wird gezeigt, dass die Erhöhung der Temperatur eines Magnonengases durch Erhöhung der Pumpleistung zu einer ausgeprägten Umverteilung der gasartigen Magnonen und somit zum Verschwinden

des BEC führt. Im Bericht 4.2 “Phonon mediated Bose-Einstein condensation of magnons” wird die Beobachtung einer magnetoelastischen Magnonenmode im parametrisch gepumpten Magnonengas vorgestellt und der denkbare Einfluss auf die Bildung des Magnonen-BEC diskutiert. Dieses Experiment liefert die ersten experimentellen Anzeichen für den Beitrag der Phononen zur Thermalisierung des Magnonengases und der Magnonenkondensatbildung. In Bericht 4.3 zeigen wir, wie eine inhomogene Magnetisierung zu einer Veränderung der erzeugten Mode im superkritischen Bereich der parametrischen Verstärkung führt.

4.1 Dynamics of hot magnon Bose-Einstein condensate in wavevector-space

A. A. Serga and B. Hillebrands

In collaboration with: D. Bozhko, Department of Radiophysics, Taras Shevchenko National University of Kyiv, 01601 Kyiv, Ukraine.

It is known that, in order to obtain Bose-Einstein condensation (BEC) of magnons, a low temperature is not required because the number of quasi-particles is readily increased by external pumping [1]. However, as it has been already shown [2], the pumping process influences the magnon BEC in a very nontrivial way: On the one hand the pumping plays the role of the magnon source, but on the other hand it is a strong spurious factor for the entire magnon system. This is especially pronounced in time-resolved Brillouin light scattering (BLS) experiments with pulsed pumping applied to in-plane magnetized single-crystal yttrium iron garnet (YIG) films. As it is expected, the intensity of the BLS signal produced by parametrically injected magnons sharply falls down just after the pumping pulse is switched off. This fast decay (can be around 10 ns) is mainly caused by intensive four-magnon scattering and thermalization of this dense magnon group. The gaseous magnon phase, which lies between the region of parametrically excited magnons and the bottom of the magnon spectrum, also decays after the pumping pulse ends. This decay is very clearly non-exponential and happens on a much longer time scale than the thermalization of the primary injected magnons. Nevertheless, the BLS signal from the bottom of the spectrum has a different, unexpected behaviour when the pumping is switched off: The density of the bottom magnons dramatically jumps upward. Moreover, its rise time perfectly correlates with the fall of the gaseous magnon phase. After reaching a peak value the condensate then exponentially decays with the spin-lattice relaxation time of about 400 ns, which is the intrinsic decay time of the YIG material used.

In spite of the fact, that the first observation of this unusual magnon dynamics was reported by us in 2009 (see Ref. [3]) the theoretical interpretation and understanding of the described phenomenon were delayed due to the lack of data about the bottom magnons. As the dispersion curve of the low-energy magnons is very flat (the wavenumber q varies here from 10^4 to 10^5 rad/cm in a frequency band of 150 MHz, which usually corresponds to the resolution of the Fabry-Pérot interferometer) a simple frequency analysis is not enough for the confident detection of BEC. Thus, it was not clear if the observed jump of the BLS signal, which is detected in frequency band of 150 MHz around the minimal energy, can be really associated with the magnon BEC. The detected light could be potentially scattered not by the BEC but gaseous magnons distributed in the wide range of wavenumbers apart from the energy minimum.

In order to answer this question the spectral distribution of magnon gas densities has been measured as a function of the frequency (energy) and wavevector (momentum) using time- and wavevector-resolved BLS spectroscopy [4]. Special attention was focused on spectral areas where the transition between gaseous and condensed magnon phases is expected to occur. Precise time-dependent measurements of the magnon distribution in a momentum-space was performed near the minimum energy of the magnon gas for different pumping powers. The obtained results have evidenced the connection of the described BLS signal jump with the dynamics of the magnon BEC density and revealed the peculiarities of the dynamics both of externally driven and freely evolving magnon gases.

The experiment was performed using the experimental setup schematically shown in Fig. 1. The main part of the setup is a yoke which is mounted on top of a rotating plate in order to vary the

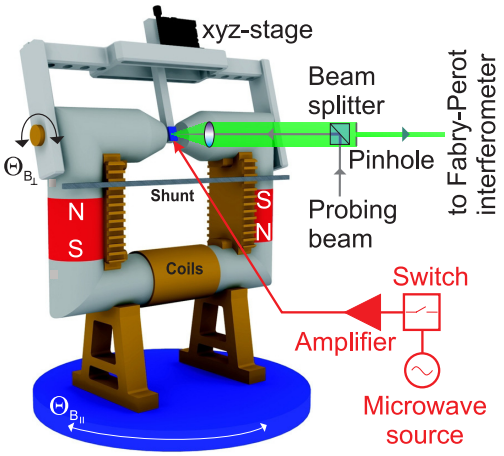

Fig. 1: 2D wavevector-resolved BLS setup. The setup consists of a yoke with two permanent magnets which are mounted on top of a rotating plate in order to vary the angle $\Theta_{B\|}$. The tuning of the field between the two poles is realized by iron shunts mounted parallel to the poles and a small electromagnet. The YIG sample is placed on a 50 µm wide microstrip antenna which is fabricated on top of an aluminum nitride substrate. A microwave source, a switch, and a power amplifier are directly connected to the antenna in order to drive the spin-wave system.

angle $\Theta_{B\|}$ between the sample and the probing beam in the horizontal plane. By varying this angle, spin waves which are oriented parallel to the external magnetic field $\mathbf{H}_0$ can be investigated. The sample itself is mounted on a freely pivotable lever using a small *xyz* stage, which allows precise positioning of the sample. By changing $\Theta_{B\perp}$ the in-plane component of the wavevector oriented perpendicular to the bias field can be selected and investigated. The yoke itself consists of two NdFeB-permanent magnets in order to satisfy the demands of long-term stability of the bias magnetic field in combination with a sufficiently large field strength of 2100 Oe. Iron shunts are used to effectively control the magnetic field in the pole gap. For the automated fine tuning of the bias magnetic field a small electric coil in combination with a Hall sensor has been installed. Thus, the magnetic field strength can be tuned from 1300 to 2100 Oe, with an accuracy of 0.5 Oe. The probing light source is a single-mode solid state laser with 532 nm wavelength. The light coming from the source is redirected by a polarizing beam-splitter cube and sent through an objective to the sample. A pinhole is placed in the beam of the inelastically scattered light to assure that only the light coming directly through the middle of the objective is passing to the interferometer. For reasons of proper focusing and spatial stabilization the setup is additionally equipped with a CCD camera and a white light source in order to enable permanent control of the position of the probing laser spot. The described setup allows us the detection of magnon with wavenumbers up to $2.36 \cdot 10^5$ rad/cm and a resolution of $4.1 \cdot 10^3$ rad/cm. Time resolution is 250 ps, frequency resolution 150 MHz, and spatial resolution 25 µm.

An in-plane magnetized YIG single crystal film of 5 µm thickness is placed on a 50 µm wide microstrip antenna. The antenna itself is fabricated on top of an aluminum nitride substrate which was used due to its excellent thermal conductivity to suppress possible heating effects caused by high microwave power. A pump circuit consisting of a microwave source, a switch, and a power amplifier feeds the antenna with 1.5 µs long microwave pulses at 13.62 GHz carrier frequency. The microstrip antenna is oriented for application of the pumping Oersted field along the bias field direction. Thus, the case of the parallel parametric pumping is realized. The bias magnetic field is tuned to $H_0 = 1710$ Oe to allow the excitation of parametric magnons at the ferromagnetic resonance (FMR) frequency. In this case the direct scattering of the parametric magnons to the bottom of the spin-wave spectrum is prohibited by the conservation laws, and thus the conditions for efficient multistage four-magnon scattering, which is necessary for magnon gas thermalization, and consequently for BEC formation, are satisfied.

The results of the wavevector-resolved measurements are shown in Fig. 2 for different pumping powers. In all cases the thermalized magnons appear at the bottom of the spectrum after some

delay relative to the application of the pumping pulse. This delay decreases from 200 ns to 100 ns with increasing pumping power, and thus with intensifying the four-magnon scattering inside of the parametrically injected magnon group. It is also interesting that the population of the lowest energy states always begins with the short-wavelength magnons having $q \geq 10^5$ rad/cm. However, the following evolution of the magnon gas differs drastically for different pumping powers.

At a relatively small pumping power 1 W, after some transition time of $\simeq 0.5\,\mu$s, the excess magnons occupy the wavenumber range from $2 \cdot 10^4$ rad/cm to $7 \cdot 10^4$ rad/cm and condense exactly in the global energy minimum at $3.8 \cdot 10^4$ rad/cm. The small increase of the pumping power to 2 W and afterwards to 4 W results in a significant decrease of the relative density of the BEC and broadening of the populated wavenumber range (see Fig. 2b-c). However, just after the pumping pulse the magnons concentrate in the energy minimum at $3.8 \cdot 10^4$ rad/cm and form there a pronounced BEC peak. At the pumping power of 25 W no visible overpopulation of the energy minimum exists anymore during the entire pumping time. Moreover, the density distribution of the low-energy magnons is shifted to the region of the high wavenumbers above $5 \cdot 10^4$ rad/cm (see Fig. 2d). But, as previously, when the pumping is switched off the magnons rush to the lowest energy state and form there a huge BEC density peak.

This behaviour is relatively easily explained once one realizes that the thermalization of the pumped magnon gas occurs only within a narrow energy region near the bottom of the spectrum, where the magnon gas is strongly overheated by pumping. In the case of a low pumping power of 1 W, and thus in the case of moderate heating of the magnon gas, the clearly visible concentration of magnons at the global energy minimum (see Figs. 2a) near $q = 4 \cdot 10^4$ rad/cm occurs. In the case of strong pumping power of 25 W the magnon gas is too hot and no Bose-Einstein condensation is possible during the pumping pulse. At the same time, as a result of nonlinear magnon-magnon scattering, a magnon may gain additional energy and leave the low-energy thermalization region, thus reducing the average energy of the remaining magnons. This mechanism is similar to the well known process of evaporative cooling in real atomic gases. After an external heater (pumping) is switched off it can significantly and fast (on a time scale of the four-magnon scattering inside of the gaseous magnon phase $\simeq 45$ ns in our experiment) reduce the temperature of the bottom spectral area. For such short time the quantity of the excess magnons, which depends on the magnon-phonon relaxation time of $\simeq 400$ ns, does not change visibly, and thus the perfect conditions for the BEC formation are established. A simple analytical model of such “evaporative cooling”of a quasi-equilibrium magnon gas, which has been developed in collaboration with V. Tiberkevich and A. Slavin (USA), gives a good quantitative explanation of the experimentally observed phenomena. A publication of these results is in preparation.

We can conclude that in the case of a weak pumping the injected magnons thermalize in energy-wavevector space, populate the bottom of the spectrum, and create the magnon BEC. In the case of strong pumping the magnon BEC does not form during the pumping pulse and appears only after the pump is switched off. The absence of the magnon BEC and corresponding spectral redistribution of gaseous magnons can be understood as the result of the spectrally localized heating of the magnon gas by parametrically injected magnons. Therefore, the formation of the BEC of magnons after the pumping pulse is caused by cooling of the magnon gas. The new physical interpretation of magnon gas thermalization and magnon BEC formation suggests new ways to control formation of the condense magnon phase by enhancing or suppressing the process of evaporative cooling.

Financial support by the Deutsche Forschungsgemeinschaft within the SFB/TRR 49 is gratefully acknowledged.

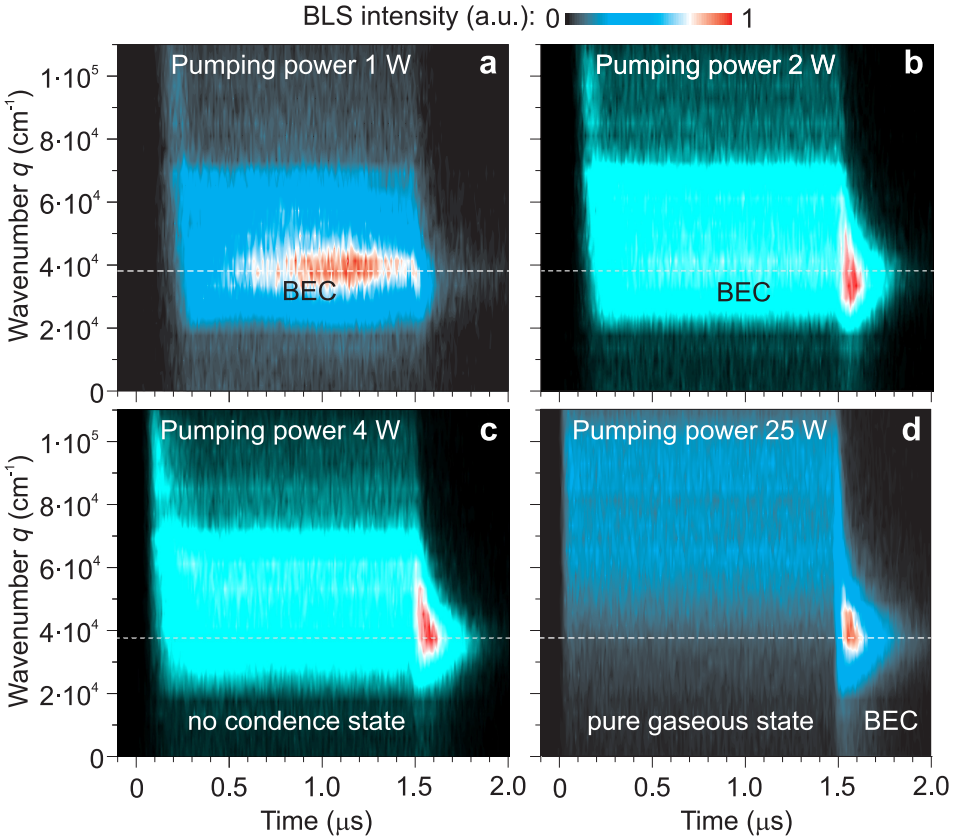

Fig. 2: Time evolution of Bose-Einstein condensate of magnons in q-space. The pump pulse of 1.5 µm duration is switched on at zero time. The BLS intensities are measured in a frequency band of 150 MHz near the bottom of the magnon spectrum for different magnon wavevectors q along the magnetization direction. a) In the case of a low pumping power the parametrically injected magnons thermalize in energy-wavevector space, populate the bottom of magnon spectrum, and create the magnon BEC at the global energy minimum near wavenumber $q = 4 \cdot 10^4\,\mathrm{rad/cm}$. b) In the case of a stronger pumping the magnon BEC density decreases during the pumping pulse and increases after its end. c)-d) The magnon gas significantly overheated by the strong pumping does not condense at all during the pumping pulse and BEC appears only as a result of the evaporative cooling after the pump is switched off.

References

[1] S.O. Demokritov, V.E. Demidov, O. Dzyapko, G.A. Melkov, A.A. Serga, B. Hillebrands, A.N. Slavin, *Bose-Einstein condensation of quasi-equilibrium magnons at room temperature under pumping*, Nature **443**, 430 (2006).

[2] A.A. Serga, V. Tiberkevich, C. Sandweg, V. Vasyuchka, A. Chumak, B. Obry, G. Melkov, A. Slavin, B. Hillebrands, *Magnon gases and condensates* (INVITED). Abstract Book of 2nd International Workshop on Magnonics: From Fundamentals to Applications, Recife, Brasil, p. 20-21 (2011).

[3] C.W. Sandweg, A.A. Serga, V.I. Vasyuchka, T. Neumann, A.V. Chumak, B. Obry, H. Schultheiss, B. Hillebrands *Pumping-free dynamics of Bose-Einstein condensate of magnons*, Annual Report 2009: http://www.physik.uni-kl.de/hillebrands/publications/annual-reports/annual-report-2009

[4] C.W. Sandweg, M.B. Jungfleisch, V.I. Vasyuchka, A.A. Serga, P. Clausen, H. Schultheiss, B. Hillebrands, A. Kreisel, P. Kopietz, *Wide-range wavevector selectivity of magnon gases in Brillouin light scattering spectroscopy*, Rev. Sci. Instrum. **81**, 073902 (2010).

4.2 Phonon mediated Bose-Einstein condensation of magnons

A. A. Serga, P. Clausen, A. V. Chumak, and B. Hillebrands

In collaboration with: D. Bozhko and G. Melkov, Department of Radiophysics, National Taras Shevchenko University of Kyiv, Kyiv, Ukraine.

It has already been recognized that the revelation of the interplay between the magnon and phonon subsystems is of crucial importance for a proper understanding of such various things as the magnetic relaxation and the magnon temperature [1], thermoelectric magnetic phenomena [1, 2], the non-equilibrium time evolution and thermalization of an overpopulated magnon gas [3].

Here we report on the first observation of a magneto-elastic magnon (MEM) mode populated due to the thermalization of a parametrically driven magnon gas (see Fig. 1). In a single-crystal yttrium iron garnet (YIG) film, which is in-plane magnetized by a bias magnetic field of 1710 Oe, this mode lies near the bottom of a magnon spectrum and is practically frequency degenerated with a Bose-Einstein magnon condensate (BEC). However, it has approximately twice the wavenumber of the BEC, and thus can be resolved using wavenumber-sensitive Brillouin light scattering (BLS) spectroscopy. It is remarkable that the MEM mode starts to be visible at pumping powers at least ten times smaller than the threshold of the BEC formation. It allows us to assume the existence of a novel highly-efficient phonon-mediated thermalization channel to the bottom part of the magnon spectrum. In addition, with increasing the pumping power (and consequently of the BEC density) the growth of the MEM mode is suppressed. This can evidence the role of the MEM as an intermediate magnon reservoir enhancing the BEC formation.

BLS studies of both static and dynamic distributions of a parametrically driven magnon gas were performed both in frequency- and wavenumber-spaces using the experimental setup described in the previous Report 4.1 (see Fig. 1 there). In the experiment an in-plane magnetized 6.7 µm thick YIG film was used. The number of magnons, and thus the temperature and the chemical potential μ of a magnon gas in the film were controlled by means of parametric electromagnetic pumping applied at 13.62 GHz. The parametric magnons were excited at half of the pumping frequency near the frequency of the ferromagnetic resonance. The probing laser beam was focused on the YIG film in a 50 µm spot placed just on the longitudinal axis of the pumping stripe. As opposed to the previous experiment the width of the pump stripe is increased to 500 µm in order to improve both the spatial uniformity of the pumping Oersted field and the wavenumber resolution of the setup.

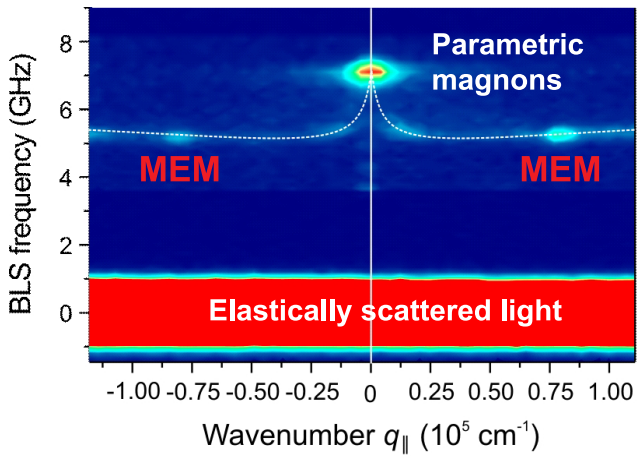

Fig. 1: Intensity map of a scattered light in frequency – wavenumber coordinates. $q_{\parallel}$ is the wavenumbers of magnons propagating in the YIG film plane along the magnetization direction. The white dashed line denotes the dispersion curve of the lowest magnon mode. A relatively low pumping power of 2.6 W is used to drive the magnon gas, thus no BEC is observed. The bright spots at $q_{\parallel} = \pm 8.58 \cdot 10^4$ rad/cm correspond to the MEM mode.

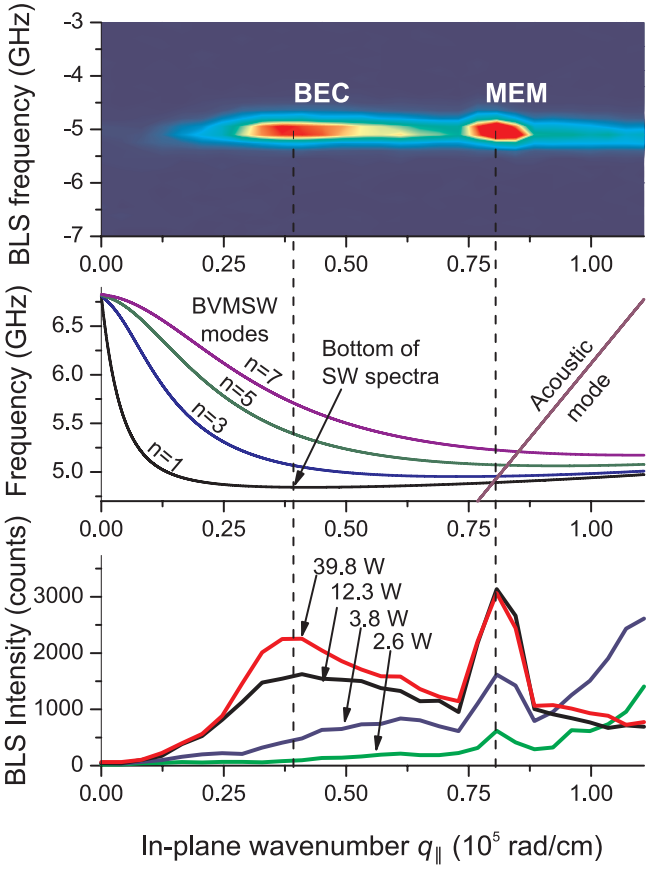

Fig. 2: Comparison of bottom magnon modes with calculated dispersion relations. a) Detailed view of the "BEC hump"and MEM mode simultaneously observed for pump power of 39.8 W. b) The cross point of the dispersion characteristics of BVMSW thickness modes and a transversal acoustic wave. c) Evolution of the BEC hump at the global energy minimum at $q_{\parallel} = 3.93 \cdot 10^4$ rad/cm and MEM mode at $q_{\parallel} = 8.58 \cdot 10^4$ rad/cm with change of microwave pumping power.

A complex structure of highly populated magnon states is detected near the bottom of the spin-wave spectrum. Along with the wide spectral hump around the energy minimum of the magnon spectrum clear visible in Fig. 2a at $q_{\parallel} = 3.93 \cdot 10^4$ rad/cm (it can be referred as "BEC hump"), we detect an additional much sharper peak at $q_{\parallel} = 8.58 \cdot 10^4$ rad/cm (see Fig. 1 and Fig. 2a). From the analysis of the dipolar-exchange magnon spectrum it has been found that the latter is placed at a cross point of the dispersion characteristics of a Backward Volume Magnetostatic Wave (BVMSW) and a transversal acoustic wave (see Fig. 2b), and thus can be associated with a magneto-elastic magnon mode (MEM). An additional experiment, which was performed at higher bias magnetic field, corroborated this assumption: We observed the predicted displacement of the MEM peak to smaller wavenumbers caused by the upward shift of the magnon spectrum.

Both the BEC and the MEM intensity maxima appear at specific pumping powers after the reaching a critical magnon density but the MEM mode peak is formed at a 10 times smaller power level relative to the formation of the BEC hump (see Fig. 1 and Fig. 2c). Furthermore, in contrast to the BEC hump, the width of the MEM mode peak is practically independent from the magnon density and is as narrow as the q-number resolution of the experimental setup. A further increase of the pumping power leads to the saturation and even to a decrease of the MEM mode peak on the background of the increasing and narrowing of BEC peak. This effect can be caused by a magnon cross-flow between the MEM mode and the BEC forming in the global energy minimum. It is worth to note that in the case of a very strong pumping field (realized, for example, like in the previous report, due to the concentration of the microwave current in the narrow pump stripe) the MEM mode is inconspicuous on the background of the huge BEC peak.

The observations of the temporal dynamics of the magnon gas give us additional information about the interplay between the MEM mode and the BEC phase. As it shown in Fig. 3 the first thermal-

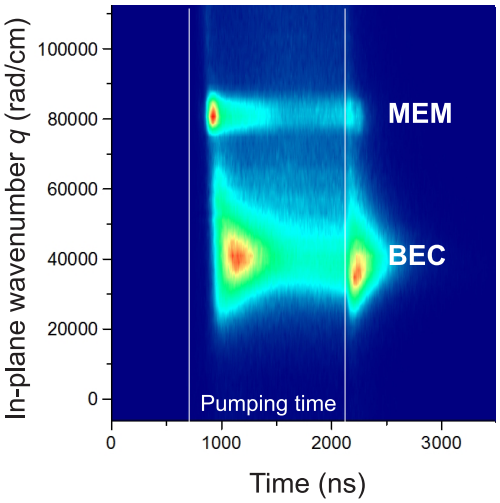

Fig. 3: Temporal dynamics of the MEM mode and BEC. The thin vertical lines mark the start and end of the pump pulse. The data are collected near the bottom of the magnon spectrum in the frequency range of 150 MHz.

ized magnons, which appear at the bottom part of the magnon spectrum, are short-wavelength exchange magnons with $q_{\parallel} \geq 1.1 \cdot 10^5\,\mathrm{rad/cm}$ (this fact differs drastically from results of Ref. [3] and [4] that show a significant role of the long-wavelength dipolar magnons in the thermalization process). The MEM mode intensity reaches its maximum just before the magnon condensate formation and decreases afterwards. The pump-free behaviour of the MEM mode is similar to the BEC hump: Both intensities jump up just after the pump pulse, when evaporative cooling of the magnon gas is expected (see the previous report). At the same time, the BEC jump is much more pronounced. This difference can be caused by an effective absorbtion of the MEM magnons by the free evolving BEC.

The nature of the dominant population as well as the extreme small peak width of the MEM mode is not clear yet. The phenomenon can be understood as a result of a phonon induced coupling of high BVMSW modes, and thus the formation of an effective transfer channel of the thermalized magnons to the bottom of the spin-wave spectrum. In addition, the MEM mode can intercept and accumulate the short-wavelength magnons on their way to the BEC.

Financial support by the Deutsche Forschungsgemeinschaft within the SFB/TRR 49 is gratefully acknowledged.

References

[1] M. Agrawal, V.I. Vasyuchka, A.D. Karenowska, A.A. Serga, G.A. Melkov, B. Hillebrands *Magnon-phonon coupling unmasked: a direct measurement of magnon temperature*, arXiv:1209.3405v1 (2012).

[2] K. Uchida, H. Adachi, T. An, T. Ota, M. Toda, B. Hillebrands, S. Maekawa, E. Saitoh, *Long-range spin Seebeck effect and acoustic spin pumping*, Nature Materials **10**, 737 (2011).

[3] J. Hick, T. Kloss, P. Kopietz, *Thermalization of magnons in yttrium-iron garnet: nonequilibrium functional renormalization group approach*, arXiv:1206.6689v2 (2012).

[4] V.E. Demidov, O. Dzyapko, M. Buchmeier, T. Stockhoff, G. Schmitz, G.A. Melkov, S.O. Demokritov, Phys. Rev. Lett. **101**, *Magnon kinetics and Bose-Einstein condensation studied in phase space*, 257201 (2008).

4.3 Supercriticality of parmetrically generated magnons in Py microstructures

T. Brächer, P. Pirro, A. A. Serga, and B. Hillebrands

Parallel parametric amplification, or parallel pumping, [1, 2] is a technique that has widely been used to generate [3, 4] and manipulate [5, 6] spin waves in ferromagnetic films. Recently, it was shown that this technique is also applicable to microstructures [7, 8]. The strong concentration of microwave currents in a microstructured coplanar waveguide (CPW), used as pumping inductor, allows for sufficiently large alternating Oersted fields to exceed the threshold of parametric generation, i.e. the amplification of thermal magnons. As shown in [7], the preferably amplified spin wave in a thin $Ni_{81}Fe_{19}$ microstripe is its lowest transverse eigenmode. Thus, the parametric technique can be used for effective amplification of this mode and allows for a significant enhancement of the signal transmission length in spin-wave conduits. However, the behavior of the system at supercritical power levels as well as the occurring scattering processes and saturation mechanisms have not been addressed yet. Therefore, a profound understanding of this high power regime is needed in order to achieve an optimal amplification and in order to fully exploit the capacities of the technique.

In this Report we present a power dependent study of the spin-wave mode profiles at comparably low magnetic fields in a $Ni_{81}Fe_{19}$ microstripe, demonstrating how the nonlinear damping can lead to a change of the preferably amplified mode. In addition, we show that this effect appears to be unique for low magnetic fields.

Parametric generation describes the parametric amplification of thermal spin waves. By interaction of the dynamic microwave field with the longitudinal component of the dynamic magnetization magnon pairs with opposite wavevectors are created by photon extinction, as sketched in Fig. 1 where a pumping photon with wavevector $k \approx 0$ and $f_p = 12\,\mathrm{GHz}$ splits into two magnons at $f = 6\,\mathrm{GHz}$ with opposite wavevectors. If the energy added to a magnon group exceeds the damping losses, the density of this magnon group increases exponentially in time. However, several contributions will limit the increase. The two most important contributions are the reduction of the coupling of the spin-wave mode to the applied pumping field [10] and the increase of the nonlinear damping [10, 11], both arising from large angle precession and influenced by the parametric generation of additional spin-wave modes as the applied pumping power exceeds their threshold.

In this study, we investigate the power dependent evolution of the mode profile in the supercritical regime, when the applied microwave power is significantly higher than the threshold power needed for parametric generation of the lowest transverse mode, in different magnetization states. The study is carried out by the use of Brillouin light scattering microscopy (μBLS) [12]. As the BLS intensity is proportional to the spin-wave intensity, it provides a space- and frequency-resolved analysis of the generated spin waves. The investigated structure consists of a $Ni_{81}Fe_{19}$ microstripe (thickness $t_s = 40\,\mathrm{nm}$, width $w_s = 2.5\,\mu\mathrm{m}$, length $l_s = 75\,\mu\mathrm{m}$) on top of a Cu waveguide and has been patterned by electron beam lithography and lift-off technique. The $Ni_{81}Fe_{19}$ film has been grown by molecular beam epitaxy and the Cu film by electron beam evaporation.

In the experiments described in this Report the $Ni_{81}Fe_{19}$ stripe has been magnetized by a bias field applied along its short axis (as shown in Fig. 1) by applied fields below $\mu_0 H_{ext} = 20\,\mathrm{mT}$. In order to get a better understanding of the internal field distribution and the magnetization in the stripe at the experimentally investigated magnetic fields, micromagnetic simulations using OOMMF [13]

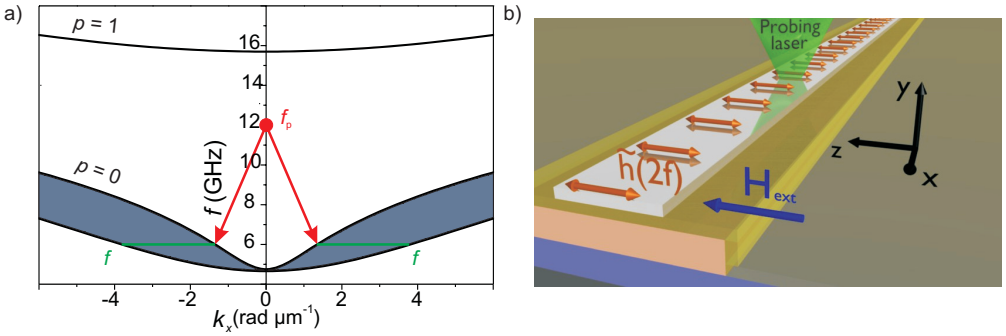

Fig. 1: a) Scheme of the photon splitting that leads to the creation of magnon pairs with opposite wavevector. The created magnons can have any wavevector in the spin-wave manifold as long as energy conservation is fulfilled. The circle at $f = f_\mathrm{p} = 12\,\mathrm{GHz}$ represents the pumping photon and the horizontal lines at $f = 6\,\mathrm{GHz}$ mark the potentially pumped spin waves. The preferably pumped mode is determined by the coupling of the mode to the applied pumping field and by its damping. The shown dispersion relations were calculated following Ref. [9] and represent the spin wave band for the lowest perpendicular standing spin-wave mode $p = 0$ (lower curves) and the first perpendicular standing spin wave mode $p = 1$ (upper curve). b) Schematic sample design: A $Ni_{81}Fe_{19}$ microstripe (width $w_\mathrm{s} = 2.5\,\mu\mathrm{m}$, thickness $t_\mathrm{s} = 40\,\mathrm{nm}$, length $l_\mathrm{s} = 75\,\mu\mathrm{m}$) is placed on top of a Cu waveguide (width $w_\mathrm{a} = 6\,\mu\mathrm{m}$, thickness $t_\mathrm{a} = 200\,\mathrm{nm}$) which is connected to a microwave generator. The Cu and the $Ni_{81}Fe_{19}$ layers are separated by an insulation layer (HSQ) (thickness $t = 30\,\mathrm{nm}$), and the $Ni_{81}Fe_{19}$ is capped with a $t_\mathrm{c} = 2\,\mathrm{nm}$ thick layer of aluminum oxide (not shown). As a substrate an oxidized Si sample is used ($t_\mathrm{Oxide} = 200\,\mathrm{nm}$) to minimize microwave absorption by the substrate. An alternating current is passed through the Cu waveguide, creating an alternating Oersted field $\tilde{h}$ parallel to the externally applied field H_ext, which is applied along the short axis of the stripe.

have been performed. As can be seen in Fig. 2a, for an applied external field of $\mu_0 H_\mathrm{ext} = 12\,\mathrm{mT}$ the internal field inside the stripe vanishes, as the demagnetizing field cancels out the external field. Additionally, as shown in Fig. 2b, the magnetization in the center of the stripe is almost aligned in a 45° angle with respect to the external field as $M_\mathrm{x} \approx M_\mathrm{y}$ and $M_\mathrm{z} \approx 0\,\mathrm{kAm^{-1}}$. In comparison, Fig. 2c and d show the internal field and the components of the static magnetization for an applied field of $\mu_0 H_\mathrm{ext} = 20\,\mathrm{mT}$. In the latter case the magnetization in the center of the stripe is aligned parallel to the external field while the magnetization in the edge region is aligned along the long axis of the stripe, as is expected by the shape anisotropy.

Hence, as can be seen from Fig. 2, the two simulated fields represent very different geometries: While in the latter case the magnetization is quasi-saturated, for $\mu_0 H_\mathrm{ext} = 12\,\mathrm{mT}$ no saturation of the static magnetization inside the stripe occurs. In order to study the influence of these geometries on the generated spin-wave modes, space-resolved μBLS measurements across the width of the $Ni_{81}Fe_{19}$ stripe are performed. The microwave power is applied in the pulsed regime to avoid sample heating. The results for a pulsed parametric generation at an applied external field of $\mu_0 H_\mathrm{ext} = 12\,\mathrm{mT}$ are shown in Fig. 3. The pulses are carried at $f = 13.3\,\mathrm{GHz}$ with a pulse duration of $d = 400\,\mathrm{ns}$ and a repetition rate of $\tau = 500\,\mathrm{ns}$. Above the threshold of parametric generation, which lies near $P \approx 30\,\mathrm{mW}$, the spin-wave mode profiles show one anti-node across the stripe, as is shown in Fig. 3 for an exemplary microwave pumping power of $P = 80\,\mathrm{mW}$. This is identified with the first transversally standing spin-wave mode $n = 1$. An increase in the power up to $P = 100\,\mathrm{mW}$ does not change the recorded profile significantly. However, a further increase of the power by $\Delta P = 1\,\mathrm{dBm}$ to $P = 126\,\mathrm{mW}$ leads to a significant change of the mode profile, as for this power and higher powers (see Fig. 3) the profile shows two anti-nodes and one node across the width of the stripe. To get a better understanding of this change of the mode profile a time-resolved analysis of the evolution of the spin-wave mode at high powers has been performed. As can be seen in Fig. 4a the profile evolves as a centered mode for the first nanoseconds. However, after roughly

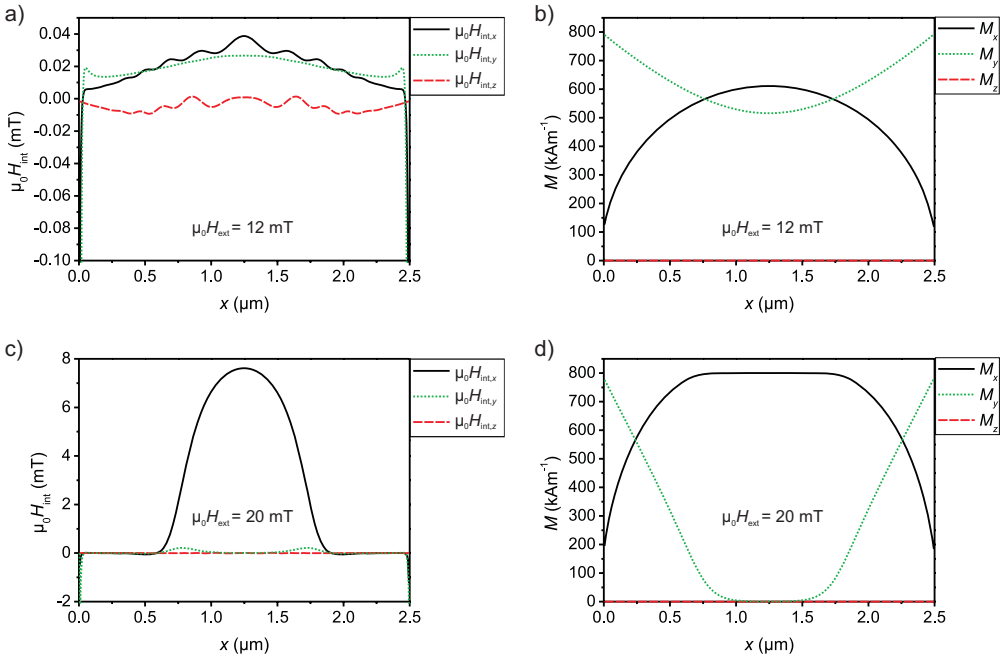

Fig. 2: a OOMMF simulated internal field (a, c) and magnetization (b, d) inside the considered stripe for an applied external field of $\mu_0 H_{\text{ext}} = 12\,\text{mT}$ (a, b) and $\mu_0 H_{\text{ext}} = 20\,\text{mT}$ (c, d). The considered stripe is a $w_s = 2.5\,\mu\text{m}$ wide, $t_s = 40\,\text{nm}$ thick $Ni_{81}Fe_{19}$ microstripe of infinite length with standard material parameters for $Ni_{81}Fe_{19}$ (i.e. saturation magnetization $M_s = 800\,\text{kAm}^{-1}$ and exchange constant $A = 1.6 \cdot 10^{-11}\,\text{Jm}^{-1}$).

ten nanoseconds the node in the center appears. To further illustrate this, Fig. 4b shows the BLS intensity as a function of time in the center of the stripe and at the position of one of the anti-nodes for $P = 320\,\text{mW}$. 10 ns after the pumping is applied and after a first rise of the spin-wave intensity, the intensity drops down to a constant value. As can be seen in Figs. 4a and b for larger times there is no further change to the profile.

As the strong increase of the BLS intensity in Fig. 4b shows, the magnon density in the center of the stripe is first increasing with time as expected. However, after approximately 10 ns the intensity does not only saturate but it even decreases. This indicates that either the damping has increased or the coupling has decreased as mentioned above. Moreover, the intensity drops only in the center of the stripe. Off center, the intensity is simply saturating, as can be retraced in Figs. 4a and b. As a reduction of the coupling should rather lead to a saturation for the dominant group [5], it is likely that the decrease of the BLS intensity is caused by a nonlinear damping of the first mode. As for larger times the mode profile rather corresponds to the second standing transverse spin-wave mode, it seems that the nonlinear damping for the mode $n = 1$ increases its losses, so that its generation

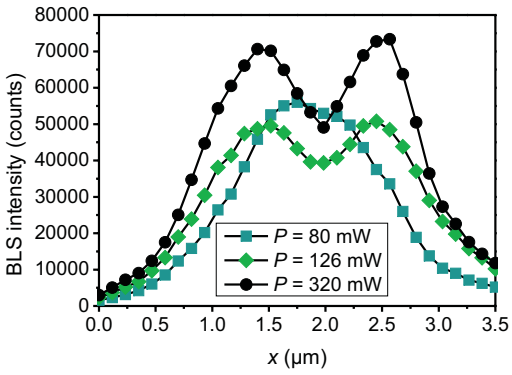

Fig. 3: Spin-wave mode profiles recorded at different microwave powers P for a pumping frequency of $f = 13.3\,\text{GHz}$ at an applied external field $\mu_0 H_{\text{ext}} = 12\,\text{mT}$. The pumping was applied pulsed to avoid sample heating, the pulse duration was chosen to $d = 400\,\text{ns}$ with a repetition rate of $\tau = 500\,\text{ns}$.

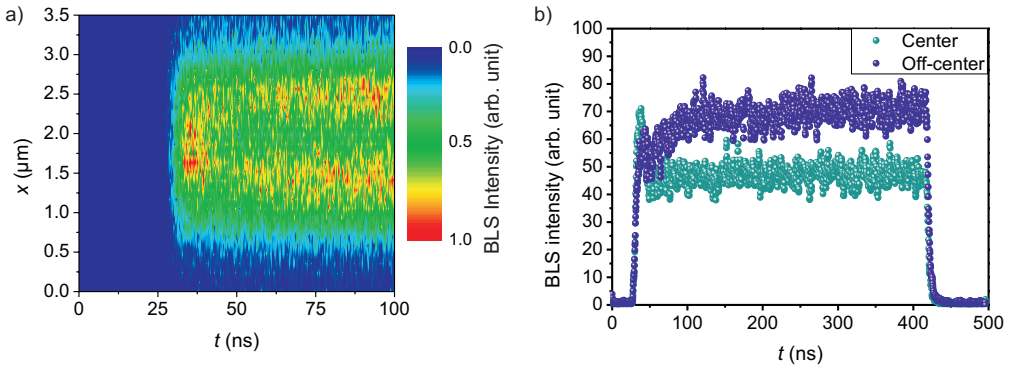

Fig. 4: a) BLS intensity recorded as a function of time and space for an applied microwave power of $P = 320\,\mathrm{mW}$ and a pumping frequency of $f = 13.3\,\mathrm{GHz}$ at an applied external field $\mu_0 H_{\mathrm{ext}} = 12\,\mathrm{mT}$. b) BLS intensity in the center of the stripe and at the position of one of the anti-nodes for $P = 320\,\mathrm{mW}$ as a function of time recorded for the parameters of a. In both cases the pulse duration has been chosen to $d = 400\,\mathrm{ns}$ with a repetition rate of $\tau = 500\,\mathrm{ns}$.

becomes quite ineffective. At this point, the next possible mode ($n = 2$) takes over and acts as new dominant group. For fields around $\mu_0 H_{\mathrm{ext}} = 12\,\mathrm{mT}$ this behavior can be observed at various frequencies. However, if the field is increased to $\mu_0 H_{\mathrm{ext}} = 20\,\mathrm{mT}$, the node in the intensity profile of the dynamic magnetization cannot be observed anymore in the experimentally accessible region of applied microwave power, as is shown in Fig. 5 for a carrier frequency of $f = 12\,\mathrm{GHz}$. As shown in Fig. 2 and mentioned above, the internal field and the magnetization in the two cases of an applied field of $\mu_0 H_{\mathrm{ext}} = 12\,\mathrm{mT}$ and $\mu_0 H_{\mathrm{ext}} = 20\,\mathrm{mT}$ differ qualitatively. In the first case the internal field almost vanishes and the magnetization points approximately in a 45° angle with respect to the external field, while in the latter case the magnetization is well aligned in the central region of the stripe by a finite internal field. Due to this the magnetization at low fields is in a rather unstable equilibrium state, where the dynamic fields of the generated spin waves easily overcome the internal field and thus the precession angle of the dynamic magnetization becomes quite large. As a consequence of this, the precession angle and thus the nonlinear damping might be much higher at $\mu_0 H_{\mathrm{ext}} = 12\,\mathrm{mT}$ than at $\mu_0 H_{\mathrm{ext}} = 20\,\mathrm{mT}$.

In conclusion, we demonstrated nonlinear mode-conversion as an example for supercritical parametric excitation in a $Ni_{81}Fe_{19}$ microstripe. It is shown that close to the threshold the first standing transverse mode appears to be the dominant group. However, as the applied pumping power is increased, the second transversally standing spin-wave mode takes over. It was shown by a time-resolved analysis that also in the case of high power excitation the first transversally standing

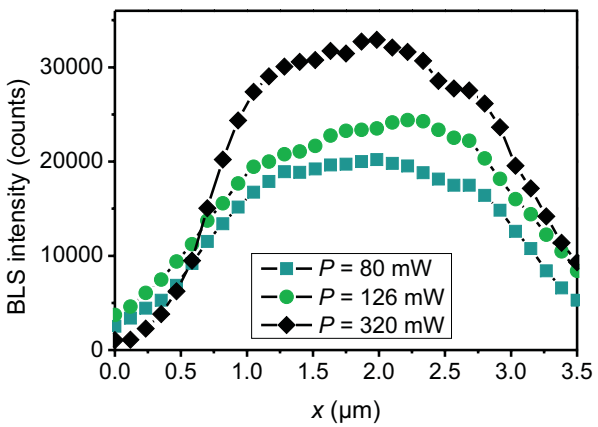

Fig. 5: Spin-wave mode profiles recorded at different microwave powers P for a pumping frequency of $f = 12\,\mathrm{GHz}$ at an applied external field $\mu_0 H_{\mathrm{ext}} = 20\,\mathrm{mT}$. The pumping was applied pulsed with a pulse duration of $d = 400\,\mathrm{ns}$ and a repetition rate of $\tau = 500\,\mathrm{ns}$.

spin-wave mode starts to be the dominant mode. Still, as soon as a certain spin-wave intensity is overcome, the first mode seems to be nonlinearly damped and the spin-wave intensity in the center of the stripe drops down. This instability occurs only at fairly low applied external magnetic fields, which we attribute to the rather unstable equilibrium distribution of the internal magnetic field and the magnetization, as these lead to rather large precession angles.

Thomas Brächer is supported by a fellowship of the Graduate School Materials Science in Mainz (MAINZ) through DFG-funding of the Excellence Initiative (GSC 266). Philipp Pirro acknowledges financial support by the Carl-Zeiss-Stiftung via the OPTIMAS Carl-Zeiss doctoral program.

References

[1] E. Schlömann, J.J. Green, and U. Milano, *Recent developments in ferromagnetic resonance at high power levels*, J. Appl. Phys. **31**, S386 (1960).

[2] V.E. Zakharov, V.S. L'vov, S. S. Starobinets, *Spin-wave turbulence beyond the parametric excitation threshold*, Soviet Physics Uspekhi **17**, 896 (1975).

[3] B.A. Kalinikos, M.P. Kostylev, *Parametric amplification of spin wave envelope solitons in ferromagnetic films by parallel pumping* , IEEE Transactions on Magnetics **33**, 3445 (1994).

[4] S.O. Demokritov, V.E. Demidov, O.Dzyapko, G.A. Melkov, A.A. Serga, B. Hillebrands, A.N. Slavin, *Bose-Einstein condensation of quasi-equilibrium magnons at room temperature under pumping*, Nature **443**, 430 (2006).

[5] S. Schäfer, V. Kegel, A.A. Serga, B. Hillebrands, M.P. Kostylev, *Variable damping and coherence in a high-density magnon gas* , Phys. Rev. B **83**, 184407 (2011).

[6] K.R. Smith, V.I. Vasyuchka, M. Wu, G.A. Melkov, and C.E. Patton, *Cloning and trapping of magnetostatic spin-wave pulses by parametric pumping*, Phys. Rev. B **76**, 054412 (2007).

[7] T. Brächer, P. Pirro, B. Obry, B. Leven, A.A. Serga, and B. Hillebrands, *Mode selective parametric excitation of spin waves in a $Ni_{81}Fe_{19}$ microstripe*, Appl. Phys. Lett. **99**, 162501 (2011).

[8] H. Ulrichs, V.E. Demidov, S.O. Demokritov, and S. Urazhdin, *Parametric excitation of eigenmodes in microscopic magnetic dots*, Phys. Rev. B **84**, 094401 (2011).

[9] B.A. Kalinikos and A.N. Slavin, *Theory of dipole-exchange spin wave spectrum for ferromagnetic films with mixed boundary conditions*, J. Phys. C **19**, 7013 (1986).

[10] V. S. L'vov and L. A. Prozorova, *Spin waves above the threshold of parametric excitation*, in A. S. Borovik-Romanov and S. K. Sinha, Eds., *Spin waves and magnetic excitations*, North-Holland, Amsterdam, 1988.

[11] A. Y. Dobin, and R. H. Victora, *Intrinsic nonlinear ferromagnetic relaxation in thin metallic films*, Phys. Rev. Lett. **90**, 167203 (2003).

[12] V.E. Demidov, S.O. Demokritov, B. Hillebrands, M. Laufenberg, and P.P. Freitas, *Radiation of spin waves by a single micrometer-sized magnetic element*, Appl. Phys. Lett. **85**, 2866 (2004).

[13] M.J. Donahue and D.G. Porter, Interagency Report NISTIR **6376**, *OOMMF User's Guide, Version 1.0*, National Institute of Standards and Technology, Gaithersburg, MD (Sept 1999).

[14] H. Suhl, *The theory of ferromagnetic resonance at high signal powers*, J. Phys. Chem. Solids **1**, 209 (1957).

B. Magnon Spintronics

Spintronics is the field of spin-based data storage and processing. In conventional spintronics the electron is used as a carrier of spin. In particular, the manipulation of spin currents in nanostructures has potential applications in computing devices and magnetic memory. For the successful utilization of spin information, difficulties like the short distance over which an electron retains memory of its spin direction, the so-called spin diffusion length, have to be overcome. Here, a promising approach is the combination of standard spintronics with spin-wave dynamics resulting in *magnon spintronics*. A magnon, i.e. the quantum of a spin wave, carries an angular momentum or spin as well and can be used for storage, processing and transport of spin information, building on its outstanding properties such as long lifetime and potential for dissipationless transport. The field of magnon spintronics is currently emerging, and the three main objects of studies are of particular interest: (1) magnon conduits providing efficient transfer of spin information over macroscopic distances, (2) magnon flow to charge current converters, and (3) converters from charge- and spin-currents into magnons allowing their generation as well as amplification.

The first two Reports of the chapter (Reports 4.4 and 4.5) are devoted to different solutions of the same problem: realization of two-dimensional magnon conduits. Due to the strong anisotropy of the in-plane magnetized magnetic films, spin waves propagating under different angles have strongly different characteristics. Thus “turning”of the wave on 90 degrees and realization of two-dimensional conduits is a serious problem which requires separate deep studies. In Report 4.4 a direct current flowing in bi-layered spin-wave waveguide was used to guide spin waves around a curvature. In Report 4.5 a T-like waveguiding microstructure was used to generate backward volume spin waves from Damon Eshbach spin waves, which are transverse to them.

Ferromagnetic insulator/nonmagnetic metal bilayer structures like yttrium iron garnet/platinum (YIG/Pt) attract great attention in the field of spintronics nowadays. It is known that due to the combination of the spin pumping and the inverse spin Hall effects (ISHE), these bi-layers can be used for efficient conversion of magnons in YIG into spin- and charge-currents in the attached Pt layer. In Report 4.6 our results on the influence of processing of the YIG surface before the Pt deposition on spin pumping are presented. We have shown a significant difference in spin pumping efficiency up to factor of 152 between different surface treatments. In Report 4.7 we use a spatially separated spin-wave source and an ISHE detector in combination with time-resolved measurements to demonstrate for the first time the spin pumping effect by traveling magnons. The opposite effect to the spin pumping effect, the spin transfer torque (STT) effect, allows the conversion of a spin current into magnons in the YIG/Pt bi-layers. Usually, the STT effect is driven by the direct spin Hall effect (SHE) converting charge current into a transverse spin current. In Report 4.8 we utilize a high-sensitive resonator-based method to measure SHE-induced STT in YIG-Pt bi-layers. It has been shown that the damping in YIG can be changed up to 20 percent by applying of a DC current to the Pt layer.

B. Magnon-Spintronik

Die Spintronik umfasst das Gebiet der Spin-basierten Informationsspeicherung und Verarbeitung. Bei der konventionellen Spintronik wird das Elektron als Träger des Spins verwendet. Ein besonderes Augenmerk im Hinblick auf potentielle Anwendungen in Computern oder magnetischen Speichern liegt auf der Manipulation von Spinströmen in Nanostrukturen. Für eine erfolgreiche Nutzung der Spininformationsübertragung ist es allerdings notwendig, Schwierigkeiten wie die

vergleichbar kurze Länge der Spinkonservierung in Materialien, der sogenannten Spindiffusionslänge, zu überwinden. Ein sehr erfolgreicher Ansatz ist hier die Kombination der Spintronik mit der Spinwellendynamik, die "Magnon-Spintronik". Ein Magnon, das Quant einer Spinwelle, trägt ebenfalls einen Drehimpuls oder Spin und kann analog zur konventionellen Spintronik für den Spin-basierten Datentransfer und die Datenverarbeitung genutzt werden, bietet aber zusätzlich herausragende Möglichkeiten wie z.B. lange Lebensdauern und verlustfreien Transport. Das Feld der Magnon-Spintronik befindet sich derzeit in der Entwichlungsphase. Drei Hauptziele sind von besonderem Interesse: (1) Magnonenleiter zur effizienten Spininformations-Übertragung über makroskopische Distanzen, (2) Konverter für die Umwandlung von Magnonen- in Ladungsströme und (3) Konverter für Ladungs- und Spinströme in Magnonen, was die Erzeugung und Verstärkung von Magnonen erlaubt.

Die ersten beiden Berichte 4.4 und 4.5 stellen zwei unterschiedliche Lösungen für das selbe Problem vor: die Realisierung von zweidimensionalen Magnonenleitern. Aufgrund der starken Anisotropie eines *in-plane* magnetisierten Films weisen Spinwellen, die unter verschiedenen Winkeln propagieren, sehr unteschiedliche Charakteristiken auf. Daher stellen die Ablenkung einer Welle um 90 Grad und die Realisierung von zweidimensionalen Leitern Probleme dar, welche getrennt voneinander näher untersucht werden müssen. In Bericht 4.4 wird ein Gleichstrom, der in einem doppelschichtigem Spinwellen-Wellenleiter fließt, verwendet, um die Magnetisierung im Wellenleiter vorzugeben und so Spinwellen um eine Kurve zu leiten. In Bericht 4.5 wird ein T-förmiger Mikrostruktur-Wellenleiter verwendet um *Backward Volume*-Spinwellen aus *Damon Eshbach*-Spinwellen zu erzeugen.

Doppelschichtige Strukturen aus ferromagnetischen Isolatoren/nichtmagnetischen Metallen wie Yttrium Eisen Granat/Platin (YIG/Pt) erfahren heute eine große Aufmerksamkeit. Durch die Kombination von Spinpumpen und inversem Spin Hall Effekt (ISHE) können diese Doppelschichten für die Umwandlung von Magnonen im YIG in Spin- und Ladungsströme im Platin verwendet warden. In Beitrag 4.6 werden unsere Ergebnisse zum Einfluß der Oberflächenbehandlung des YIGs vor der Pt-Aufbringung auf das Spinpumpen vorgestellt. Wir weisen einen beträchtlichen Unterschied in der Spinpumpeffizienz bis zu einem Faktor von 152 zwischen den einzelnen Oberflächenbehandlungsverfahren nach. Im anschließenden Bericht 4.7 zeigen wir erstmalig das Spinpumpen von propagierenden Magnonen. Hierzu verwenden wir in einem zeitaufgelösten Experiment eine vom ISHE-Detektor örtlich separierte Spinwellen-Quelle. Der zum Spinpumpen umgekehrte Prozess, der *Spin Transfer Torque* (STT)-Effekt, erlaubt in YIG/Pt Doppelschichten die Umwandlung von Spinströmen in Magnonen. Üblicherweise wird der STT-Effekt vom direkten Spin Hall Effekt (SHE) getrieben. Der SHE erlaubt die Umwandlung von Ladungs- in Spinströme, die transvers zum Ladungsstrom fließen. In Bericht 4.8 verwenden wir einen hochempfindlichen Resonator, um den SHE-induzierten STT-Effekt in YIG/Pt-Doppelschichten zu messen. Wir zeigen eine Veränderung der Dämpfung in YIG um 20 Prozent, in dem wir einen Gleichstrom an die Pt-Schicht anlegen.

4.4 Spin waves turning a corner

K. Vogt and B. Hillebrands

In collaboration with: H. Schultheiss, S. Jain, J. E. Pearson, A. Hoffmann, S. D. Bader, Materials Science Division, Argonne National Laboratory, Argonne, Illinois, USA.

The rapidly growing field of magnon spintronics [1–4] aims towards the exploitation of spin waves for data processing. Since spin waves carry angular moment and can propagate over much larger distances than the spin diffusion length, they are promising candidates for future spintronic devices. The characteristics of spin-wave transport in simple micro-waveguides [5–8] and those of varying width [9–11] has been studied quite extensively during the last decade. If one thinks about the application of spin waves in actual devices, however, it will be inevitable to guide spin waves without disturbances in more complicated structures. Even devices as fundamental as a Mach-Zehnder-type interferometer [12, 13] will require unimpeded spin-wave propagation past curves and corners in waveguides of constant width. Global external fields that are employed to magnetize such two-dimensional micro-structures lead to inhomogeneities in the demagnetizing fields. The resulting non-uniform distribution of the effective field alters the character of the propagating spin wave [14] or even prevents transport altogether. Additionally, the spin-wave dispersion strongly depends on the angle between the propagation direction of the spin wave and the magnetization direction. These conditions complicate transport in two-dimensional micro-structures when global fields are applied to align the magnetization. The waveguide will always be magnetized along the external field so that inside a curved region the orientation of the magnetic moments will rotate with respect to the stripe's edges, hampering free spin-wave propagation.

In this work, we analyze spin-wave transport in a Au/$Ni_{81}Fe_{19}$ bilayer waveguide that exhibits a smooth, *S*-shaped bend. With a direct current flowing in the gold layer, the locally generated Oersted field can be utilized to effectively guide spin waves around the curvature, whereas an externally applied magnetic field prevents any spin-wave propagation inside the bend. Our results provide ways to direct spin waves in two-dimensional microstructures and also to avoid bulky magnets that, up to now, are used to provide global fields necessary for magnetizing the waveguide.

A schematic view of the investigated micro-structure is shown in Fig. 1a. Using electron beam lithography and conventional lift-off techniques, a bilayer of a 50 nm thick sputtered gold film and a 30 nm thick polycrystalline $Ni_{81}Fe_{19}$ (permalloy, Py) film was patterned into a 2 µm wide spin-wave waveguide that exhibits a smooth, *S*-shaped bend starting in 8 µm distance from the antenna. The curvatures of the two bent regions have a radius of 5 µm. The magnetization precession inside the waveguide is excited by a microwave current flowing through a strip line made of 100 nm thick gold.

Using an externally applied magnetic field, the magnetization inside the permalloy can be forced to point along the x-direction, as depicted by the arrows in Fig. 1b. For the given geometry, a field of 10.3 mT is needed to fully saturate the waveguide along its short axis. This configuration ensures the excitation of spin waves with high group velocities propagating perpendicularly to the magnetization direction. [15] However, to allow transport of spin waves through the bend, the orientation between their wave vector and the magnetization would need to gradually change from being perpendicular before, parallel inside, and again perpendicular behind the bend. Due to the strong anisotropy of the spin-wave dispersion, the character of the spin wave would need to adapt to the local magnetization configuration in order to pass through the bend. In addition, varying demagnetizing fields inside the bend will result in a strongly inhomogeneous internal field

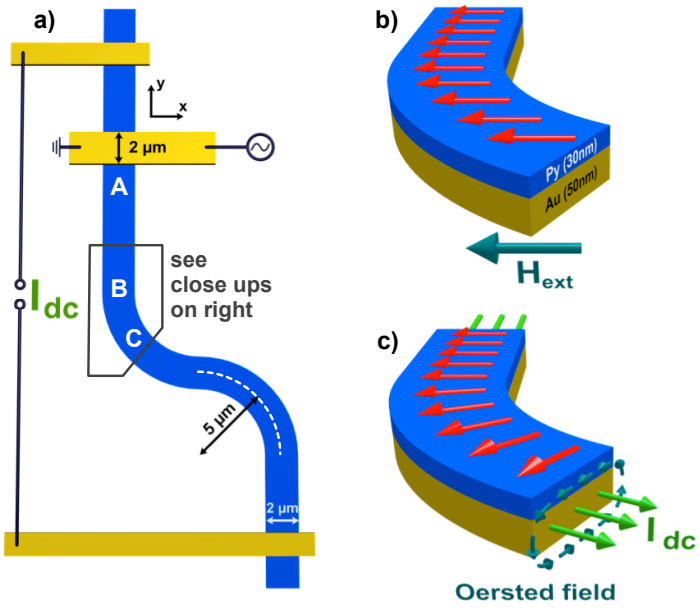

Fig. 1: (a) Schematic view of the investigated structure. A microstrip antenna excites spin waves in a 2 µm wide waveguide fabricated from a Au(50 nm)/Py(30 nm) bilayer. In 8 µm distance from the antenna, the waveguide exhibits a smooth, *S*-shaped bend. Au contacts at both ends of the waveguide allow for a direct current I_{dc} to flow through the Au/Py bilayer. A, B, and C indicate the positions of the BLS measurements shown in Fig. 2. (b) Red arrows depict the magnetization configuration inside the spin-wave waveguide when an external field is applied. (c) With a direct current I_{dc} flowing through the bilayer the resultant Oersted field always aligns the magnetic moments perpendicularly to the stripe's edges.

distribution in this region, further hindering a smooth spin-wave propagation through the curved waveguide.

Therefore, we follow a different approach to direct spin waves in a curved waveguide. Instead of employing a global external field to align the magnetic moments, a direct current I_{dc} can be applied to the Au/Py bilayer using two Au-contacts at both ends of the waveguide (see Fig. 1a). Due to the different resistances and thicknesses of the gold and permalloy layer, the majority of the applied current flows through the gold. As shown by the arrows in Fig. 1c, the local Oersted field generated by this current always orients the magnetic moments inside the permalloy along the short axis of the spin-wave waveguide, smoothly following the curvature. This maintains a perpendicular orientation between the wave vector of a spin wave propagating along the waveguide and the magnetization direction, even inside the bend, and the local effective fields are homogeneous even with the demagnetizing fields.

We employed Brillouin light scattering (BLS) microscopy to investigate how the spin-wave intensity inside the bent region depends on the magnetization configuration. This technique allows the direct mapping of the spin-wave intensity distribution with a spatial resolution of 250 nm. [16, 17] The data obtained from the BLS measurements are summarized in Fig. 2. Each of the three graphs contains the results of two separate sets of measurements obtained in 1 µm (panel A), 8 µm (panel B), and 11 µm (panel C) distance from the antenna, corresponding to positions A, B, and C in Fig. 1a. First, no external magnetic field was applied, but a direct current was flowing through the bilayer waveguide. In order to avoid heating, we used current pulses with a duration of 150 ns and a repetition rate of 3 µs. The spin waves were excited by 100 ns long microwave pulses synchronized to the *dc* pulses. For each current amplitude ranging from 18 to 56.7 mA, the BLS intensity was recorded and plotted for different excitation frequencies between 2.1 and 3.9 GHz (filled symbols). For the second set of measurements, we excited spin-wave pulses with the same duration and frequencies as before. But this time, we switched off the direct current and, instead, varied the magnitude of the external magnetic field from 5 to 15 mT. Again, for each field value the BLS intensity was recorded and plotted in the same graph (empty symbols).

Panel A of Fig. 2 shows our results when we perform those two separate measurements in 1 µm

distance from the antenna. An immediately apparent feature is that no spin waves can be observed in the waveguide for small fields or small currents, respectively. The shape anisotropy aligns the magnetization parallel to the waveguide, which results in a low group velocity of spin waves propagating in this direction and, hence, in a strong spatial decay. Only above a certain current/field value the measured spin-wave intensity increases, which means that the Oersted field generated by the current flowing inside the gold or, in the other experiment, the externally applied field is sufficiently high to magnetize the waveguide along its short axis. In the investigated current range, the excitation characteristics of the spin waves are the same, independent of whether an external field or a direct current is employed to align the magnetic moments. We further see that a direct current of 54 mA is needed to generate a magnetic field of 10 mT. Duty cycle measurements performed with shorter *dc* pulses and the same repetition rate yield the same excitation spectra ensuring that Joule heating can be neglected. The maximum applied current density of $1.1 \cdot 10^{11}\,\mathrm{A/m^2}$ is too small to expect a contribution of spin transfer torque to the measured spin-wave intensity. [18]

In order to see if the propagation behavior of the spin waves in the waveguide is different for the two magnetization configurations, we performed the same measurement at larger distances from the antenna. The data displayed in panel B of Fig. 2 were recorded for a 8 µm distance, *i.e.*, right where the curvature begins. At this location the spin-wave intensity starts to increase at higher fields and higher currents compared to the measurements in region A closer to the antenna. This is related to forced spin-wave excitations outside the spin-wave band that can still be detected in the vicinity of the antenna, but they do not propagate along the waveguide and, thus, vanish when moving away from the antenna. However, the results for an applied magnetic field (empty symbols) are similar to those obtained for a direct current flowing through the waveguide (filled symbols). Since the magnetization configuration in region B is the same for both the external magnetic field

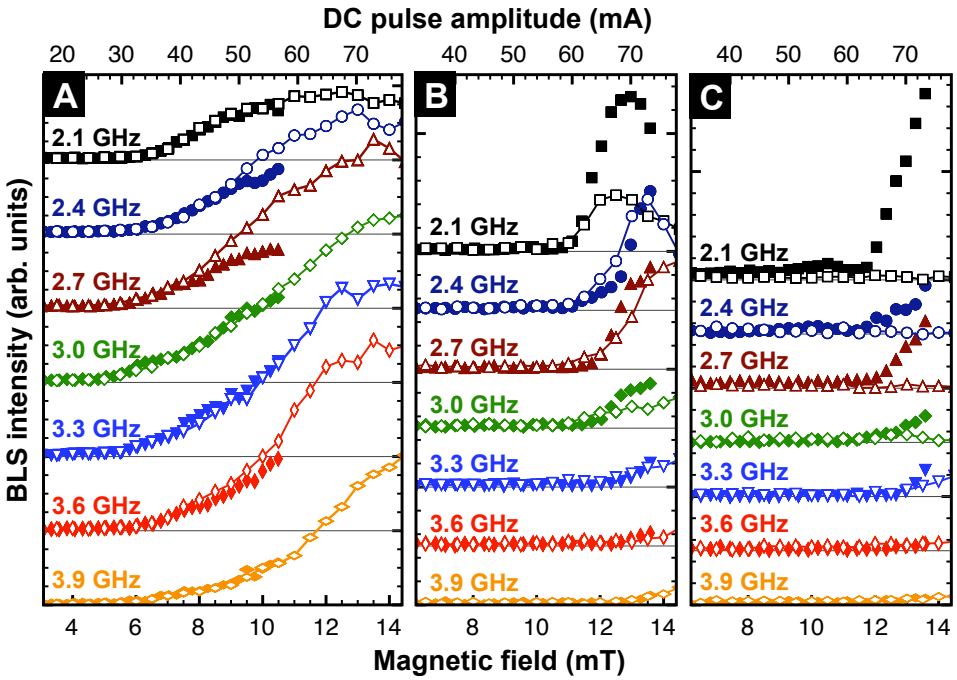

Fig. 2: Empty symbols show the BLS intensity measured as a function of an externally applied magnetic field for excitation frequencies ranging from 2.1 to 3.9 GHz. Filled symbols show the results of the BLS measurement with *dc* current pulses through the Au/Py bilayer waveguide and without applying an external magnetic field. The measurement positions of panels A, B and C are indicated in Fig. 1a; the results were obtained 1 µm, 8 µm and 11 µm away from the antenna.

and the applied direct current, the spin-wave spectra should not differ. In particular, the rise in the spin-wave intensity coincides for the direct current as well as for the external fields, which shows that the propagation characteristics of the spin waves in the straight section of the waveguide is the same for both magnetization configurations. A comparison of the spin-wave intensity at position B for the highest external magnetic fields and *dc* currents shows that for some frequencies there is a strong difference in the measured intensities. The reason for this is that in the case of an externally applied magnetic field the spin waves cannot propagate into the curved section and are reflected back. As a result a standing wave pattern is created in front of the curved section and the intensity measured at point B oscillates as a function of the applied excitation frequency.

When we move farther away from the antenna into the curved region of the waveguide, we observe differences in the spin-wave spectra. Panel C of Fig. 2 compares the results of the measurements made 11 µm away from the antenna, inside the bend. As the empty symbols show, no spin-wave signal can be detected inside the curvature when an external field is employed to magnetize the waveguide. However, with a current flowing through the bilayer (filled symbols), the intensity of the spin wave excited at 2.1 GHz strongly increases when the currents exceed 63 mA, corresponding to a field of about 11.7 mT. For excitation frequencies up to 3 GHz those differences in the spin-wave intensity remain visible. The overall intensity of spin waves drops for higher frequencies because the group velocity decreases, which generally results in an increased spatial decay of the spin waves. Due to the high damping, [19] the spin-wave intensity at the center of the *S*-shaped bend is strongly attenuated and vanishes altogether behind it.

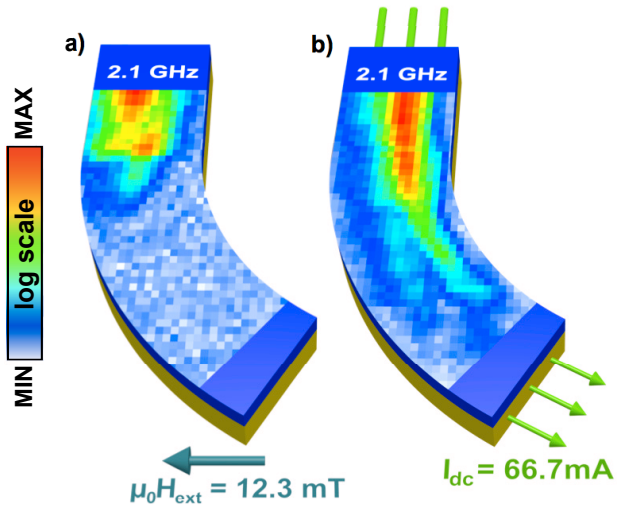

Fig. 3: Two-dimensional intensity distributions of spin waves excited at 2.1 GHz with (a) an externally applied magnetic field of 12.3 mT and (b) applied *dc* pulses with an amplitude of 66.7 mA. The intensity scale is logarithmic and color-coded.

These results show that spin-wave propagation in curved waveguides is not possible as long as all magnetic moments are aligned in one direction by a global external field. Only when a local Oersted field maintains a transverse magnetization of the waveguide, it is possible to detect a spin-wave signal inside the bend.

To better visualize this result, we mapped the two-dimensional intensity distribution of spin waves excited at 2.1 GHz in the bent region of the waveguide. In Fig. 3, the results of spatially resolved BLS microscopy measurements are displayed together with the schematic layout of the sample. The spin-wave intensity scale is logarithmic and color-coded, where white (red) represents minimum (maximum) values. As can be seen from Fig. 3a, the spin wave dies as soon as it enters the curved section of the waveguide when an external field of $\mu_0 H_{\text{ext}} = 12.3\,\text{mT}$ is applied. However, if a direct current is flowing through the bilayer, the spin wave is smoothly guided within the curved

waveguide. With 66.7 mA, the amplitude of the current pulses was chosen to yield the same field as for the externally applied field.

In conclusion, we have shown two effects: First, if no external magnetic field or dc current is applied, spin waves do not propagate in the investigated waveguide. Due to the shape anisotropy the magnetization always points along the waveguide, *i.e.*, parallel to the stripe's edges. This causes the excitation of spin waves with low group velocities that decay rapidly. Second, a favorable geometry for spin-wave transport, where the magnetization is always aligned perpendicularly to the propagation direction, can be achieved in micro-structured waveguides without applying any external magnetic field. The Oersted field generated by a direct current flowing in a gold layer underneath the Py is sufficiently high to attain transverse magnetization of the waveguide. Employing the direct current for locally aligning the magnetization, we further realized spin-wave propagation inside a curved waveguide. This demonstrates a crucial step towards new spin-wave based applications: artificially guiding the propagation direction of a spin wave in the sample plane.

Financial support by the Carl-Zeiss-Stiftung is gratefully acknowledged.

References

[1] A. Khitun, M. Bao, and K.L. Wan, *Magnonic logic circuits*, J. Phys. D **43**, 264005 (2010).

[2] T. Schneider, A.A. Serga, B. Leven, B. Hillebrands, R.L. Stamps and M.P. Kostylev, *Realization of spin-wave logic gates*, Appl. Phys. Lett. **92**, 022505 (2008).

[3] M.P. Kostylev, A.A. Serga, T. Schneider, B. Leven, and B. Hillebrands, *Spin-wave logical gates*, Appl. Phys. Lett. **87**, 153501 (2005).

[4] V.V. Kruglyak, S.O. Demokritov, and D. Grundler, *Magnonics*, J. Phys. D **43**, 264001 (2010).

[5] K. Vogt, H. Schultheiss, S.J. Hermsdoerfer, P. Pirro, A.A. Serga, and B. Hillebrands, *All-optical detection of phase fronts of propagating spin waves in a $Ni_{81}Fe_{19}$ microstripe*, Appl. Phys. Lett. **95**, 182508 (2009).

[6] V.E. Demidov, S.O. Demokritov, K. Rott, P. Krzysteczko, and G. Reiss, *Nano-optics with spin waves at microwave frequencies*, Appl. Phys. Lett. **92**, 232503 (2008).

[7] V.E. Demidov, J. Jersch, K. Rott, P. Krzysteczko, G. Reiss, and S.O. Demokritov, *Nonlinear propagation of spin waves in microscopic magnetic stripes*, Phys. Rev. Lett. **102**, 177207 (2009).

[8] D.R. Birt, B. O'Gorman, M. Tsoi, X. Li, V. E. Demidov, and S.O. Demokritov, *Diffraction of spin waves from a submicrometer-size defect in a microwaveguide*, Appl. Phys. Lett .**95**, 122510 (2009).

[9] K. Perzlmaier, G. Woltersdorf, and C.H. Back, *Observation of the propagation and interference of spin waves in ferromagnetic thin films*, Phys. Rev. B **77**, 054425 (2008).

[10] V.E. Demidov, S.O. Demokritov, D. Birt, B. O'Gorman, M. Tsoi, and X. Li, *Radiation of spin waves from the open end of a microscopic magnetic-film waveguide*, Phys. Rev. B **80**, 014429 (2009).

[11] V.E. Demidov, J. Jersch, S.O. Demokritov, K. Rott, P. Krzysteczko, and G. Reiss, *Transformation of propagating spin-wave modes in microscopic waveguides with variable width*, Phys. Rev. B **79** 054417 (2009).

[12] R. Hertel, W. Wulfhekel, and J. Kirschner, *Domain-wall induced phase shifts in spin waves*, Phys. Rev. Lett. **93**, 257202 (2004).

[13] K.-S. Lee and S.-K. Kim, *Conceptual design of spin wave logic gates based on a Mach-Zehnder-type spin wave interferometer for universal logic functions*, J. Appl. Phys. **104**, 053909 (2008).

[14] P. Clausen, K. Vogt, H. Schultheiss, S. Schäfer, B. Obry, G. Wolf, P. Pirro, B. Leven, and B. Hillebrands, *Mode conversion by symmetry breaking of propagating spin waves*, Appl. Phys. Lett. **99**, 162505 (2011).

[15] R.W. Damon and J.R. Eshbach, *Magnetostatic modes of ferromagnetic slab*, J. Appl. Phys. **31**, 104 (1960).

[16] V.E. Demidov, S.O. Demokritov, B. Hillebrands, M. Laufenberg, and P. Freitas, *Radiation of spin waves by a single micrometer-sized magnetic element*, Appl. Phys. Lett. **85**, 2866 (2004).

[17] H. Schultheiss, S. Schäfer, P. Candeloro, B. Leven, B. Hillebrands, and A.N. Slavin, *Observation of coherence and partial decoherence of quantized spin waves in nanoscaled magnetic ring structures*, Phys. Rev. Lett. **100**, 047204 (2008).

[18] K. Sekiguchi, K. Yamada, S.-M. Seo, K.-J. Lee, D. Chiba, K. Kobayashi, and T. Ono, *Time-domain measurement of current-induced spin wave dynamics*, Phys. Rev. Lett. **108**, 017203 (2012).

[19] T. Sebastian, Y. Ohdaira, T. Kubota, P. Pirro, T. Brächer, K. Vogt, A.A. Serga, H. Naganuma, M. Oogane, Y. Ando, and B. Hillebrands, *Low-damping spin-wave propagation in a micro-structured $Co_2Mn_{0.6}Fe_{0.4}Si$ Heusler waveguide*, Appl. Phys. Lett. **100**, 112402 (2012).

4.5 Excitation of propagating backward volume spin waves via phase dependent mode conversion

T. Brächer, P. Pirro, J. Westermann, T. Sebastian, and B. Hillebrands

The excitation and the propagation of spin waves in microstructured spin-wave waveguides [1–5] have received an increased attention in the recent years due to the promising applications of spin waves in spin-wave logic devices [6] and spin-wave signal processors [4] and as information carriers in devices utilizing spin-wave spin currents [7]. The field has widely benefited from the improvement of the methods for experimental investigation, [8, 9] numerical simulation [10] and sample preparation. However, most simulations showing the functionality of spin-wave logic elements [6] and also the interaction of spin waves with domain walls [11] have been carried out in the backward volume geometry, where the magnetization is aligned parallel to the waveguide, and thus spin waves propagate along the waveguide parallel to the magnetization **M**. In contrast, most experimental investigations of spin waves in microstructured waveguides have been carried out in the Damon Eshbach geometry, [5] where the magnetization is aligned perpendicular to the long axis of the waveguide and thus spin waves in the waveguide propagate perpendicular to **M**. This is due to the fact that spin waves in this geometry are easy to excite with microstripe antennas and exhibit a high group velocity in thin magnetic layers. On the other hand, the excitation of propagating backward volume spin waves has proven to be challenging and no experiments proving propagating spin waves in microstructures in this geometry have been reported so far. The main problem with the excitation of spin waves in longitudinally magnetized microstripes is the following: Due to the system geometry the waves are excited through coupling of the out-of-plane components of the alternating Oersted field induced by microstrip or coplanar antennas with an out-of-plane component of the dynamic magnetization. However, due to the shape anisotropy in thin ferromagnetic films the latter component is small, and thus the coupling is weak.

In this Report we present the generation of propagating backward volume spin waves by mode conversion of two counterpropagating Damon Eshbach spin waves interfering in a T-like waveguiding microstructure. First, we present micromagnetic simulations underlining the basic conversion principles. Consecutively, we demonstrate by experiment the spin-wave propagation in backward volume geometry and we prove the possibility to determine the type of spin-wave mode generated in the backward volume spin-wave conductor by changing the phase between the sources exciting the Damon Eshbach spin waves.

A scheme of the investigated "T" structure is shown in Fig. 1. Counterpropagating Damon Eshbach spin waves are excited by two conventional microwave antennas in a $Ni_{81}Fe_{19}$ stripe which is saturated along its short axis by an external applied magnetic field [5] (dark grey in Fig. 1) and is thus referred to as Damon Eshbach stripe in the following report. In the center of the structure origins another stripe patterned perpendicularly to the Damon Eshbach one. Thus, in this stripe spin waves propagate in the backward volume geometry. Hence, it is referred to as backward volume stripe (light grey in Fig. 1). By employing Brillouin light scattering microscropy (μBLS) we show that the colliding Damon Eshbach spin waves are converted into backward volume spin waves propagating along the backward volume stripe.

In an unstructured film, this conversion from Damon Eshbach into backward volume spin waves is impossible as backward volume and Damon Eshbach spin waves exist in different frequency regions. However, in a spin-wave waveguide, the quantization of spin-waves across the width of the

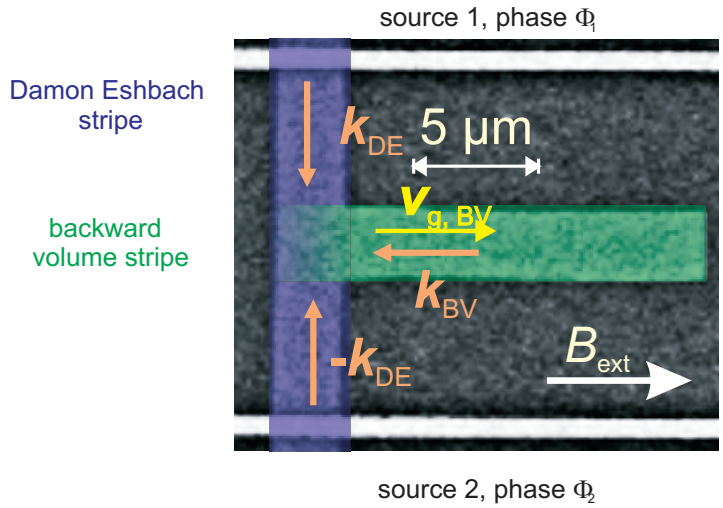

Fig. 1: SEM image of an exemplary "T" structure: Two microstripe antennas have been fabricated on top of a $Ni_{81}Fe_{19}$-spin-wave waveguide which is magnetized along its short axis (Damon Eshbach stripe, dark grey). In the center of the structure a second waveguide origins out of the Damon Eshbach stripe, which is magnetized along its long axis (backward volume stripe, light grey). The arrows indicate the directions of the external field B_{ext}, the wavevector $\mathbf{k}$ in propagation direction and the direction of the group velocity $\mathbf{v}_{\mathrm{g}}$.

stripe, which leads to transversal spin waves, shifts the spin-wave dispersion relations and allows for a coexistence of spin waves propagating parallel to the magnetization and spin waves propagating perpendicular to the magnetization at the same frequency. In addition to the quantization, the internal field H_{eff} in a perpendicularly magnetized stripe differs from the internal field in a longitudinally magnetized waveguide. In the latter case, the demagnetization is negligible and thus $H_{\mathrm{ext}} \approx H_{\mathrm{eff}}$. In a transversally magnetized stripe, the demagnetization field can be quite large and will reduce the internal field significantly [12]. For instance, in a $w_{\mathrm{s}} = 1.5\,\mu\mathrm{m}$ wide, $t_{\mathrm{s}} = 40\,\mathrm{nm}$ thick $Ni_{81}Fe_{19}$-stripe (saturation magnetization $M_{\mathrm{s}} = 760\,\mathrm{kA/m}$, exchange constant $A = 1.6 \cdot 10^{-11}\,\mathrm{J/m}$) an applied external field of $\mu_0 H_{\mathrm{ext}} = 70\,\mathrm{mT}$ leads to an internal field $\mu_0 H_{\mathrm{eff}} = 58\,\mathrm{mT}$ in the center of the stripe. Moreover, the effective width of the stripe turns out to be smaller than the geometrical width, as the internal field distribution in the stripe is inhomogeneous. In the case of the stripe discussed above the effective width reduces to approximatively $w_{\mathrm{eff}} = 1.3\,\mu\mathrm{m}$. The reduction of the internal field will lower the spin-wave dispersion relation in a transversally magnetized stripe further, allowing for a larger energetic overlap of the backward volume spin-wave and Damon Eshbach spin-wave dispersion curves. This is illustrated in Fig. 2, where the spin-wave dispersion relation calculated following Ref. [13] for the first transversal spin-wave mode in a $Ni_{81}Fe_{19}$-stripe - with the dimensions and material parameters stated above - perpendicularly magnetized (DE) for an internal field of $\mu_0 H_{\mathrm{eff}} = 58\,\mathrm{mT}$ is shown. In addition, Fig. 2 shows the first two transverse eigenmodes for a longitudinally magnetized stripe (BV) with $\mu_0 H_{\mathrm{eff}} = 70\,\mathrm{mT}$. As the translational symmetry is broken in the "T" structure, momentum conservation does not need to be fulfilled and thus the transition from the first transversal spin wave mode in the Damon Eshbach stripe into any transversal spin-wave mode in the backward volume stripe is possible as long as energy is conserved.

In order to proof the possibilities to realize the conversion of Damon Eshbach into backward volume spin waves in such a "T" structure, micromagnetic simulations have been performed. Figure 3 shows snapshots of the out of plane component of the dynamic magnetization for a fixed time obtained from such simulations of an exemplary structure, consisting of two perpendicular $w_{\mathrm{s}} = 1.5\,\mu\mathrm{m}$ wide, $l_{\mathrm{s}} = 5\,\mu\mathrm{m}$ long and $t_{\mathrm{s}} = 40\,\mathrm{nm}$ thick ferromagnetic stripes in a $5\mathrm{x}5\mathrm{x}0.04\,\mu\mathrm{m}^3$ mesh with $5\mathrm{x}5\mathrm{x}40\,\mathrm{nm}^3$ unit cells. A bias magnetic field of $\mu_0 H_{\mathrm{ext}} = 70\,\mathrm{mT}$ is applied in x-direction. In this simulation the excitation sources are modeled as spatially homogeneous, alternating magnetic fields applied in y-direction, which are localized to the shaded areas. The excitation frequency $f = 8.4\,\mathrm{GHz}$ has been chosen to resonantly excite propagating spin waves in the Damon Eshbach

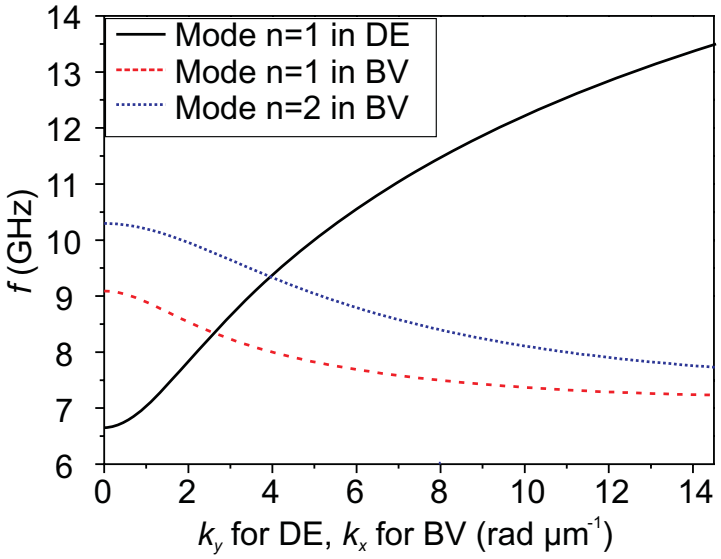

Fig. 2: Spin wave dispersion relations, calculated following [13], for the first transverse eigenmode in a $w_{\mathrm{eff}} = 1.3\,\mu\mathrm{m}$ wide, $t_{\mathrm{s}} = 40\,\mathrm{nm}$ thick $Ni_{81}Fe_{19}$-stripe (saturation magnetization $M_{\mathrm{s}} = 760\,\mathrm{kA/m}$, exchange constant $A = 1.6 \cdot 10^{-11}\,\mathrm{J/m}$) perpendicularly magnetized (De for an internal field $\mu_0 H_{\mathrm{eff}} = 58\,\mathrm{mT}$ (corresponding to an applied external field of $\mu_0 H_{\mathrm{ext}} = 70\,\mathrm{mT}$) and the first two transverse eigenmodes for a $w_{\mathrm{s}} = 1.5\,\mu\mathrm{m}$ wide longitudinally magnetized (BV) stripe for $\mu_0 H_{\mathrm{eff}} = 70\,\mathrm{mT}$.

stripe. In Figs. 3a and b the phase fronts of these propagating spin waves are clearly visible due to the alternating sign of the dynamic magnetization. Moreover, alternating phase fronts in the backward volume stripes can be seen. In Fig. 3a the two spin-wave sources excite spin waves in phase. As a consequence of this, in the center of the Damon Eshbach stripe an anti-node is formed. In contrast, in Fig. 3b the two sources are exciting out of phase, which results in the formation of a node in the center. As can be seen from the figures, whether a node or an anti-node is formed has great impact on the profile of the spin wave propagating inside the backward volume stripe. While the in-phase excitation results in the first transversal spin-wave eigenmode of the stripe, which exhibits one anti-node across the width of the stripe, the out-of-phase excitation leads to the generation of the second transversal spin-wave eigenmode (two anti-nodes).

In the real experiment, the excitation is not as confined as in the simulation. While the in-plane component of the dynamic Oersted field created by the microwave current in the antenna, which is mainly responsible for the excitation of the Damon Eshbach spin waves, is confined quite well under the stripline, the out-of-plane component reaches comparably far out. Consequently, it exerts a torque on the magnetization in the backward volume stripe. As the wavelength of the microwaves is much larger than the structure itself, this out-of-plane field will excite a forced oscillation with homogeneous phase in the backward volume stripe. The propagating spin waves generated in the center of the "T" structure are going to interfere with this homogeneous excitation. This interference leads to the formation of a standing pattern that can be used to measure the wavelength of the propagating waves, as the separation between two nodes corresponds to the wavelength of the propagating wave.

This behavior is shown in Fig. 4a for a "T" structure with a $w_{\mathrm{DE}} = 4.2\,\mu\mathrm{m}$ wide, $t_{\mathrm{DE}} = 40\,\mathrm{nm}$ thick Damon Eshbach stripe with an antenna separation of $L_{\mathrm{DE}} = 4.9\,\mu\mathrm{m}$ and a $w_{\mathrm{BV}} = 2.2\,\mu\mathrm{m}$ wide, $t_{\mathrm{BV}} = 40\,\mathrm{nm}$ thick and $L_{\mathrm{BV}} = 13\,\mu\mathrm{m}$ long backward volume stripe. An external magnetic field $\mu_0 H_{\mathrm{ext}} = 48\,\mathrm{mT}$ and a microwave frequency $f = 7.13\,\mathrm{GHz}$ have been applied continuously and the BLS intensity in the center of the structure is recorded along the backward volume stripe. On the left side of the figure ($x = 0 - 4.2\,\mu\mathrm{m}$) one can see an anti-node formed in the center of the Damon Eshbach stripe, as the phases of the antennas are matched to be equal. However, it can be noted that the anti-node is slightly off-center, which is due to the fact that the emission of the microstripe antennas is non-reciprocal in the Damon Eshbach geometry and thus matching the intensities to be exactly equal is a challenging task. Still, the spin-wave intensity converted into

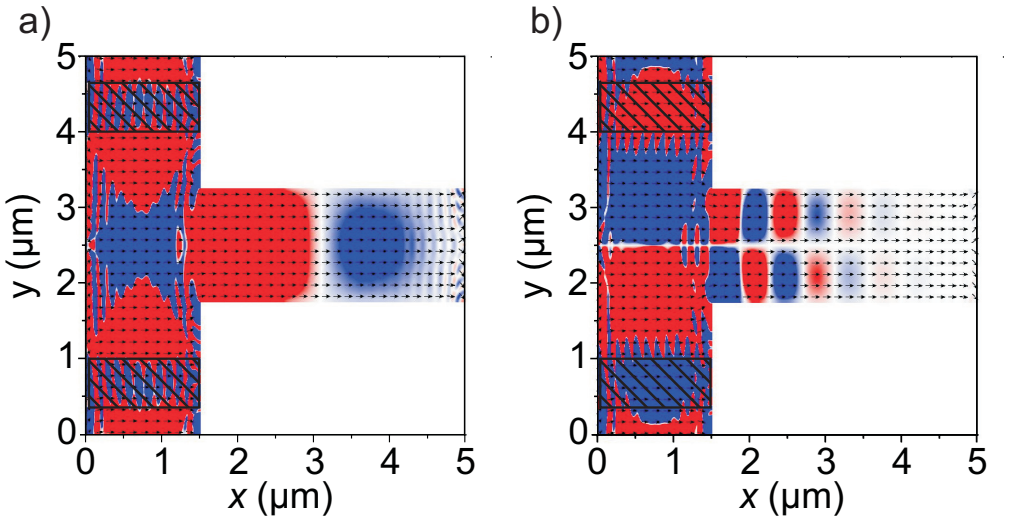

Fig. 3: Snapshots of the out-of-plane component of the magnetization for a fixed time out of an OOMMF simulation. The simulated structure consists of two perpendicular $w_s = 1.5\,\mu$m wide, $l_s = 5\,\mu$m long and $t_s = 40\,$nm thick ferromagnetic stripes in a 5x5x0.04 µm^3 mesh with 5x5x40 nm^3 unit cells. A bias magnetic field of $\mu_0 H = 70\,$mT is simulated in x-direction. The color coding represents the out-of-plane component of the magnetization, while grey corresponds to positive and black to negative values. In the shaded areas a homogeneous alternating field in $y-$direction is emulating the excitation of spin waves with a frequency of $f = 8.4\,$GHz. In a) the two spin-wave sources are oscillating in phase and in b) with opposite phase. In both snapshots the wavelength of propagating spin waves in the Damon Eshbach stripes is clearly visible, as the out-of-plane component changes sign with the wavelength of the spin waves. Also, in both snapshots the wavelength of propagating spin waves in the backward volume stripe is visible the same way. However, while the excitation in phase leads to the formation of the first transversal spin-wave mode in the backward volume stripe, the out of phase excitation generates the second mode.

the backward volume stripe shows one anti-node across the width of the backward volume stripe, which corresponds to the first transversal spin-wave mode in the stripe. A clear formation of nodes and anti-nodes along the backward volume stripe can be seen, which is caused by the interference of the propagating spin waves with the homogeneous excitation by the out-of-plane component of the microstripe antennas as discussed above. This is a clear indication that the phase of the converted spin waves is changing in space and that the converted spin waves are thus propagating waves. The separation of the anti-nodes allows for a first estimation of the spin-wave wavelength to be $\lambda_{BV} \approx 3.4\,\mu$m.

To get a clearer proof of the propagation of the spin waves in the backward volume stripe and to obtain a more precise measurement of the spin-wave wavelength we employ phase resolved Brillouin light scattering microscopy (PR-μBLS) [14] to record the phase of the spin-waves as a function of the x-position in the center of the backward volume stripe. As can be seen in Fig. 4b, the phase linearly decreases in space, as expected for the backward volume geometry (cf. Fig. 1, $\mathbf{k}_{BV} \parallel -\mathbf{v}_{g,BV}$). The slope, which corresponds to the wavevector component in propagation direction of the spin waves, yields a wavelength $\lambda = 3.4 \pm 0.1\,\mu$m, which is in good agreement with the anti-node-separation and with the value expected from the dispersion relation for thin films.

As illustrated in Fig. 3, the phase between the two spin wave sources in the Damon Eshbach stripe will determine the type of mode generated in the center of the "T" structure. Figure 5 shows the transition of the excited mode with changing phase between the two sources for a "T" structure with $w_{DE} = w_{BV} = 2.2\,\mu$m and thickness $t_{DE} = t_{BV} = 40\,$nm for an applied microwave frequency $f = 7.13\,$GHz at an applied field $\mu_0 H_{ext} = 52\,$mT. At the left end of each intensity map, half of

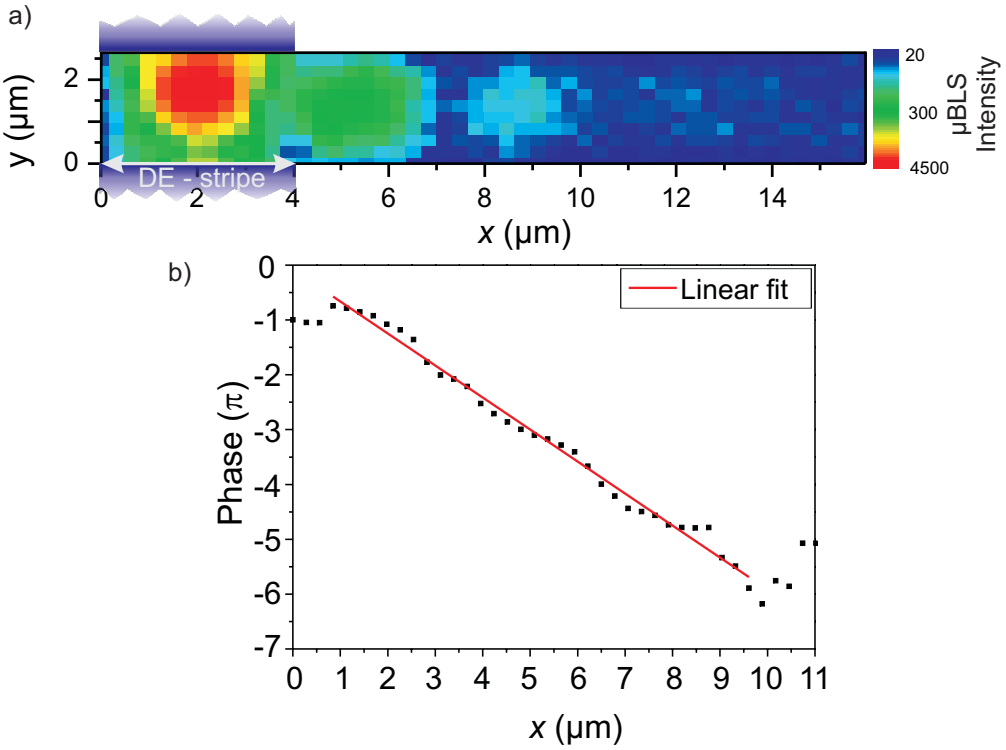

Fig. 4: a) Color coded BLS-intensity in the center of a "T" structure with a $w_{DE} = 4.2\,\mu m$ wide, $t_{DE} = 40\,nm$ thick Damon Eshbach stripe with an antenna separation of $L_{DE} = 4.9\,\mu m$ and a $w_{BV} = 2.2\,\mu m$ wide, $t_{BV} = 40\,nm$ thick and $L_{BV} = 13\,\mu m$ long backward volume stripe. An external magnetic field of $\mu_0 H_{ext} = 48\,mT$ and a microwave frequency $f = 7.13\,GHz$ have been applied. In the Damon Eshbach stripe ($x = 0 - 4.2\,\mu m$) the formation of an anti-node of the spin-wave intensity can be observed, while in the backward volume stripe a set of anti-nodes and nodes along the stripe is visible. This behavior in the backward volume stripe corresponds to the propagation of the first transversal spin-wave mode along the stripe interfering with the forced excitation with constant phase created by the microstripe antennas. b) Phase accumulation of the spin waves propagating in the backward volume stripe obtained with phase resolved μBLS. Both, the phase resolved measurement and the separation between the interference maxima reveal a wavelength of $\lambda \approx 3.4\,\mu m$ for the propagating spin waves.

the Damon Eshbach stripe is shown ($x = 0 - 1\,\mu m$). In Fig. 5a the phase difference between the antennas is approximatively $\Delta\Phi = 0\,rad$ and in the center of the stripe (near $y \approx 1\,\mu m$) a maximum of the spin-wave intensity can be observed. The mode propagating into the backward volume stripe shows no nodes across the width of the stripe and in accordance with Fig. 4a corresponds to the first transversal spin-wave mode. If the phase difference between the antennas is changed to $\Delta\Phi \approx \pi/2\,rad$ (cf. Fig. 5 b, the intensity maximum is moved out of the center of the Damon Eshbach stripe and the intensity profile in the backward volume stripe shows a zig-zag-like evolution. This behavior is the well known interference of the first and second transversal spin-wave mode [15], thus for this phase difference a mixture of this set of modes is generated. In contrast, in Fig. 5c the phase difference between the antennas is $\Delta\Phi \approx \pi\,rad$ and in this case the BLS intensity in the Damon Eshbach stripe shows a node in the center while the spin-wave intensity in the backward volume stripe rather hops from one side of the stripe to the other. As can be seen in Fig. 3b the second transversal spin-wave mode possesses two anti-nodes with opposite phase, thus the observed intensity pattern in Fig. 5c reflects the interference of this mode with the homogeneous excitation by the out-of-plane components of the antenna fields, as, while one of the anti-nodes is in phase with this excitation, the other is out of phase. In Figs. 5d and e the phase difference between the antennas is $\Delta\Phi \approx 3\pi/2\,rad$ and $\Delta\Phi \approx 2\pi\,rad$ respectively. Thus, these two measurements

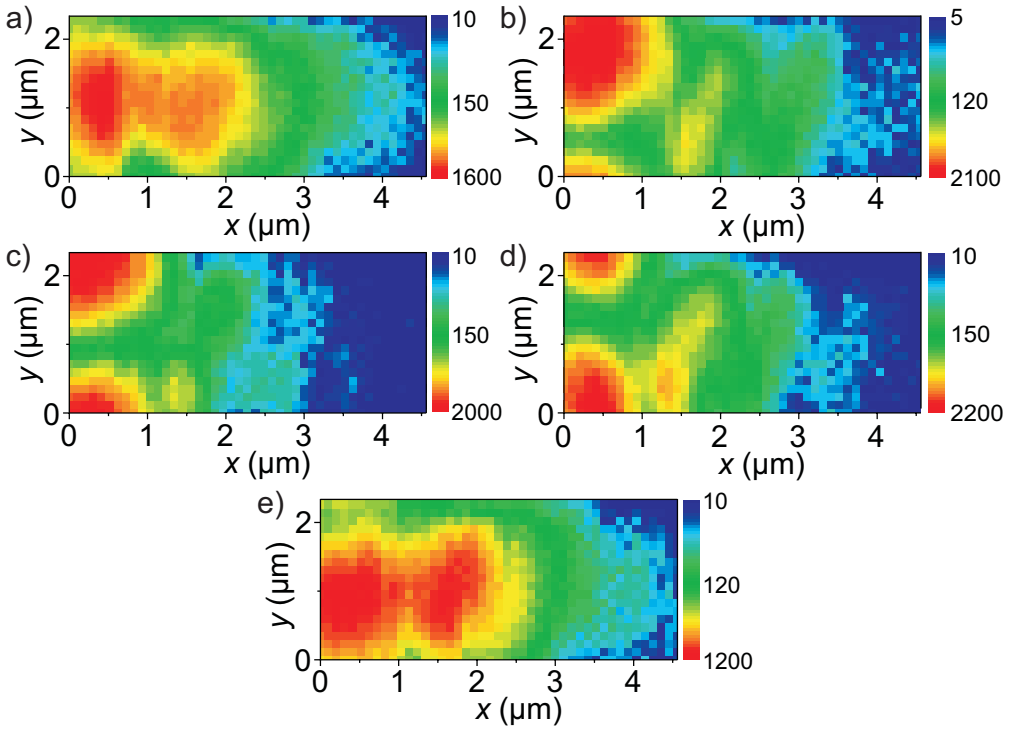

Fig. 5: Color coded BLS-intensity in the center of a "T" structure with a $w_{DE} = 2.2\,\mu m$ wide, $t_{DE} = 40\,nm$ thick Damon Eshbach and a $w_{BV} = 2.2\,\mu m$ and $t_{BV} = 40\,nm$ thick backward volume stripe for an applied external magnetic field $\mu_0 H_{ext} = 52\,mt$ and an applied microwave frequency $f = 7.13\,GHz$ for different phase differences between the two spin-wave sources in the Damon Eshbach stripe. a) $\Delta\Phi = 0\,rad$. b) $\Delta\Phi \approx \pi/2\,rad$. c) $\Delta\Phi \approx \pi\,rad$. d) $\Delta\Phi \approx 3\pi/2\,rad$. e) $\Delta\Phi \approx 2\pi\,rad$.

should correspond to Fig. 5b and a respectively and the observed intensity patterns show a good agreement.

To summarize, we have shown the phase-sensitive generation of propagating backward volume spin-waves out of counterpropagating Damon Eshbach spin waves in a "T" shaped structure, where the phase of the Damon Eshbach spin waves determines the transversal profile of the generated mode. As the relative phase of the spin waves determines whether a node or anti-node is formed in the center of the "T", this determines whether the first or the second transversal spin wave propagates into the backward volume stripe. By employing phase resolved BLS we have proven that the spin waves generated in the center of the "T" are propagating into the backward volume stripe over a distance of approximatively $\Delta x = 10\,\mu m$, showing that this is a quite effective method to generate propagating backward volume waves. We have shown that the direct excitation by the microstripe antennas furthermore allows for the direct optical detection of the wavelength of the propagating waves and thus also proves their propagation. Furthermore, we want to stress the usability of this kind of structure to read out the phase of the Damon Eshbach spin waves. As the second mode has no net magnetic moment across the width of the stripe and can thus not be detected by a microwave antenna, the propagating first mode can be picked up by an antenna placed over the backward volume stripe. Hence depending on the phase of the Damon-Eshbach spin waves, a readout in a backward volume stripe shows either "one", if the first mode is created, or zero. Thus, this kind of structures can also prove as spin-wave logical cell for the emerging field of magnon spintronics.

Thomas Brächer is supported by a fellowship of the Graduate School Materials Science in Mainz (MAINZ) through DFG-funding of the Excellence Initiative (GSC 266). Philipp Pirro acknowl-

edges financial support by the Carl-Zeiss-Stiftung via the OPTIMAS Carl-Zeiss doctoral program.

References

[1] B. Lenk., H. Ulrichs, F. Garbs, and M. Münzenberg, *The building blocks of magnonics*, Physics Reports **507**, 107 (2011).

[2] K. Vogt, H. Schultheiss, S. Jain, J.E. Pearson, A. Hoffmann, S.D. Bader, and B. Hillebrands, *Spin waves turning a corner*, Appl. Phys. Lett. **101**, 042410 (2012).

[3] H. Ulrichs, V.E. Demidov, S.O. Demokritov and S. Urazhdin, *Spin-torque nano-emitters for magnonic applications*, Appl. Phys. Lett. **100**, 162406 (2012).

[4] A. V. Chumak, P. Pirro, A. A. Serga, M. P. Kostylev, R. L. Stamps, H. Schultheiss, K. Vogt, S. J. Hermsdoerfer, B. Laegel, P.A. Beck, and B. Hillebrands, *Spin-wave propagation in a microstructured magnonic crystal*, Appl. Phys. Lett. **95**, 262508 (2009).

[5] P. Pirro, T. Brächer, K. Vogt, B. Obry, H. Schultheiss, B. Leven, and B. Hillebrands, *Interference of coherent spin waves in micron-sized ferromagnetic waveguides*, Phys. Status Solidi B **248**, No. 10, 2404 (2011).

[6] K.-S. Lee, and S.-K. Kim, *Conceptual design of spin wave logic gates based on a Mach-Zehnder-type spin wave interferometer for universal logic functions* , J. Appl. Phys. **104**, 053909 (2008).

[7] Y. Kajiwara1, K. Harii, S. Takahashi, J. Ohe, K. Uchida, M. Mizuguchi, H. Umezawa, H. Kawai, K. Ando, K. Takanashi, S. Maekawa, and E. Saitoh, *Transmission of electrical signals by spin-wave interconversion in a magnetic insulator*, Nature **464**, 262-266 (11 March 2010).

[8] V.E. Demidov, S.O. Demokritov, B. Hillebrands, M. Laufenberg, and P.P. Freitas, *Radiation of spin waves by a single micrometer-sized magnetic element*, Appl. Phys. Lett. **85**, 2866 (2004).

[9] K. Sekiguchi, K. Yamada1, S. Seo, K. Lee, D. Chiba, K. Kobayashi, and T. Ono, *Time-domain measurement of current-induced spin wave dynamics*, Phys. Rev. Lett. **108**, 017203 (2012).

[10] M.J. Donahue and D.G. Porter, *OOMMF User's Guide, Version 1.0*, Interagency Report NISTIR **6376**, National Institute of Standards and Technology, Gaithersburg, MD (Sept 1999).

[11] D.-S. Han, S.-K. Kim, J.-Y,. Lee, S.J. Hermsdoerfer, H. Schultheiss, B. Leven, and B. Hillebrands, *Magnetic domain-wall motion by propagating spin waves*, Appl. Phys. Lett. **94**, 112502 (2009).

[12] S.O. Demokritov, V.E. Demidov, *Spin wave confinement*, chapter *quantized spin- wave modes due to lateral confinement*, Pan Stanford Publishing (2008).

[13] B.A. Kalinikos and A.N. Slavin, *Theory of dipole-exchange spin wave spectrum for ferromagnetic films with mixed boundary conditions*, J. Phys. C **19**, 7013 (1986).

[14] K. Vogt, H. Schultheiss , S. J. Hermsdoerfer , P. Pirro , A. A. Serga and B. Hillebrands, *All-optical detection of phase fronts of propagating spin waves in a $Ni_{81}Fe_{19}$ microstripe*, Appl. Phys. Lett. **95**, 182508 (2009).

[15] P. Clausen, K. Vogt, H. Schultheiss, S. Schäfer, B. Obry, G. Wolf, P. Pirro, B. Leven, and B. Hillebrands, *Mode conversion by symmetry breaking of propagating spin waves*, Appl. Phys. Lett. **99**, 162505 (2011).

4.6 Optimization of spin pumping in YIG/Pt structures

M. B. Jungfleisch, V. Lauer, R. Neb, A. V. Chumak, and B. Hillebrands

In the last decades, there was a rapidly increasing interest in the field of spintronics. The promising aim is to exploit the intrinsic spin of electrons to build new efficient magnetic storage devices and computing units. A relatively new sub-field of spintronics is magnon spintronics, where magnons, the quanta of spin waves (collective excitations of coupled spins in a magnetically ordered solid), are used as spin currents. In this case spin angular momentum is not transferred by electrons, but by spin waves. Spin waves can even be utilized in ferromagnetic insulators for the transfer of spin information. Since spin-wave spin currents in insulators are not accompanied by charge currents, parasitic heating by the movement of electrons can be excluded. Thus, the energy consumption might be drastically reduced in comparison to conventional electronics.

Magnons can be detected by a combination of the spin pumping method and the inverse spin Hall effect (ISHE) [1]. Spin pumping refers to the generation of spin polarized electron currents in heavy noble metals like platinum (Pt) by the magnetization precession in an attached ferromagnetic layer [2,3], whereas the ISHE transforms a spin current into a conventional charge current [2,4,5].

Many studies on spin pumping and ISHE are focused on ferromagnetic insulator/nonmagnetic metal bilayer structures like yttrium iron garnet/platinum (YIG/Pt). Since YIG is an insulator with a band gap of 2.85 eV [6] no direct transition of spin polarized electron currents from the YIG into the Pt layer is possible. Thus, spin pumping is the only method applicable in these structures to inject spin currents into the Pt layer. Spin pumping in YIG/Pt structures is an interface effect and, thus, it is of crucial importance to investigate the effect of surface processing of the ferromagnetic YIG layer before the Pt deposition. Moreover, the ISHE strongly depends on the quality of the used nonmagnetic metal and, thus, on the growth conditions of this metallic layer. Up to now, there are no systematic, quantitative studies on the YIG/Pt interface treatment.

In this Report, we present our results on the influence of processing of the YIG surface before the Pt deposition on spin pumping efficiency. The spin currents generated by spin pumping are detected by the ISHE. Three sets of YIG/Pt samples with different YIG thicknesses (two sets with 2.1 µm and one set with 4.1 µm) and constant Pt thickness of 10 nm were investigated. Spin pumping was driven by the ferromagnetic resonance excited by a microwave signal. Due to spin pumping a spin polarized electron current is injected from the YIG waveguide into the adjacent Pt layer [3] and subsequently transformed into a conventional charge current by the ISHE (see Fig. 1b) [1, 4, 5]. We measure the FMR spectra using a conventional microwave technique, as well as the inverse spin Hall voltage, allowing us to calculate the spin pumping efficiency, defined as the ratio of the detected ISHE charge current to the absorbed microwave power. Our experimental results clearly show a significant difference (up to factor of 150) between the seven different surface treatments.

A sketch of the experimental setup is shown in Fig. 1a. The YIG samples of 2.1 µm and 4.1 µm thickness and a size of 3×4 mm were grown by liquid phase epitaxy on both sides of 500 µm thick gadolinium gallium garnet (GGG) substrates. Since the GGG substrate between the two YIG layers is with 500 µm rather thick, the second YIG layer has no influence on our studies.

After a conventional pre-cleaning, all samples were cleaned by acetone and isopropanol in an ultrasonic bath. Afterwards, the following surface treatments have been applied:

- Cleaning in piranha etch, a mixture of H_2SO_4 and H_2O_2. This method is strongly oxidizing and,

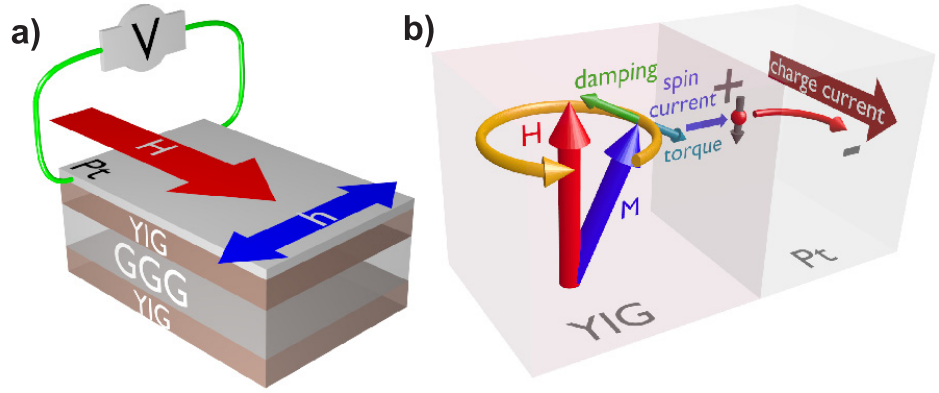

Fig. 1: a) Sketch of the sample and the setup geometry. b) Illustration of spin pumping and inverse spin Hall effect. Details see text.

thus, removes most organic matter. Among the used surface treatments, piranha cleaning is the only one, which was performed outside the molecular beam epitaxy (MBE) chamber. Thus, we cannot exclude, that the samples are contaminated by microscopic dirt or a water film due to air exposure.

The following surface treatments were performed *in-situ*:

- Heating at 200 °C for 30 min in order to remove water from the sample surfaces.
- Heating at 500 °C for 5 hours in order to remove water from the sample surfaces. It might be that for this method lattice misfits in the YIG crystal are annealed as well [7, 8].
- Ar^+ plasma cleaning at energies of $50-100$ eV for 10 min. The used energies are below the threshold for sputtering and thus, this cleaning method acts mechanically.
- O^+/Ar^+ plasma at a ratio of 1:1 at energies around $50-100$ eV for 10 min. In addition to the mechanical cleaning effect, O^+ oxidizes organic matter.

The used surface processings are summarized in Table 1. After cleaning, the 10 nm thick Pt layer was grown by MBE at a pressure of 5×10^{-8} mbar and a growth rate of 0.01 nm/s. It is important to note that the Pt film was deposited on each of the samples of one set simultaneously, ensuring the same growing conditions.

The experiment was performed in the following way: an external magnet field H was applied in the YIG film plane (see Fig. 1a). The magnetization precession was excited at a constant frequency of $f = 6.8$ GHz by a 0.6 mm wide Cu microstrip antenna. We applied microwave powers P_{mw} of 1 mW, 10 mW and 100 mW in order to study the linear, quasi-linear and non-linear regime. The Pt layer and the microstrip antenna were electrically isolated by a rather thick silicon oxide layer of 100 µm thickness in order to avoid overcoupling. While sweeping the external magnetic field the microwave reflection and transmission (Fig. 2b) as well as the inverse spin Hall voltage U_{ISHE} (Fig. 2a) were recorded. The voltage U_{ISHE} was measured using a lock-in technique. The microwave amplitude was modulated with a frequency of 500 Hz. The complicated absorption and reflection spectra depicted in Fig. 2b are due to the interference of spin-wave signals reflected from the YIG sample and the edges of the microstrip line [9]. This behavior does not influence our studies: the maximum at the ferromagnetic resonance is used to calculate the spin pumping efficiency (see Fig. 2c). Knowing the applied microwave power P_{applied} and measuring microwave reflection P_{refl} and transmission P_{trans} (see Fig. 2b) enables us to calculate the absorbed power as $P_{\mathrm{abs}} = P_{\mathrm{applied}} - (P_{\mathrm{trans}} + P_{\mathrm{refl}})$. The results are depicted in Fig. 2. At the ferromagnetic resonance field $H_{\mathrm{FMR}} \approx 170$ mT, energy is transferred most effectively into the magnetic system and, thus, the

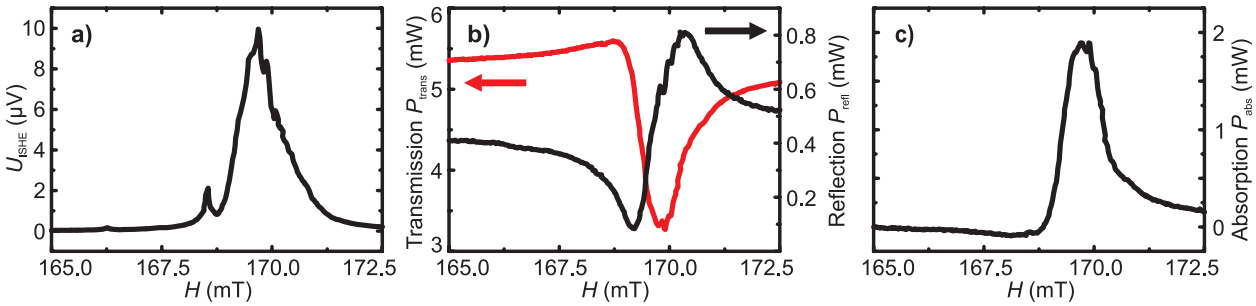

Fig. 2: a) ISHE voltage as a function of the applied magnetic field. b) Transmitted and reflected microwave power. c) Absorbed microwave power. Applied microwave power $P_{\text{applied}} = 10\,\text{mW}$, YIG thickness: 2.1 µm.

microwave absorption is maximal (see Fig. 2c). In resonance condition (when the angle of precession is maximal), spin currents are efficiently pumped from the YIG into the Pt layer (Fig. 1b) and transformed into an electric current by the ISHE [5]. Subsequently, we measure the maximal ISHE voltage U_{ISHE} at H_{FMR} across the edges of the Pt layer perpendicular to the external magnetic field (see Fig. 2a). Changing the external magnetic field to the opposite direction results in an inverted voltage proving the ISHE nature of the observed signal.

In Fig. 3 the ISHE voltages U_{ISHE} are shown as a function of the external magnetic field for one set (YIG thickness 2.1 µm) of six samples (see Tab. 1) at a microwave power of 10 mW. The result for the seventh sample of this set is shown in Fig. 2a. It is obvious that the different surface treatments before the Pt deposition change drastically the maximum of the ISHE voltage, whereas the absorbed microwave power is nearly independent on it. Please note that the intensity and characteristics of the detected mode spectra are attributed to the cutting of the YIG samples and can be hardly controlled. These modes are width modes. Hence, they are different for each sample and of minor interest for the present studies.

In order to investigate the different cleaning methods described above we used three sets of samples. We measure the spectra for microwave powers P_{mw} of 1 mW, 10 mW and 100 mW. In order to compare the samples of one set we introduce the spin pumping efficiency as

$$\eta(P_{\text{applied}}, n) = \frac{U_{\text{ISHE}}^{\text{FMR}}}{R \cdot P_{\text{abs}}^{\text{FMR}}} \quad , \tag{1}$$

where n is the number of the sample (i. e. the number of the cleaning method, see Tab. 1), $U_{\text{ISHE}}^{\text{FMR}}$ is the maximal ISHE voltage in resonance H_{FMR}, R is the electric resistance of the Pt layer, P_{applied} is the applied microwave power and $P_{\text{abs}}^{\text{FMR}}$ is the absorbed microwave power at H_{FMR}.

Further, we introduce the power and thickness independent parameter ε by normalizing the efficiency of the n-th sample to the first sample of each set $n = 1$ as

$$\varepsilon(n) = \frac{\eta(n, P_{\text{applied}})}{\eta(n = 1, P_{\text{applied}})} \quad . \tag{2}$$

The ε-parameter is a measure for the enhancement of the spin pumping efficiency due to the surface treatements. For each of the used surface treatments we calculate the ε-values: 3 microwave powers for each set. Our studies have shown, that the ε-parameters practically do not depend on the absorbed microwave power. Thus, we introduce the mean value $\bar{\varepsilon}$ of these ε-values. The standard deviation is given by $\sigma(\bar{\varepsilon})$. The results are summarized in Tab. 1.

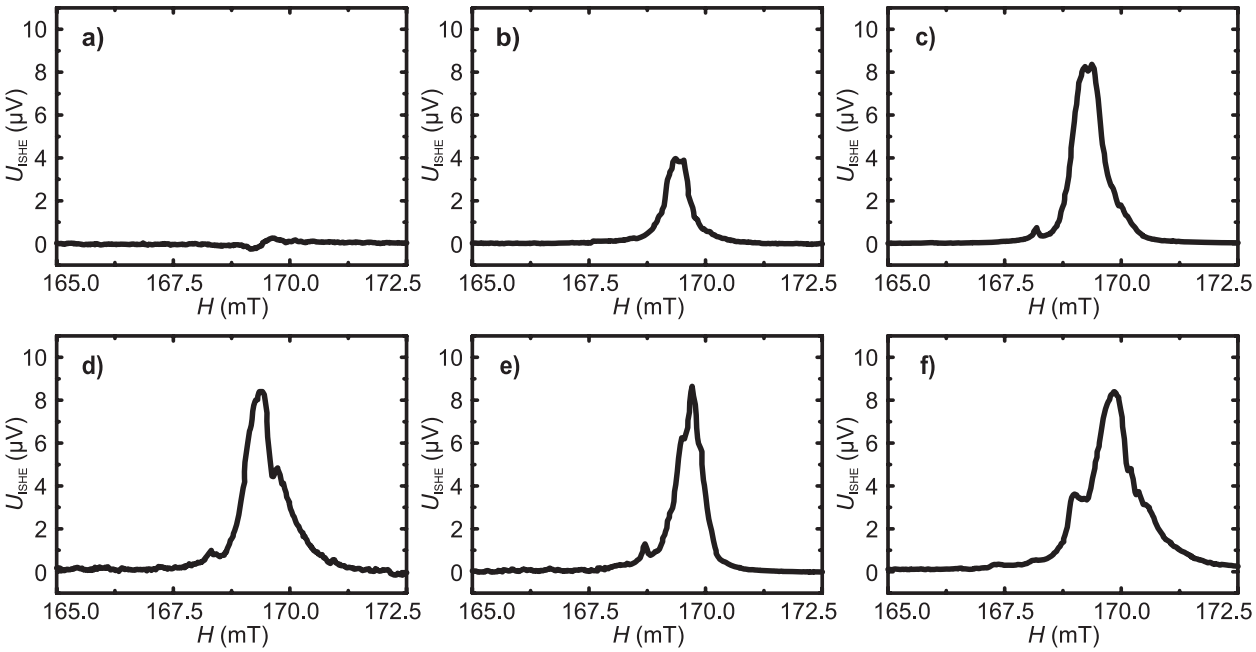

Fig. 3: a) Simple cleaning by acetone and isopropanol. b) Piranha. c) Piranha and heating at 200 °C. d) Piranha and Ar^+ plasma. e) Piranha and O^+/Ar^+ plasma. f) Piranha and heating at 500 °C. Applied microwave power $P_{\text{applied}} = 10\,\text{mW}$, YIG thickness: 2.1 μm.

The general tendency is the same for all series of measurements. The conventional cleaning by acetone and isopropanol in an ultrasonic bath (1) achieves the worst results ($\bar{\varepsilon} = 1$, see Fig. 3a, $U_{\text{ISHE}} = 270\,\text{nV}$ for $P_{\text{mw}} = 10\,\text{mW}$). Surface cleaning by piranha (Fig. 3b) improves the efficiency by a factor of 14, but this method is not reliable (standard deviation of $\sigma(\bar{\varepsilon}) = 131\,\%$ is very large). This might be due to the fact that piranha etch is a chemical-mechanical cleaning method and thus, removes coarse dirt. Since this surface treatment takes place outside the MBE chamber and since the sample is in air contact after cleaning, it could be that the sample is contaminated again by dirt or water before the Pt deposition. Heating the samples after piranha cleaning in the MBE chamber at 200 °C for 30 min (sample 3, Fig. 3c) removes mainly the water film from the surface and results in a 64 times higher efficiency. However, this cleaning method also does not guarantee a high ISHE voltage, which is reflected in the high standard deviation. Using an Ar^+ plasma (method 4) is more efficient (see Fig. 3d) and particularly more reliable. Method 4 acts mechanically and removes water as well as other dirt from the sample surface. The best results ($\bar{\varepsilon} = 152$) are obtained for the O^+/Ar^+ plasma (5, see Fig. 2). The additional advantage of this surface treatment is the removal of organic matter. In order to check the reliability of the O^+/Ar^+ plasma cleaning (method 5), we substituted the piranha cleaning by heating the sample: even without piranha etching, but with heating at 200 °C and O^+/Ar^+ plasma (method 6), we achieve a considerable spin pumping efficiency of $\bar{\varepsilon} = 86$ (see Fig. 3e). This is mainly attributed to the O^+ plasma. It is remarkable that purely heating the sample at 500 °C for 5 hours (method 7) results in a comparable high efficiency of $\bar{\varepsilon} = 104$ (see Fig. 3f). The physical reason might be, that the temperature is sufficient high to anneal crystal defects of the YIG samples [7, 8].

In conclusion, we have shown a strong dependence of the spin pumping effect on the interface condition of YIG/Pt bilayer structures. We improved the ISHE signal strength by a factor of more than 150 using a combination of piranha etch and *in-situ* O^+/Ar^+ plasma treatment in comparison to standard ultrasonic cleaning. The combined cleaning by piranha etch and heating at 500 °C yields a comparable enhancement of the spin pumping efficiency (by a factor of 104). Since

sample n	process	$\bar{\varepsilon}$	$\sigma(\bar{\varepsilon})$ [%]	Figure
1	simple cleaning	1	—	3a
2	piranha	14	131	3b
3	piranha and 200°C	64	93	3c
4	piranha and Ar^+ plasma	79	54	3d
5	piranha and O_2/Ar^+ plasma	152	61	2a
6	200° C and O_2/Ar^+ plasma	86	52	3e
7	piranha and 500°C	104	40	3f

Table 1: $\bar{\varepsilon}$ is the calculated mean value of the ε-parameter, which is the thickness and power independent spin pumping efficiency (Eq. 2), for nine performed series of measurements (six series in case of piranha and 200°C), $\sigma(\bar{\varepsilon})$ is the standard deviation.

the voltage generated by the ISHE scales with the length of the Pt electrode (perpendicularly oriented to the external magnetic field), optimal interface conditions are extremely essential for the utilization of spin pumping and ISHE in micro-scaled devices. Our results are important for the reversed effects as well: the amplification [10] and excitation [2] of spin waves in YIG/Pt structures by the direct spin Hall effect and spin-transfer torque effect are also dependent on the interface condition of YIG and Pt layer.

Financial support by the Deutsche Forschungsgemeinschaft CH 1037/1-1 is gratefully acknowledged.

References

[1] J.E. Hirsch, *Spin Hall effect*, Phys. Rev. Lett. **83**, 1834 (1999).
[2] Y. Kajiwara, K. Harii1, S. Takahashi, J. Ohe, K. Uchida, M. Mizuguchi , H. Umezawa, H. Kawai, K. Ando, K. Takanashi, S. Maekawa, E. Saitoh, *Transmission of electrical signals by spin-wave interconversion in a magnetic insulator*, Nature **464**, 262 (2010).
[3] Y. Tserkovnyak, A. Brataas, G.E.W. Bauer, *Enhanced Gilbert damping in thin ferromagnetic films*, Phys. Rev. Lett. **88**, 117601 (2002).
[4] E. Saitoh, M. Ueda, H. Miyajima, G. Tatara, *Conversion of spin current into charge current at room temperature: Inverse spin-Hall effect*, Appl. Phys. Lett. **8**8, 182509 (2006).
[5] C.W. Sandweg, Y. Kajiwara, A.V. Chumak, A.A. Serga, V.I. Vasyuchka, M.B. Jungfleisch, E. Saitoh, B. Hillebrands, *Spin pumping by parametrically excited exchange magnons*, Phys. Rev. Lett. **106**, 216601 (2011).
[6] X. Jia, K. Liu, K. Xia, G.E.W. Bauer, *Spin transfer torque on magnetic insulators*, Europhys. Lett. **96**, 17005 (2011).
[7] O.G. Ramer, C.H. Wilts, *Surface effects in spin-wave resonance in thin YIG films*, phys. stat. sol. (b) **79**, 313 (1977).
[8] Duk Yong Choi, Su Jin Chung, *Annealing behaviors of lattice misfit in YIG and La-doped YIG films grown on GGG substrates by LPE method*, J. Cryst. Growth **191**, 754 (1998).
[9] W. Barry, *A broad-band, automated, stripline technique for the simultaneous measurement of complex permittivity and permeability*, IEEE Trans. Microwave Theory Tech. **MTT-34**, 1 (1986).
[10] Z. Wang, Y. Sun, M. Wu, V. Tiberkevich, A. Slavin, *Control of spin waves in a thin film ferromagnetic insulator through interfacial spin scattering*, Phys. Rev. Lett. **107**, 146602 (2011).

4.7 Detection of magnon spin transport by spin pumping and inverse spin Hall effect

M. B. Jungfleisch, A. V. Chumak, A. A. Serga, R. Neb, and B. Hillebrands

In collaboration with: D. A. Bozhko, Faculty of Radiophysics, Taras Shevchenko National University of Kyiv, Kyiv, Ukraine and V. S. Tiberkevich, Department of Physics, Oakland University, Rochester, Michigan, USA.

Spin pumping [1] and the inverse spin Hall effect [2] are the two main mechanisms to convert spin waves in a ferromagnetic waveguide into spin and, consecutively, charge currents in the adjacent nonmagnetic metal layer. The utilization of spin pumping and inverse spin Hall effect (ISHE) opens up the door to insulator-based spintronics, in which spin waves are used as carriers of angular momentum. This allows for the transfer of a spin over macroscopic distances, since the spin-wave freepath is normally orders of magnitude larger than the spin-diffusion length in metals. Furthermore, a spin wave itself can serve as an information processing element [4–6].

The potential applications as well as interesting underlying physics have resulted in a fast growth of studies of the magnetic insulator yttrium-iron garnet (YIG)/platinum (Pt) structures [2, 7, 9–11]. Nevertheless, in spite of a considerable progress in the field, the studies of spin-wave detection by means of spin pumping and ISHE were mostly concentrated on the investigation of standing spin-wave modes [2, 7, 12, 13], secondary-excited dipolar-exchange waves [9], and short-wavelength exchange waves [10, 11].

In this Report, we use a spatially separated spin-wave source and an ISHE detector in combination with time-resolved measurements to demonstrate the magnon spin transport [8]. The transmitted signal is detected as a DC pulse with a delay corresponding to the spin-wave propagation time.

A sketch of the structure under investigation is shown in Fig. 1. It consists of a 2.1 µm thick YIG waveguide ($19 \times 3\,\mathrm{mm}^2$) with a 10 nm thick ($0.2 \times 0.2\,\mathrm{mm}^2$) Pt strip deposited on the top (Pt resistance along its long axis is 400 Ohm). The length of the Pt layer is 200 µm and thus, it is small enough to avoid strong spin-wave distortions. An external bias magnetic field of $H_0 = 1754$ Oe is applied along the long axis of the YIG waveguide, providing conditions for backward volume magnetostatic wave (BVMSW) propagation. The spin waves are excited by a 50 µm wide Cu microstrip antenna, that is placed at a distance of 3 mm away from the Pt strip. The transmitted spin waves have been detected at the Pt antenna in two different ways: (1) as an inductive AC microwave signal (the Pt strip works as an inductive receiver such as a Cu microstip antenna) or (2) as an ISHE DC voltage. Both signals were measured by the the same circuit comprising a high input impedance preamplifier and an oscilloscope. In the first case a microwave detector is utilized to rectify the signal (note, "AC"denotes the envelope of this signal), while for the DC measurements the detector is substituted by a low-pass filter.

It is not possible to use lock-in technique in fast time-resolved measurements and therefore the values of the detected voltages are of great importance for the studies. Thus, prior to the described experiment we have tested the same YIG/Pt sample using the ferromagnetic resonance technique as shown in our recent investigations [9]. The ISHE voltage may reach values of up to 1.5 mV for an applied microwave power of 1 W. This ensures a high quality of the YIG/Pt interface and allows the measurement of the ISHE voltage from the traveling waves (which is drastically smaller due to the smaller excitation efficiency by a narrow antenna and due to the spin-wave damping during its propagation).

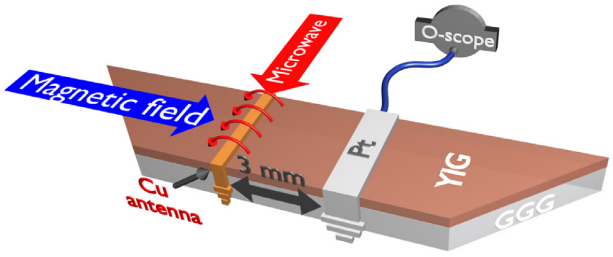

Fig. 1: Schematic illustration of the experimental setup: spin-wave packets are excited in the YIG waveguide using a microstrip antenna and detected at a 3 mm separated Pt detector as electromagnetically induced AC and as ISHE DC signals.

The experiment was performed in the following way: At the time $t = 0\,\text{ns}$ microwave pulses having a carrier frequency of $f_s = 7\,\text{GHz}$ and a duration τ_s in the range from 30 ns to 1 µs are applied to the input microstrip antenna. Traveling wave packets are excited and propagate towards the Pt strip [14]. The transmitted spin-wave packet is detected with a delay of approximately 200 ns (determined by the spin-wave group velocity) as an AC signal at the Pt antenna (see solid lines in Fig.2a and Fig.2b). Switching the setup to the DC regime shows that the ISHE DC pulse is also detected with practically the same delay (see Fig.2c and Fig.2d). An increase in the duration τ_s results in an increase in the amplitude and the duration of both the AC and the DC signal. This proves the spin-wave origin of our observations, since an increase of the spin-wave intensity with τ_s occurs due to a better passing of the input pulse through the limited spin-wave frequency band. Moreover, changing of the magnetic field polarity results in a change of the detected voltage sign, which is a signature of the ISHE [2].

A comparison of the spin-wave intensity and the ISHE voltage measured at the Pt strip shows that the maximum of the DC signal is slightly shifted towards larger times compared to the AC signal. Furthermore, the DC pulse shows a slower decay. These effects have been recently studied in [9] and are due to the contribution to the spin pumping of secondary-excited spin waves. In the linear case ($P_s = 10$ mW), these waves are known to be dipolar-exchange spin waves (DESWs) excited as a result of elastic two-magnon scattering of the propagating wave [3, 15, 16]. DESWs are not detectable by the microstrip antenna due to their small wavelengths [10, 14], but they contribute significantly to the spin pumping and, thus, to the ISHE voltage [9]. Due to their small velocity and damping, DESWs contribute to the ISHE voltage even after the traveling magnons have left the Pt region resulting in the slower decay of the DC pulse.

We have estimated the contribution of the DESWs to the ISHE voltage pulse. Since the antenna's width is larger than the DESWs propagation length, but much smaller than the decay distance of the primary spin waves, one can neglect the propagation of DESWs and a feedback reaction of DESWs on the primary spin-wave dynamics. In this case the dynamics of the number n_k of magnons in the k-th DESW mode can be modeled as

$$\partial n_k/\partial t + 2\Gamma_k n_k = 2R_k n_0(t) \quad , \tag{1}$$

where Γ_k is the damping parameter of the k-th DESW, R_k is the intensity of two-magnon scattering from spin waves to k-th DESW, and $n_0(t)$ is the time profile of primary spin waves under the antenna. Assuming, for simplicity, that all DESWs have the same damping rate $\Gamma_k = \Gamma = const$, one can derive a simple expression for the total density $n_{\text{sum}}(t) = n_0(t) + \sum_k n_k(t)$ of magnons under the antenna:

$$n_{\text{sum}} = n_0(t) + 2R \int_{-\infty}^{t} n_0(t) e^{-2\Gamma(t-t')dt'} \quad , \tag{2}$$

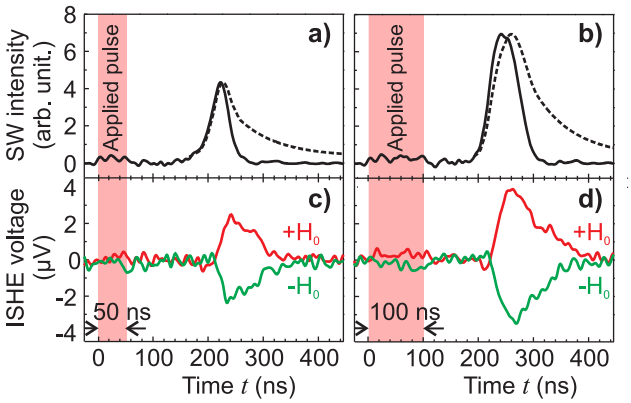

Fig. 2: Temporal evolution of the spin-wave intensity a) and b), and the ISHE voltage for both field polarities c) and d). Measured for the input signal durations $\tau_s = 50\,\text{ns}$ a) and c), and 100 ns b) and d), magnetic field $H_0 = 1754\,\text{Oe}$, applied power $P_s = 10\,\text{mV}$. Dashed lines in a) and b) show normalized total magnon densities n_{sum} calculated according Eq. 2 [8].

where $R = \sum_k R_k$ is the total intensity of two-magnon scattering.

In Fig. 2a and Fig. 2b, the numerically calculated normalized density n_{sum} is shown with dashed lines. The damping $\Gamma = 7 \cdot 10^6\,\text{rad/s}$ and the scattering efficiency $R = 20 \cdot 10^6\,\text{rad/s}$ were used as fitting parameters. This value of Γ corresponds to a resonance linewidth $\Delta H = 0.8\,\text{Oe}$ which is larger than the literature values of $0.1 - 0.2\,\text{Oe}$ and might be caused by the additional DESW losses due to spin pumping. DESWs accumulate during the duration of the primary spin-wave pulse. This results in a substantial DESWs contribution to the ISHE voltage: at the maxima, $n_{sum}/n_0 \approx 1.8$ for $\tau_s = 50\,\text{ns}$ and $n_{sum}/n_0 \approx 2.1$ for $\tau_s = 100\,\text{ns}$. As a result we observe a slower decay (see Fig. 2) and a shift of the maxima for n_{sum}.

The dependencies of the spin-wave intensity and ISHE voltage on the applied microwave power P_s are shown in Fig. 3. Three different regions are visible in the Figure. In the first linear regime the detected ISHE voltage is practically proportional to the spin-wave intensity. With increasing power (second regime), the spin-wave intensity as well as the ISHE voltage drop due to nonlinear multi-magnon scattering processes which suppress and strongly disturb the propagating spin-wave packets [15, 17]. This processes mainly takes place under the input antenna, and the linear (but already suppressed) traveling waves propagate toward the Pt detector. The secondary magnons, which are slower, practically do not reach the detector area. Nevertheless, if we increase P_s further, the system reaches a new regime: the density of the secondary magnons is so high that even a small number of them arrive at the Pt detector and contribute to the ISHE voltage more than the traveling

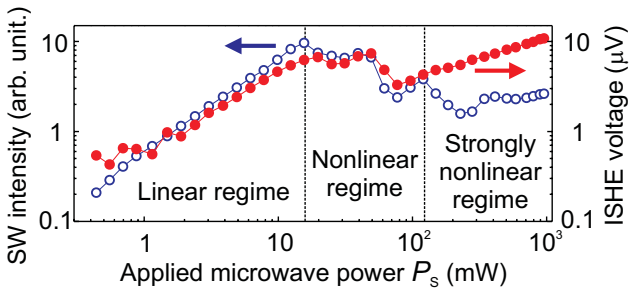

Fig. 3: The transmitted spin-wave intensity (open circles) and ISHE voltage (filled circles) as functions of the applied microwave power P_s (pulse duration $\tau = 100\,\text{ns}$) [8].

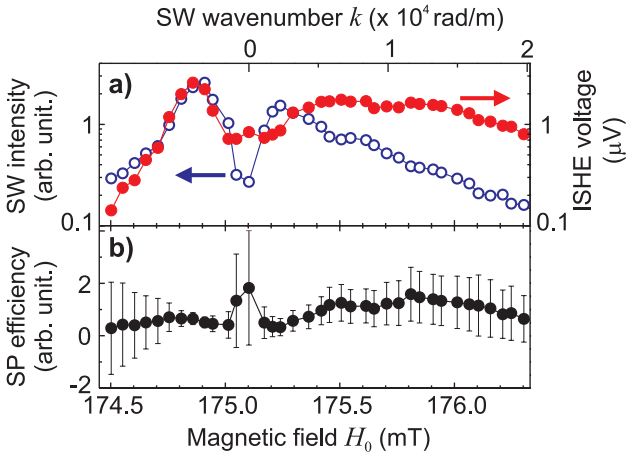

Fig. 4: Transmitted spin-wave intensity (open circles) and ISHE voltage (filled circles) shown in panel a) as functions of the applied magnetic field H_0. Corresponding BVMSW wavenumbers k are shown on the top scale. The spin pumping efficiency in panel b) is found as a ratio of the ISHE voltage to the spin-wave intensity with additional account of the spin-wave detection efficiency $F(k)$ ($f_s = 7\,\text{GHz}$, $\tau_s = 1\,\mu\text{s}$) [8].

spin-waves. This is visible as an increase of the ISHE voltage independent from the spin-wave intensity.

A narrow input antenna is used in our experiment which allows for spin-wave excitation in a certain range of wavenumbers k by varying the external field H_0 [14]. The transmitted spin-wave intensity as a function of H_0 is shown in Fig. 4a. The wavenumbers of the excited BVMSWs are shown on the top scale. We observe a standard dependence for BVMSWs: it has its maximum close to the point of uniform excitation $k = 0$ and decreases with increase in k due to the drop of excitation and AC detection efficiencies [14]. The dependence of the ISHE voltage on k is shown in the same Figure with filled circles. With an increase in H_0 the voltage decreases slower in comparison to the spin-wave intensity. This might suggest that the spin pumping efficiency, which is the ratio of the detected ISHE voltage to the spin-wave intensity, increases with an increase in k. However, this is not the case and can easily be explained by taking into account the k-dependence of the AC detection efficiency $F(k) = (\sin(kw/2)/(kw))^2$ by the Pt antenna (width of Pt strip: $w = 200\,\mu\text{m}$) [18]. As one can see from Fig. 4b the corrected spin pumping efficiency is independent of the k-vector of the traveling spin wave within the experimental uncertainty. The region left to the point $k = 0$ corresponds to the magnetostatic surface spin-wave mode propagating under some angle to the external magnetic field. No dependence of the spin-pumping efficiency on the spin-wave wavenumber is visible here as well.

In conclusion, we have shown magnon spin transport over a macroscopic distance detected as spin and charge currents in the attached nonmagnetic metal. This suggests the utilization of magnons in spintronics for the transfer of information over centimeter distances. The contribution of secondary excited magnons to the ISHE voltage is measured and estimated theoretically. It has been shown that, in spite of the small efficiency of the secondary magnons excitation, their contribution to the ISHE voltage is comparable to that of the originally excited traveling magnons. Additionally, we have shown, that the spin pumping efficiency in YIG/Pt bilayers does not depend on the spin-wave wavelength.

This work has been recently published in Applied Physiscs Letters [8].

Financial support by the Deutsche Forschungsgemeinschaft CH 1037/1-1 and by the Grant No. ECCS-1001815 from National Science Foundation of the USA is gratefully acknowledged. We

also thank G. E. W. Bauer and G. A. Melkov for valuable discussions and the Nano-Structuring Center, TU Kaiserslautern, for technical support.

References

[1] Y. Tserkovnyak, A. Brataas, G.E.W. Bauer, *Spin pumping and magnetization dynamics in metallic multilayers*, Phys. Rev. B **66**, 224403 (2002).
[2] E. Saitoh, M. Ueda, H. Miyajima, G. Tatara, *Conversion of spin current into charge current at room temperature: Inverse spin-Hall effect*, Appl. Phys. Lett. **88**, 182509 (2006).
[3] A.G. Gurevich and G.A. Melkov, *Magnetization oscillations and waves* (CRC, New York, 1996).
[4] T. Schneider, A.A. Serga, B. Leven, B. Hillebrands, R. L. Stamps, M.P. Kostylev, *Realization of spin-wave logic gates*, Appl. Phys. Lett. **92**, 022505 (2008).
[5] A. Khitun, M. Bao, J. Lee, K. Wang, D.W. Lee, S. Wang, *Spin wave based logic circuits*, Materials Research **998** (2007).
[6] A.V. Chumak, V.S. Tiberkevich, A.D. Karenowska, A.A. Serga, J.F. Gregg, A.N. Slavin, B. Hillebrands, *All-linear time reversal by a dynamic artificial crystal*, Nature Commun. **1**, 141 (2010).
[7] Y. Kajiwara, K. Harii, S. Takahashi, J. Ohe, K. Uchida, M. Mizuguchi, H. Umezawa, H. Kawai, K. Ando, K. Takanashi, S. Maekawa, E. Saitoh, *Transmission of electrical signals by spin-wave interconversion in a magnetic insulator*, Nature **464**, 262 (2010).
[8] A.V. Chumak, A.A. Serga, M.B. Jungfleisch, R. Neb, D.A. Bozhko, V.S. Tiberkevich, B. Hillebrands, *Direct detection of magnon spin transport by the inverse spin Hall effect*, Appl. Phys. Lett. **100**, 082405 (2012).
[9] M.B. Jungfleisch, A.V. Chumak, V.I. Vasyuchka, A.A. Serga, B. Obry, H. Schultheiss, P.A. Beck, A.D. Karenowska, E. Saitoh, B. Hillebrands, *Temporal evolution of inverse spin Hall effect voltage in a magnetic insulator-nonmagnetic metal structure*, Appl. Phys. Lett. **99**, 182512 (2011).
[10] C.W. Sandweg, Y. Kajiwara, A.V. Chumak, A.A. Serga, V.I. Vasyuchka, M.B. Jungfleisch, E. Saitoh, B. Hillebrands, *Spin pumping by parametrically excited exchange magnons*, Phys. Rev. Lett. **106**, 216601 (2011).
[11] H. Kurebayashi, O. Dzyapko, V.E. Demidov, D. Fang, A.J. Ferguson, S.O. Demokritov, *Spin pumping by parametrically excited short-wavelength spin waves*, Appl. Phys. Lett. **99**, 162502 (2011).
[12] M.V. Costache, M. Sladkov, S.M. Watts, C.H. van der Wal, B.J. van Wees, *Electrical detection of spin pumping due to the precessing magnetization of a single ferromagnet*, Phys. Rev. Lett. **97**, 216603 (2006).
[13] K. Ando, J. Ieda, K. Sasage, S. Takahashi, S. Maekawa, E. Saitoh, *Electric detection of spin wave resonance using inverse spin-Hall effect*, Appl. Phys. Lett. **94**, 262505 (2009).
[14] A.A. Serga, A.V. Chumak, B. Hillebrands, *YIG magnonics*, J. Phys. D: Appl. Phys. **43**, 264002 (2010).
[15] M. Sparks, *Ferromagnetic relaxation theory* (McGraw-Hill, New York, 1964).
[16] G.A. Melkov, V.I. Vasyuchka, Yu. V. Kobljanskyj, A.N. Slavin, *Wave-front reversal in a medium with inhomogeneities and an anisotropic wave spectrum*, Phys. Rev. B **70**, 224407 (2004).
[17] V.S. L'vov, *Wave turbulence under parametric excitations: applications to magnetics* (Springer, Berlin, 1994).
[18] A.K. Ganguly, D.C. Webb, *Microstrip excitation of magnetostatic surface waves: theory and experiment*, IEEE Trans. Microwave Theor. and Techn. **MTT-23**, 998 (1975).

4.8 Spin-Hall effect induced spin transfer torque in YIG-Pt bi-layers

A. V. Chumak, M. B. Jungfleisch, A. A. Serga, and B. Hillebrands

In collaboration with: D. A. Bozhko, A. V. Talalaevskyy, Y. V. Koblyanskyy, V. Y. Malyshev and G. A. Melkov, Department of Radiophysics, National Taras Shevchenko University of Kyiv, Kyiv, Ukraine, and A. N. Slavin, Department of Physics, Oakland University, Rochester, Michigan, USA.

Nowadays, bi-layers consisting of an insulating ferromagnetic film and a non-magnetic metal are attracting much attention to the field of spintronics. As it has been shown theoretically by Tserkovnyak, Brataas, and Bauer [1], and proven experimentally [2–5], the precession of the magnetization of a ferromagnet can transfer spin into an adjacent non-magnetic material creating a spin current. This effect is known as spin pumping. The opposite effect, the spin-transfer torque (STT) effect, allows the conversion of an electron-carried spin current in non-magnetic metal into magnetization precession of a ferromagnetic layer [6]. One of the most efficient ways for spin current to be generated in this non-magnetic layer is based on the spin Hall effect (SHE): Due to spin-orbit-coupling the scattering direction of an electron scattered from an impurity in a solid is spin dependent. This allows the conversion of a charge current into a spin current [7, 8]. It has recently been shown that the combination of SHE and STT allows the manipulation of spin-wave damping using a DC current [9, 10] or even a spin-wave generation [11]. Nevertheless, in spite of pronounced progress in these studies, many questions remain unanswered due to set of parasitic effects such as heating or a DC-generated Oersted fields accompanying the SHE-STT experiments. Moreover, reproducibility of some of the effects reported in literature is still questionable and requires further and deeper studies.

In a close collaboration with the group of Prof. Melkov from Kyiv, we have utilized a high-sensitive resonator-based method of damping measurements in ferrimagnetic films covered with metallic layers. With the use of this method it has been shown that the damping can be increased or decreased up to 20 percent, depending on the DC current direction relative to the applied magnetic field.

The sample used in our experiment comprises a 2.1 µm thick yttrium iron garnet (YIG) film with a 13 nm thick Platinum (Pt) layer deposited on the top. The YIG-Pt bi-layer has been placed in a cavity having a resonance frequency of $f_0 = 9.2\,\mathrm{GHz}$. A biasing magnetic field B was oriented in a way in which maximum efficiency of the magnetization procession excitation was provided. The field B was swept in a range from 253 to 256 mT while the frequency of the applied microwave signal f_0 was kept constant. The applied microwave power $P_0 = 0.5\,\mathrm{mW}$ was chosen to be small enough to avoid non-linear effects [12]. In order to apply STT to YIG, an in-plane current was sent through the Pt layer in a direction perpendicular to the field B providing highest efficiency of the spin Hall effect [7, 8]. In order to minimize the heating of Pt due to the high-density DC current, a pulsed regime was used: Current pulses having 2 µs duration were applied with a repetition period of 200 ms. The reflected power P_{refl} as a function of the field B was measured with and without an applied DC current.

The schematic showing the characteristics of the reflected power $P_{\mathrm{relf}}(B)$ are shown in Fig. 1a. In the absence of a DC current one expects a typical ferromagnetic resonance (FMR) behavior: The reflected power is minimal when the applied frequency f_0 is equal to the FMR frequency and the precession angle is maximal. The width of this characteristics ΔH determines the magnetization precession damping and is proportional to the Gilbert damping parameter α [13]. With applied DC

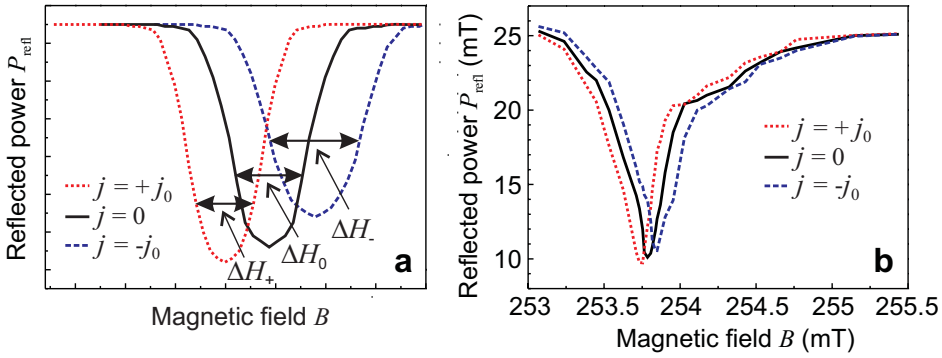

Fig. 1: (Color online) a) Schematic characteristics of the reflected microwave power as a function of the biasing magnetic field for the case where no current is sent through the Pt layer and for the currents applied in both polarities. b) Measured dependencies of the reflected power on the field. Current density $j_0 = 2.25 \cdot 10^{10}\,\mathrm{A/m^2}$.

current to the Pt several effects take place: the FMR resonance frequency is shifted due to the DC current-induced Oersted field, and the minima of reflected power as well as the FMR linewidth are changed. In a real experiment, the determination of the FMR linewidth ΔH_0 with high precision is problematic since it is based on a fit which is not accurate for real non-Lorenzian reflection characteristics (see Fig. 1b) [13]. However, the minimum of the reflected power (which can be recalculated into the linewidth ΔH_0) can be measured with high precision. This is the main idea of the proposed resonator-based method, which allows the detection of even very small variations of the YIG damping.

In order to obtain the damping parameter α of the YIG, first of all, we have determined the absorbed microwave power P_{abs} as the difference between the applied P_0 and the reflected P_{refl} powers. Next, the maximum of the absorbed power $P_{\mathrm{abs}}^{\mathrm{max}}$ at the FMR field has been used to obtain the minimal reflection parameter: $\Gamma = (P_0 - P_{\mathrm{abs}}^{\mathrm{max}})/P_0$. Finally, the ratio of $\Gamma(j)$, measured in the presence of the DC current, to the reference zero-current Γ_0 was used to determine the STT-induced variation of the damping $\alpha(j)/\alpha_0$.

The measured dependency $\alpha(j)/\alpha_0$ is shown in Fig. 2 for both polarities of the DC current and bias magnetic field. It can be seen that the application of the current having a density as large as $2.25 \cdot 10^{10}\,\mathrm{A/m^2}$ results in an increase or a decrease in the damping parameter α by up to 20 percent depending on the polarity of the current. It is important to note that the sign of the effect changes with a change of the magnetic field polarity, which is a signature of the SHE effect [7, 8].

The results presented in this Report clearly show that SHE-induced spin-transfer torque can be used

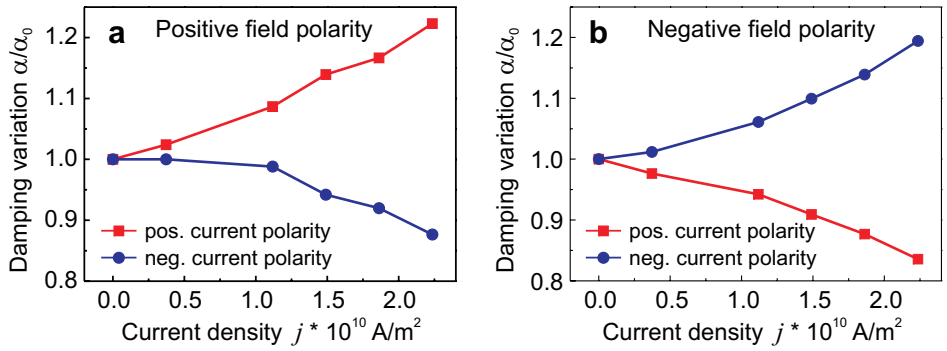

Fig. 2: (Color online) The dependance of the YIG damping variation on the applied DC current for positive ($B \approx 253.8\,\mathrm{mT}$) a) and negative ($B \approx -253.8\,\mathrm{mT}$) b) field polarities.

for the tailoring the damping parameter even in relatively thick (2.1 µm) YIG films. These results take us a step closer towards magnon-based information processing in damping-less magnetic media.

We acknowledge financial support by Deutsche Forschungsgemeinschaft (CH 1037/1-1).

References

[1] Y. Tserkovnyak, A. Brataas, G.E.W. Bauer, *Enhanced Gilbert damping in thin ferromagnetic films*, Phys. Rev. Lett. **88**, 117601 (2002).
[2] M.V. Costache, M. Sladkov, S.M. Watts, C.H. van der Wal, and B.J. van Wees, *Electrical detection of spin pumping due to the precessing magnetization of a single ferromagnet*, Phys. Rev. Lett. **97**, 216603 (2006).
[3] C.W. Sandweg, Y. Kajiwara, A.V. Chumak, A.A. Serga, V.I. Vasyuchka, M.B. Jungfleisch, E. Saitoh, B. Hillebrands, *Spin pumping by parametrically excited exchange magnons*, Phys. Rev. Lett. **106**, 216601 (2011).
[4] M.B. Jungfleisch, A.V. Chumak, V.I. Vasyuchka, A.A. Serga, B. Obry, H. Schultheiss, P.A. Beck, A.D. Karenowska, E. Saitoh, B. Hillebrands, *Temporal evolution of inverse spin Hall effect voltage in a magnetic insulator-nonmagnetic metal structure*, Appl. Phys. Lett. **99**, 182512 (2011).
[5] A.V. Chumak, A.A. Serga, M.B. Jungeisch, R. Neb, D.A. Bozhko, V.S. Tiberkevich, B. Hillebrands, *Direct detection of magnon spin transport by the inverse spin Hall effect*, Appl. Phys. Lett. **100**, 082405 (2012).
[6] J.C. Slonczewski, *Current-driven excitation of magnetic multilayers*, J. Magn. Magn. Mater. **159**, L1 (1996).
[7] M.I. D'Yakonov, V.I. Perel, *Possibility of orientating electron spins with current*, JETP Lett. **13**, 467 (1971).
[8] J.E. Hirsch, *Spin Hall Effect*, Phys. Rev. Lett. , **83**, 1834 (1999).
[9] Z. Wang, Y. Sun, M. Wu, V. Tiberkevich, A. Slavin, *Control of spin waves in a thin film ferromagnetic insulator through interfacial spin scattering*, Phys. Rev. Lett. **107**, 146602 (2011).
[10] Z. Wang, Y. Sun, Y.Y. Song, M. Wu, H. Schulthei, J.E. Pearson, A. Hoffmann, *Electric control of magnetization relaxation in thin film magnetic insulators*, Appl. Phys. Lett. **99**, 162511 (2011).
[11] Y. Kajiwara, K. Harii, S. Takahashi, J. Ohe, K. Uchida, M. Mizuguchi, H. Umezawa, H. Kawai, K. Ando, K. Takanashi, S. Maekawa, E. Saitoh, *Transmission of electrical signals by spin-wave interconversion in a magnetic insulator*, Nature **464**, 262 (2010).
[12] A.A. Serga, A.V. Chumak, B. Hillebrands, *YIG magnonics*, J. Phys. D **43**, 264002 (2010).
[13] S.S. Kalarickal, P. Krivosik, M. Wu, C.E. Patton, M.L. Schneider, P. Kabos, T.J. Silva, J.P. Nibarger, *Ferromagnetic resonance linewidth in metallic thin films: Comparison of measurement methods*, J. Appl. Phys. **99**, 093909 (2006).

C. Magnonic Crystals

A magnonic crystal is a wave transmission medium which features an artificial lattice created by a wavelength-scale modulation in its material properties. Such systems belong to the class of so-called meta-materials: synthetic media with properties derived from an engineered, mesoscopic (rather than atomic-scale or molecular) structure. The wave transmission spectra of artificial crystals typically include band gaps: frequency intervals over which propagation is prohibited.

The simplest type of a magnonic crystal can be produced in the form of a spin-wave waveguide with an array of parallel grooves chemically etched into its surface. In this Chapter we have demonstrated that such crystals can be a key element for new data storage concepts. In order to operate information in the crystal, the data is coded into a packet of traveling waves of magnetization which propagates through the crystal. In a conventional plane magnetic film, this wave packet would simply carry the data from the device input to its output with a certain speed. This delays the information for a fixed time but does not result in its storage and restoration on demand. A magnonic crystal allows one to store information because the wave packet cannot run through it and is "locked" inside due to multiple reflections in the structure. Thus, the carried information is then stored in the magnonic crystal's eigen excitations for a certain time. When it is necessary to read out the stored data a control signal pulse is applied which both, amplifies and releases the wave package. The released package is then detected at the device output.

Simulation results on an alternative micro-scaled magnonic crystal are presented in Report 4.9. The crystal is designed in a form of a permalloy waveguide with a periodical variation of its saturation magnetization. In real structures the variation of magnetization can be achieved by using an ion implantation technique. We show that the spin-wave transmission characteristics exhibits pronounced frequency band gaps which depend on both the ratio and the size of the area with a reduced magnetization. Furthermore, it has been found that the magnonic crystal works as series of coupled resonators which can enhance an effective spin-wave propagation length.

In Report 4.10 we study the mechanism of data storage (see the AG Magnetismus Annual Report 2010 for details on the parametric pumping-based restoration mechanism). We have found out that unlike the conventional scheme used in photonics, the trapping occurs not due to the deceleration of the incident wave when it enters the periodic structure but due to excitation of the quasinormal modes of the artificial crystal. This result not only has exciting implications for future information storage, but also offers fascinating new insight into the fundamental physics of signals and waves.

C. Magnonische Kristalle

Magnonische Kristalle sind Wellenleiterstrukturen, die eine periodische Modulation ihrer Materialeigenschaften aufweisen, wobei die Periodizitätslängen in der Größenordnung der Wellenlängen der propagierenden Wellen liegen. Solche Systeme, wie auch die eng verwandten photonischen Kristalle, gehören zur Klasse der sogenannten Metamaterialien: künstliche Materialien mit Eigenschaften, die durch eine gezielt entworfenen mesoskopischen Struktur hervorgerufen werden. Die Transmissionsspektren künstlicher Kristalle weisen typischerweise Bandlücken auf, also Frequenz-Bereiche, in denen die Wellenpropagation unterdrückt ist.

Die einfachste Realisierung eines magnonischen Kristalls ist ein eindimensionaler Spinwellen-Wellenleiter, bei dem durch chemisches Ätzen von parallelen Gräben eine periodische Änderung der Dicke in Propagationsrichtung der Spinwellen im Wellenleiter erzeugt wird. In diesem Kapitel

wird gezeigt, dass solch ein Kristall ein Schlüsselelement für ein neues Konzepts zur Datenspeicherung sein kann. Um Informationen in einem Kristall zu verarbeiten, werden die Daten in ein propagierendes Spinwellenpaket umgewandelt, welches sich durch den Kristall bewegt. In einem konventionellen Wellenleiter würde dieses Spinwellenpaket die Informationen vom Eingang des Bauteils mit einer bestimmten Geschwindigkeit zum Bauteilausgang transportieren. Informationen werden so um eine feste Zeit verzögert, aber daraus resultiert keine Speicherung oder Wiederherstellung auf Abruf. Ein magnonischer Kristall ermöglicht die Informationsspeicherung, da das Spinwellenpaket nicht einfach durchlaufen kann, sondern durch Mehrfachreflexionen in der Struktur gefangen wird. Folglich werden die übertragenen Informationen für eine bestimmte Zeit in den Eigenanregungen des magnonischen Kristalls gespeichert. Sollen die gespeicherten Daten ausgelesen werden, wird ein Puls eines Kontrollsignals angelegt, welcher das gespeicherte Wellenpaket sowohl verstärkt als auch freigibt. Das freigegebene Wellenpaket kann dann am Bauteilausgang detektiert werden.

Im Bericht 4.9 werden die Ergebnisse einer Simulation eines alternativen mikroskalierten magnonischen Kristalls präsentiert. Der magnonischen Kristall basiert auf einem Permalloy-Wellenleiter mit einer periodischen Variation seiner Sättigungsmagnetisierung. In realen Strukturen kann die Variation der Magnetisierung durch Verwendung der Ionen-Implantationstechnik erreicht werden. Wir zeigen, dass die Transmissionseigenschaften von Spinwellen ausgeprägte Lücken im Frequenzband aufweisen, die sowohl von dem Verhältnis, als auch von der Größe der Bereiche mit verringerter Magnetisierung abhängen. Weiterhin wurde heraus gefunden, dass der magnonische Kristall als eine Reihe gekoppelte Resonatoren arbeitet, die die effektive Spinwellen-Propagationslänge verbessern.

Im Bericht 4.10 wird der Mechanismus der Datenspeicherung diskutiert (für Details zur Speicherung und Wiederherstellung von Spinwellensignalen durch parametrisches Pumpen siehe Jahresbericht 2010). Es zeigt sich, dass im Gegensatz zum gebräuchlichen Modell aus der Photonik die Speicherung nicht durch die Verzögerung der einlaufenden Welle geschieht, wenn diese in die periodische Struktur einläuft, sondern aufgrund der Anregung der Quasi-Normalmoden des künstlichen Kristalls. Dieses Ergebnis hat nicht nur erstaunliche Konsequenzen für künftige Informationsspeicherung sondern bietet auch spannende neue Einblicke in die physikalische Grundlagenphysik von Signalen und Wellen.

4.9 Micromagnetic study of magnonic band gaps in waveguides with a periodic variation of the saturation magnetization

F. Ciubotaru, A. V. Chumak, B. Obry, A. A. Serga, and B. Hillebrands

The transmission spin-wave spectra in magnonic crystals (MC) show evidence of special properties as rejection bands - frequency intervals over which the spin wave propagation is forbidden [1, 2], delay lines [3], localized modes [4], etc. Hence, the spin-wave propagation in such devices is intensively studied due to their potential technological application for signal processing in magnonic devices [5–9].

The design of the allowed and forbidden spin-wave modes can be realized by the artificial periodic modulation of the MC magnetic properties, e.g. fabrication with different magnetic materials [5, 10], different shapes [9, 11] or local variation of the bias field [12, 13]. Many studies were concentrated on MCs based on yttrium-iron-garnet (YIG) ferrite films due to extremely small spin-wave loss in this material [14, 15]. However, modern microwave devices require micro-sized patterned elements which cannot be produced from YIG. Previous studies performed on shape modulated Permalloy waveguides have demonstrated the possibility to control the number of the band gaps by a proper choice of the MC geometry even in the case of relatively strong magnon damping [9, 11]. The next task is to avoid the non-resonance spurious spin-wave scattering from geometrical non-uniformities which exist in shape modulated MCs and still preserve the band-gap deepness. Theoretical [16] and experimental [5] studies on a bi-component material magnonic crystal, which comprises alternating areas with different saturation magnetization, have shown the tunability of the band gaps by applied magnetic fields [17, 18].

Here we present a micromagnetic study of a one-component alternative magnonic crystal based on a Permalloy (Py) waveguide with a periodical variation of its saturation magnetization. In real structures the variation of magnetization can be achieved by using an ion implantation technique [19]. We show that the spin-wave transmission characteristics exhibits pronounced frequency band gaps which depend on both the ratio and the size of the area with a reduced magnetization M/M_0. Furthermore, the role of the higher-order spin-wave width modes on the MC properties is discussed as well.

The magnonic crystal structure is presented in Fig. 1. A 2 µm -wide Permalloy waveguide of 40 nm thickness is magnetized transversal to its long axis by a static biasing magnetic field of $B_0 = 50\,\mathrm{mT}$. The length of the waveguides is 9.5 µm. The simulated area was discretized into $N_x \times N_y \times N_z = 950 \times 200 \times 4$ cells, each cell having a size of $10 \times 10 \times 10$ nm^3. The typical material parameters of Py were used: saturation magnetization $\mu_0 M_0 = 1\,\mathrm{T}$, exchange stiffness constant $A = 1.3 \times 10^{-11}\,\mathrm{J/m}$ and zero magnetocystalline anisotropy. In order to avoid spin-wave reflection at the ends of the structure ($x = 0$ and $x = 9.5\,\mu\mathrm{m}$) the damping boundary conditions were used: In the boundary areas (~ 1 on each side) the damping parameter α in the Landau-Lifshitz-Gilbert equation gradually increases more than fifty times resulting in a strong decay of the spin-wave intensity towards the boundaries [20]. The MC lattice constant, i.e. the periodicity of the area where the saturation magnetization was decreased, is $\Lambda = 1\,\mu\mathrm{m}$.

In order to excite spin waves within a wide frequency range we apply a rectangular pulse of magnetic field with a duration of 70 ps and an amplitude of 3 mT. The field is oriented in the x-direction and is uniformly distributed in a 300 nm wide area across the Py waveguide. This area plays the role of a spin-wave antenna. The cut-off limit of the frequency given by the pulse duration is

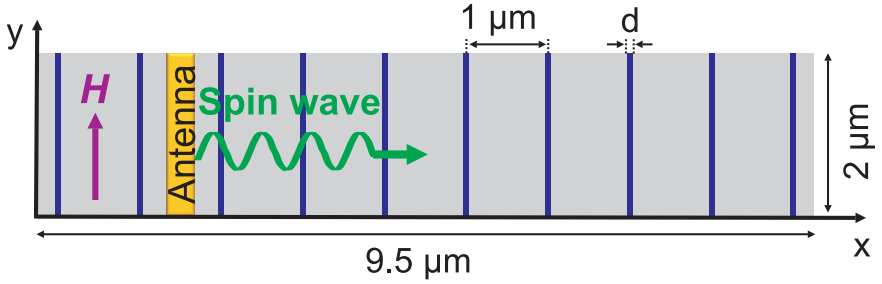

Fig. 1: Sketch of the simulated structures: MC based on a Py waveguide with a periodic variation of its saturation magnetization. The dark blue lines denote the areas where the saturation magnetization has been reduced with a certain percentage.

$\sim$13.5 GHz while the antenna can excite spin-waves with wavenumbers up to $k_{\max} = 21\,\mathrm{rad/\mu m}$ (that corresponds to a frequency of 54.6 GHz at $B_0$50 mT applied field). The static applied magnetic field satisfies the conditions for the excitation and propagation of the magnetostatic surface spin waves (MSSWs). These waves are known to have the highest values of the group velocity in magnetic microstructures and ensure spin-wave free paths of the order of several micrometers in a Permalloy film.

First we simulated a regular Permalloy waveguide with the same dimensions as the magnonic crystal that will serve as reference for the spin-wave propagation. The spin-wave intensity extracted from simulation as a function of the frequency and of the propagation distance from the antenna is displayed in Fig. 2a. One can observe that no spin-wave transmission is allowed below a frequency of 6.1 GHz, which corresponds to the ferromagnetic resonance (FMR) frequency. The intensities observed below $\sim$6.1 GHz come from forced excitation of the magnetization dynamics and are detected only close to the antenna. The maximum intensity corresponds to long-wavelength spin waves with the highest excitation efficiency and the highest group velocity that are exited just above the FMR frequency. With increasing frequency and, implicitly, an increase in the spin-wave wavenumber, the excitation efficiency decays [22]. Furthermore, one can notice a frequency as well as a distance dependent oscillation of the spin-wave intensity which suggests that the interference between the fundamental and higher order width modes play an important role in the spin-wave propagation.

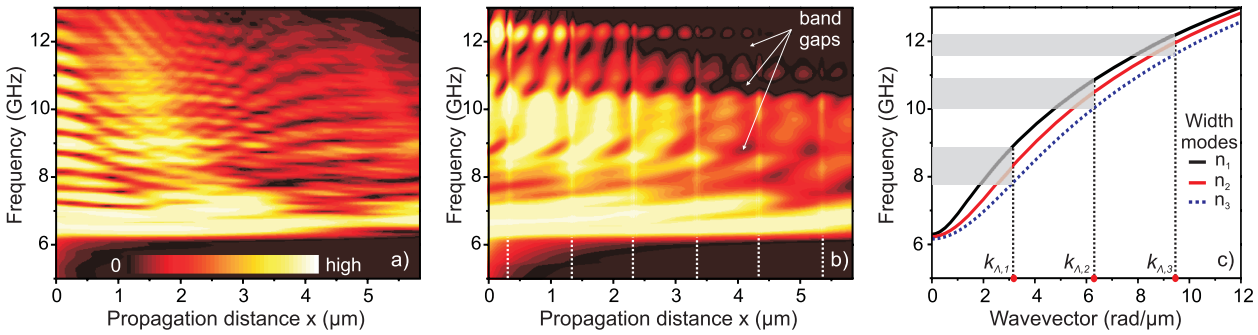

Fig. 2: Spin-wave transmission characteristics for a simple permalloy waveguide a) and a magnonic crystal b) as a function of the propagation distance (x) from the excitation antenna. The dashed white lines in b) denote the positions of the areas where the saturation magnetization was decreased. c) Dispersion relations calculated for the first three width spin-wave modes. The shaded regions mark the frequency intervals corresponding to band gaps observed in the transmission characteristic in b), while $k_{\Lambda,n}$ represent the Bragg reflection wavenumbers.

The spin-wave intensity map obtained by simulating a magnonic crystal with a periodical reduction of 10% of the saturation magnetization over an area width $d = 70\,\text{nm}$ (see Fig. 1) remains virtually unchanged. However, a further decrease in the saturation magnetization to 20% changes the spin-wave intensity map drastically, as can be seen in Fig. 2b. Three spin-wave band gaps are visible and their frequencies are closely correlated with the Bragg reflection wavenumbers as can be seen by looking at the dispersion relations displayed in Fig. 2c. The spin-wave band gap corresponding to the first Bragg wavenumber $k_{\Lambda 1} = \pi/\Lambda = 3.14\ \text{rad}/\mu\text{m}$ is visible at $\sim$8 GHz. The second band gap ($k_{\Lambda 2} = 2\pi/\Lambda = 6.28\ \text{rad}/\mu\text{m}$) and the third one ($k_{\Lambda 3} = 3\pi/\Lambda = 9.42\ \text{rad}/\mu\text{m}$) are very pronounced near 10.7 GHz and 11.8 GHz, respectively. The fact that the first band gap is not so clearly defined can be understood by taking into account that higher order width spin-wave modes are exited along with the fundamental one. The Bragg reflection for the each width mode occurs at different frequencies (see Fig. 2c). At a given frequency when one mode is Bragg reflected the other width modes are still transmitted, thus the total intensity is not so strong affected. However, this effect becomes less important for higher-order band gaps since the frequencies of the width modes are getting closer to each other. Thus, one can conclude that the higher order spin-wave width modes play an important role: The frequency position and width of the band gaps are determined by the superposition of the partial band gaps formed by individual spin-waves width modes.

Comparing the two spin-wave intensity maps obtained for a regular Py waveguide and for the 20% MC (Fig. 2) one can remark that the decay of the spin-wave amplitude over distance is smaller in the case of the latter structure. Furthermore, a periodic variation of the spin-wave intensity as a function of the propagation distance is clear visible inside of the MC. This variation manifests in the appearance of local intensity maxima in the crystal areas with unchanged saturation magnetization. One maximum at 10 GHz, two maxima at 11 GHz and three at 12.3 GHz are visible inside of these areas. They can be understood as formation of quasi-standing modes due to multiple reflections at the boundaries where M_0 was reduced. One should note that the wavelength of the quasi-standing modes fulfill the condition $\lambda \approx na/2$, where n is an integer parameter and a is the width of the area of unchanged magnetization. These observations brings us to an important conclusion: A magnonic crystal works as a series of coupled resonators which can enhance the spin-wave propagation length.

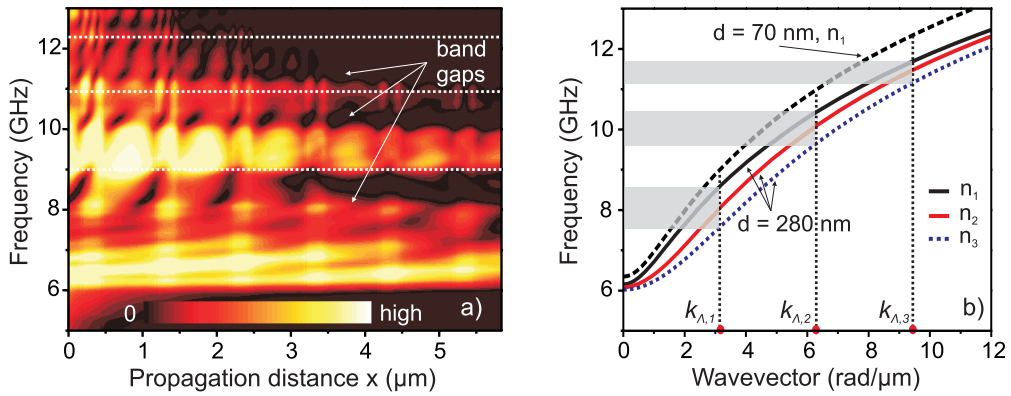

Fig. 3: a) Spin-wave transmission characteristics as a function of the propagation distance (x) from the excitation antenna for a magnonic crystal with $d = 280\,\text{nm}$. The dotted lines represent the frequency band gap position for a MC with $d = 70\,\text{nm}$ (Fig. 2b). b) Dispersion relations calculated taking into account a saturation magnetization averaged over the entire crystal for a MC with $d = 70\,\text{nm}$ (first width mode) and a MC with $d = 280\,\text{nm}$ (three width modes). The shaded regions mark the frequency intervals corresponding to band gaps observed in the transmission characteristic in (a), $k_{\Lambda,n}$ represent the Bragg reflection wavenumbers.

The frequency of the band gaps is determined by the Bragg wavenumbers and the dispersion relation. The dispersion relation is strongly dependent on M_0 and on the bias magnetic field. A change in the magnetic field shifts the spin-wave dispersion relation up or down and, implicitly, increases or decreases the frequency of the band gap at the fixed Bragg wavenumbers. A variation of the MC lattice constant Λ changes the wavelength of spin waves that satisfy the reflection Bragg condition $2\Lambda = n\lambda$ (n integer), and consequently the band gap frequency.

The band gap depth control can be achieved by manipulating both the width of the implanted areas and the level of the magnetization variation M/M_0. However, the latter leads to a stronger spin-wave decay caused by reflection between the areas of different values of the magnetization. For example, spin waves above 10 GHz can propagate only for $\sim$1.5 µm in the MC with a 30% reduced magnetization. Keeping 20% reduction of M_0 and increasing the "dopping" area length by increasing d to 280 nm we observe deeper band gaps while the propagation distance in the transmission bands remains nearly unchanged, as can be seen from Fig. 3a. In this case we can notice that a pronounced first band gap starts to form after three periods of the magnonic crystal. An additional difference was found by comparing the two MCs with $d = 70$ nm and $d = 280$ nm. The band gaps for the latter structure are shifted to lower frequencies (the white dot lines mark the position of the band gaps for the MC with $d = 70$ nm). This effect can be understood by taking into account that the wavelength of spin waves are not coupled only to the local magnetization but are sensitive to the average magnetization of the sample. This fact was proven by analyzing the dispersion relations calculated using an average saturation magnetization of the entire structure of $\mu_0 M_{av} = 0.94$ T (see Fig. 3b). One can observe that the dispersion relation is shifted to lower frequencies and the band gap positions match very well the ones obtained from simulation.

In summary, we performed a micromagnetic study of the spin-wave transmission in 1D magnonic crystals based on a Permalloy waveguide with a periodic variation of its saturation magnetization. The appearance of frequency band gaps have been clearly observed and studied in the space and frequency domains. The band gaps are determined by the superposition of individual band gaps of the fundamental and of the higher order spin-wave width modes. Furthermore, the rejection bands depend strongly on both the level of magnetization variation and the size of area with a reduced magnetization: The reduction of the saturation magnetization over a larger area leads to the formation of more pronounced band gaps. At the same time the magnetization M_{av} averaged over the MC must be taken into account for the spin-wave dispersion relation: M_{av} shifts down the spin wave dispersion characteristics, i.e. the band gaps appear at lower frequencies. In addition, it was found that the magnonic crystal works as series of coupled resonators which can enhance the spin-wave propagation length.

Financial support by the Deutsche Forschungsgemeinschaft SE-1771/1-2 is gratefully acknowledged.

References

[1] Yu.V. Gulyaev, A.A. Nikitov, *Magnonic crystals and spin waves in periodic structures*, Dokl. Phys. **46**, 687 (2001).

[2] S.L. Vysotskii, S.A. Nikitov, Yu.A. Filimonov, *Magnetostatic spin waves in two-dimensional periodic structures (magnetophoton crystals)*, J. Exp. Theor. Phys. **101**, 547 (2005).

[3] A.B. Ustinov, A.V. Drozdovskii, B.A. Kalinikos, *Multifunctional nonlinear magnonic devices for microwave signal processing*, Appl. Phys. Lett. **96**, 142513 (2010).

[4] S. Tacchi, B. Botters, M. Madami, J.W. Klos, M.L. Sokolovskyy, M. Krawczyk, G. Gubbiotti, G. Carlotti, A.O. Adeyeye, S. Neusser, D. Grundler, *Mode conversion from quantized to propagating spin waves in a rhombic antidot lattice supporting spin wave nanochannels*, Phys. Rev. B **86**, 014417 (2012).

[5] Z.K. Wang, V.L. Zhang, H.S. Lim, S.C. Ng, M.H. Kuok, S. Jain, A.O. Adeyeye, *Observation of frequency band gaps in a one-dimensional nanostructured magnonic crystal*, Appl. Phys. Lett. **94**, 083112 (2009).
[6] K.S. Lee, D.S. Han, S.K. Kim, *Physical origin and generic control of magnonic band gaps of dipole-exchange spin waves in width-modulated nanostrip waveguides*, Phys. Rev. Lett. **102**, 127202 (2009).
[7] S.K. Kim, K.S. Lee, D.S. Han, *A gigahertz-range spin-wave filter composed of width-modulated nanostrip magnonic-crystal waveguides*, Appl. Phys. Lett. **95**, 082507 (2009).
[8] V.V. Kruglyak, R.J. Hicken, A.N. Kuchko, V.Y. Gorobets, *Spin waves in a periodically layered magnetic nanowire*, J. Appl. Phys. **98**, 014304 (2005).
[9] A.V. Chumak, P. Pirro, A.A. Serga, M.P. Kostylev, R.L. Stamps, H. Schultheiss, K. Vogt, S.J. Hermsdoerfer, B. Laegel, P.A. Beck, B. Hillebrands, *Spin-wave propagation in a microstructured magnonic crystal*, Appl. Phys. Lett. **95**, 262508 (2009).
[10] V.V. Kruglyak, R.J. Hicken, *Magnonics: Experiment to prove the concept*, J. Magn. Magn. Mater. **306**, 191 (2006).
[11] F. Ciubotaru, A.V. Chumak, N.Yu Grigoryeva, A.A. Serga, B. Hillebrands, *Magnonic band gap design by the edge modulation of micro-sized waveguides*, J. Phys. D **45**, 255002 (2012).
[12] A.V. Chumak, T. Neumann, A.A. Serga, B. Hillebrands, M.P. Kostylev, *A current-controlled, dynamic magnonic crystal*, J. Phys. D textbf42, 205005 (2009).
[13] A.V. Chumak, V.S. Tiberkevich, A.D. Karenowska, A.A. Serga, J.F. Gregg, A.N. Slavin, B. Hillebrands, *All-linear time reversal by a dynamic artificial crystal*, Nat. Commun. textbf94, 141 (2010).
[14] A.V. Chumak, A.A. Serga, B. Hillebrands, M.P. Kostylev, *Scattering of backward spin waves in a one-dimensional magnonic crystal*, Appl. Phys. Lett. **93**, 022508 (2008).
[15] A.V. Chumak, A.A. Serga, S. Wolff, B. Hillebrands, M.P. Kostylev, *Scattering of surface and volume spin waves in a magnonic crystal*, Appl. Phys. Lett. **94**, 172511 (2009).
[16] M. Krawczyk, H. Puszkarski, *Plane-wave theory of three-dimensional magnonic crystals*, Phys. Rev. B **77**, 054437 (2008).
[17] G. Gubbiotti, S. Tacchi, G. Carlotti, N. Singh, S. Goolaup, A.O. Adeyeye, M. Kostylev, *Collective spin modes in monodimensional magnonic crystals consisting of dipolarly coupled nanowires*, Appl. Phys. Lett. **90**, 092503 (2007).
[18] M. Kostylev, P. Schrader, R.L. Stamps, G. Gubbiotti, G. Carlotti, A.O. Adeyeye, S. Goolaup, N. Singh, *Partial frequency band gap in one-dimensional magnonic crystals*, Appl. Phys. Lett. **92**, 132504 (2008).
[19] J. Fassbender, J. von Borany, A. Mücklich, K. Potzger, W. Möller, J. McCord, L. Schultz, R. Mattheis, *Structural and magnetic modifications of Cr-implanted Permalloy*, Phys. Rev. B **73**, 184410 (2006).
[20] M. Dvornik, A.N. Kuchko, V.V. Kruglyak, *Micromagnetic method of s-parameter characterization of magnonic devices*, J. Appl. Phys. **109**, 07D350 (2011).
[21] The simulations were performed using the OOMMF open code: M.J. Donahue, D.G. Porter, Report NISTIR 6376, NIST, Gaithersburg, MD, USA (1999).
[22] V.E. Demidov, M.P. Kostylev, K. Rott, P. Krzysteczko, G. Reiss, S.O. Demokritov, *Excitation of microwaveguide modes by a stripe antenna*, Appl. Phys. Lett. **95**, 112509 (2009).

4.10 Storage-recovery phenomenon in a magnonic crystal

A. V. Chumak, V. I. Vasyuchka, A. A. Serga, and B. Hillebrands

In collaboration with: M.P. Kostylev, School of Physics, University of Western Australia, Crawley, Australia, and V. S. Tiberkevich, Department of Physics, Oakland University, Rochester, USA.

The deceleration or even the full stop of light due to the modification of the light dispersion in photonic crystals has been a topic of intense experimental and theoretical studies over the last decade [1, 2]. A wave of light propagating through a photonic crystal couples with the internal standing crystal mode and generates a slow light mode. In terms of the dispersion characteristics this means that the slope of the dispersion curve decreases at the edges of the band gaps which results in an extremely small value of the group velocity. It has been demonstrated that slow light can be used for time-domain processing including buffering (storage and recovery) of optical signals as well as for an enhancement of nonlinear effects due to the spatial compression of optical energy [1, 2].

Magnonic crystals (MCs) are the magnetic counterpart of photonic crystals which operate with spin waves, i.e. the collective oscillations of the spin lattice of a magnetic material [3–8]. The storage of a spin wave in a magnonic crystal is complicated due to significant intrinsic spin wave damping which limits the maximum number of structure periods to about 20 (see Ref. [9] and references therein). The small number of periods implies that the slope of the MC dispersion does not become zero at the edges of the magnonic band gap in contrast to the light dispersion at the edges of photonic gaps. Hence, rather than vanishing, the group velocity of spin waves only slightly decreases at the gap edges.

Nevertheless, in one of our previous reports [10] we have shown that storage-recovery has been successfully realized in a magnonic crystal. A spin-wave packet propagating through the MC area has been partially stored in it and was recovered after a considerably long time using parametric amplification. The pronounced recovered signal has been observed for frequencies corresponding to the edges of the magnonic-crystal band gaps.

However, in spite of the confident experimental evidences of the signal recovery, the mechanism of the storage itself remained unclear. In this Report we show that unlike the conventional scheme

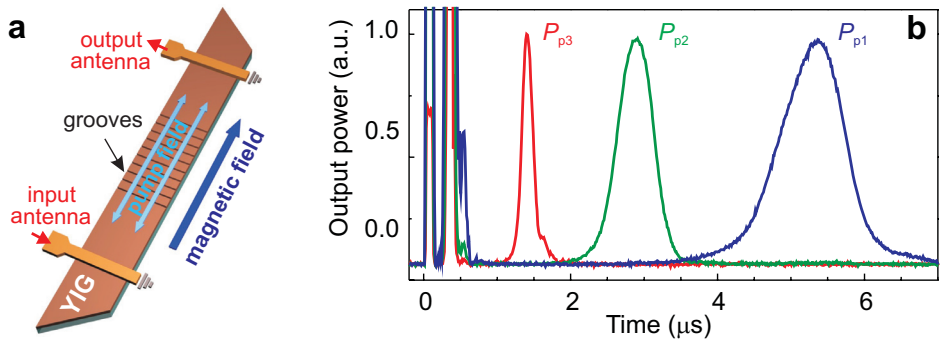

Fig. 1: a) Sketch of the experimental setup. The MC is fabricated in the form of a YIG spin-wave waveguide with 10 grooves on its surface. The Rf pump magnetic field is parallel to the bias field B. b) The normalized time profiles of the restored signal measured at field $B = 186\,\mathrm{mT}$ for different pumping powers: $P_{p1} = 50\,\mathrm{mW}$, $P_{p2} = 90\,\mathrm{mW}$, $P_{p3} = 320\,\mathrm{mW}$ [11].

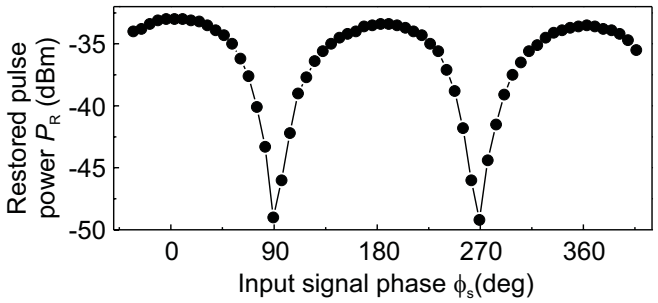

Fig. 2: Dependence of the restored signal power on the input signal phase. The signal and pump generators were locked-in [11].

used in photonics, in magnonic crystals the storage occurs not due to the deceleration of the incident wave when it enters the periodic structure but due to excitation of the quasi-normal modes of the artificial crystal [11].

The magnonic crystal used in our experiment had been produced in the form of a stripe of a low-damping magnetic insulator (5.1 µm-thick yttrium iron garnet (YIG) film) with an array of parallel grooves chemically etched into its surface (see Fig. 1a) [4]. The array comprises ten 300 nm-deep and 30 µm-wide grooves placed 270 µm apart (lattice constant 300 µm). The bias magnetic field is applied along the stripe in order to form conditions for propagation of backward volume magnetostatic spin waves (BVMSW) [9]. The waves were excited and detected in the YIG film waveguide using microwave stripline antennas placed at equal distances from both ends of the grooved area and 8 mm apart from each other (Fig. 1a). A microwave power of 0.3 mW applied to the input antenna was sufficiently low to avoid non-linear effects which can potentially influence the input spin wave and the storage process.

The storage-recovery experiment was performed in the following way. A 100 ns-long microwave pulse of $f_s = 7.212$ GHz frequency is applied to the input antenna in order to excite a traveling spin-wave packet which propagates toward the output antenna. The time traces of the output signal are shown in Fig. 1b. First, the output antenna receives a practically rectangular pulse without any delay, caused by a direct electromagnetic leakage from the input antenna at the time $t = 0$. Approximately 0.3 µs afterwards a pulsed signal carried by spin waves arrives at the output antenna. In order to recover the signal, which is partially trapped in the MC area, parallel parametric pumping has been used: Well after the detection of the transmitted signal (the delay was varied between 0.4 µs and 1.4 µs) we apply a 10 µs-long pumping pulse at a frequency of $f_p = 2f_s = 14.424$ GHz [11]. This resulted in the amplification of the stored spin-wave mode and in the appearance of an additional bell-shaped pulse at the output antenna shown in Fig. 1b.

The restoration mechanism used in our experiments has been described in detail in the Report [10] and in the Ref. [11]. We skip its detailed description and mention only that it is the same mechanism as previously used to recover the signals stored in standing thickness spin-wave modes in plane magnetic films [12]. The restoration is based on the competitive parametric amplification of several spin-wave modes and, as a result, the main characteristics of the restored pulse (amplitude, delay and the width) are determined by the parametric pumping signal [13].

Completely new and specific for the restoration process in this experiment is the fact that the MC mode, which is used in the experiment for the signal storage, consists of two counter propagating waves with strictly coupled phases. The phase φ_k of the wave propagating towards the output antenna is determined by the phase of an applied microwave signal φ_s. The phase of the counter-propagating wave φ_{-k} is also φ_s and is due to the reflection inside of the Bragg lattice. Importantly, the parallel pumping process, being a parametric process, also couples two counter-propagating waves. The sum of their phases is defined by the phase of the pump φ_p: $\varphi_k + \varphi_{-k} = \varphi_p + \pi/2$

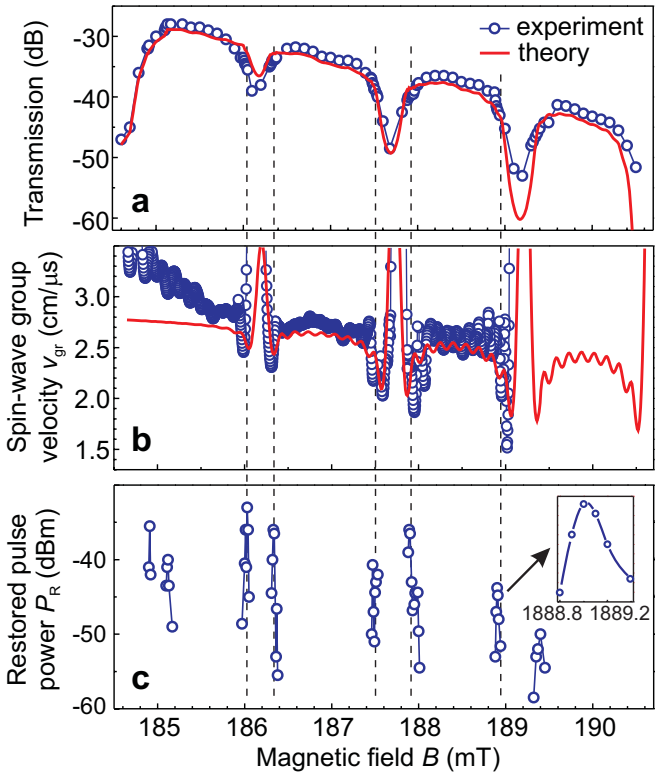

Fig. 3: a) Transmission of the spin-wave signal as a function of bias magnetic field (open circles - experiment, line - theory). b) Dependence of the group velocity v_{gr} on the field B. The slight decrease in v_{gr} at the edges of the band gap is visible. c) Measured restored signal power P_R as a function of field B. One sees that the restored signal is visible only at the edges of the band gaps [11].

[9, 14]. Thus, the restoration process in a MC combines two different mechanisms of coupling of two counter-propagating waves, and the phase conditions for both mechanisms should be met simultaneously. As a result the characteristics of the restored pulse is influenced by the phase shift between the signal wave and the pumping.

Indeed, we have experimentally registered the strong dependence of the restored power (more than 15 dB) on the input signal phase (see Fig. 2). The maxima and minima of the restored signal power P_R correspond to the input signal phases $\varphi_{s\,max} = \varphi_p/2+\pi/4+2\pi n$ and $\varphi_{s\,min} = \varphi_p/2-\pi/4+2\pi n$, respectively (where n is an integer value). As a result the phase distance between neighboring minima and maxima is exactly 90°. The observed phase dependence clearly demonstrates that the signal stored inside the MC is phase correlated to the input microwave signal: in spite of the distortion of the time profile of the original pulse its phase information is conserved. Furthermore, these results are evidence of the fact that a standing mode of a magnonic crystal, consisting of two waves of opposite wavevectors, participates in the storage-recovery process.

In order to understand the nature of this mode we have compared the spectral characteristics of the magnonic crystal with the corresponding dependence of the restoration efficiency. The power of the transmitted spin-wave signal, the spin-wave group velocity v_{gr}, and the power of the restored signal P_R are shown in Fig. 3 as a function of the applied magnetic field. As the experiment has been performed for the fixed signal frequency f_s, the variation in the bias field in this case results in the variation of the spin-wave wavenumber. We used the transfer matrix approach [4, 15] to model the field dependence of the spin-wave transmission through the magnonic crystal. As seen in Fig. 3a, the simulated characteristics are in good agreement with the experiment (parameters for the simulations were taken from [15]).

We also calculated the group velocity v_{gr} and compared it with the experimental data [11]. From Fig. 3b one clearly sees that both the measured and the calculated group velocities decrease at the edges of the band gaps where the slope of spin-wave dispersion decreases. This decrease is 20

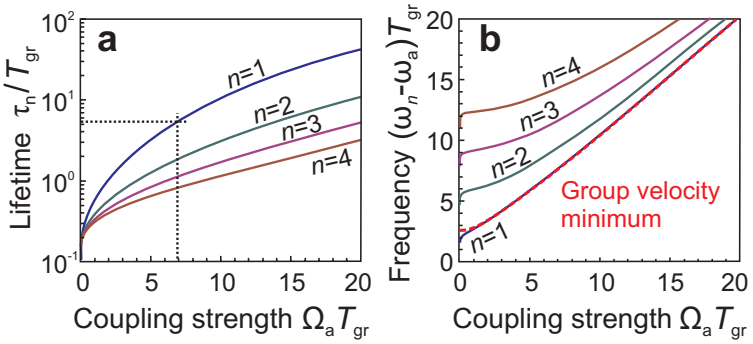

Fig. 4: (Color online) Lifetime τ_n a) and frequency ω_n b) of the quasi-normal MC modes in the first pass-band calculated for $n = 1-4$ as functions of the MC band gap half-width Ω_a. Frequencies in (b) are measured from the center of the band gap ω_a. The MC traveling time $T_{gr} = L/v_{gr}$, where L is the length of MC, is used as a normalization factor. The group velocity minimum frequency near the band gap edge is shown by a dashed line. The dotted line in a) indicates the experimental conditions for the first band gap [11].

percent at most (for the first band gap where the restored signal is maximal) and cannot be used in a slowing-down approach to store information for a reasonably long time as in the case of photonic crystals [2]. However, as one can see from Fig. 3c, the maxima of the restored pulse correlate well with the minima of the group velocity. The field width of the regions where the restoration takes place (see inset in Fig. 3c) is very narrow (approximately 0.04 mT) and is comparable with the ferromagnetic resonance linewidth (0.05 mT in our case).

The appearance of the restored pulse at the band gap edges can be understood in the frame of the proposed model which assumes that the storage of the spin-wave signal is based on quasi-normal modes [16] of the magnonic crystal. Any artificial crystal of finite length L presents an *open* system which is coupled to the outside medium. Respectively, internal excitations of such crystal can be excited from outside (in contrast to normal modes of a *closed* system) and, in turn, lose their energy by radiating traveling waves. Mathematically, the time-evolution operator of this system is not Hermitian anymore, and consequently the eigenfunctions are not normal modes but quasi-normal modes (QNMs) whose frequencies are complex, $\omega = \omega' + i\omega''$. The life time of a QNM is equal to the inverse of the imaginary part of the frequency, $\tau = 1/\omega''$, and it can be substantially larger than the corresponding traveling time $T_{gr} = L/v_{gr}$ in a homogeneous medium. Please note that τ includes only the radiation losses, and thus is longer than the full life time.

Moreover, we would like to emphasize the principal difference between the traveling time T_{gr} and the life time τ for storage purposes. In the case of a traveling wave packet the storage time does not exceed the time T_{gr} at which the spin-wave energy completely leaves the magnonic crystal. On the contrary, in the case of quasi-normal mode the time τ characterizes its decay rate only. Since this mode does not propagate, and thus remains permanently in the magnonic crystal, its energy is stored until the amplitude of this mode falls down to the level of thermal fluctuations. Consequently, the storage time can significantly exceed the lifetime τ.

The QNM eigenfrequencies can be found numerically as complex eigenvalues of the crystal's transfer matrix and correspond to the local minima of the SW group velocity. In our magnonic crystal inside of each MC pass-band there are nine QNMs located symmetrically relative to the centers of the MC band gaps ω_a (see Fig. 3b). Both the frequency and the life time of each of these modes strongly depend on the SW coupling with the groove structure which, in turn, is determined by the SW reflectivity from the single groove and can be characterized by the half-width of the MC band gap Ω_a. These dependencies are presented in Fig. 4 for four modes from the first pass-

band. One can see that the life time is maximal for the mode which is closest to the band gap edge ($n = 1$). Furthermore, for our experimental conditions, the frequency of this mode coincides with the global minima of v_{gr} (see Fig. 4b). Thus $n = 1$ QNM conserves energy for the longest time $\tau_{n=1}/T_{gr} \simeq 5.3$, as $T_{gr} \simeq 110\,\text{ns}$ and $\Omega_a = 2\pi \cdot 10\,\text{MHz}$ for the first band gap in our experiment) and can interact with the parametric pumping long after the exciting traveling spin wave packet has passed. As a result, the restoration phenomenon is observed only at the global minima of v_{gr}. Furthermore, the amplification of the MC mode is maximal for the mode with the lowest damping, and thus with the longest life time. This effect contributes additionally to the strong localization of the restored signals at the band gap edges.

In conclusion, we have experimentally demonstrated that spin waves can be stored in a magnonic crystal. The storage is based on the excitation of the quasi-normal mode of the crystal rather than on the deceleration of the propagating wave, which is only 20 percent at maximum in our case. The first quasi-normal mode, whose eigenfrequency coincides with a minimum of the SW group velocity at the edges of the MCs band gaps, has the longest life-time (five times longer than the spin-wave propagation time through the MC area), and thus conserves the signal energy and phase information for a long time after the propagating wave has left the MC. In order to restore the signal, a further parametric amplification of this mode is used. The dependence of the restored signal power on the phase of the input wave evidences simultaneous amplification of two phase-coupled waves of opposite wavevectors, and thus corroborates the role of the standing MC mode in the storage mechanism. The results presented here provide deeper understanding of the storage-recovery mechanisms in periodic lattices in general. Besides, they suggest a potential possibility of utilization of magnonic crystals for buffering or storage of microwave information.

This work has been recently published in Physical Review Letters [11].

Financial support by the Deutsche Forschungsgemeinschaft SE 1771/1-2 and by the Australian Research Council and technical support from the Nano-Structuring Center, TU Kaiserslautern is gratefully acknowledged. The authors thank M. Fleischhauer for helpful discussions.

References

[1] T. Krauss, *Slow light in photonic crystal waveguides*, J. Phys. D **40**, 2666 (2007).
[2] T. Baba, *Slow light in photonic crystals*, Nat. Photon. **2**, 465 (2008).
[3] S.A. Nikitov, P. Tailhades, C.S. Tsai, *Spin waves in periodic magnetic structures - magnonic crystals*, J. Magn. Magn. Mater. **236**, 320 (2001).
[4] A.V. Chumak, A.A. Serga, B. Hillebrands, M.P. Kostylev, *Scattering of backward spin waves in a one-dimensional magnonic crystal*, Appl. Phys. Lett. **93**, 022508 (2008).
[5] A.V. Chumak, P. Pirro, A.A. Serga, M.P. Kostylev, R.L. Stamps, H. Schultheiss, K. Vogt, S.J. Hermsdoerfer, B. Laegel, P.A. Beck, B. Hillebrands, *Spin-wave propagation in a microstructured magnonic crystal*, Appl. Phys. Lett. **95**, 262508 (2009).
[6] Z.K. Wang, V.L. Zhang, H.S. Lim, S.C. Ng, M.H. Kuok, S. Jain, A.O. Adeyeye, *Observation of frequency band gaps in a one-dimensional nanostructured magnonic crystal*, Appl. Phys. Lett. **94**, 083112 (2009).
[7] G. Gubbiotti, S. Tacchi, M. Madami, G. Carlotti, A.O. Adeyeye, M.P. Kostylev, *Brillouin light scattering studies of planar metallic magnonic crystals*, J. Phys. D **43**, 264003 (2010).
[8] A.V. Chumak, V.S. Tiberkevich, A.D. Karenowska, A.A. Serga, J.F. Gregg, A.N. Slavin, B. Hillebrands, *All-linear time reversal by a dynamic artificial crystal*, Nat. Commun. **1:141** doi: 10.1038/ncomms1142 (2010).
[9] A.A. Serga, A.V. Chumak, B. Hillebrands, *YIG magnonics*, J. Phys. D **43**, 264002 (2010).
[10] V.I. Vasyuchka, A.V. Chumak, A.A. Serga, B. Hillebrands, *Parametrical recovery of a spin-wave signal stored in a magnonic crystal*, AG Magnetismus Annual Report, 31 (2010).
[11] A.V. Chumak, V.I. Vasyuchka, A.A. Serga, M.P. Kostylev, B. Hillebrands, *Storage-recovery phenomenon in magnonic crystal*, Phys. Rev. Lett. **108**, 257207 (2012).

[12] A.A. Serga, A.V. Chumak, A. André, G.A. Melkov, A.N. Slavin, S.O. Demokritov, B. Hillebrands, *Parametrically stimulated recovery of microwave signal stored in standing spin-wave modes of a magnetic film*, Phys. Rev. Lett. **99**, 227202 (2007).
[13] A.V. Chumak, A.A. Serga, G.A. Melkov, V. Tiberkevich, A.N. Slavin, B. Hillebrands, *Parametric recovery of a microwave signal using standing spin-wave modes of a magnetic film*, Phys. Rev. B **79**, 014405 (2009).
[14] V.S. L'vov, *Wave turbulence under parametric excitations: applications to magnetics* (Springer, Berlin, 1994).
[15] A.V. Chumak, A.A. Serga, S. Wolff, B. Hillebrands, M.P. Kostylev, *Design and optimization of one-dimensional ferrite-film based magnonic crystals*, J. Appl. Phys. **105**, 083906 (2009).
[16] E.S.C. Ching, P.T. Leung, A. Maassen van den Brink, W.M. Suen, S.S. Tong, K. Young, *Quasinormal-mode expansion for waves in open systems*, Rev. Mod. Phys. **70**, 1545 (1998).

D. Spin Caloric Transport

Spin Caloric Transport is a new and dynamically growing field of research, which investigates the interplay between spin- and heat-based transport phenomena. The observation of the spin Seebeck effect in a magnetic insulator demonstrates the crucial role of collective magnetization excitations, i.e. spin waves and their quanta, magnons, in spin caloric transport processes, and illustrates the conceptual distinction between this phenomenon and conventional thermoelectric generation. Most interesting and important is the conversion of a heat flow into magnon currents and vice versa in a magnetic insulator. On a long time scale this may lead to the utilization of heat currents to support the transfer and processing of spin information.

In Report 4.11 the manipulation of magnetization relaxation utilizing an applied temperature difference across the thickness of an yttrium iron garnet/platinum (YIG/Pt) hetero-structure is demonstrated. The heat-induced variation of the damping is detected by microwave techniques as well as by the inverse spin Hall effect. Report 4.12 presents the first measurements of the spatial distribution of the magnon temperature in a magnetic system subject to a lateral thermal gradient. It is shown that, contrary to the currently accepted theory, the magnon and phonon temperatures do not differ even in YIG, which is known to have significantly weaker magnon-phonon coupling than magnetic metals. The conversion of magnon currents into a heat flow in magnetic insulators is studied in the next two reports. In Report 4.13 we present the results on the magnon mediated heating in a monocrystalline YIG film. The possibility to control the direction of heating and its dependence on the spin-wave wavelength are investigated. In Report 4.14 the dynamic heating effects of a polycrystalline ferrimagnetic sample in a wide range of magnetic fields are reported.

D. Spin-kalorischer Transport

Der spin-kalorische Transport ist ein neues und rasant wachsendes Forschungsfeld, das das Zusammenspiel zwischen Spin-basierten und Wärme-basierten Transportphänomenen untersucht. Die Untersuchungen des Spin-Seebeck-Effekts in magnetischen Isolatoren zeigen dabei die wichtige Rolle auf, welche die kollektiven Anregungen des magnetischen Systems - also Spinwellen - in spinkalorischen Transport-Prozessen spielen. Weiterhin verdeutlichen diese Beobachtungen die konzeptuelle Unterscheidung zwischen diesen Phänomenen auf der einen sowie konventionellen thermoelektrischen Effekten auf der anderen Seite. Von größtem Interesse und von größter Wichtigkeit in diesem Forschungsgebiet ist die Untersuchung der Umwandlung von Wärmeflüssen in reine Spinströme in Isolatoren. Perspektivisch kann das Verständnis dieser Prozesse zur Nutzung von Wärmeströmen für den Transport sowie die Verarbeitung von Spin-Information beitragen.

In Kapitel 4.11 wird die Manipulation der Magnetisierungsrelaxation durch Anlegen einer Temperaturdifferenz über die Dicke einer Yttrium-Eisen-Granat/Platin(YIG/Pt)-Heterostruktur demonstriert. Die wärmeinduzierte Veränderung der Dämpfung wird unter Zuhilfenahme von Mikrowellen-Messtechniken sowie mit Hilfe des inversen Spin-Hall-Effektes nachgewiesen. Kapitel 4.12 beinhaltet die erstmalige Messung der räumlichen Verteilung der Magnonentemperatur in einem magnetischen System, das einem lateralen thermischen Gradienten ausgesetzt ist. Es wird gezeigt, dass im Gegensatz zur bisher akzeptierten Theorie die Magnonentemperatur und die Photonentemperatur nicht einmal in YIG voneinander abweichen, obwohl hier im Vergleich zu anderen magnetischen Materialien die Magnon-Phonon-Kopplung signifikant geringer ist. Die Konversion eines Magnonenstroms in einen Wärmestrom innerhalb eines magnetischen Isolators wird in den darauf folgenden beiden Kapiteln untersucht: In Kapitel 4.13 stellen wir die Ergebnisse der

durch Magnonen vermittelten Erwärmung in einem monokristallinen YIG-Film vor. Es wird untersucht, inwiefern die Richtung des Wärmestroms kontrolliert werden kann und wie stark dieser von der Spinwellen-Wellenlänge abhängt. In Kapitel 4.14 wird über dynamische Heizeffekte einer polykristallinen ferrimagnetischen Probe in einem großen magnetischen Feldbereich berichtet.

4.11 Heat-induced damping manipulation in magnetic insulator/non-magnetic metal structures

M. B. Jungfleisch, V. I. Vasyuchka, A. V. Chumak, A. A. Serga, and B. Hillebrands

In collaboration with: T. An, K. Ando, Y. Kajiwara, K. Uchida, and E. Saitoh, IMR, Tohoku University, Sendai, Japan.

Magnon spintronics is a new, emerging field in spintronics, that utilizes magnons (quanta of spin waves) as carriers of spin angular momentum. Within magnon spintronics, the spin Hall effect (SHE) and the inverse spin Hall effect (ISHE) attracted great attention in the last years due to potential applications and challenging underlying physical phenomena [1, 2]. The combination of spin pumping and ISHE became a standard technique to detect magnons beyond the wavenumber limitations of most other existing detection methods [2]. Spin caloritronics, a relatively new subfield in spintronics, is concerned with the interplay of heat and (magnon) spin currents [3, 4].

An important goal in magnon spintronics is the manipulation of magnetization relaxation and generation of spin waves. A common method to compensate spin-wave damping is parametric amplification, where an external microwave source with twice the spin-wave frequency is used [2, 5]. Recently, it was shown, that traveling spin waves can also be amplified by injecting a spin polarized electron current due to the SHE and the spin-transfer torque (STT) effect [6] and by the spin Seebeck effect (SSE) [7]. Spin relaxation was manipulated by SHE and STT in $Ni_{81}Fe_{19}$ [8] and by thermally-induced interfacial spin transfer in yttrium iron garnet/platinum (YIG/Pt) bilayer structures [9]. All the experiments have in common, that the magnetization dynamics is measured by using microwave techniques. As shown in Refs. [10, 11] (see also Report 4.7), two-magnon scattering can lead to the excitation of secondary, short-wavelength spin waves, which contribute substantially to the spin pumping [12, 13], but they cannot be detected by inductive antennas or cavities. Thus, microwave measurements do not necessarily give a complete insight into magnetization dynamics.

In this Report, we show the thermal manipulation of spin-wave damping measured by both spin pumping as well as by microwave techniques. The investigated sample is a YIG/GGG/YIG/Pt multilayer. Applying a temperature difference across the thickness of this multilayer gives rise to the longitudinal SSE: an imbalance between the effective magnon and the effective electron temperatures causes a spin current across the YIG/Pt interface [3, 4]. Since the created spin current transfers spin angular momentum, a torque is exerted on the magnetization (Fig. 1b). Consequently, the magnetization precession is either enhanced or suppressed depending on the sign of the temperature difference. This damping variation can be expressed as a change of the ferromagnetic resonance linewidth ΔH_{FMR} that is detected by spin pumping as well as microwave reflection.

The experimental setup is depicted in Fig. 1a. A 2.1 µm thick YIG film was grown by means of liquid phase epitaxy on both sides of a 500 µm thick gadolinium gallium garnet (GGG) substrate. The 10 nm thick Pt layer was deposited on one side of the YIG slab by molecular beam epitaxy. We use a Peltier element, mounted on top of the Pt layer, to establish a temperature difference across the multilayer. Since sapphire is known to be a good thermal conductor, we mount a rectangularly-shaped sapphire substrate on top of the second YIG surface to increase the temperature flow from the sample. This sapphire substrate is connected to a heat bath. The second YIG layer neither influences the magnetic nor the electric measurements but it should be noted that the temperature difference is applied across the entire Pt/YIG/GGG/YIG sample stack. The magnetization precession is excited by a 500 µm wide copper microstrip antenna that is placed above the Pt layer (see

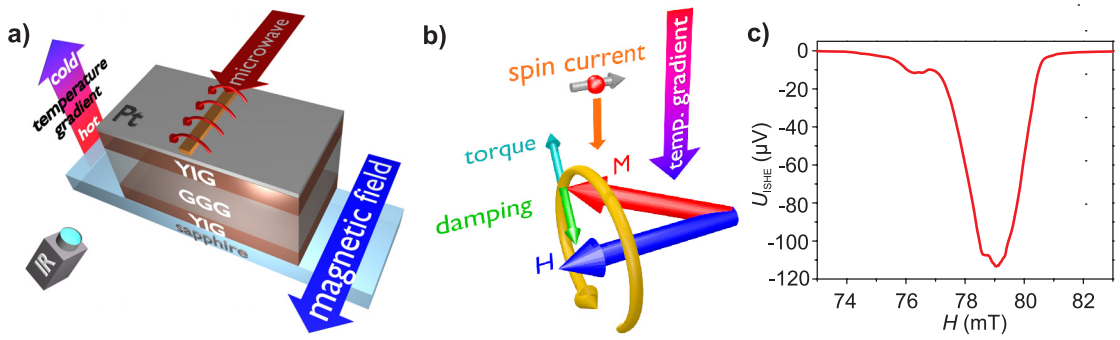

Fig. 1: a) Scheme of the experimental setup. b) Heat-induced spin-torque effect on the magnetization precession in the YIG film. **M** denotes the magnetization. c) Typical example for a measurement of U_{ISHE} as a function of the applied magnetic field H for zero temperature difference.

Fig. 1a). We monitor the temperature difference using an infrared camera (the sapphire substrate is transparent for infrared radiation), calibrated by two thermocouples.

The experiment is performed in the following fashion: an external magnetic field **H** is applied perpendicularly to the YIG waveguide in the YIG film plane. The alternating magnetic field $\mathbf{h}(t)$ of a continuous microwave signal drives the magnetization precession (see Fig. 1a and b) with a carrier frequency of 4 GHz and powers of $P_{\mathrm{MW}} = +14\,\mathrm{dBm}$, $+20\,\mathrm{dBm}$ and $+25\,\mathrm{dBm}$. While a temperature difference ΔT across the sample thickness is applied (monitored by the infrared camera), we sweep the external magnetic field **H** and measure U_{ISHE} (see Fig. 1c) and the microwave reflection simultaneously.

In Fig. 2a the voltage U_{ISHE} is shown as a function of the applied magnetic field H for four different temperature differences ΔT. Due to heating and cooling of the sample, the saturation magnetization M_{S} is changed and, thus, the resonance peak shifts to higher or lower magnetic fields. As it is obvious from Fig. 2(a), not only one but several modes contribute to the ISHE voltage. It is known that the damping of the YIG film is enhanced by adding the Pt layer [8,12]. This can be understood taking into account that the transfer of spin angular momentum from the YIG to the Pt layer due to spin pumping deprives the magnetization precession, which gives rise to additional damping and, thus, to a widening of the linewidth [8]. The data are processed in the following way: the envelope of U_{ISHE} is fitted for each temperature difference by a Gaussian function $f(x) = a \cdot \exp(-(x-b)^2/(2c^2))$, where c defines the linewidth ΔH which is a measure for the relaxation time τ of the magnetization precession and, thus, the damping α_0. The linewidth ΔH that is determined in this way, does not necessarily coincide with the real ferromagnetic resonance linewidth ΔH_{FMR} but is proportional to it, i. e. $\Delta H \propto \Delta H_{\mathrm{FMR}}$. The linewidth ΔH as a function of the temperature difference ΔT is illustrated in Fig. 2b for different microwave powers P_{MW}. The linewidth ΔH decreases for one polarity of ΔT and increases for the other. Due to non-linear effects, the linewidth at $\Delta T = 0$ is larger for higher microwave powers [16–18]. It is remarkable, that the linewidth changes about 6 % for a temperature difference of $\Delta T \approx \pm 4\,^{\circ}\mathrm{C}$, independent of the microwave power. The variation of the linewidth per 1 °C temperature difference (slope in Fig. 2b) is approximately the same for all microwave powers. We also performed a deconvolution of the spectrum and fitted each mode separately but the qualitative behavior for each mode remains the same: when the Pt layer is hotter than the YIG film, the linewidth is decreased, whereas it is enhanced when the YIG film is hotter than the Pt capping.

In the following we compare how the linewidth changes under the influence of a longitudinal temperature difference measured by both spin pumping as well as microwave techniques. As it is

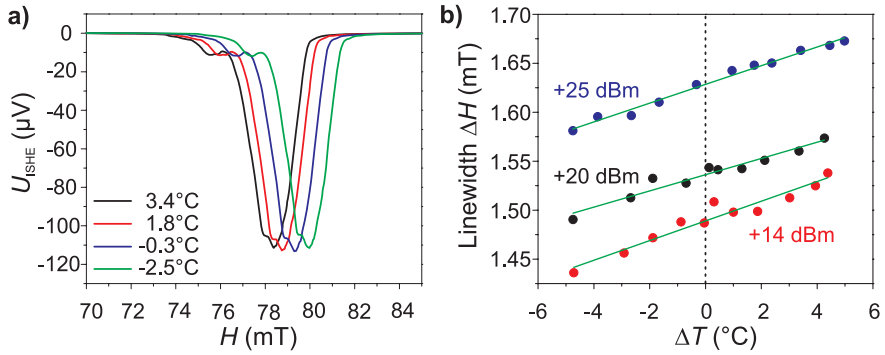

Fig. 2: a) Typical spectra for four different temperature differences at +25 dBm. For positive (negative) temperature differences, the Pt is colder (hotter) than the YIG. b) Measured resonance linewidth ΔH as a function of the applied temperature difference ΔT for different microwave powers.

shown in Ref. [10,11] and Report 4.7, the spin pumping is insensitive to the spin-wave wavenumber and thus, the directly excited spin-wave modes as well as short-wavelength secondary waves contribute to the detected signal. However, in microwave measurements mainly the primary excited uniform mode is detected. The summarized results are presented in Fig. 3. For both measurement techniques, the linewidth qualitatively behaves the same in the investigated range of temperature differences. Nevertheless, one can see that the slopes of the two curves diverge leading to the assumption that the directly excited uniform FMR mode is mostly effected by the heat-induced STT. However, a quantitative statement is not possible. The results show that even though the Pt layer acts as a spin sink or source in the present experiment, it is also possible to utilize spin pumping and SHE as a detector for the heat-induced STT.

Based on the model developed in Ref. [8], we calculate the variation of the magnetization relaxation in YIG/Pt structures due to a heat-induced spin current. The motion of the magnetization is described by the Landau-Lifshitz-Gilbert (LLG) equation [19]. The Gilbert damping coefficient α_0 is composed of the intrinsic damping α_F and additional damping due to spin pumping into the adjacent Pt layer $\Delta\alpha_{SP}$ [12]. The modified Gilbert damping coefficients can be written as $\alpha_0 = \alpha_F + \Delta\alpha_{SP} + \Delta\alpha_{STT}^{SSE}$. This allows us to distinguish between an effective damping $\alpha_{eff} = \alpha_F + \Delta\alpha_{SP}$ that is not affected by temperature at all and a temperature-dependent part $\Delta\alpha_{STT}^{SSE}$. The damping can be calculated by $\alpha_0 = \gamma/4\pi f\Delta H$, where ΔH is the resonance linewidth. The generalized LLG can be written as

$$\frac{d\mathbf{M}}{dt} = -\gamma\mathbf{M}\times\mathbf{H}_{eff} + \frac{\alpha_{eff}}{M_s}\mathbf{M}\times\frac{d\mathbf{M}}{dt} - \frac{\gamma J_S^{STT}}{M_s^2 V_F}\mathbf{M}\times(\mathbf{M}\times\sigma) \quad , \tag{1}$$

where $\mathbf{M}$ is the magnetization, γ the gyromagnetic ratio, $\mathbf{H}_{eff}$ the effective magnetic field, M_s the saturation magnetization, V_F the volume of the YIG layer, and σ the spin polarization vector. J_S^{STT} describes the spin torque. Assuming σ is parallel to the precession axis, we can solve the LLG with respect to the precession axis and derive an analytical expression for $\mathbf{M}$. By further assuming that $\gamma M_s/f \approx 1$ and $\gamma J_S^{STT}/2\pi f M_S V_F \ll 1$, we can calculate the total Gilbert damping coefficient $\alpha_0 = \alpha_{eff} + \Delta\alpha_{STT}^{SSE}$ with

$$\Delta\alpha_{STT}^{SSE} \approx \frac{\gamma J_S^{STT}}{2\pi f M_s V_F} \quad . \tag{2}$$

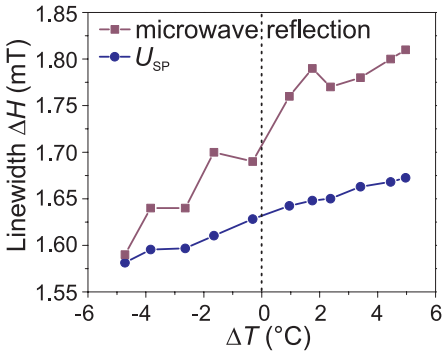

Fig. 3: Measured linewidth ΔH as a function of the applied temperature difference ΔT for reflected microwave signal and spin pumping voltage U_{SP}.

Solving the drift-diffusion equation [8, 20, 21] for the heat-induced spin current in a bilayer film, we obtain a linear relation between the damping and the temperature difference

$$\Delta\alpha_{STT}^{SSE} \approx \frac{\hbar}{e}\frac{\gamma}{2\pi f M_s d_F} u\Delta T \quad , \tag{3}$$

where u describes the injection and charge current conversion efficiency and d_F is the thickness of the ferromagnetic layer. Using Eqs. (4) and (3), we obtain $J_S^{STT} = A_F\frac{\hbar}{e}u\Delta T$, where A_F is the cross section of the ferromagnetic layer. Fitting our data enables us to determine the pre-factor in Eq. (3) $v = (\hbar/e)(\gamma/2\pi f M_s d_F)u$ and thus, to calculate u as well as J_S^{STT}. J_S^{STT} can be expressed as:

$$J_S^{STT} = A_F v\frac{2\pi f M_s d_F}{\gamma}\Delta T \quad , \tag{4}$$

where v is the slope obtained by fitting our results (Fig. 2(b)). The spin-current density is given by $J_S = 2e/(\hbar A_F)J_S^{STT}$.

The calculated spin torque J_S^{STT} and the spin current density J_S are summarized for different microwave powers in Table 1. For these calculations, we assumed M_S to be constant since ΔT leads to variations of about 1 % of M_S which cannot explain the observed linewidth change. The control of magnetization relaxation by the heat-induced STT practically does not depend on the microwave power so that J_S^{STT} and J_S are not power dependent as well. We found, that our calculated heat-induced spin current density per 1 °C is one to two orders of magnitude higher than those generated by the SHE for the maximal DC voltage pulses used in Ref. [6] of $U = 8\,V$ ($J_S = 10^8\,A/m^2$, $R_{Pt} \approx 30\,\Omega$, $\tau_{pulse} = 300\,ns$, $\tau_{repetition} = 10\,ms$).

In conclusion, the heat-induced variation of the damping in YIG/Pt hetero-structures has been shown. The modulation of the relaxation coefficient has been demonstrated by microwave techniques as well as by spin pumping. Both techniques qualitatively show the same behavior. The

P_{MW} (dBm)	$J_S^{STT}(\times 10^{-11}\frac{Nm}{°C}\Delta T)$	$J_s(\times 10^{9}\frac{A}{m^2 °C}\Delta T)$
+14	1.74	3.70
+20	2.11	4.49
+25	2.01	4.27

Table 1: Comparison of spin torque J_S^{STT} and spin current density J_s for different mircowave powers P_{MW}.

spin transfer due to the temperature difference across the YIG/Pt interface has been estimated and has been compared to previous works that use SHE-generated spin currents. It turns out that the thermally-induced spin current density per 1 °C is at least one order of magnitude higher than any spin current densities generated by the SHE reported so far.

Financial support by the Deutsche Forschungsgemeinschaft within the projects SE 1771/4-1 (Priority Program 1538 Spin Caloric Transport) and CH 1037/1-1 is gratefully acknowledged.

References

[1] E. Saitoh, M. Ueda, H. Miyajima, G. Tatara, *Conversion of spin current into charge current at room temperature: inverse spin-Hall effect*, Appl. Phys. Lett. **88**, 182509 (2006).
[2] C.W. Sandweg, Y. Kajiwara, A.V. Chumak, A.A. Serga, V.I. Vasyuchka, M.B. Jungfleisch, E. Saitoh, B. Hillebrands, *Spin pumping by parametrically excited exchange magnons*, Phys. Rev. Lett. **106**, 216601 (2011).
[3] K. Uchida, J. Xiao, H. Adachi, J. Ohe, S. Takahashi, J. Ieda, T. Ota, Y. Kajiwara, H. Umezawa, H. Kawai, G.E.W. Bauer, S. Maekawa, E. Saitoh, *Spin Seebeck insulator*, Nature Mater. **9**, 894 (2010).
[4] K. Uchida, H. Adachi, T. Ota, H. Nakayama, S. Maekawa, E. Saitoh, *Observation of longitudinal spin-Seebeck effect in magnetic insulators*, Appl. Phys. Lett. **97**, 172505 (2010).
[5] A.G. Gurevich and G.A. Melkov, *Magnetization oscillations and waves* (CRC, New York, 1996).
[6] Z. Wang, Y. Sun, M. Wu, V.S. Tiberkevich, A. Slavin, *Control of spin waves in a thin film ferromagnetic insulator through interfacial spin scattering*, Phys. Rev. Lett. **107**, 146602 (2011).
[7] E. Padrón-Hernández, A. Azevedo, S.M. Rezende, *Amplification of spin waves by thermal spin-transfer torque*, Phys. Rev. Lett. **107**, 197203 (2011).
[8] K. Ando, S. Takahashi, K. Harii, K. Sasage, J. Ieda, S. Maekawa, E. Saitoh, *Electric manipulation of spin relaxation using the spin Hall effect*, Phys. Rev. Lett. **101**, 036601 (2011).
[9] L. Lu, Y. Sun, M. Jantz, M. Wu, *Control of ferromagnetic relaxation in magnetic thin films through thermally induced interfacial spin transfer*, Phys. Rev. Lett. **108**, 257202 (2012).
[10] M.B. Jungfleisch, A.V. Chumak, V.I. Vasyuchka, A.A. Serga, B. Obry, H. Schultheiss, P.A. Beck, A.D. Karenowska, E. Saitoh, B. Hillebrands, *Temporal evolution of inverse spin Hall effect voltage in a magnetic insulator-nonmagnetic metal structure*, Appl. Phys. Lett. **99**, 182512 (2011).
[11] A.V. Chumak, A.A. Serga, M.B. Jungfleisch, R. Neb, D.A. Bozhko, V.S. Tiberkevich, B. Hillebrands, *Direct detection of magnon spin transport by the inverse spin Hall effect*, Appl. Phys. Lett. **100**, 082405 (2012).
[12] Y. Tserkovnyak, A. Brataas, G.E.W. Bauer, *Enhanced Gilbert damping in thin ferromagnetic films*, Phys. Rev. Lett. **88**, 117601 (2002).
[13] M.V. Costache, M. Sladkov, S.M. Watts, C.H. van der Waal, B.J. van Wees, *Electrical detection of spin pumping due to the precessing magnetization of a single ferromagnet*, Phys. Rev. Lett. **97**, 216603 (2006).
[14] K. Uchida, T. Ota, H. Adachi, J. Xiao, T. Nonaka, Y. Kajiwara, G.E.W. Bauer, S. Maekawa, E. Saitoh, *Thermal spin pumping and magnon-phonon-mediated spin-Seebeck effect*, J. Appl. Phys. **111**, 103903 (2012).
[15] J.E. Hirsch, *Spin Hall effect*, Phys. Rev. Lett. **83**, 1834 (1999).
[16] Y. Khivintsev, Bijoy Kuanr, T.J. Fal, M. Haftel, R.E. Camley, Z. Celinski, D.L. Mills, *Nonlinear ferromagnetic resonance in permalloy films: a nonmonotonic power-dependent frequency shift*, Phys. Rev. B **81**, 054436 (2010).
[17] Y.S. Gui, A. Wirthmann, C.-M. Hu, *Foldover ferromagnetic resonance and damping in permalloy microstrips*, Phys. Rev. B **80**, 184422 (2009).
[18] V.E. Demidov, H. Ulrichs, S.O. Demokritov, S. Urazhdin, *Nonlinear scattering in nanoscale magnetic elements: overpopulation of the lowest-frequency magnon state*, Phys. Rev. B **83**, 020404(R) (2011).
[19] L.D. Landau, E.M. Lifshitz, *On the theory of the dispersion of magnetic permeability in ferromagnetic bodies*, Physikalische Zeitschrift der Sowjetunion **8**, 153 (1935).
[20] T. Valet, A. Fert, *Theory of the perpendicular magnetoresistance in magnetic multilayers*, Phys. Rev. B **48**, 7099 (1993).
[21] S. Takahashi, S. Maekawa, *Nonlocal spin Hall effect and spin-orbit interaction in nonmagnetic metals*, J. Magn. Magn. Mater. **310**, 2067 (2007).
[22] K. Uchida, T. Ota, H. Adachi, J. Xiao, T. Nonaka, Y. Kajiwara, G.E.W. Bauer, S. Maekawa, E. Saitoh, *Thermal spin pumping and magnon-phonon-mediated spin-Seebeck effect*, J. Appl. Phys. **111**, 103903 (2012).

4.12 Magnon-phonon coupling unmasked: a direct measurement of magnon temperature

M. Agrawal, V. I. Vasyuchka, A. A. Serga, and B. Hillebrands

In collaboration with: G. A. Melkov, Faculty of Radiophysics, Taras Shevchenko National University of Kyiv, Ukraine, and A. D. Karenowska, Department of Physics, Clarendon Laboratory, University of Oxford, Oxford, UK.

The thermoelectric properties of magnetic media are determined by the detailed interplay between their electron, phonon, and magnon (spin) systems. In magnetic insulators, due to the absence of free electron, the phonon and magnon systems are of greatest significance. In general, the spin-lattice relaxation time of these systems is higher than the intra-relaxation times of magnons or phonons [1]. Therefore, it is expected that both of these subsystems establish internal thermal equilibria much faster than their mutual equilibration and, thus, can be characterized by their individual temperatures [2]. In Ref. [3], the authors have predicated that the thermal gradient ∇T, applied along a ferromagnetic material, creates a higher density of magnons in the hot regions which diffuse towards the cold regions and increase the temperature of magnons there. Therefore, in this case the magnon temperature T_m goes higher than the phonon temperature T_p at the cold end and lower at the hot end. The transport of the thermal magnons depends on the magnon-phonon coupling and the magnon-magnon scattering parameters. In the case of a strong magnon-phonon coupling, the magnons will rather quickly be in equilibrium with the phonon bath and follow the temperature profile of the phonons. On the other hand, for a weak coupling, the local T_p has a weaker influence on T_m, hence the difference between the magnon temperatures at the opposite ends of the magnetic system will be smaller [2].

Magnons are bosonic quasiparticles whose population at a temperature T_m is described by Bose-Einstein statistics and given by $[\exp(\hbar\omega/k_\mathrm{B}T_\mathrm{m})-1]^{-1}$, where k_B is Boltzmann constant and ω is frequency of magnons [4]. As each of the thermal magnons reduces the total magnetization of the system by one Bohr magneton [5], the magnetization of the material is a measure of the magnon population, and hence of the magnon temperature. Therefore, the spatial distribution of the magnon temperature can be determined by measuring the local magnetization of the system. A very precise measurement of local magnetization is not possible with conventional methods like Magneto-optical Kerr Microscopy (MOKE), etc. The Brillouin light scattering spectroscopy technique (BLS) enables us to measure the local magnetization of the system. The spatial variation of the magnetization caused by the thermal gradient is studied here by measuring the frequency shift of a particular magnon mode with the thermal gradient at different local phonon temperatures.

Our experiment was performed using the low-magnetic-damping ferrimagnetic material Yttrium Iron Garnet (YIG, $Y_3Fe_5O_{12}$). A monocrystalline ($\langle 111\rangle$) YIG film of dimensions 3 mm×10 mm with a thickness of 6.7 µm was grown by the liquid phase epitaxy technique on a 0.5 mm thick Gallium Gadolinium Garnet (GGG, $Gd_3Ga_5O_{12}$) substrate. The film was magnetized in-plane by a magnetic field of $B = 250$ mT. The schematic diagram of the experimental setup is shown in Fig. 1a. Two Peltier elements for heating and cooling purposes are kept apart by an edge-to-edge separation of 3.2 mm to create a thermal gradient along the length of the film. The thermal gradient was measured by an infra-red (IR) camera with a temperature resolution of 0.1 °C and a spatial resolution of 40 µm. A small laser power of 7 mW was used for all regular measurements to minimize the local sample heating, and to avoid the formation of spurious thermal gradients around the laser spot. During the measurement process the laser spot temperature was kept stable

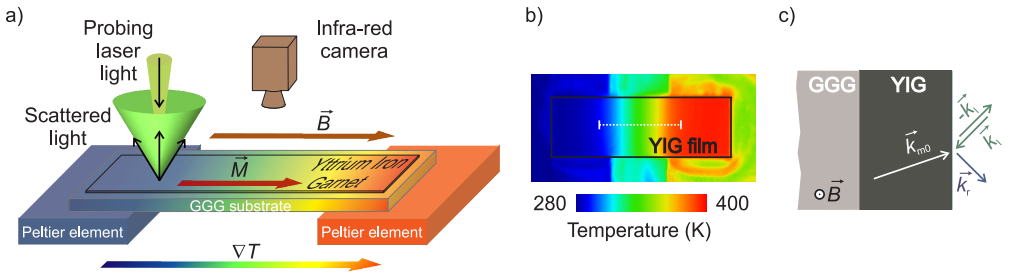

Fig. 1: a) Sketch of experimental setup. The YIG film was magnetized in-plane with an externally applied magnetic field $B = 250\,\mathrm{mT}$ parallel to ∇T and the magnon temperature was measured using Brillouin light scattering (BLS). An infra-red (IR) camera was used to obtain thermal images of the system. b) Infra-red image of the YIG film. The dashed line indicates the path along which the laser was scanned in order to perform the magnon temperature measurements. c) The orientation of the incident (probing) ($\mathbf{k}_\mathrm{I}$), reflected ($\mathbf{k}_\mathrm{r}$), and back-scattered (signal) ($-\mathbf{k}_\mathrm{I}$) photon wavevectors relative to the YIG film surface. The magnon wavevector, $\mathbf{k}_{\mathrm{m}0}$ satisfies the momentum conservation condition, $|\mathbf{k}_{\mathrm{m}0}| = 2n|\mathbf{k}_\mathrm{I}|$, where $n = 2.36$ is the refractive index of the YIG.

with an accuracy of $\pm 0.3\,^\circ\mathrm{C}$. The thermal spin-wave spectrum was captured by the BLS setup. All the BLS measurements were performed in the second free spectral range (FSR) region to improve the frequency resolution [6].

Typically, in micron-order thick YIG films, a broad spectrum of magnons is excited by the thermal energy at room temperature [4, 7]. One can investigate the different magnon modes through the BLS measurements by changing the direction of the incident-photon wavevector relative to the magnetization of the film [8]. Nevertheless, a particular magnon mode always exists which travels along the probing light inside the film and satisfies a specific momentum conservation condition, $\mathbf{k}_\mathrm{sw} = 2n\mathbf{k}_\mathrm{I}$, where $\mathbf{k}_\mathrm{sw}$ is the magnon wavevector, n ($= 2.36$ for YIG [9]) is the refractive index of the film, and $k_\mathrm{I} = 1.18 \times 10^5\,\mathrm{rad/cm}$ (for the green light laser of wavelength 532 nm) is the photon wavevector. The momentum conservation condition implies that the incident photon will be scattered back by the thermal magnons at an angle of $180\,^\circ$. We assign this mode as a back-scattering magnon (BSM) mode (See Fig 1c). For our experimental conditions, the BSM mode lies in the region of the exchange-dominated spin waves with $k_\mathrm{sw} = 5.67 \times 10^5\,\mathrm{rad/cm}$ and a wavelength equal to 110 nm. The position of this mode on the spin-wave dispersion curves of an in-plane magnetized YIG film at $B = 250\,\mathrm{mT}$ is depicted in Fig. 2a at two temperatures: 300 K and 400 K. Due to the small wavelength, these spin waves are strongly dependent on the local magnetization. Therefore, this particular thermal magnon mode is excellently suited for measuring the local magnetization of the system [See Fig. 1c].

In a first reference experiment, BLS measurements were carried out to obtain the thermal dependence of the BSM mode on a homogeneously heated sample without a thermal gradient. These measurements were performed in the middle of the YIG film keeping both heat reservoirs at same temperature. In this configuration, a uniform phonon temperature was observed along the length of the YIG strip in the gap between the Peltier elements. The measurements exhibit that the spin wave frequency declines monotonically with increasing temperature of the YIG film which happens due to a rise in the thermal magnon population in YIG [See Fig. 2b]. Generally, in magnetic systems where the phonon temperature is uniform throughout the system, magnons establish an equilibrium with phonons via magnon-phonon interaction and attain a temperature equal to the phonon temperature [2]. Thus, by fitting the BSM frequency versus the phonon temperature curve with a third order polynomial, as shown in Fig. 2b, the BSM frequency can be expressed as a function of

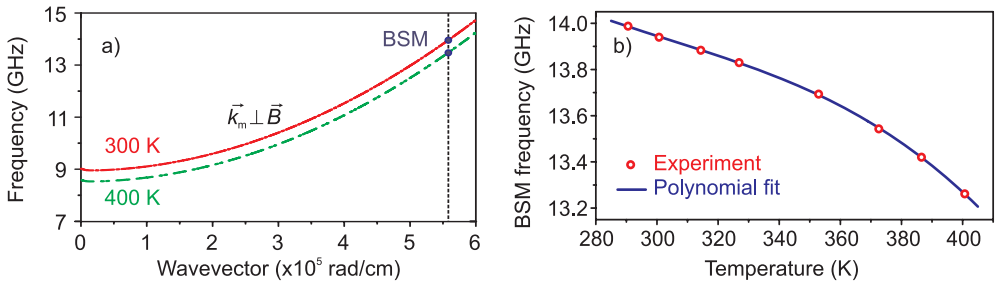

Fig. 2: a) The dispersion relations of spin waves propagating perpendicular to the magnetization at temperatures of 300 K and 400 K for a 6.7 µm thick YIG film magnetized by a field of $B = 250$ mT. Bullets show the positions of the BSM mode at $k_{sw} = 5.67 \times 10^5$ rad/cm. b) Measured and polynomially fitted BSM frequency as a function of the temperature of the YIG film.

the magnon temperature T_m.

In a second experiment, a thermal gradient ∇T was created along the YIG strip by passing electric currents through the Peltier elements in opposite directions [Fig. 1b]. The phonon temperature profile was observed to be practically linear between the hot and the cold edges of the heat reservoirs ($\Delta T_p \leq 85$ K). The BLS frequency of the BSM mode was captured simultaneously with the phonon temperature at different positions on the YIG film along the thermal gradient in between and close to the inner edges of the heat reservoirs. To prove the repeatability of the measurement, and to estimate the measurement errors, the experiment was repeated four times and statistics was accumulated.

In Fig. 3, the phonon temperature T_p and the magnon temperature T_m, calculated from the frequency of the BSM mode, are plotted as a function of the probing position on the YIG film. One can easily see that T_m follows the trend of T_p within the limit of experimental errors. The difference between these two temperatures as a function of position on the film is depicted in the inset in Fig. 3 with a 95 % confidence level. It is important to notice here that the maximal difference between T_p and T_m is only about 2.8 % of ΔT_p, and in contrast to the theoretical expectations, this difference does not change monotonically between the hot and the cold edges.

Apparently, T_p and T_m are coupled with each other by the magnon-phonon interaction and, within the framework of a one-dimensional model as described in Ref. [2], have the following relationship:

$$\frac{d^2 T_m(x)}{dx^2} + \frac{1}{\lambda^2}[T_p(x) - T_m(x)] = 0 \tag{1}$$

where λ is a characteristic length parameter proportional to the square root of the magnon-phonon relaxation time. The equation implies that in a magnetic system where the relaxation time is large, hence a large λ, the difference in $T_p(x)$ and $T_m(x)$ will be pronounced at the boundaries. However, no experiment has been reported so far to determine the value of λ in magnetic insulators. Moreover, the theoretical estimation for λ in YIG is quite uncertain and varies from 0.85 mm to 8.5 mm [3].

Here we have solved Eq. (1) to determine the value of λ for our experimental conditions. To obtain a continuous dependence of the phonon temperature $T_p(x)$, the experimentally measured data are fitted with the Boltzmann sigmoid function [See Fig. 3]. The fitted function is substituted in the equation to get a second order differential equation only in $T_m(x)$ which has been solved

numerically for different values of λ. In the calculation, $dT_m(x)/dx$ is assumed to be zero at the sample boundaries because the heat can dissipate only through the phonons at the boundaries, as the flow of magnons outside of the sample boundaries is not possible. From the experimental findings we determine the maximal possible difference between $T_m(x)$ and $T_p(x)$ at the position $x = \pm 2\,\mathrm{mm}$, and numerically calculate the value of $\lambda_{max} \approx 0.47\,\mathrm{mm}$, which is about one order of magnitude smaller than the value estimated by Xiao *et al.* [3] for YIG using the experimental data of the spin Seebeck effect experiments reported in Ref. [10].

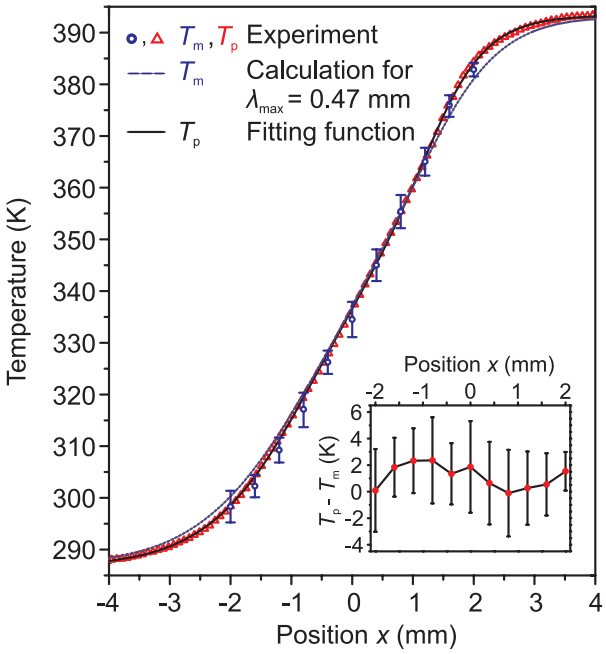

Fig. 3: Measured phonon temperature T_p (open triangles) and magnon temperature T_m (open circles) at different positions on the YIG film along the laser scan line are shown in Fig. 1(b). The T_p data is fitted with a Boltzmann sigmoid function (solid line). The profile of $T_m(x)$ is numerically calculated for the characteristic length parameter $\lambda_{max} = 0.47\,\mathrm{mm}$ (dashed line). The inset shows the difference between T_p and T_m with a 95 % of confidence level.

From our findings, one could suppose that the magnon contribution to the spin Seebeck effect [10–14], even in magnetic insulators where the magnon-phonon interaction is weaker compared to magnetic metals such as Permalloy, is negligible or rather small. However, the impact of long-wavelength magnons, mainly the dipolar magnons, is not accounted in our experiment. In the temperature range of our experiment, the population of exchange magnons in YIG is much higher than the dipole magnons, therefore, the magnetization is primarily dependent on the exchange magnons. For the exchange (small-wavelength) magnons, having $k_{sw} \gtrsim 10^5\,\mathrm{rad/cm}$, three-particle processes, like the Cherenkov processes, in analogy to the Cherenkov radiation phenomenon, provide extra channels for the spin-lattice (magnon-phonon) relaxation. These processes, where a magnon emits or absorbs a phonon, do not change the total number of magnons, but lead to establish the thermal equilibrium between the phonon and magnon thermal bathes. As the contribution of exchange determined Cherenkov processes to the total magnon damping increases with k_{sw}^2 it starts to be equal to relativistic spin-lattice relaxation mechanisms in YIG for $k_{sw} \gtrsim 10^6\,\mathrm{rad/cm}$ [4, 15].

Since the magnon-phonon coupling mechanisms for the exchange magnons are quite different from the dipolar magnons, the dipolar magnons must be described by their own temperature. As a result, we can assume that the temperature of dipolar magnons might not be equal to the phonon temperature and this magnon group can contribute to the spin Seebeck effect.

In conclusion, we have presented a channel to measure the spatial distribution of the magnon temperature in the magnetic insulator YIG by studying the frequency shift of the BSM mode with an in-plane temperature gradient. We experimentally determine the crucial length scale parameter λ

and find it to be rather less than previously expected [3, 16]. Furthermore, the study reveals that in the magnetic insulator YIG having the lowest known magnetic damping, the contribution of exchange magnons to the spin Seebeck effect is negligible and this phenomenon should be associated with low-energy long-wavelength dipolar magnon group. The results are useful to understand the functionality of thermal magnons in the spin Seebeck effect and valuable for the development of spin caloritronics.

The authors thank A.C. Parra, B. Obry, P. Pirro, and A.V. Chumuk for valuable discussions. Financial support by the Deutsche Forschungsgemeinschaft (SE 1771/4-1) within Priority Program 1538, “Spin Caloric Transport”is greatly acknowledged. M. Agrawal is financially supported by the Graduate School of Excellence Materials Science in Mainz through DFG-funding of the Excellence Initiative (GSC 266).

References

[1] C. Kittle, E. Abrahams, *Relaxation process in ferromagnetism*, Rev. Mod. Phys. **25**, 233 (1953).
[2] D.J. Sanders, D. Walton, *Effect of magnon-phonon thermal relaxation on heat transport by magnons*, Phys. Rev. B **15**, 1489 (1977).
[3] J. Xiao, G.E.W. Bauer, K. Uchida, E. Saitoh, S. Meakawa, *Theory of magnon-driven spin Seebeck effect*, Phys. Rev. B **81**, 214418 (2010).
[4] A.G. Gurevich, G.A. Melkov, *Magnetization oscillations and waves* (CRC, New York, 1996).
[5] The statement is strictly applicable for the exchange magnons.
[6] R. Mock, B. Hillebrands, R. Sandercock, *Construction and performance of a Brillouin scattering set-up using a triple-pass tandem Fabry-Perot interferometer*, J. Phys. E: Sci. Instrum. **20**, 656 (1987).
[7] A.A. Serga, A.V. Chumak, B. Hillebrands, *YIG magnonics*, J. Phys. D: Appl. Phys. **43**, 264002 (2010).
[8] C.W. Sandweg, M.B. Jungfleisch, V.I. Vasyuchka, A.A. Serga, P. Clausen, H. Schultheiss, B. Hillebrands, A. Kreisel, P. Kopietz, *Wide-range wavevector selectivity of magnon gases in Brillouin light scattering spectroscopy*, Rev. Sci. Instrum. **81**, 073902 (2010).
[9] V. Doormann, J.P. Krumme, C.P. Klages, M. Erman, *Measurement of the refractive index and optical absorption spectra of epitaxial Bismuth substituted Yttrium Iron Garnet films at uv to near-ir wavelengths*, Appl. Phys. A **34**, 223 (1984).
[10] K. Uchida, S. Takahashi, K. Harii, J. Ieda, W. Koshibae, K. Ando, S. Maekawa, E. Saitoh, *Observation of the spin Seebeck effect*, Nature (London) **455**, 778 (2008).
[11] K. Uchida, J. Xiao, H. Adachi, J. Ohe, S. Takahashi, J. Ieda, T. Ota, Y. Kajiwara, H. Umezawa, H. Kawai, G.E.W. Bauer, S. Maekawa, E. Saitoh, *Spin Seebeck insulator*, Nature Mater. **9**, 894 (2010).
[12] K. Uchida, H. Adachi, T. An, T. Ota, M. Toda, B. Hillebrands, S. Maekawa, E. Saitoh, *Long-range spin Seebeck effect and acoustic spin pumping*, Nature Mater. **10**, 737 (2011).
[13] C.M. Jaworski, J. Yang, S. Mack, D.D. Awschalom, R.C. Myers, J.P. Heremans, *Spin-Seebeck effect: a phonon driven spin distribution*, Phys. Rev. Lett. **106**, 186601(2011).
[14] K. Uchida, H. Adachi, T. Ota, H. Nakayama,S. Maekawa, E. Saitoh, *Observation of longitudinal spin-Seebeck effect in magnetic insulators*, Appl. Phys. Lett. **97**, 172505(2010).
[15] M.I. Kaganov, V.M. Tsukernik, *Phenomenological theory of kinetic processes in ferromagnetic dielectric. II. Interaction of spin waves with phonons*, Sov. Phys. JETP 7,151 (1959).
[16] J.-i. Ohe, H. Adachi, S. Takahashi, S. Maekawa, *Numerical study on the spin Seebeck effect*, Phys. Rev. Lett. **83**, 115118 (2011).

4.13 Magnon mediated heating in a magnetic insulator

V. I. Vasyuchka, A. V. Chumak, A. A. Serga, and B. Hillebrands

The interaction of spins with heat currents in magnetic media leads to a variety of spin-dependent thermoelectric effects and it is the keystone for the field of spin caloritronics [1]. Spin-caloric effects were discovered in magnetic insulators, where a spin is transported via magnetic excitations (spin waves) [2, 3]. These materials differ profitably from metallic magnets due to the absence of conduction electrons, which results in a low magnetic damping and in the absence of the anomalous Nernst effect [4]. Important is the weak coupling between magnons and the lattice in magnetic insulators (see Report 4.12).

A study of the magnon-phonon interaction in the magnetic insulators gives the necessary background required for the understanding of already discovered spin-caloric effects. In addition, new phenomena, such as the magnon-dependent Peltier effect, can be expected in magnetic insulators by the analogy with the recently reported spin Peltier effect in metallic magnets [5].

In this Report we present the results on magnon mediated heating in films of a magnetic insulator using a thermography technique. We have found conditions when the direction of the heating of the sample can be controlled by an external magnetic field. In this case a large shift of the temperature maximum away from the excitation antenna up to a few millimeters was observed. It was understood as a result of the interplay between the unidirectional heating and the diffusion of heat into the cold part of the film. We found a good agreement between this shift and the group velocity of spin waves.

Figure 1a shows a sketch of the experimental setup used for our studies. The experiments were performed using a single-crystal $Y_3Fe_5O_{12}$ yttrium iron garnet (YIG) film of 30 µm thickness epitaxially grown on a gadolinium gallium garnet (GGG) substrate of 500 µm thickness. The YIG/GGG sample had the length of 26 mm and the width of 1.7 mm. The ends of the stripe were cut with an acute angle in order to minimize reflections. As it is shown in Fig. 1a, the YIG/GGG stripe was magnetized by an in-plane magnetic field of $H = 1750$ Oe.

The sample was placed close to a narrow microstrip antenna of 50 µm width. The distance between the YIG surface and the excitation antenna was 100 µm in order to increase a thermal isolation of the sample. A continuous microwave signal was applied to the antenna for the excitation of spin waves in the YIG film.

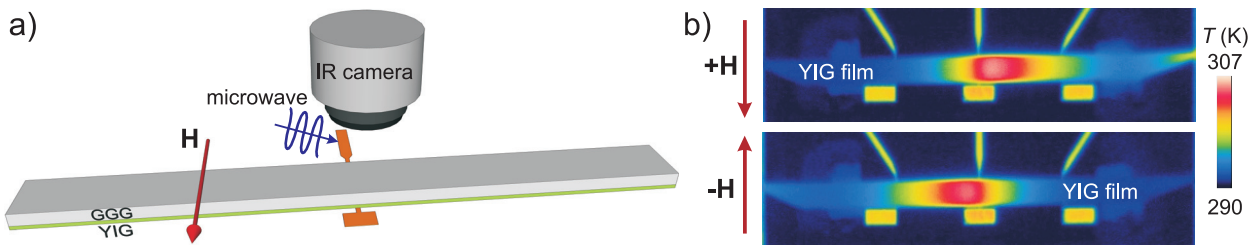

Fig. 1: a) Sketch of the experimental setup for measurements of the thermal distribution in a single-crystal yttrium iron garnet (YIG) film on a gadolinium gallium garnet (GGG) substrate using an infrared camera. b) Thermal images of the YIG/GGG sample with excited magnetostatic surface spin waves (MSSW) for opposite orientations of the bias magnetic field. Microwave frequency $f = 7$ GHz, power $P = 230$ mW, bias magnetic field $H = 1750$ Oe.

The magnetostatic surface spin wave (MSSW) can be excited in the YIG film by the antenna, when the in-plane magnetic field is oriented perpendicularly to the stripe (see Fig. 1a) [6]. The MSSW has an exponential profile of the dynamic magnetization across the YIG thickness. The concentration of the spin-wave intensity on one surface depends on the thickness of the YIG film and it is more pronounced for relative thick films (on the order of tens of micrometers). The direction of propagation of the surface wave depends on the orientation of the magnetic field, a property which is known as the nonreciprocity of surface spin waves [6, 7].

An infrared thermography technique was used to detect the thermal distribution created as a result of the relaxation of coherent spin waves in the film. Thermal images of the YIG/GGG sample, monitored using an infrared camera FLIR SC655, are shown in Fig. 1b for opposite orientations of the bias magnetic field. A strong heating nearby the central microstrip antenna caused by the relaxation of excited surface spin waves can be seen. We obtained an increase of the temperature of 14 K, when the applied microwave power was $P = 230\,\mathrm{mW}$.

The thermal distribution along the YIG/GGG sample is shown in Fig. 2. The temperature of the sample remains equal to the room temperature, when the microwave is switched on but the magnetic field is zero (see solid line in Fig. 2). Once the proper field is applied, the temperature of the sample increases and results in the thermal distribution shown in Fig. 2. The maximal heating was expected at the excitation point, i.e. directly over the microstrip antenna. But the an unsymmetrical distribution with the shift of the temperature maximum Δx was observed in this case (see Fig. 2). The unsymmetry of this distribution can be understood as a result of the interplay between the unidirectional heating by MSSWs and the diffusion of heat into the cold part of the YIG film. It is in an agreement with the nonreciprocal excitation of surface waves [6,7]. Therefore, the direction of the heating can be controlled by changing the orientation of the bias magnetic field.

The temperature maximum $T_{\max}$ as well as its position relative to the excitation antenna Δx were measured as functions of the microwave frequency for the applied power $P = 50\,\mathrm{mW}$ and bias magnetic field $H = 1750\,\mathrm{Oe}$ (see Fig. 3a). These dependencies are shown together with the measured transmission characteristic of magnetostatic surface spin waves in the YIG film for the distance of 6.55 mm (solid line in Fig. 3a).

Unexpectedly, the maximal heating was observed at the end of the MSSW transmission (microwave frequencies around 7.3 GHz), where excited spin waves have relatively small wavelengths (high wavenumbers). At the same time the shift of the temperature maximum Δx is the smallest for this region. This effect can be a result of the decrease of the group velocity for MSSWs with high wavenumbers. The maximal shift of the heat Δx was obtained for the long-wavelength spin waves, which have the highest group velocities. But $T_{\max}$ in this region is small and is comparable with the heating outside of the spin-wave bandwidth due to the forced excitation.

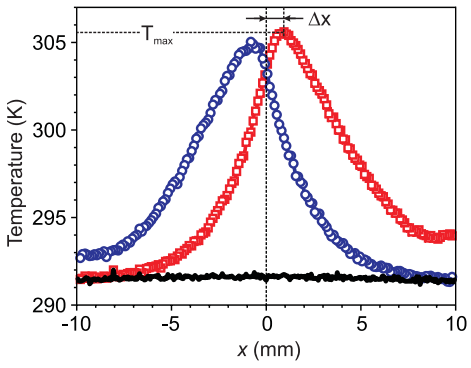

Fig. 2: The heat profile along the center of the YIG/GGG sample for two opposite magnetic fields $H = +1750\,\mathrm{Oe}$ (open squares) and $H = -1750\,\mathrm{Oe}$ (open circles). The solid line corresponds to the heat profile along the sample, when the microwave is switched on but $H = 0\,\mathrm{Oe}$. All other parameters are the same as in Fig. 1b.

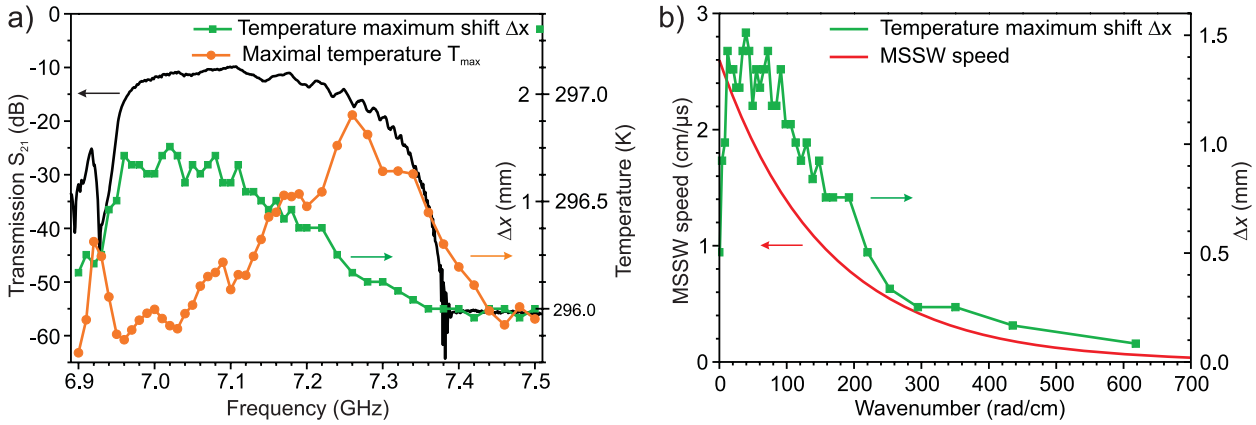

Fig. 3: a) Experimental dependence of the temperature maximum T_{max} in the yttrium iron garnet (YIG) film (circles) and the shift of this maximum Δx relative to the excitation antenna (squares) on the microwave frequency. Applied microwave power $P = 50\,\mathrm{mW}$ and the bias magnetic field $H = 1750\,\mathrm{Oe}$. The measured transmission characteristic of magnetostatic surface spin waves (MSSW) in the YIG film for the distance 6.55 mm is shown as a solid line. b) Shift of the temperature maximum Δx (squares) and the calculated speed of excited surface spin waves (solid line) as functions of the MSSW wavenumber.

In Fig. 3b the shift of the temperature maximum Δx is shown together with the calculated speed of surface spin waves as functions of the excited MSSW wavenumber. It can be seen that the large shift (more than 1 mm) can be observed only for surface spin waves with high group velocity and corresponding small wavenumbers ($< 200\,\mathrm{rad/cm}$). The decrease of the spin-wave group velocity leads to the concentration of heat around the excitation antenna.

The microwave power for the last experiments was decreased to $P = 50\,\mathrm{mW}$. Increasing the applied power leads to the expected growing of the heating effect but also to a decreasing of the shift of the temperature maximum Δx. This can be due to the nonlinear dissipation of strongly excited spin waves, which results in the increase of the heating close to the excitation point.

In conclusion, the infrared thermography technique can be successfully used for the study of interactions between magnon and phonon systems of a magnetic insulator. The presented results demonstrate the unidirectional heating in the YIG sample by magnetostatic surface spin waves. The direction of the heat deposition can be controlled using a bias magnetic field. The temperature maximum and its shift relative to the excitation antenna on the spin-wave wavelength strongly depend on the speed of spin waves.

Financial support by the Deutsche Forschungsgemeinschaft (DFG) within priority program SPP 1538 “Spin Caloric Transport” is gratefully acknowledged.

References

[1] G.E.W. Bauer, E. Saitoh, B.J. van Wees, *Spin caloritronics*, Nature Mater. **11**, 391 (2012).
[2] K. Uchida, J. Xiao, H. Adachi, J. Ohe, S. Takahashi, J. Ieda, T. Ota, Y. Kajiwara, H. Umezawa, H. Kawai, G.E.W. Bauer, S. Maekawa, E. Saitoh, *Spin Seebeck insulator*, Nature Mater. **9**, 894 (2010).
[3] K. Uchida, H. Adachi, T. An, T. Ota, M. Toda, B. Hillebrands, S. Maekawa, E. Saitoh, *Long-range spin Seebeck effect and acoustic spin pumping*, Nature Mater. **10**, 737 (2011).
[4] M. Weiler, M. Althammer, F.D. Czeschka, H. Huebl, M.S. Wagner, M. Opel, I.M. Imort, G. Reiss, A. Thomas, R. Gross, S.T.B. Goennenwein, *Local charge and spin currents in magnetothermal landscapes*, Phys. Rev. Lett. **108**, 106602 (2012).
[5] J. Flipse, F.L. Bakker, A. Slachter, F.K. Dejene, B.J. van Wees, *Direct observation of the spin-dependent Peltier effect*, Nature Nanotech. **7**, 166 (2012).

[6] A.A. Serga, A.V. Chumak, B. Hillebrands, *YIG magnonics*, J. Phys. D: Appl. Phys. **43**, 264002 (2010).
[7] T. Schneider, A.A. Serga, T. Neumann, B. Hillebrands, M.P. Kostylev, *Phase reciprocity of spin-wave excitation by a microstrip antenna*, Phys. Rev. B **77**, 214411 (2008).

4.14 Dynamical heating of a ferrimagnetic sample in a wide range of magnetic fields

T. Langner, V. I. Vasyuchka, M. B. Jungfleisch, A. V. Chumak, A. A. Serga, and B. Hillebrands

In collaboration with T. An and E. Saitoh, Institute for Materials Research, Tohoku University, Sendai 980-8577, Japan.

Since the observation of the spin Seebeck effect [1–4] the influence of heat and temperature gradients on the behavior of a magnetic system has attracted a lot of interest and has even created an own research field [5]. In order to have a full understanding of the interaction between magnetic systems and heat, the self induced generation of heat by magnetic excitations has to be taken into account. It is well known that the excitation of magnetic moments in magnetic materials leads to an absorption of energy and, thus, to heating effects for example by magnon-phonon interaction. This heating is maximal at the ferromagnetic resonance, the state of uniform precession of all magnetic moments, where the absorption of energy is most efficient [6]. The generation of heat by magnetic excitations is widely used, even for medical applications [7, 8]. In polycrystalline materials the magnetic moments are not excited uniformly but every grain shows its own resonance condition. In this Report we show the thermal behavior of a microwave excited disc of polycrystalline yttrium iron garnet (YIG) exposed to an applied external magnetic field. It is shown that this structure has unexpected properties at low fields. When a microwave signal is applied to a sample that is located in a small magnetic field far away from the ferromagnetic resonance field we can see a heating. This heating drops down with increasing magnetic field. Small absorptions of microwave signals for different field values allow us to assume that another very efficient heating mechanism, such as resonant excitation of single grains, is responsible for the observed effects. Local changes of the magnetization due to grains or domain walls can obviously influence the thermal properties of a magnetic structure. In this sense this is an addition to the assumption that domain walls can be moved by a temperature gradient [9].

Figure 1a shows a scheme of the used experimental setup. The investigated sample is either a disc of polycrystalline YIG with a thickness of 500 µm and a diameter of 4 mm or a monocrystalline YIG disc with a thickness of 30 µm and a diameter of 4 mm that is epitaxially grown on a gallium gadolinium garnet (GGG) substrate. The disc is set on top of a 3 mm wide copper strip antenna from which it is electrically and thermally isolated by a thin plastic foam layer. One end of the antenna is connected to a microwave source, the other end is connected to a microwave load to avoid back reflection at the end of the antenna. The applied microwave current creates an Oersted field around the antenna that excites the magnetic moments in the YIG sample. A microwave amplifier is used to apply a power level of about 1 W. An external bias magnetic field is applied parallel to the microstrip antenna. The temperature of the sample was screened by a high-resolution ultrafast (ms range) infrared (IR) camera (FLIR SC 6500). The transmission spectrum measured with a spectrum network analyzer is shown in Fig. 1b.

In the microwave frequency range between 2 GHz and 4 GHz the temperature of the polycrystalline disc shows a dependency of the bias magnetic field as it is shown in Fig. 2a for a microwave frequency of 3.5 GHz. The spatial temperature distribution is considered as homogeneous, so the temperature here is measured in only one point in the center of the structure. Without applied mag-

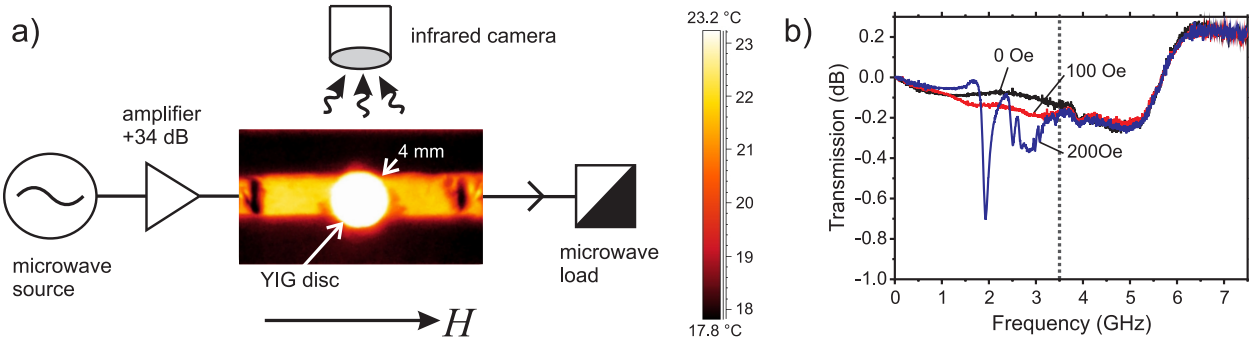

Fig. 1: a) Scheme of the experimental setup with an example of an infrared picture made in the experiment. The output signal of the microwave source is amplified and applied to a copper stripline on which the sample is mounted. The sample here is a polycrystalline YIG disc with a diemater of 4 mm and a thickness of 500 µm. A microwave load absorbs the transmitted microwave signals. The temperature of the disc is screened by an infrared camera. An external magnetic field is applied parallel to the stripline. b) Absorption spectra for the external applied magnetic fields 0 Oe, 100 Oe and 200 Oe. The dashed line shows the absorption at 3.5 GHz.

netic field the temperature of the microwave excited polycrystalline disc rises up to a value that is more than 6 °C higher than the room temperature of 16.5 °C. For higher magnetic fields this heating is almost switched off, i.e. the disc temperature decreases drastically with the highest negative slope at a magnetic field of about 100 Oe. For magnetic fields higher than 200 Oe the temperature stays on a constant level. The heating of the disc for magnetic fields higher than 350 Oe takes place due to better absorption of energy close to the ferromagnetic resonance (FMR) condition.

In every case the absorption of microwaves leads to an excitation of magnetic moments, thus the creation of magnons inside the disc. The decay of these magnons causes an energy transfer to the phonon system and thus to a heating of the disc. Close to the FMR condition the excitation of magnons becomes much more efficient, and the higher total number of decaying magnons leads to a higher energy absorption and thus to a higher temperature by excited phonons due to magnon-phonon interaction [10]. The surprising result is the dynamical generation of heat depending of the external magnetic field for polycrystalline YIG structures in the frequency range between 2 GHz and 4 GHz. Since the absorption of microwaves that might potentially cause a heating is always practically the same for low magnetic fields as it is shown in Fig. 1b, another very efficient mechanism that transmits energy from the magnetic system into the phonon system has to exist. Since we deal with a polycrystalline YIG structure we can assume that the resonant excitation of magnetic moments in the grains that the structure consists of is of crucial importance. Without applied magnetic field the orientation of the magnetic moments in every grain points into a different direction. Each grain is assumed to have a different resonance condition. The interaction between different grains with different local resonance conditions can lead to strong damping effects that produce a lot of heat. For the magnetic field of about 100 Oe where we can see the decrease in temperature the orientations of the magnetic moments in the grains are aligning parallel and thus their interaction shows not that significant production of heat anymore. According to M. Guyot and A. Globus [11] the energy loss during one hysteresis curve cycle in a polycrystalline YIG structure can be calculated in a model formalism. In this formalism a global anisotropy K describes natural stresses specific to the composition of the material. For a deeper understanding the influence of changes in susceptibility by high power microwaves should also be taken into account [12].
The assumption that eigenexcitations of grains in the polycrystalline YIG cause the heating, if there is no field applied, can be confirmed by the fact that the described effects do not appear if we use

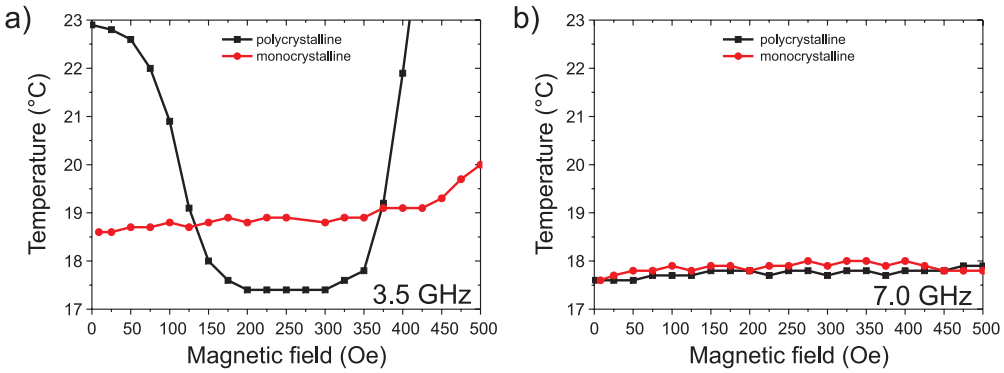

Fig. 2: Temperature of the magnetic disc with respect to the applied external magnetic field. The excitation frequency is a) 3.5 GHz and b) 7.0 GHz. The drop in temperature at about 100 Oe for the polycrystalline disc and an excitation frequency of 3.5 GHz can clearly be seen. The increase after 350 Oe takes place due to higher energy absorption close to the FMR. The difference in the bottom temperature of the monocrystalline and the polycrystalline disc is caused by a different room temperature for both measurements.

a monocrystalline disc instead. In Fig. 2a it is seen that the temperature in this case stays constant independent of the magnetic field. Monocrystalline structures do not consist of grains, nevertheless magnetic domains exist in the case of no external magnetic field. But the effect caused by only their existence is obviously not pronounced. Moreover we see that there is no significant influence of nonlinear effects like three-magnon splitting since this would appear in monocrystalline structures [13] as well. It is seen that the increase in temperature of the monocrystalline disc due to the ferromagnetic resonance starts at a higher field value compared to the temperature increase for the polycrystalline disc. Since the significant heating for low magnetic field values does also not appear for higher excitation frequencies, as it is seen in Fig. 2b for a microwave frequency of 7.0 GHz, it can also likely be explained by the excitations of local resonances in single grains that appear only in the mentioned frequency regime.

Financial support by Deutsche Forschungsgemeinschaft (DFG) within priority program SPP 1538 “Spin Caloric Transport” is gratefully acknowledged.

References

[1] K. Uchida, S. Takahashi, K. Harii, J. Ieda, W. Koshibae, K. Ando, S. Maekawa, E. Saitoh, *Observation of the spin Seebeck effect*, Nature **455**, 778-781 (2008).
[2] K. Uchida, J. Xiao, H. Adachi, J. Ohe, S. Takahashi, J. Ieda, T. Ota, Y. Kajiwara, H. Umezawa, H. Kawai, G.E.W. Bauer, S. Maekawa, E. Saitoh, *Spin Seebeck insulator*, Nature Mater. **9**, 894-897 (2010).
[3] C.M. Jaworski, J. Yang, S. Mack, D.D. Awschalom, J.P. Heremans, R.C. Myers, *Observation of the spin-Seebeck effect in a ferromagnetic semiconductor*, Nature Mater. **9**, 898-903 (2010).
[4] K. Uchida, H. Adachi, T. Ota, H. Nakayama, S. Maekawa, E. Saitoh, *Observation of longitudinal spin-Seebeck effect in magnetic insulators*, Appl. Phys. Lett. **97**, 172505 (2010).
[5] G.E.W. Bauer, E. Saitoh, B.J. van Wees, *Spin caloritronics*, Nature Mater. **11**, 391-399 (2012).
[6] N. Yoshikawa, T. Kato, *Ferromagnetic resonance heating of Fe and Fe_3O_4 by 5.8 GHz microwave irradiation*, J. Phys. D **43**, 425403 (2010).
[7] R. Hergt, S. Dutz, R. Müller, M. Zeisberger, *Magnetic particle hyperthermia: nanoparticle magnetism and materials development for cancer therapy*, J. Phys.: Condens. Matter **18**, S2919-S2934 (2006).
[8] Q.A. Pankhurst, J. Connolly, S. K. Jones, J. Dobson, *Applications of magnetic nanoparticles in biomedicine*, J. Phys. D **36**, R167-R181 (2003).
[9] D. Hinzke, U. Nowak, *Domain wall motion by the magnonic spin Seebeck effect*, Phys. Rev. Lett. **107**, 027205 (2011).

[10] K. P. Sinha, U.N. Upadhyaya, *Phonon-magnon interaction in magnetic crystals*, Phys. Rev. **127**, 432 (1962).
[11] M. Guyot, A. Globus, *Determination of the domain wall energy from hysteresis loops in YIG*, Phys. Stat. Sol. (b) **59**, 447 (1973).
[12] T. Kohane, E. Schlömann, *Longitudinal susceptibility of porous polycrystalline YIG at microwave frequencies*, J. Appl. Phys. **37**, 1073 (1966).
[13] H. Kurebayashi, O. Dzyapko, V. E. Demidov, D. Fang, A.J. Ferguson, S.O. Demokritov, *Controlled enhancement of spin-current transmission by three-magnon splitting*, Nature Mater. **10**, 660-664 (2011).

E. New Materials and Heusler Compounds

Heusler compounds are promising as a new class of materials due to their possible use in the novel field of spin-dependent or *spintronic* devices, such as non-volatile memories with low energy consumption and new types of magnetic sensors. The interest in Heusler compounds comes mainly from the half-metallic character of their spin-split band structure, as predicted by ab-initio calculations for many compounds of this material class. Half-metallic character means that the material provides metallic behavior for electrons with one spin component (e.g. for electrons with spins oriented 'up'), and insulating behavior for the other spin orientation (e.g. for electrons with spins oriented 'down'). These materials may exhibit a 100 % spin polarization at the Fermi level, which would make them ideal candidates for e.g. spin polarizers or spin detectors. Heusler compounds are materials with the very general composition X_2YZ (with X, Y being a transition metal and Z an element from the III-V groups), where each element X, Y, Z can be chosen from 10 different candidates. Hence, the desired properties of the Heusler compounds can be tuned by adjusting their composition. The most well-known example is the group of Co_2YZ compounds showing a large Curie temperature and a large magnetic moment.

Our group is part of an international project, the Japanese-German Research Program "*Advanced Spintronic Materials and Transport Phenomena*" ASPIMATT, which is devoted to develop the foundations for future spintronics. The Heusler compounds play a key role in order to overcome some drawbacks of the conventional 3d ferromagnets, especially when trying to combine spintronics with standard industrial CMOS technologies. Our contribution in ASPIMATT is to explore fundamental issues of nonlinear spin dynamics and spin-wave radiation in Heusler-based microstructures. In this context, an additional property present in some of the Heusler alloys becomes very attractive. A low damping, smaller than for most of the standard 3d ferromagnets (Permalloy, CoFe or CoFeB) has been observed. This allows increased spin-wave propagation distances and opens up the way for the design of new functionalities.

In Report 4.15 a nonlinear generation of higher harmonics from a localized spin-wave edge mode in a micro-structured Heusler waveguide causing the emission of caustic spinwave beams is demonstrated. This is the first observation of the nonlinear emission of higher harmonics from a spatially localized spin-wave mode.

In Report 4.16 an experimental observation of a magnon instability in the Heusler compound $Co_2Mn_{0.6}Fe_{0.4}Si$, which has an outstanding low Gilbert damping is shown. This process can be observed for a wide frequency range of the primary spin waves and is always characterized by a very clear threshold behavior.

E. Neue Materialien und Heusler-Legierungen

Heusler-Verbindungen sind eine vielversprechende Materialklasse aufgrund ihrer möglichen Verwendung für neuartige, den magnetischen Spin nutzende (*spintronische*) Bauteile, z.B. für nichtflüchtige Computerspeicher mit geringem Energiebedarf oder für neue magnetische Sensoren. Aufgrund ihrer spin-aufgespaltenen Bandstruktur zeigen diese synthetischen anorganischen Verbindungen ein halbmetallisches Verhalten: Für eine der beiden Spinorientierungen (z.B. Spin "up") verhält sich das Material wie ein Metall, für die entgegengesetzte Orientierung (z.B. Spin "down") wie ein Isolator. Diese Verbindungen können daher eine vollständige Spinpolarisation an der Fermi-Kante aufweisen. Damit sind Heusler-Verbindungen ideale Kandidaten für Spin-

polarisatoren oder Spindetektoren. Heusler-Verbindungen haben die chemische Struktur X_2YZ, wobei für jedes X, Y, Z aus etwa zehn verschiedenen Elementen des Periodensystems gewählt werden kann. Die gewünschten Eigenschaften der Heusler-Verbindungen können daher durch die geeignete chemische Zusammensetzung eingestellt werden. Die am besten untersuchten Beispiele sind Kobalt-basierende Verbindungen (Co_2YZ). Diese zeigen eine hohe Curie-Temperatur und ein großes magnetisches Moment.

Unsere Arbeitgruppe nimmt an dem internationalen Projekt, der deutsch-japanischen Forschungsgruppe ASPIMATT "*Advanced Spintronic Materials and Transport Phenomena*" teil, deren Hauptziel es ist, die Grundsteine für die Spintronik der Zukunft zu bauen. Heusler-Verbindungen spielen eine sehr wichtige Rolle in dieser Initiative, da einige Nachteile der konventionellen 3d-Ferromagnete sich damit überwinden lassen. Inbesondere können Heusler Verbindungen helfen, die Spintronik mit der etablierten CMOS-Technologie zu kombinieren. Der Beitrag unserer Arbeitsgruppe in ASPIMATT ist die Untersuchung von grundlegenden Fragen der nichtlinearen Spindynamik und der Spinwellenausbreitung in Heuler-basierten Strukturen. In dieser Hinsicht, ist eine zusätzliche Eigenschaft der Heusler-Verbindungen sehr interessant. In einigen Heusler-Verbindungen wurde eine reduzierte Dämpfung bezüglich der 3d-Ferromagneten (z.B. Permalloy, CoFe oder CoFeB) beobachtet. Dies könnte die Ausbreitung von Spinwellen auf größeren Längenskalen erlauben. Damit eröffnet sich eine Vielfalt von neue Anwendungen und Forschungsrichtungen.

In Bericht 4.15 wird über eine nichtlineare Erzeugung höherer Harmonischer aus einer lokalisierten Spinwellen-Randmode in einem mikrostrukturierten Wellenleiter berichtet.

In Bericht 4.16 wird die experimentelle Beobachtung der magnonischen Instabilität in der Heusler-Verbindung $Co_2Mn_{0.6}Fe_{0.4}Si$ beschrieben. Dieser Prozess wird in einem breiten Frequenzbereich der primären Spinwellen beobachtet und ist durch ein Schwellwertverhalten charakterisiert.

4.15 Spin-wave caustic formation by nonlinear higher harmonic radiation from edge modes in a $Co_2Mn_{0.6}Fe_{0.4}Si$ waveguide

T. Sebastian, P. Pirro, T. Brächer, A. A. Serga, and B. Hillebrands

In collaboration with: T. Kubota, WPI Advanced Institute for Materials Research, Tohoku University, Sendai, Japan, and H. Naganuma, M. Oogane, Y. Ando, Department of Applied Physics, Graduate School of Engineering, Tohoku University, Sendai, Japan.

In the last years nonlinear spin dynamics in magnetic microstructures made of metallic ferromagnetic thin films or layer stacks have gained large interest [1–5]. The intrinsically nonlinear Landau-Lifshitz and Gilbert equation (LLG), that governs the spin dynamics, gives rise to a variety of nonlinear effects [6, 7].

Among the metallic ferromagnets, the class of cobalt-based Heusler materials is very promising for perspective *magnon spintronic* devices and the observation of new phenomena of magnonic transport. The reasons for the interest in these materials are the small magnetic Gilbert damping, the high spin-polarization, and the high Curie temperature [8].

As shown recently, the full Heusler compound $Co_2Mn_{0.6}Fe_{0.4}Si$ (CMFS) is a very suitable material to be used as a micro-structured spin-wave waveguide due to the increased decay length which was observed for wave propagation in the linear regime [9]. The reason for this observation is the low Gilbert damping of $\alpha = 3 \times 10^{-3}$ of CMFS compared to $Ni_{81}Fe_{19}$ with $\alpha = 8 \times 10^{-3}$, which is the material commonly used in related studies [8]. The decreased magnetic losses not only lead to an increase of the decay length but also to the pronounced occurrence of a number of nonlinear effects, which can qualitatively change the excitation and propagation characteristics of spin waves. Therefore, the investigation and the thorough understanding of phenomena related to the spin-wave propagation in the nonlinear regime in Heusler compounds is crucial. In addition to the results discussed below, the kinetic instability - a special kind of nonlinear four-magnon scattering - in a CMFS waveguide is addressed in article 4.16.

In this article, we report the nonlinear generation of higher harmonics from a localized spin-wave edge mode [10, 11] in a micro-structured Heusler waveguide causing the emission of caustic spin-wave beams [12, 13]. While higher harmonic generation in general has been investigated before in magnetic microstructures [2, 3], this is the first observation of the nonlinear emission of higher harmonics from a spatially localized spin-wave mode. The emitted spin-wave caustics are characterized by the small transversal aperture of a beam, which practically does not increase during propagation, and the well-defined direction of propagation. The propagation direction of spin-wave caustic beams can be controlled via the externally applied field, which might be a key for the realization of future magnon-spintronic devices based on two-dimensional spin-wave propagation.

A sketch of the sample layout is shown in Fig. 1. The investigated structure comprises a 5 µm wide spin-wave waveguide, patterned from a 30 nm thick film of the Heusler compound CMFS, and a copper antenna with a width of $\Delta x = 1\,\mu m$ placed across the waveguide. Details about the fabrication and the material properties can be found in Refs. [9, 14, 15].

All observations have been carried out using Brillouin light scattering microscopy (µBLS) described in [16] and Section 3.1.

In the following description, the waveguide is positioned in the x-y-plane with the long axis pointing in x-direction. The origin of the coordinate system is given by the position of the antenna

between $x = -1\,\mu m$ and $x = 0\,\mu m$. An external magnetic field of $H_{ext} = 48\,mT$ was applied transversely to the waveguide in y-direction resulting in Damon-Eshbach geometry [17] for spin waves propagating along the waveguide.

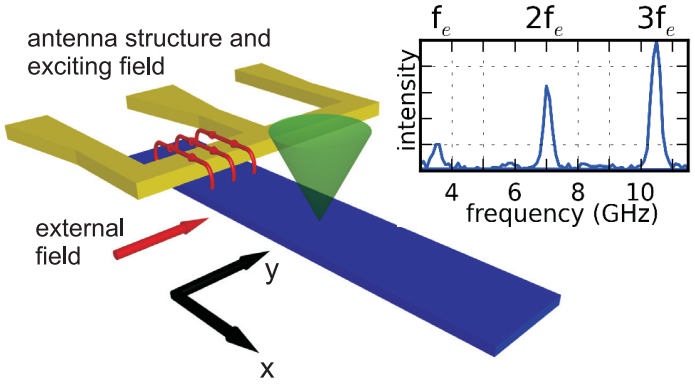

Fig. 1: Sketch of the sample design. The shortened end of a coplanar waveguide is used as an antenna structure to excite spin dynamics in a 5 µm wide CMFS waveguide with a thickness of 30 nm. The external magnetic field is applied transversely to the waveguide. The figure includes a µBLS spectrum taken at a distance of 4.5 µm from the antenna in the center of the waveguide for an excitation frequency of $f_e = 3.5\,GHz$, a microwave power of 20 mW, and an external field $H_{ext} = 48\,mT$.

Together with the sample layout, Fig. 1 shows a µBLS spectrum for an excitation frequency of $f_e = 3.5\,GHz$ and a microwave power of 20 mW at a distance of 4.5 µm from the antenna in the center of the waveguide. The spectrum shows not only a peak at $f_e = 3.5\,GHz$ but also at $2f_e = 7.0\,GHz$ and $3f_e = 10.5\,GHz$. Remarkably, the intensity of the directly excited spin wave at 3.5 GHz is lower than for the higher harmonics at the point of observation. As we will see, this is a consequence of the different propagation characteristics of the observed spin-wave modes. Thus, the intensity ratio varies for different probing positions.

To analyze the higher harmonic generation quantitatively, we investigated their dependencies on the applied microwave power. Figure 2a) shows the results for the directly excited mode and the higher harmonics. The measurements have been performed close to the edge of the waveguide and near the antenna at $x = 0.7\,\mu m$ and $y = 0.8\,\mu m$. The data is presented on a log-log scale with fits according to

$$I_n(p) = A_n p^{s_n} + b \quad , \tag{1}$$

where I_n is the µBLS intensity, A_n a coupling parameter, p the applied microwave power, and b the noise-level in our measurement. As expected, the observed nonlinear processes do not show a threshold power level [2, 3, 7], but reliable detection on the background of the noise is not possible for powers below 5 mW for $f_d = 3f_e = 10.5\,GHz$. The slopes of the curves for the different spin-wave modes n are caused by the different power-laws specified by the exponent s_n. A least square fit of the data yields $s_{1f} = 0.9 \pm 0.1$, $s_{2f} = 2.1 \pm 0.1$, and $s_{3f} = 2.8 \pm 0.3$. These experimental findings close to the integer values 1, 2, and 3 are in accordance with previously reported experimental data and theoretical predictions for the nonlinear generation of higher harmonics [3, 7].

In addition, Fig. 2b) shows the dispersion relation in the center of the CMFS waveguide calculated according to Ref. [18]. The frequencies of the directly excited mode and the higher harmonics are marked by dashed lines. As we can see and in contrast to the frequencies of the higher harmonics, the excitation frequency $f_e = 3.5\,GHz$ is far below the lower cut-off frequency.

To understand the nature of the different spin-wave modes and their intensity ratio shown in Fig. 1, we recorded two-dimensional µBLS intensity maps for the detection frequencies $f_d = f_e$, $f_d = 2f_e$,

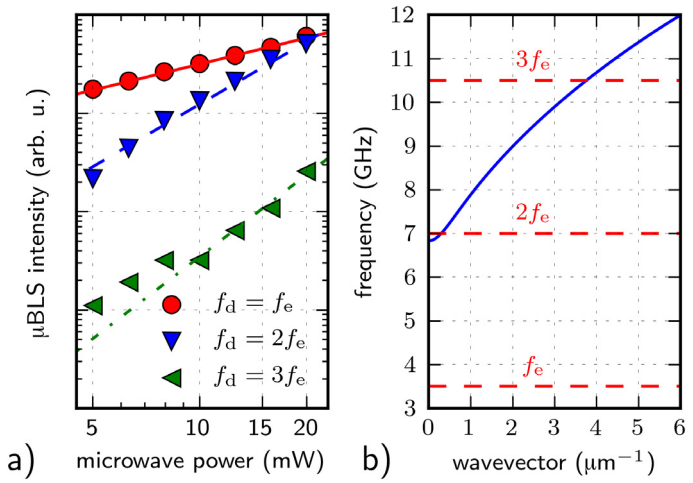

Fig. 2: a) Power dependencies of the μBLS intensity for the detection frequencies $f_d = 3.5\,\text{GHz}$, 7.0 GHz, and 10.5 GHz at a fixed excitation frequency $f_e = 3.5\,\text{GHz}$. Please note the log-log presentation of the data. The lines in the graph correspond to fits according to Eq. 1. These least square fits yield $s_{1f} = 0.9 \pm 0.1$, $s_{2f} = 2.1 \pm 0.1$, and $s_{3f} = 2.8 \pm 0.3$. b) Calculated dispersion relation for the center of the CMFS waveguide according to Ref. [18] as well as excitation frequency f_e and the detection frequencies f_d for the higher harmonics (dashed lines).

and $f_d = 3f_e$. The results are presented in Fig. 3. Figure 3a) reveals a strong localization of the intensity at the edges of the waveguide for $f_d = f_e = 3.5\,\text{GHz}$. This intensity profile is in accordance with the dispersion calculation shown in Fig. 2b) and can be associated with the presence of modes commonly referred to as edge modes [10, 11]. In the center of the waveguide, the assumption of a homogeneous magnetization is a very good approximation. However, the demagnetizing fields created by the magnetization pointing transversely to the waveguide are responsible for a strongly inhomogeneous and decreased effective field near its edges. This field configuration allows for the existence of the localized edge modes energetically far below the spin-wave dispersion for propagating modes in the waveguide.

Figures 3b) and c) show intensity maps for the detection frequencies $f_d = 2f_e = 7.0\,\text{GHz}$ and

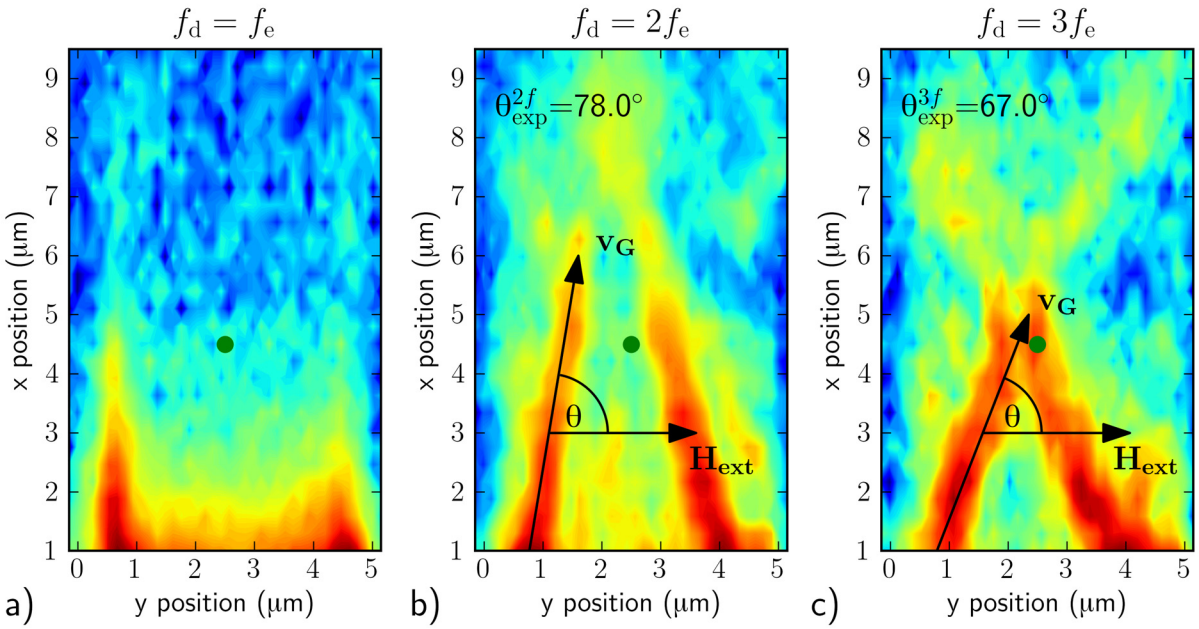

Fig. 3: μBLS intensity distributions for a) $f_d = f_e = 3.5\,\text{GHz}$, b) $f_d = 2f_e = 7.0\,\text{GHz}$, and c) $f_d = 3f_e = 10.5\,\text{GHz}$. While we observed a localized edge mode for $f_d = f_e$, the intensity maps of the higher harmonics show strongly directed spin-wave beams along the angle $\theta = \angle(\mathbf{H_{ext}}, \mathbf{v_G})$. The lines in these maps are guides to the eye to identify the propagation angle θ. The green circles in the graphs indicate the position of the measurement presented in Fig. 1.

$f_d = 3f_e = 10.5\,\mathrm{GHz}$, respectively. In both cases the waves radiated from the position of the edge mode are strongly directed, have a small transversal aperture, and show nondiffractive behavior [13]. The propagation direction of the higher harmonics can be described by using the angle $\theta = \angle(\mathbf{H_{ext}}, \mathbf{v_G})$, formed by the group velocity of the spin waves $\mathbf{v_G}$ and the external field $\mathbf{H_{ext}}$.

These radiation characteristics are responsible for the intensity distribution shown in the spectrum in Fig. 1. The position of the probing point is indicated in the corresponding intensity maps with a green circle. Since the spin wave at $f_d = 3.5\,\mathrm{GHz}$ is localized at the edges of the waveguide, its intensity is comparably weak in the center. In contrast, the higher harmonics have frequencies above the cut-off frequency of the spin-wave dispersion and can propagate in the center of the waveguide supporting the intensity ratio recorded in our measurement.

In the following, we will describe the observed beam formation and propagation directions using the properties of the anisotropic spin-wave dispersion in a magnetic thin film [12, 13, 18]. Because of this anisotropy, the direction of the group velocity $\mathbf{v_G}$ of the investigated spin wave can differ significantly from the direction of its wavevector $\mathbf{k}$. As we will see, the direction of the group velocity can be assumed to be constant for most wavevectors that are excited. This finally leads to the formation of the caustics in our experiment.

Iso-frequency curves $f(k_x, k_y) = const$ can be calculated analytically from the dispersion relation. Calculations for $f = 2f_e = 7.0\,\mathrm{GHz}$ and $f = 3f_e = 10.5\,\mathrm{GHz}$ are illustrated in Fig. 4a) where k_y is shown as a function of k_x. Using this data, we calculate the direction θ of the flow of energy of the spin waves relative to the externally applied field by:

$$\theta = \angle(\mathbf{H_{ext}}, \mathbf{v_G}) = \arctan(v_y/v_x) = \arctan(dk_y/dk_x) \quad . \tag{2}$$

Figure 4b) shows the calculated propagation angle θ in the CMFS waveguide as a function of k_y. The most important feature in the trend of θ is the small variation of $\Delta\theta \leq 2^\circ$ for both frequencies $f = 2f_e$ and $f = 3f_e$. The calculations yield $\theta^{2f}_{calc} = 79^\circ$ and $\theta^{3f}_{calc} = 66^\circ$ as mean values, respectively. The dash-dotted lines in Fig. 4b) represent the propagation angles of the spin-wave beams observed experimentally and shown in Figs. 3b) and c) ($\theta^{2f}_{exp} = 78^\circ$ and $\theta^{3f}_{exp} = 67^\circ$). The comparison of our experimental findings and analytical calculations shows an agreement within the expected accuracy of our measurement setup and is, therefore, supporting our conclusion of the formation of spin-wave caustic beams. Higher harmonics with $k_y \leq 2\,\mu\mathrm{m}^{-1}$ are emitted with strongly varying directions from the edge mode and can be regarded as a negligible background in our measurement.

In summary, we reported the nonlinear higher harmonic generation from a localized spin-wave

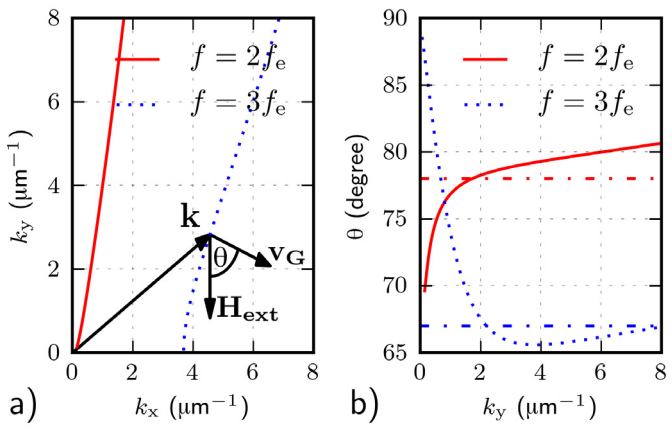

Fig. 4: Analytical calculations according to Ref. [18]. a) Iso-frequency curves $f_{const} = f(k_x, k_y)$ for $f = 2f_e = 7.0\,\mathrm{GHz}$ and $f = 3f_e = 10.5\,\mathrm{GHz}$. Based on these calculations exemplary directions for $\mathbf{k}$, $\mathbf{v_G}$, $\mathbf{H_{ext}}$ and the propagation angle $\theta = \angle(\mathbf{H_{ext}}, \mathbf{v_G}) = \arctan(dk_y/dk_x)$ are shown in the graph. b) Radiation direction θ calculated from the iso-frequency curves shown in a). Dash-dotted lines correspond to the angles θ_{exp} observed in the experiment.

mode in a micro-structured CMFS waveguide leading to the emission of strongly directed spin-wave beams or caustics. All experimental results are in agreement not only with theoretical predictions and related experimental findings but also with our quantitative analysis using the dispersion relation for spin waves in magnetic thin films.

Financial support by the Deutsche Forschungsgemeinschaft Research Unit 1464 and the Strategic Japanese-German Joint Research from JST: ASPIMATT is gratefully acknowledged. Thomas Brächer is supported by a fellowship of the Graduate School Materials Science in Mainz (MAINZ) through DFG-funding of the Excellence Initiative (GSC 266). We thank our colleagues from the *Nano Structuring Center* of the TU Kaiserslautern for their assistance in sample preparation.

References

[1] H. Schultheiss, X. Janssens, M. van Kampen, F. Ciubotaru, S.J. Hermsdoerfer, B. Obry, A. Laraoui, A.A. Serga, L. Lagae, A.N. Slavin, B. Leven, B. Hillebrands, *Direct current control of three magnon scattering processes in spin-valve nanocontacts*, Phys. Rev. Lett. **103**, 157202 (2009).

[2] V.E. Demidov, M.P. Kostylev, K. Rott, P. Krzysteczko, G. Reiss, S.O. Demokritov, *Generation of the second harmonic by spin waves propagating in microscopic stripes*, Phys. Rev. B **83**, 054408 (2011).

[3] V.E. Demidov, H. Ulrichs, S. Urazhdin, S.O. Demokritov, V. Bessonov, R. Gieniusz, A. Maziewski, *Resonant frequency multiplication in microscopic magnetic dots*, Appl. Phys. Lett. **99**, 012505 (2011).

[4] H.T. Nembach, K.L. Livesey, M.P. Kostylev, P. Martin-Pimentel, S.J. Hermsdoerfer, B. Leven, J. Fassbender, B. Hillebrands, *Magneto-optical observation of four-wave scattering in a 15-nm $Ni_{81}Fe_{19}$ film during large-angle magnetization precession*, Phys. Rev. B **84**, 184413 (2011).

[5] H. Schultheiss, K. Vogt, B. Hillebrands, *Direct observation of nonlinear four-magnon scattering in spin-wave microconduits*, Phys. Rev. B **86**, 054414 (2012).

[6] T.L. Gilbert, *A phenomenological theory of damping in ferromagnetic materials*, IEEE T. Magn. **40**, 3443 (2004).

[7] A.G. Gurevich, G.A. Melkov, *Magnetization oscillations and waves*. Boca Raton, FL: CRC (1996).

[8] S. Trudel, O. Gaier, J. Hamrle, B. Hillebrands, *Magnetic anisotropy, exchange and damping in cobalt-based full-Heusler compounds: an experimental review*, J. Phys. D: Appl. Phys. **43**, 193001 (2010).

[9] T. Sebastian, Y. Ohdaira, T. Kubota, P. Pirro, T. Brächer, K. Vogt, A.A. Serga, H. Naganuma, M. Oogane, Y. Ando, B. Hillebrands, *Low-damping spin-wave propagation in a micro-structured $Co_2Mn_{0.6}Fe_{0.4}Si$ Heusler waveguide*, Appl. Phys. Lett. **100**, 112402 (2012).

[10] G. Gubbiotti, M. Conti, G. Carlotti, P. Candeloro, E.D. Fabrizio, K.Y. Guslienko, A. André, C. Bayer, N. Slavin, *Magnetic field dependence of quantized and localized spin wave modes in thin rectangular magnetic dots*, J. Phys. Cond. Matt. **16**, 7709 (2004).

[11] C. Bayer, J.P. Park, H. Wang, M. Yan, C.E. Campbell, P.A. Crowell, *Spin waves in an inhomogeneously magnetized stripe*, Phys. Rev. B **69**, 134401 (2004).

[12] V.E. Demidov, S.O. Demokritov, D. Birt, B. O'Gorman, M. Tsoi, X. Li, *Radiation of spin waves from the open end of a microscopic magnetic-film waveguide*, Phys. Rev. B **80**, 014429 (2009).

[13] T. Schneider, A.A. Serga, A.V. Chumak, C.W. Sandweg, S. Trudel, S. Wolff, M.P. Kostylev, V.S. Tiberkevich, A.N. Slavin, B. Hillebrands, *Nondiffractive subwavelength wave beams in a medium with externally controlled anisotropy*, Phys. Rev. Lett. **104**, 197203 (2010).

[14] T. Kubota, S. Tsunegi, M. Oogane, S. Mizukami, T. Miyazaki, H. Naganuma, Y. Ando, *Half-metallicity and Gilbert damping constant in $Co_2Fe_xMn_{1-x}Si$ Heusler alloys depending on the film composition*, Appl. Phys. Lett. **94**, 122504 (2009).

[15] M. Oogane, T. Kubota, Y. Kota, S. Mizukami, H. Naganuma, A. Sakuma, Y. Ando, *Gilbert magnetic damping constant of epitaxially grown Co-based Heusler alloy thin films*, Appl. Phys. Lett. **96**, 252501 (2010).

[16] V.E. Demidov, S.O. Demokritov, B. Hillebrands, M. Laufenberg, P.P. Freitas, *Radiation of spin waves by a single micrometer-sized magnetic element*, Appl. Phys. Lett. **85**, 2866 (2004).

[17] R.W. Damon, J.R. Eshbach, *Magnetostatic modes of a ferromagnet slab*, J. Phys. Chem. Solids **19**, 308 (1961).

[18] B. Kalinikos, A. Slavin, *Theory of dipole-exchange spin wave spectrum for ferromagnetic films with mixed exchange boundary conditions*, J. Phys. C: Solid State **19**, 7013 (1986).

4.16 Nonlinear magnon instability in Heusler waveguides

P. Pirro, T. Sebastian, T. Brächer, A. A. Serga, and B. Hillebrands

In collaboration with: D. Bozhko and G. A. Melkov, Department of Radiophysics, National Taras Shevchenko University of Kyiv, Kyiv, Ukraine, T. Kubota, WPI Advanced Institute for Materials Research, Tohoku University, Sendai, Japan, H. Naganuma, M. Oogane, Y. Ando, Departement of Applied Physics, Graduate School of Engineering, Tohoku University, Sendai, Japan.

The huge market for devices communicating with microwave frequencies in the GHz range creates a demand for inexpensive, highly efficient and miniaturized microwave processors, which can be based on micro-structured spin-waves devices. In addition, computational devices working with spin waves as information carriers [1] can be combined with recently discovered phenomena like the spin Hall effect to form the new class of *magnon spintronic* devices. To successfully develop this area further, the class of Cobalt-based Heusler materials is of great interest as the small magnetic Gilbert damping allows for a long spin-wave lifetime and propagation length. But one has to consider that, as this damping extrinsic to the spin-wave system is less pronounced, the importance of the intrinsic damping (the magnon-magnon redistribution) increases. It has been shown that due to the intrinsic nonlinearity of the Landau-Lifshitz and Gilbert equation, which is governing the spin dynamics in magnetic elements, the nonlinear spin-wave interaction can become the dominant relaxation process also for ferromagnetic metals [2, 3]. Thus, a development of new low Gilbert damping materials calls for a study of the occurring nonlinear spin-wave instabilities as they will be the dominating energy redistribution process.

In this Report we present the experimental observation of a magnon instability in the Heusler compound $Co_2Mn_{0.6}Fe_{0.4}Si$ (in the following referred to as CMFS), which has an outstanding low Gilbert damping ($\alpha = 0.003$) and a high saturation magnetization ($M_s = 1003\,\mathrm{kA/m}$, for details see [4] and [5]) leading to a good coupling to external excitation with dynamic magnetic fields and to high oscillation amplitudes. We observe and characterize a second-order instability [6–9] of

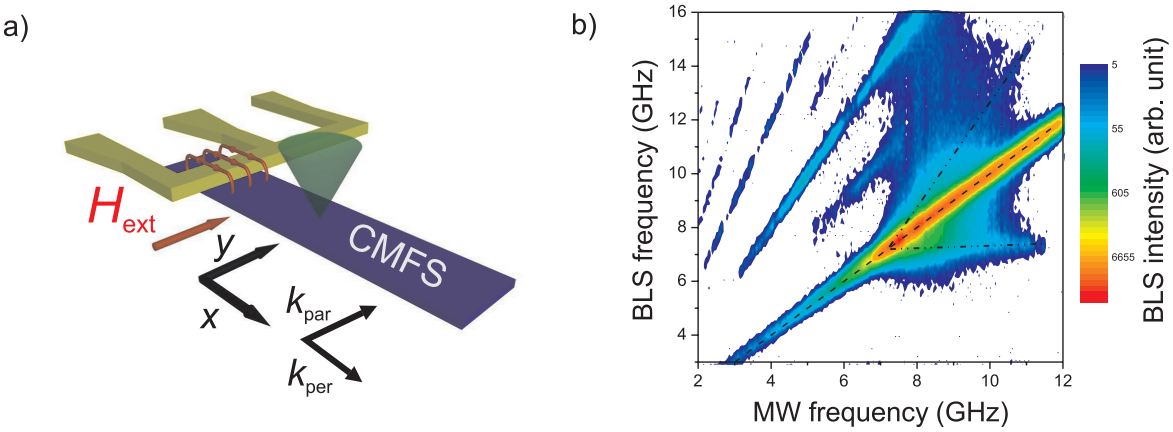

Fig. 1: a) Schematic view of the investigated sample: spin-waves in a 5 µm wide waveguide of CMFS are excited by means of a 1 µm wide Ti/Cu antenna which is connected to a microwave source via a coplanar waveguide. An external magnetic field of 48 mT is applied perpendicular to the waveguide's long axis. b) BLS spectra as function of the applied microwave frequency f_{MW} for a microwave power of 13 dBm. The direct excitation is marked with the dashed lines, the dash-dotted lines are a guide to the eye indicating the frequencies of the four-magnon instability with the lowest threshold.

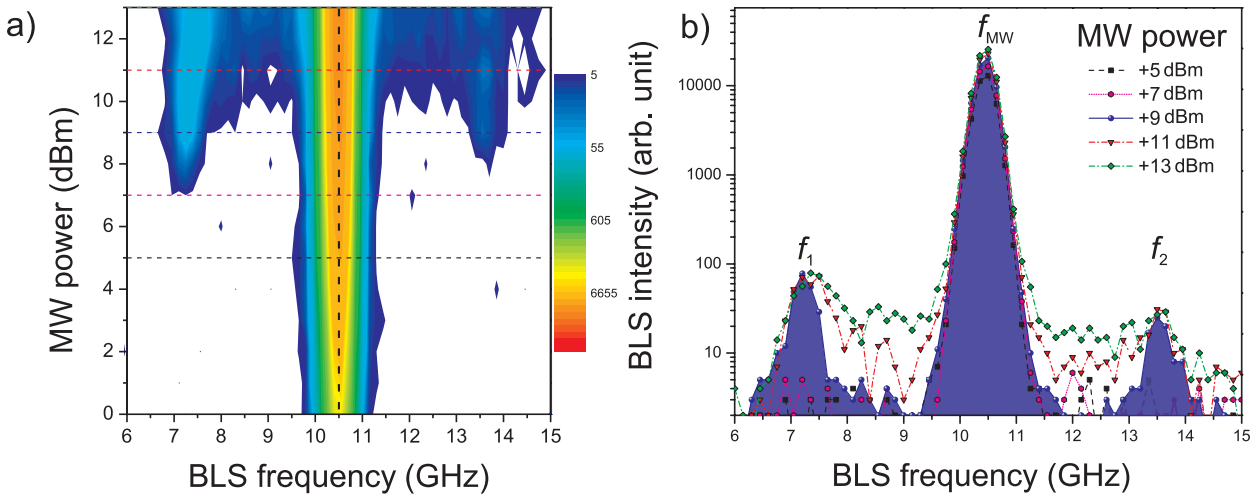

Fig. 2: a) BLS spectra for $f_{MW} = 10.5\,GHz$ at different microwave powers (external field of 48 mT). The spectra marked with horizontal lines are shown in b), where the spectrum just above threshold (at 9 dBm) is shown as a filled curve. It can be clearly seen that for supercritical powers (higher than 9 dBm), the spectrum gets continuously broadened and a small shift of the peak frequency f_1 can be observed.

propagating spin-waves with frequency f_{MW} (also referred to as primary magnons) in which two magnons at f_{MW} scatter into two different spin-wave modes with well defined frequencies f_1 and f_2 (also referred to as secondary magnons). This process is often also labeled as four-magnon-scattering. In the CMFS waveguide, the frequency of the mode f_1 always stays in the vicinity of the ferromagnetic resonance frequency f_{FMR}, whereas the mode f_2 adjusts its frequency to fulfill energy conservation according to $2f_{MW} = f_1 + f_2$.

The experimental design is shown in Fig. 1a: A 5 µm wide CMFS waveguide (30 nm thick) with a capping layer of Ta (5 nm) has been patterned by electron-beam lithography and argon ion beam etching. Then, a w_a =1 µm wide antenna (made of Ti/Cu) has been produced on top of the waveguide by electron beam evaporation and lift off. A microwave current with variable frequency is passed through the antenna to create dynamic magnetic Oersted fields which consequently excite coherent spin waves propagating in the CMFS waveguide. We detect the resulting spin-wave manifold by Brillouin light scattering microscopy (BLS) [10]. Figure 1b shows the detected BLS spectrum for a systematic variation of the frequency f_{MW} of the microwave current (applied power approximately +13 dBm). The static external magnetic field (in the following fixed to $\mu_0 H_{ext} = 48\,mT$) which is applied perpendicular to the waveguide's long axis as depicted in Fig. 1a allows for the efficient excitation of spin waves propagating perpendicular to H_{ext} (commonly labeled as Damon-Eshbach spin waves). Using a spectrum analyzer and frequency dependent microwave filters, we make sure that our microwave source delivers a single-frequency signal (all other spectral components are suppressed by at least 90 dB).

Different types of excitations can be distinguished in Fig. 1b): the direct excitation ($1f$, spin waves with the frequency f_{MW}, marked by the dashed line) and the second-order instability (between approximately $7 - 12\,GHz$, dash-dotted lines are guides to the eye). In addition, higher harmonics with spin-wave frequencies equal to integer multiples ($2f$ to $4f$) and half-integer multiples ($1.5f$ and $2.5f$) of the external excitation frequency can be found. These integer harmonics are treated in article 4.15 of this Report and are not connected to the four-magnon instability process discussed here.

First, we want to discuss briefly the peculiarities of the $1f$ excitation (see Fig. 1b). Under a

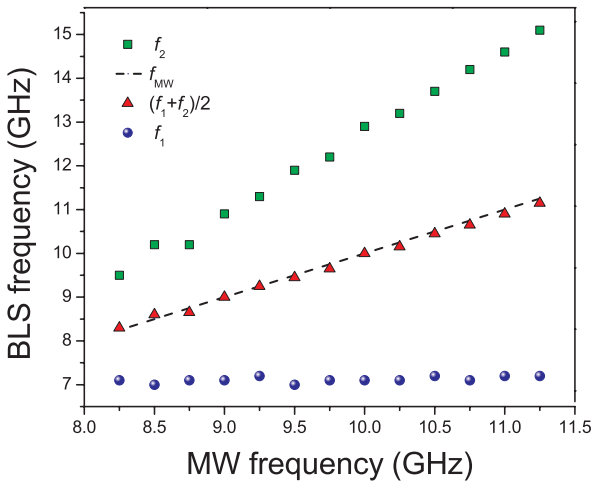

Fig. 3: The frequencies f_1 and f_2 of the secondary magnons (circles and squares, respectively) as function of the microwave frequency f_{MW} at the threshold power. f_1 is practically independent of f_{MW} and constant at $f_1 \approx 7.2\,\text{GHz}$, while f_2 increases linearly with f_{MW}. The mean energy of the two secondary magnons (triangles) agrees with the mean energy of the primary magnons (f_{MW}, dashed line) within the experimental accuracy, proving that energy conservation $2f_{MW} = f_1 + f_2$ is fulfilled.

minimum frequency $f_{min} \approx 6.5\,\text{GHz}$ the excitation stays rather weak compared to its maximum intensity. f_{min} can be correlated with the low-frequency limit of the spin-wave dispersion which is calculated using the analytical theory developed in Ref. [11] with an effective field value obtained from a micromagnetic simulation ($B_{eff} = 46\,\text{mT}$, using oommf [12], material parameters: saturation magnetization $M_s = 1003\,\text{kA/m}$, exchange constant $A_{ex} = 11\,\text{pJ/m}$, cubic anisotropy field $K_1/M_s \approx 2\,\text{mT}$). Thus, spin waves with $f_{SW} < f_{min}$ are no Eigenstates of the magnetic system in the small perturbation limit but forced oscillations due to the strong external excitation.

Now, we will focus our discussion on the second-order spin-wave instability. The scan of the microwave frequency shown in Fig. 1b provides a good overview of the different magnon-magnon processes, but to study the four-magnon process in detail, it is more convenient to change the microwave power at a fixed frequency. The reason to proceed in this way is that our antenna excites increasing spin-wave frequencies above f_{FMR} with a decreasing efficiency (see Ref. [13] for details) until the first local minimum of the excitation is reached for $k_{per} = 2\pi/w_a$ (in our case, $f(k_{per} = 2\pi/w_a) > 12\,\text{GHz}$). As a consequence, sweeping the microwave frequency, as shown in Fig. 1b, leads to a change of the amplitude of the directly excited spin-wave mode ($1f$), and thus to mixing of different sub- or super-critical regimes regarding the threshold of the four-magnon splitting process. For example, in Fig. 1b) one can see the subcritical regime ($12 - 11.5\,\text{GHz}$), the regime where the directly excited spin-wave amplitude just reaches the threshold of the four-magnon splitting ($11.5 - 10.5\,\text{GHz}$) and the supercritical regime where multiple spin-wave modes become unstable ($10.5 - 7.5\,\text{GHz}$). To further illustrate the influence of the applied power, Fig. 2 shows the BLS spectra at an excitation frequency $f_{MW} = 10.5\,\text{GHz}$ for different power levels. In Fig. 2b it is clearly visible that the spin-wave amplitude is subcritical at 5 dBm. The amplitude reaches the instability threshold for 9 dBm (filled curve) and two clearly defined peaks at f_1 and f_2 appear. For even higher powers, an continuum of spin-wave frequencies between f_1 and f_2 is found, whereas the intensities of the peaks at f_1 and f_2 are saturated. This almost continuously broadened spectrum resembles the results of Ref. [14], where no distinct mode with lowest threshold has been reported.

Several characteristics of a magnon-magnon instability process are predicted [15]: the intensity of the secondary spin waves increases drastically if a critical number of primary magnons has been exceeded (threshold behavior) and the scattering process conserves the energy of the magnons. In addition, the momentum (wavevector) of the magnons is conserved for those directions with an unbroken translational invariance. In this Report, we will mainly address the threshold behavior and the energy conservation.

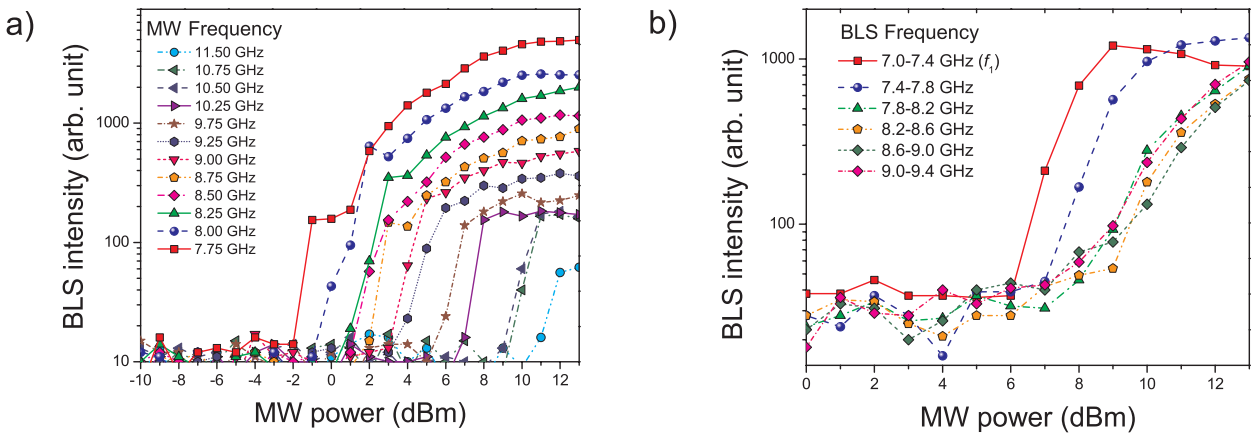

Fig. 4: a) BLS intensity at the frequency $f_1 = 7.2\,\mathrm{GHz}$ (integrated over an interval of 0.5 GHz) as a function of microwave power for different microwave frequencies f_{MW}. A clear threshold behavior of the signal at f_1 followed by a saturation process can be found for every frequency f_{MW} of the initially injected spin waves. b) BLS intensity for different parts of the spectrum at fixed $f_{\mathrm{MW}} = 10.25\,\mathrm{GHz}$ as a function of microwave power. For the frequency interval $(7.4 - 7.8\,\mathrm{GHz})$ just above the mode f_1, the threshold power is increased but the slope with which the intensity increases at the threshold is similar compared to f_1. The parts of the spectrum at even higher frequencies $(7.8 - 9.0\,\mathrm{GHz})$ all show a common threshold and an almost identical slope.

Figure 3 shows the evolution of the frequencies f_1 and f_2 as function of the frequency of the primary spin waves (f_{MW}). These frequencies are obtained just at the threshold power of the instability which depends on the particular f_{MW} as already mentioned above. It is remarkable that f_1 is almost independent of f_{MW}. This indicates that the mode at f_1 features a reduced effective damping compared to competitive modes or an enhanced coupling for the four-magnon interaction. Concerning the mode at f_2, a linear increase with f_{MW} can be observed, which is necessary to conserve the total energy. This energy conservation is demonstrated by comparing the mean energy of the primary magnons with the mean energy of the secondary magnons. The perfect agreement for all f_{MW} within the accuracy of the experimental setup proves that energy conservation is fulfilled in all cases.

The threshold character of the instability has already been addressed shortly for one microwave frequency in Fig. 2. As the frequency f_1 is found to be constant (see Fig. 3), we can easily analyze the threshold behavior for the spin waves at f_1 in more detail as a function of f_{MW} as shown in Fig. 4a). A clear threshold behavior followed by a saturation of the spin-wave intensity can be found for all f_{MW} in the range $7.75 - 11.5\,\mathrm{GHz}$, supporting our interpretation that the mode f_1 has the minimum threshold and that the instability occurs in a similar manner for the whole

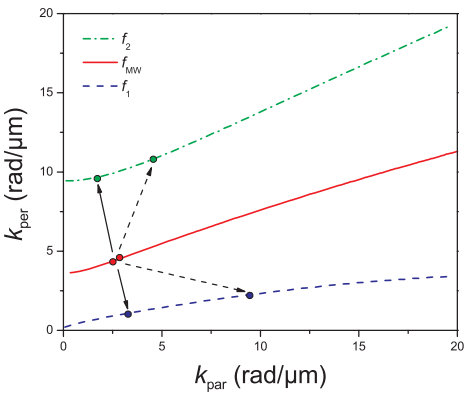

Fig. 5: First quadrant of the isofrequency curves for the experimental conditions of Fig. 2: $f_1 = 7.2\,\mathrm{GHz}$ (dashed line), $f_{\mathrm{MW}} = 10.5\,\mathrm{GHz}$ (solid line), $f_2 = 13.8\,\mathrm{GHz}$ (dashed-dotted line). Two possible four-magnon-splitting processes of two magnons at f_{MW} are schematically illustrated with arrows. In both examples, the wavevectors $\mathbf{k}$ of the primary magnons are assumed parallel, whereas k_{per} of the secondary magnons are in both cases antiparallel. The k_{par} components of the secondary magnons are antiparallel for the splitting indicated with dashed arrows.

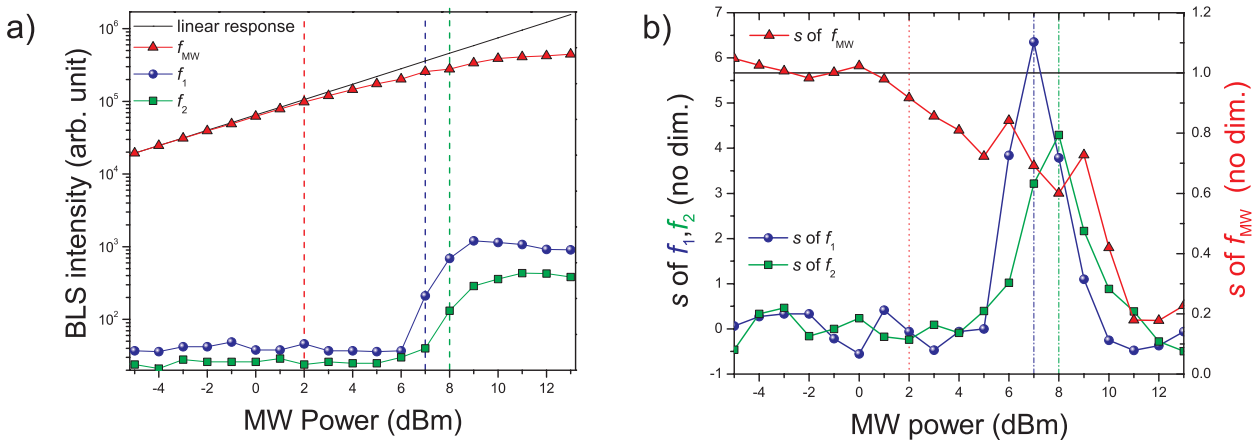

Fig. 6: a) BLS intensity as a function of the applied microwave power for a fixed microwave frequency $f_{MW} = 10.25\,\text{GHz}$ ($f_1 = 7.2\,\text{GHz}$, $f_2 = 13.3\,\text{GHz}$). The intensity at f_{MW} deviates from a linear increase with power (straight solid line) at around 2 dBm whereas the intensity at f_1 and f_2 develops only at 7 dBm. The same behavior can be observed in b), where the slope s of the logarithmic intensity is shown. In this representation, $s = 1$ corresponds to a linear increase of the intensity with microwave power.

mentioned frequency range. Proceeding similarly to Ref. [13], we verified that the increase of the threshold power with f_{MW} scales with the decrease of the excitation efficiency of the primary spin waves. Thus, the critical amplitude of the primary spin waves is independent of f_{MW} within the accuracy of our measurement. In contrast, Fig. 4b shows the threshold behavior of different parts of the spin-wave spectrum for a fixed $f_{MW} = 10.25\,\text{GHz}$. The spin-waves with frequencies near $f_1 = 7.2\,\text{GHz}$ have the lowest threshold as mentioned above, then the waves at slightly higher frequencies get unstable. For frequencies above 7.8 GHz, the threshold behavior is less pronounced and the threshold power stays constant. As the increase of the magnon density in this frequency interval is uniform in frequency and correlates well with the pronounced saturation of the intensity of the lowest threshold mode f_1, we can assume that these states are populated by magnons scattered from the initially generated f_1, f_2 and f_{MW}-modes in multistep four-magnon collisions. These supercritical processes lead to the homogenous broadening shown in Fig. 2b).

To summarize our discussion up to this point, we have proven that the instability exhibits a pronounced threshold behavior, conserves energy, and that a particular mode f_1 has the lowest threshold for this process. The remaining conservation law, the conservation of the spin-wave momentum (wavevector), cannot be verified as easily, as wavevector resolved measurements are not possible in our experimental situation. Also the approximative approach to consider only one transversal waveguide mode and to assume a linear dispersion (see [14]) is not appropriate here, as the group velocity in the CMFS waveguide varies by more than a factor of two in the investigated frequency range, clearly demonstrating that a linear approximation of the dispersion law is inadequate. A more general way to verify whether the wave vector conservation can be fulfilled is to calculate the isofrequency curves for the observed frequencies (see Fig. 5), here demonstrated exemplarily for the experimental conditions given in Fig. 2. The next steps are to determine if the scattering process to the f_1 and f_2-modes is a one- or multi-step process and then to search for possible combinations that conserve the total magnon momentum. A first evidence that the described scattering is indeed a multi-step process is presented in Fig. 6. The intensity of the spin-waves at f_{MW}, f_1 and f_2 (Fig. 6a) and their slopes s (Fig. 6b, $s = \partial \log(I)/\partial \log(P)$, where I is the spin-wave intensity and P is the microwave power) indicate that a first nonlinearity process sets in at a microwave power near 2 dBm, whereas the increase of the spin-wave signal at f_1 and f_2 occurs at significantly higher

powers. This first nonlinearity process might be interpreted as a parametric four-magnon instability, which forms a condensate of phase correlated magnon pairs at the frequency of the directly excited spin wave f_{MW} [6, 8]. Due to this frequency degeneration, these waves cannot be resolved separately by our setup. As the magnons emerging from this process are phase correlated but incoherent, the following second instability can only be understood as a kinetic instability [16] which would preferably populate the mode with the lowest effective damping at f_1 and the corresponding mode f_2 to satisfy energy conservation.

To conclude, we have demonstrated that spin waves which are excited in the low-damping Heusler compound $Co_2Mn_{0.6}Fe_{0.4}Si$ undergo, among others, a pronounced four-magnon instability. This process can be observed for a wide frequency range of the primary spin waves and is always characterized by a very clear threshold behavior. In this Heusler waveguide one particular mode f_1, whose frequency is roughly independent of the frequency of the primary spin waves, has the lowest threshold for the instability. The conservation of energy in the scattering process has been verified by proofing that $2f_{MW} = f_1 + f_2$ is always fulfilled. For supercritical spin-wave amplitudes, more and more modes become unstable and the spectrum broadens homogeneously over a range of several Gigahertz. However, a further analysis dealing with the details of the instability concerning the wave vector conservation and the peculiarities of the lowest threshold mode f_1 is still needed.

We thank the *Nano Structuring Center* of the TU Kaiserslautern for assistance in sample preparation. Financial support by the Deutsche Forschungsgemeinschaft Research Unit 1464 and the Strategic Japanese-German Joint Research from JFT: ASPIMATT is gratefully acknowledged. P. Pirro acknowledges financial support by the Carl-Zeiss-Stiftung via the OPTIMAS Carl-Zeiss doctoral program. T. Brächer is supported by a fellowship of the Graduate School Materials Science in Mainz (MAINZ) through DFG-funding of the Excellence Initiative (GSC 266).

References

[1] A. Khitun, M. Bao, K.L. Wang, *Spin wave magnetic nanofabric: A new approach to spin-based logic circuitry* IEEE Trans. Magn. **44** (9), 2141-2152 (2008).

[2] A.Yu. Dobin, R.H. Victora, *Intrinsic nonlinear ferromagnetic relaxation in thin metallic films* Phys. Rev. Lett. **90**, 167203 (2003).

[3] A.Yu. Dobin, R.H. Victora, *Intrinsic nonlinear ferromagnetic relaxation (invited)* J. Appl. Phys. **95**, 7139 (2004).

[4] T. Sebastian, Y. Ohdaira, T. Kubota, P. Pirro, T. Brächer, K. Vogt, A.A. Serga, H. Naganuma, M. Oogane, Y. Ando, B. Hillebrands, *Low-damping spin-wave propagation in a micro-structured $Co_2Mn_{0.6}Fe_{0.4}Si$ Heusler waveguide*, Appl. Phys. Lett. **100**, 112402 (2012).

[5] T. Kubota, S.Tsunegi, M. Oogane, S. Mizukami, T. Miyazaki, H. Naganuma, Y. Ando, *Half-metallicity and Gilbert damping constant in $Co_2Fe_xMn_{1-x}Si$ Heusler alloys depending on the film composition* Appl. Phys. Lett. **94**, 122504 (2009).

[6] H. Suhl, *The theory of ferromagnetic resonance at high signal powers*, J. Phys. Chem. Solids. **1**, 209 (1957)

[7] S.Y. An, P. Krivosik, M.A. Kraemer, H.M. Olson, A.V. Nazarov, C.E. Patton, *High power ferromagnetic resonance and spin wave instability processes in Permalloy thin films*, J. Appl. Phys. **96**, pp. 1572 (2004).

[8] H.M. Olson, P. Krivosik, K. Srinivasan, C.E. Patton, *Ferromagnetic resonance saturation and second order Suhl spin wave instability processes in thin Permalloy films*, J. Appl. Phys. **102**, 023904 (2007).

[9] P. Kabos, C.E. Patton, G. Wiese, A.D. Sullins, E.S. Wright, L. Chen, *Butterfly curves and critical modes for second-order spin-wave instability processes in yttrium iron garnet films*, J. Appl. Phys. **80**, pp. 3962 (1996).

[10] V. E. Demidov, S. O. Demokritov, B. Hillebrands, M. Laufenberg, and P. P. Freitas, *Radiation of spin waves by a single micrometer-sized magnetic element*, Appl. Phys. Lett. **85**, 2866 (2004).

[11] B.A. Kalinikos, A.N. Slavin, *Theory of dipole-exchange spin wave spectrum for ferromagnetic films with mixed exchange boundary conditions*, Journal of Physics C: Solid State Physics, **19**, 7013 (1986).

[12] M. J. Donahue and D. G. Porter, Interagency Report NISTIR **6376**, National Institute of Standards and Technology, Gaithersburg, MD (Sept 1999).

[13] P. Pirro, T. Brächer, K. Vogt, B. Obry, H. Schultheiss, B. Leven, B. Hillebrands, *Interference of coherent spin waves in micron-sized ferromagnetic waveguides*, Phys. Stat. Sol. B **248**, No. 10, 2404-2408 (2011).
[14] H. Schultheiss, K. Vogt, B. Hillebrands, *Direct observation of nonlinear four-magnon scattering in spin-wave microconduits*, Phys. Rev. B **86**, 054414 (2012).
[15] R.M. White, M. Sparks, *Ferromagnetic relaxation. III. Theory of instabilities*, Phys. Rev. **130**, 632 (1963).
[16] A.V. Lavrinenko, V.S. L´vov, G.A. Melkov, V.B. Cherepanov,*"Kinetic"instability of a strongly nonequilibrium system of spin waves and tunable radiation of a ferrite*, JETP **54**(3), 542 (1981).

F. Applied Spintronics

A substantial part of our research is devoted to fields that have a close relation to applications. Our group is aiming to intensify the communication flow between the academic and the industrial world in order to promote the necessary transfer of technology and *know-how*. Since beginning of the year 2012 we are taking part in the industrial collaboration project STeP (Spintronic Technology Platform) funded by the Ministerium für Bildung, Wissenschaft, Weiterbildung und Kultur in Rhineland-Palatinate in the frame of the European EFRE-Program. The Platform is built jointly with the industrial partner Sensitec, Mainz, and the Johannes Gutenberg University Mainz. Among its main goals, one can cite the generation of new capabilities in the field of spintronics, the construction of a R&D infrastructure directed to small and medium enterprises in Rhineland-Palatinate together with the innovation in GMR and TMR technologies with a strong emphasis on the use of industrial production lines for the creation and testing of new sensor concepts. In this project we contribute to the design and testing of new sensor concepts, the material characterization, especially of Heusler thin films and in other subjects.

In Report 4.17 the principle of fabrication of high-density magnetic storage media by applying low-dose focused ion beam irradition is demonstrated. The possibilities of improving this method is discussed using micromagnetic simulations.

In Report 4.18 a characterization of amorphous thin films of the alloy CoFeB is presented. The dynamical and quasi-static switching properties of the films are studied. This alloy is of capital importance for spintronic applications.

In Report 4.19 we present the main characteristics of our optical bridge MOKE detectors. Sensitivity, noise level and other relevant properties are presented.

F. Angewandte Spin Dynamik

Ein wesentlicher Teil unserer Aktivitäten ist auf anwendungsorientierte Forschung gerichtet. Unsere Gruppe versucht Brücken zwischen der akademischen und der industriellen Welt zu bauen, um den Technologietransfer und den Ideenaustausch zu fördern. Seit Anfang 2011 nehmen wir an der Spintronik-Technologie-Plattform (STeP) teil, finanziert vom Ministerium für Bildung, Wissenschaft, Weiterbildung und Kultur in Rheinland-Pfalz im Rahmen des europäischen EFRE-Programms. Dieses Projekt ist eine Zusammenarbeit zwischen der TU Kaiserslautern, der Universität Mainz und dem Industriepartner Sensitec, der große Erfahrung in der Sensorik und in den praktischen Anwendungen der Spintronik gesammelt hat. Als Hauptziele der Plattform kann man unter andere folgende erwähnen: den Aufbau neuer Kompetenzen auf dem Gebiet der Spintronik, die Bereitstellung der Forschungsinfrastruktur und des anwendungsorientiertem universitären *Know-How* besonders für KMUs in Rheinland-Pfalz und die Förderung von Innovation im Bereich der GMR und TMR-Technologien. Unsere Aufgabe besteht unter anderen darin, das Design neuer Sensoren mit mikromagnetischen Simulationen zu unterstützen und die Charakterisierung von Heusler-Dünnschichtsystemen vorzunehmen.

Im Bericht 4.17, wird das Prinzip der Herstellung einer neuen Art von Datenträgern mit sehr großen Speicherdichten vorgestellt. Der Datenträger wird durch Ionenbestrahlung hergestellt. Die Möglichkeiten dieses Verfahren weiterzuentwickeln werden mittels mikromagnetischer Simulationen analysiert.

Im Bericht 4.18, wird die Charakterisierung von dünnen CoFeB Schichten vorgestellt. Die dynamischen und quasi-statischen Eigenschaften der Schichten wurden untersucht. Die CoFeB-Legierung ist von großer Relevanz für spintronische Anwendungen.

Im Bericht 4.19, werden die Haupteigenschaften unserer optischen Brückenschaltung eines MOKE-Detektors dargestellt. Die Empfindlichkeit, der Rauschpegel und andere wichtige Merkmale werden diskutiert.

4.17 Fabrication of magnetic storage elements by focused ion beam irradiation

R. Neb, P. Pirro, T. Sebastian, and B. Hillebrands

In collaboration with: S. Pofahl and R. Schäfer, Leibniz-Institut für Festkörper- und Werkstoffforschung Dresden, IFW Dresden, Dresden, Germany and B. Reuscher, Institut für Oberflächen-und Schichtanalytik, IFOS, Kaiserslautern, Germany.

The fabrication of storage media with highest bit densities is vital for modern computer technology. In conventional magnetic storage media, information is stored in a granular medium, where several grains form a bit. The information is given by the orientation of the magnetization in the grains. This imposes certain limits onto the possible storage capability, which is given by the bit density of the medium. Reducing the number of grains increases the signal-to-noise ratio, while a further decrease of the grain size is prevented by the superparamagnetic limit. The maximum bit density reached with this method is currently about $1000\,\mathrm{Gbit/inch^2}$. A possible improvement in bit size might be reached with a patterned medium where the bits consist of single homogeneously magnetized object instead of a certain amount of grains. In this case, the volume of each object is relevant rather than the volume of a single grain.

This method has three advantages: Firstly, the onset of the superparamagnetic effect is shifted to significantly smaller sizes. Secondly, the antiferromagnetic coupling of the non-irradiated areas separates the storage elements from each other very effectively due to the suppression of stray fields. And, thirdly, the damaging effect on the topography is negligible, since the applied ion dose on the thin film is very low.

We have already shown that a comparably low ion dose of $3 \times 10^{14}\,\mathrm{ions/cm^2}$ is enough to render the coupling of the irradiated areas ferromagnetically (see also [4]). In order to be able to store

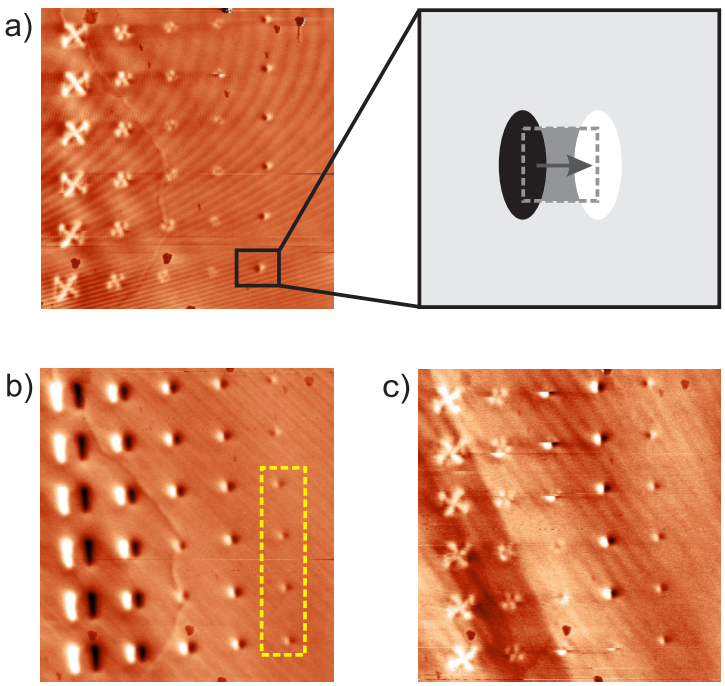

Fig. 1: a) Sample of several irradiated squares with different edge lengths (1000, 500, 300, 200, 100 nm, from left to right). The MFM image was taken at zero external field. Apparently, the squares with an edge length of 100 nm show a uniform magnetization instead of a Landau domain pattern. The drawing depicts the magnetic configuration of such a square. The black and white areas at the borders are a result of the non-vanishing divergence $\nabla \cdot \mathbf{M}$. Switching the magnetization direction also switches the black and white areas. b) Situation at an applied field of 25 mT. Note that four of the six 100 nm squares have reversed their magnetization into the direction of the magnetic field. c) Situation after switching off the external magnetic field. The 100 nm squares have stored the information.

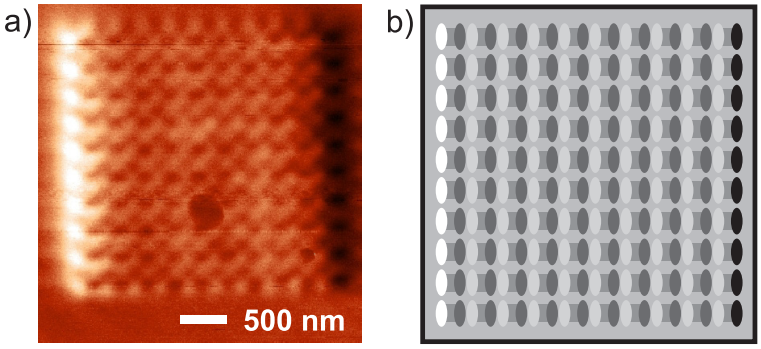

Fig. 2: a) MFM image of a 10×10 array of squares at remanence with an edge length of 100 nm and an inter-element spacing of 200 nm. The independent character of each square is visible very well. This array corresponds to a bit density of 7 Gbit/inch^2. The dark spot in the lower half of the image is generated by some dirt on the surface. b) Schematic explanation of the MFM image. The left and right borders appear more contrasted than the rest due to the finite resolution of the tip, which leads to an averaging of the magnetic signal over an area.

information, the patterned elements have to fulfil some fundamental rules: They must show two different states, corresponding to the logical states "0" and "1", these states must be stable in the absence of an external magnetic field, and it must be possible to rewrite the elements by applying a local external field. Furthermore, neighboring elements must not influence each other.

The influence of neighboring elements was analyzed in previous works (see [4]). It was shown that quadratic elements could be brought together as near as 200 nm without significant interaction. However, the elements examined were much too large for data storage application. Moreover, they were not able to store information, since in the absence of a magnetic field they always return to a Landau pattern. Thus we systematically decreased the size of the elements, as can be seen in Fig. 1a. The smallest fabricated elements with an edge length of 100 nm exhibit a uniform magnetized state in zero field. The direction of the magnetization (pointing left or right) can then be used for defining the "0" and "1" states. Figure 1b shows the effect of an external field of 25 mT. This field is large enough to switch the magnetization of four of the smallest elements, as indicated by the box. When the field is turned off, all 100 nm elements keep their magnetization direction (see Fig. 1c), which proves that these elements are able to store information.

The results suggest that it is possible to fabricate an array with a bit size of 300 nm with our method, corresponding to a bit density of 7 Gbit/inch^2. This suggestion was tested and the results are displayed in Fig. 2. All elements are visible independently, which shows that the interaction between the individual elements is sufficiently weak. We have chosen an image where all magnetizations point into the same direction for optical clarity reasons.

Although we have shown the working principle of a magnetic storage device created by ion beam irradiation, the achieved bit density up to now is much too small for practical applications. Thus we analyze the possibilities of improvement using micromagnetic simulations and propose a way to realize a densely packed storage device. The micromagnetic simulations were carried out using the Object Oriented Micromagnetic Framework (OOMMF) [9]. Small ferromagnetic elements with an edge length of 150 nm were embedded into an antiferromagnetically coupled environment. However, the elements had to be made very thin due to calculation time limitations (1 nm Fe layers, separated by a 1 nm Cr interlayer). The spacings between the elements were varied, but even for distances as low as 20 nm (see Fig. 3) no coupling between the elements was visible in

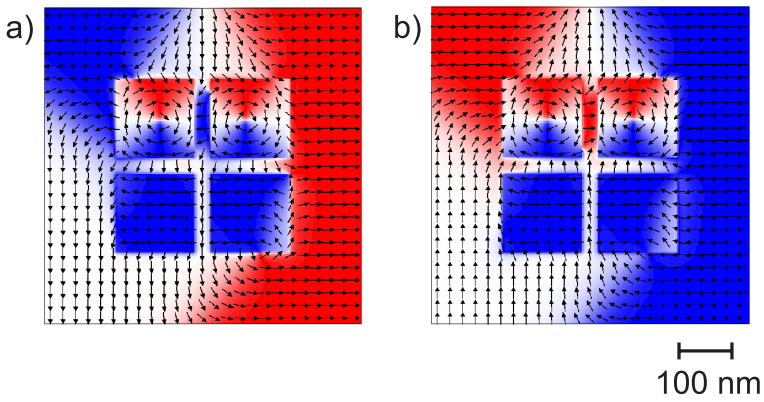

Fig. 3: OOMMF simulation of a 2×2 array of 150 nm squares. a) and b) show the results with a lateral spacing of 20 nm for the upper and lower layer and a thickness of 1 nm of each layer. The squares show no major interaction, and the antiferromagnetic coupling between the squares is still intact, indicating that there is no significant influence of the exchange coupling. The size of the squares is in a range where a Landau pattern as well as a homogeneous magnetized state can appear at the end of the relaxation process, depending on the random starting orientations of the spins. (The colors/levels of gray represent the in-plane direction of the magnetization, which is also shown by the small arrows.)

the results [10]. Note that the antiferromagnetic coupling in the region between the squares is still intact. We conclude that the spacing between two storage elements can be made smaller than 20 nm if broadening effects of the fabrication process can be suppressed.

State of the art storage media use perpendicular recording, which means that the magnetization is pointing perpendicular to the surface, since this kind of recording increases the bit density significantly. In order to obtain perpendicular magnetization by ion beam irradiation, the thickness of the irradiated elements must exceed their width, so that the shape anisotropy will force the magnetization into a perpendicular direction. Thus we need a large thickness of the elements. Apart from technical realization questions, this poses a physical problem: The coupling between two Fe layers decreases with increasing thickness of the Fe layers. At a thickness of 30 nm each, the antiferromagnetic coupling effect is already mostly suppressed. As a solution, a multilayer with alternating Fe and Cr layers can be used. If an even number of Fe layers is chosen, the overall magnetization of the non-irradiated areas is still zero. We numerically investigated a system of 4×4 squares with an edge length of 20 nm and a thickness of 65 nm, embedded into a multilayer given by six 10 nm thick Fe layers, alternating with five 1 nm thick Cr layers (see Fig. 4). As it can be seen, the elements are all perpendicularly magnetized, with random orientations due to the fact that no external field was present [11]. The simulation parameters correspond to a bit density of $400\,\mathrm{Gbit/inch^2}$. Depending on the parameters, this can be increased further. We did not do this here due to the fact that Fe reaches the superparamagnetic limit if the size is much more decreased. This is due to the well known relation $\tau = \tau_0 \exp(K_1 V/4kT)$ for the relaxation time of a ferromagnetic particle with volume V and cubic anisotropy constant K_1 (see Ref. [12]). τ_0 is typically of the order of 10^{-10} s. The exponent for the simulated elements is about 72 at room temperature, while for a stability over more than ten years an exponent of at least 42 is needed. However, since the particle is not isolated from the environment, this is only a coarse estimation. In any case, materials with higher K_1 would solve this problem.

Finally, we want to point out that a focused ion beam is inept for any industrial relevance due to the long writing time. A mask technique, combined with a wide beam, or an ion projection technique might be the method of choice for practical applications. This should also yield better results in the

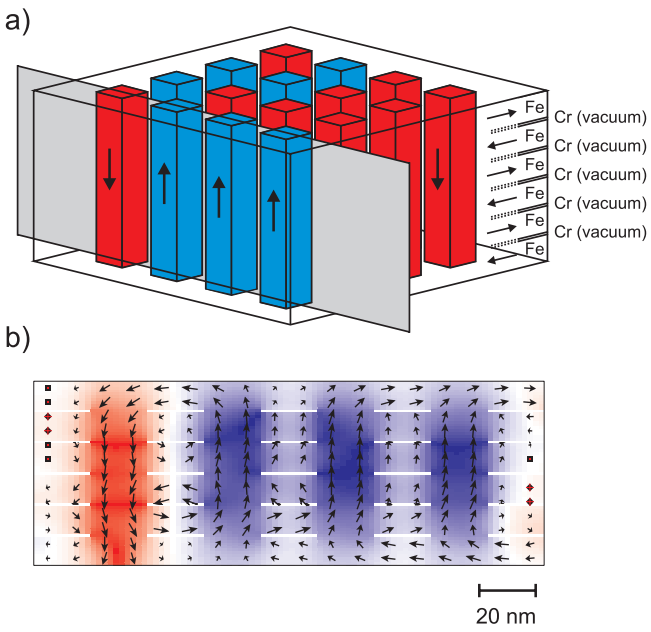

Fig. 4: OOMMF simulation of a 4×4 array of $20 \times 20\,\mathrm{nm}^2$ squares with thicknesses of 65 nm, embedded into a Fe/vacuum multilayer with six 10 nm thick Fe layers and five 1 nm thick vacuum layers representing the Cr. The antiferromagnetic coupling is included by a bilinear and biquadratic coupling term between two neighboring Fe layers. a) shows an idealized image of the whole result, while b) depicts a slice of the actual numeric result (grey area marked in a)). The perpendicular orientation of the magnetization of the elements is clearly visible, while the antiferromagnetic coupling in the area between the elements remains mainly intact. (The colors/levels of gray represent the out-of-plane component of the magnetization, which is also shown by the small arrows.)

fabrication of extremely small elements. Moreover, a 30 keV Ga^+-ion beam is not able to penetrate through a 60 nm thick multilayer system, since its energy is not sufficient. We propose an ion beam with a much lighter material (like He) and energies at least ten times as large. It will be a future task to develop concrete realizations for the advanced models we have shown in this work.

As a summary, we have shown that magnetic recording media can be fabricated by applying a focused ion beam to an antiferromagnetically coupled Fe/Cr/Fe trilayer system. Although the bit density as demonstrated here is only $7\,\mathrm{Gbit/inch}^2$, we have proven via micromagnetic simulations that much denser packed storages are feasible in principle, and that perpendicular recording should be possible.

This work has been recently published in Applied Physiscs Letters [4].

Financial support by the Deutsche Forschungsgemeinschaft (HI 380/18-3) and the Graduiertenkolleg 792 is gratefully acknowledged. We would like to thank D. Weller from TU Kaiserslautern for technical support and A. Zeuner from IFOS Kaiserslautern for the ion irradiation of some of the samples.

References

[1] M. Bolte, R. Eiselt, G. Meier, D. Kim, P. Fischer, *Real space observation of dipolar interaction in arrays of Fe microelements*, J. Appl. Phys. **99**, 08H301 (2006).

[2] J. Lohau, A. Moser, C.T. Rettner, M.E. Best, B.D. Terris, *Writing and reading perpendicular magnetic recording media patterned by a focused ion beam*, Appl. Phys. Lett. **78**, 990 (2001).

[3] M. Albrecht, C.T. Rettner, A. Moser, M.E. Best, B.D. Terris, *Recording performance of high-density patterned perpendicular magnetic media*, Appl. Phys. Lett. **81**, 2875 (2002).

[4] R. Neb, T. Sebastian, P. Pirro, B. Hillebrands, S. Pofahl, R. Schäfer, B. Reuscher, *Fabricating high-density magnetic storage elements by low-dose ion beam irradiation*, Appl. Phys. Lett. **101**, 112406 (2012).

[5] M. Rickart, B.F.P. Roos, T. Mewes, J. Jorzick, S.O. Demokritov, B. Hillebrands, *Morphology of epitaxial metallic layers on MgO substrates: influence of submonolayer carbon contamination*, Surf. Sci. **495**, 68-76 (2001).

[6] S.O. Demokritov, C. Bayer, S. Poppe, M. Rickart, J. Fassbender, B. Hillebrands, *Control of interlayer exchange coupling in Fe/Cr/Fe trilayers by ion beam irradiation*, Phys. Rev. Lett. **90**, 097201 (2003).

[7] S. Blomeier, P. Candeloro, B. Hillebrands, B. Reuscher, A. Brodyanski, M. Kopnarski, *Micromagnetism and magnetization reversal of embedded ferromagnetic elements*, Phys. Rev. B **74**, 184405 (2006).

[8] S. Blomeier, B. Hillebrands, B. Reuscher, A. Brodyanski, M. Kopnarski, R.L. Stamps, *Exchange interaction and magnetic domain formation in periodically inhomogeneous magnetic media*, Phys. Rev. B **77**, 094405 (2008).
[9] M. Donahue, D.G. Porter, OOMMF - Object Oriented MicroMagnetic Framework, Software, NIST (2004)
[10] Simulation values: $A = 2.1 \times 10^{-11}\,\mathrm{J/m}$, $K_1 = 4.5 \times 10^{4}\,\mathrm{J/m^3}$, $M_S = 1.7 \times 10^{6}\,\mathrm{A/m}$, $\sigma = -1.5 \times 10^{-3}\,\mathrm{J/m^2}$, $\sigma_2 = -1.5 \times 10^{-4}\,\mathrm{J/m^2}$, $\alpha = 0.2$, mesh size(x,y,z): $(2.5, 2.5, 1)\,\mathrm{nm}$.
[11] Simulation values are the same as before, except for the mesh size, which is now $(2, 2, 1)\,\mathrm{nm}$.
[12] J.I. Gittleman, B. Abeles, S. Bozowksi, *Superparamagnetism and relaxation effects in granular Ni-SiO_2 and Ni-Al_2O_3 films*, Phys. Rev. B **9**, 3891 (1974).

4.18 FMR and MOKE characterization of $Co_{40}Fe_{40}B_{20}$ thin films

A. Conca Parra, J. Greser, T. Sebastian, and B. Hillebrands

Magnetic tunneling junctions are being widely used for read heads for hard discs, sensors in robotics or machine controllers. The number of potential fields of application is growing rapidly following the increase in the strength of the tunneling magnetoresistance (TMR) effect. The advantages of using single crystalline barriers for achieving large magnetoresistance ratios in tunneling junctions was first predicted for Fe/ZnSe/Fe and Fe/MgO/Fe systems [1–4]. However, it was only technically possible to accomplish large tunneling magnetoresistance values with a MgO barrier [5, 6]. Later theoretical works predicted even larger TMR ratios for junctions with Co and CoFe electrodes and a MgO barrier [7]. This was experimentally confirmed by TMR values above 220% at room temperature [8]. A major breakthrough was provided by the introduction of the alloy CoFeB. First attempts reached TMR values above 200% at room temperature [9, 10]. With further control of the exact stack composition and of the annealing conditions values as large as 472% [11] and 604% [12] have been reported. These results have triggered a large interest in the properties of CoFeB alloys with different stoichiometry. The stuctural properties have been widely studied in the above cited works and others related to tunneling junctions fabrication. Considering dynamic properties, only few works for certain compositions have been published [13, 14].

Here, we report a characterization of $Co_{40}Fe_{40}B_{20}$ (CoFeB hereafter) thin films deposited by magnetron rf sputtering on SiO_x substrates in a chamber with a base pressure of $5{\cdot}10^{-7}$ mbar. The quasi-static anisotropic switching properties were measured with a magneto-optical Kerr effect setup in longitudinal geometry with a spatial resolution of about 100 μm and a laser wavelength of 635 nm. A rotational stage allows for magnetization reversal measurements for any in-plane orientation of the sample with respect to the applied field. The dynamic properties and material parameters were studied by measuring the ferromagnetic resonance using a stripline-vector network analyzer (VNA-FMR). In this work, all films were studied as-deposited, i.e. without an annealing step. The surface topology was studied with ex-situ AFM.

The surface topology of the CoFeB films is very smooth, as shown in the AFM image in Fig.1, with a root mean square roughness parameter $S_q = 0.4$ nm for a film with a thickness of 75 nm. A granular texture is seen with an average lateral grain size around 100 nm.

The CoFeB thin films are magnetically soft with a well defined but weak uniaxial anisotropy, as shown in Fig. 2 a), where the angular dependence of the coercive field H_C for a 75 nm film is plotted. The value of H_C along the easy axis lays below 0.3 mT. Since CoFeB is expected to be

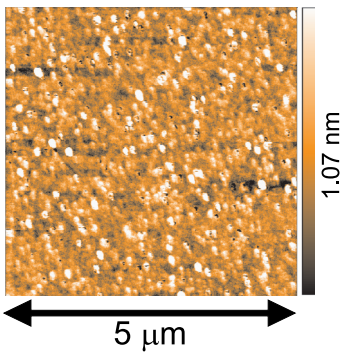

Fig. 1: AFM image of the surface of a 75 nm $Co_{40}Fe_{40}B_{20}$ thin film deposited on a SiO_x substrate. The surface is very smooth with a root mean square roughness (S_q) of 0.4 nm.

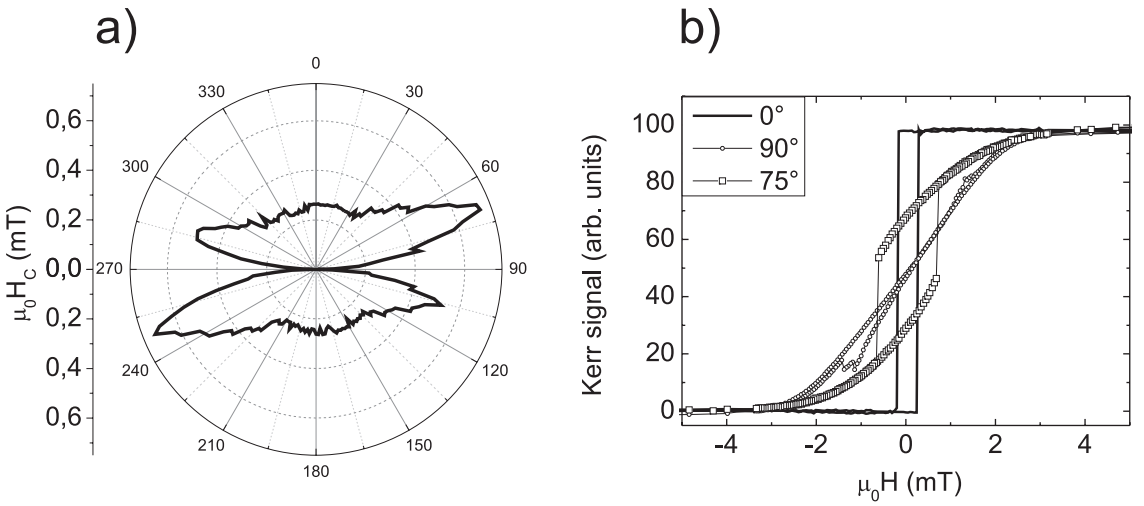

Fig. 2: a) Angular dependence of the in-plane coercive field H_C of a 75 nm $Co_{40}Fe_{40}B_{20}$ thin film deposited on a SiO_x substrate. b) Sample hysteresis loops along the easy (0°) and hard (90°) axis. The hysteresis loop for the the orientation with maximal H_C (75°) is also plotted.

amorphous in the as-deposited state, the orientation of the easy axis is defined by the rest magnetic field created by the sputtering sources in the deposition chamber. Sample hysteresis curves along the easy (0°) and hard (90°) axis are shown in Fig. 2 b). It is possible to observe that the loop along the hard axis is almost closed. Additionally, the curve for the orientation with maximal H_C is also drawn.

Figure 3 shows the dependence of the FMR frequency on the external field for a 75 nm thick film. A sample spectrum is plotted on graph b), showing directly the S_{12} and S_{11} parameters, proportional to the absorbed and reflected microwave power. In order to separate the magnetic signal of the sample from the electrical signal of the whole system including also the stripline, cables and electrical contacts, a reference spectrum is taken and used for normalization. For this purpose, the magnetic field is set to a value large enough to make the FMR peak lay above the frequency measurement range.

The data Fig. 3 a) has been fitted (light grey line) using the Kittel formula [17]:

$$f_{FMR} = \frac{|\gamma|\,\mu_0}{2\pi}\sqrt{(H_{ext}+H_{ani})(H_{ext}+H_{ani}+M_S)} \quad , \tag{1}$$

where H_{ext}, H_{ani} are the applied and anisotropy magnetic field, respectively, M_S is the saturation magnetization and γ is the gyromagnetic ratio of the free electron. Several samples were measured, taking into account the varying values from sample to sample we determine M_S for $Co_{40}Fe_{40}B_{20}$ to be $1250 \pm 30\,\mathrm{kA/m}$. Literature values for the same stoichiometry scatter between $1000\,\mathrm{kA/m}$ [15] and $1230\,\mathrm{kA/m}$ [16] for as-deposited films. It is difficult to understand the large discrepancy in the literature. In both cases, the films were deposited on glass substrates. The authors in [16] claim a nanocrystalline structure for their films while in [15] a truly amorphous phase is reported. However, the authors in [16] do not provide clear experimental evidence supporting a nanocrystalline structure. Additionally, the amorphous nature of the films in [15] has been proven by x-ray diffraction measurements, but it is known that, in case of a nanocrystalline nature, the absence of the diffraction peaks is also a possibility. A method to dilucidate between amorphous and nanocrystalline phases is HRTEM (high resolution transmission electron microscopy). Unfortunately, the HRTEM images provided in [15] lack the required resolution for this purpose.

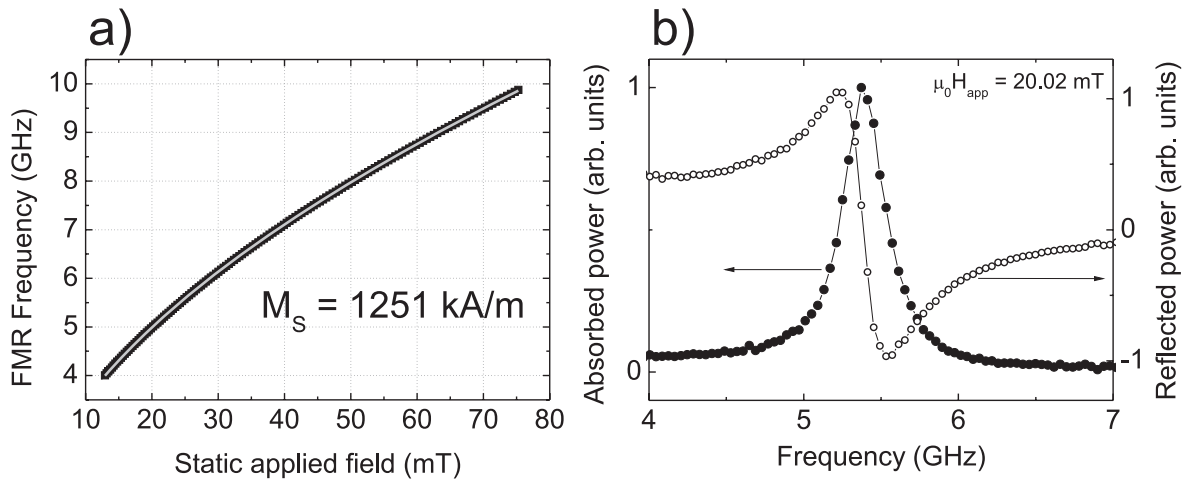

Fig. 3: a) Dependence of the FMR frequency on the external applied magnetic field for a 75 nm $Co_{40}Fe_{40}B_{20}$ thin film deposited on a SiO_x substrate. The light grey line represents a fit to the Kittel formula (see text). b) Single example FMR spectrum showing directly the normalized S_{12} and S_{11} parameters, proportional to the absorbed and reflected microwave power.

Further information about the the dynamic properties of the CoFeB films is extracted from the FMR data. The width ΔH of the FMR peak in the field-space is related to the dimensionless Gilbert damping parameter α [18]:

$$\Delta H = \Delta H_0 + \frac{4\pi\alpha}{\gamma} \quad . \tag{2}$$

An example of a FMR spectrum is plotted in Fig. 4 b). The procedure described in [18] is used to calculate these spectra from the measured data shown in Fig. 3. The a) panel shows the dependence of ΔH on the FMR frequency which nicely follows the linear behavior described in Eq. 2. The light line represents the result of a linear fit to the data. A very low value of α =0.0042 for the Gilbert damping parameter is obtained for our amorphous CoFeB films. This value is smaller than the measured one for permalloy films (0.007) [19], and it is comparable to the low values obtained for epitaxial films of some Co-based full-Heusler alloys like Co_2MnAl (0.006), Co_2MnSi (0.006) or $Co_2Fe_{0.4}Mn_{0.6}Si$ (0.003) [19–21]. The low value for amorphous $Co_{40}Fe_{40}B_{20}$ and the fact that the film growth is possible on amorphous SiO_x wafers, makes this material suitable for fields where a low damping is of advantage, such as in spinwave propagation experiments.

These results indicate the potential of amorphous CoFeB thin films for research. However, in the fabrication of tunneling junctions with MgO barriers, the CoFeB films are typically annealed at temperatures around $250-450\,^{\circ}$C [3–5]. This annealing step in required to induce the crystallization of the MgO barrier, which allows for large magnetoresistance values. It has been reported that CoFeB undergoes also a strong crystallization process during this annealing step [8–12]. Additionally, a migration of B atoms to the MgO barrier and their oxidation is also taking place [22]. It is quite clear that all these changes upon annealing must have a strong influence on the magnetic properties discussed here. As an example, in [14], a increase of the Gilbert damping parameter α from the as-deposited value 0.006 to 0.032 upon annealing at 280 °C for the alloy $Co_{72}Fe_{18}B_{10}$ is reported. For these reasons, a detailed study of the dependence of α, M_S and of the exchange constant on the annealing temperature is planned.

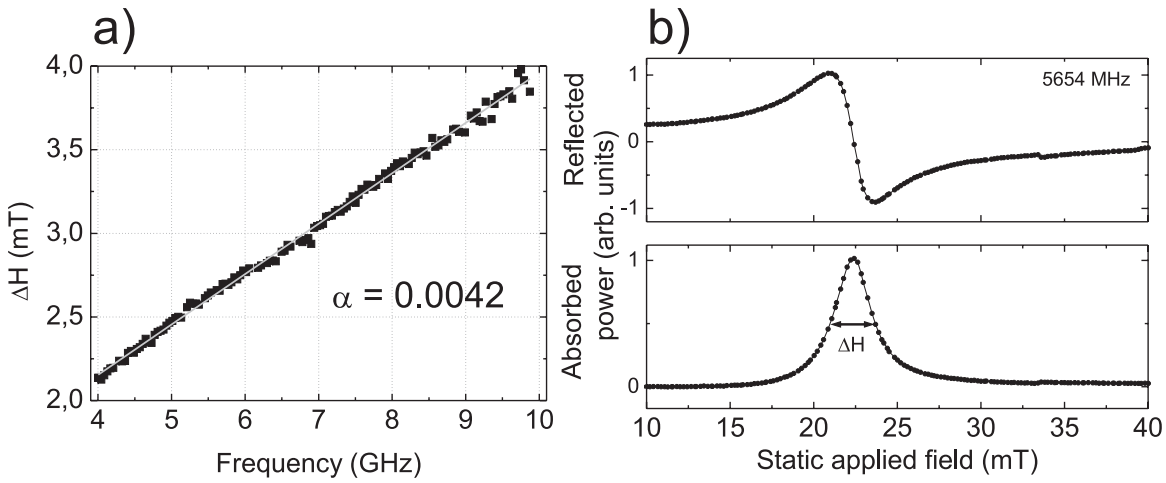

Fig. 4: a) Dependence of the width ΔH of the ferromagnetic resonance on the FMR frequency. The light line represents a linear fit to the data from where the Gilbert damping parameter α is extracted. b) Single example FMR spectrum in the field space calculated following [18].

References

[1] J. M. MacLaren, X.-G. Zhang, W. H. Butler and X. Wang, *Layer KKR approach to Bloch-wave transmission and reflection: Application to spin-dependent tunneling*, Phys. Rev. B **59**, 5470 (1999).

[2] P. H. Dederichs, Ph. Mavropoulos, O. Wunnicke, N. Papanikolaou, V. Bellini, R. Zeller, V. Drchal and J. Kudrnovský, *Importance of complex band structure and resonant states for tunneling*, J. Magn. Magn. Mater. **240**, 108 (2002).

[3] W. H. Butler, X.-G. Zhang, T. C. Schulthess and J. M. MacLaren, *Spin-dependent tunneling conductance of Fe/MgO/Fe sandwiches*, Phys. Rev. B **63**, 054416 (2001).

[4] J. Mathon and A. Umersky, *Spin-dependent tunneling conductance of Fe/MgO/Fe sandwiches*, Phys. Rev. B **63**, 220403R (2001).

[5] S. Yuasa, T. Nagahama, A. Fukushima, Y. Suzuki and K. Ando, *Giant room-temperature magnetoresistnace in single-crystal Fe/MgO/Fe magnetic tunnel junctions*, Nat. Mater. **3**, 868 (2004).

[6] S. Yuasa, A. Fukushima, T. Nagahama, K. Ando and Y. Suzuki, *High tunnel magnetoresistance at room temperature in fully epitaxial Fe/MgO/Fe tunnel junctions due to coherent spin-polarized tunneling*, Jpn. J. Appl. Phys. **43-4B**, L588 (2004).

[7] X.-G. Zhang and W. H. Butler, *Large magnetoresistance in bcc Co/MgO/Co and FeCo/MgO/FeCo tunnel junctions*, Phys. Rev. B **70**, 172407 (2004).

[8] S. S. Parkin, C. Kaiser, A. Panchula, P. M. Rice, B. Hughes, M. Samant and S.-H. Yang, *Giant tunnelling magnetoresistance at room temperature with MgO (100) tunnel barriers*, Nat. Mater. **3**, 862 (2004).

[9] D. D. Djayaprawira, K. Tsunekawa, M. Nagai, H. Maehara, S. Yamagata, N. Watanabe, S. Yuasa, Y. Suziki and K. Ando, *230% room-temperature magnetoresistance in CoFeB/MgO/CoFeB magnetic tunnel junctions* , Appl. Phys. Lett. **86**, 092505 (2005).

[10] W. G. Wang, C. Ni, A. Rumaiz, Y. Wang, X. Fan, T. Moriyama, R. Cao, Q. Y. Wen, H. W. Zhang, and J. Q. Xiao, *Real-time evolution of tunneling magnetoresistance during annealing in CoFeB/MgO/CoFeB magnetic tunnel junctions*, Appl. Phys. Lett. **92**, 152501 (2008).

[11] J. Hayakawaa, S. Ikeda, Y. M. Lee, F. Matsukura and H. Ohno *Effect of high annealing temperature on giant tunnel magnetoresistance ratio of CoFeB/MgO/CoFeB magnetic tunnel junctions*, Appl. Phys. Lett. **89**, 232510 (2006).

[12] S. Ikeda, J. Hayakawa, Y. Ashizawa, Y. M. Lee, K. Miura, H. Hasegawa, M. Tsunoda, F. Matsukura, and H. Ohno, *Tunnel magnetoresistance of 604% at 300 K by suppression of Ta diffusion in CoFeB/MgO/CoFeB pseudo-spin-valves annealed at high temperature*, Appl. Phys. Lett. **93**, 082508 (2006).

[13] A. Natarajarathinam, Z. R. Tadisina, T. Mewes, S. Watts, E. Chen, and S. Gupta, *Influence of capping layers on CoFeB anisotropy and damping*, J. Appl. Phys. **112**, 053909 (2012).

[14] C. Bilzer, T. Devolder, J.-V. Kim, G. Counil, C. Chappert, S. Cardoso and P. P. Freitas, *Study of the dynamic magnetic properties of soft CoFeB films* , J. Appl. Phys. **100**, 053903 (2006).

[15] Y.-T. Chen and S.M. Xie, *Magnetic and electric properties of amorphous $Co_{40}Fe_{40}B_{20}$ thin films*, J. of Nanomaterials **2012**, 486284 (2012).
[16] S. U. Jen, T. Y. Chou and C. Kuen Lo, *Impedance of nanometer thickness ferromagnetic $Co_{40}Fe_{40}B_{20}$ films*, Nanoscale Research Lett. **6**, 468 (2011).
[17] C. Kittel, *On the Theory of Ferromagnetic Resonance Absorption*, Phys. Rev. **73**, 155 (1948).
[18] S. S. Kalarickal, P. Krivosik, M. Wu, C. E. Patton, M. L. Schneider, P. Kabos, T. J. Silva and J. P. Nibarger, *Ferromagnetic resonance linewidth in metallic thin films: Comparison of measurement methods*, J. Appl. Phys. **99**, 093909 (2006).
[19] M. Oogane, T. Wakitani, S. Yakata, R. Yilgin, Y. Ando, A. Sakuma and T. Miyazaki, *Magnetic Damping in Ferromagnetic Thin Films*, Jpn. J. Appl. Phys. **45**, 2889 (2006).
[20] R. Yilgin, Y. Sakuraba, M. Oogane, S. Mizumaki, Y. Ando and T. Miyazaki T, *Anisotropic Intrinsic Damping Constant of Epitaxial Co_2MnSi Heusler Alloy Films*, Jpn. J. Appl. Phys. **46**, L205 (2007).
[21] T. Kubota, S. Tsunegi, M. Oogane, S. Mizukami, T. Miyazaki, H. Naganuma and Y. Ando, *Half-metallicity and Gilbert damping constant in $Co_2FexMn_{1-x}Si$ Heusler alloys depending on the film composition*, Appl. Phys. Lett. **94**, 122504 (2009).
[22] A. K. Rumaiz, C. Jaye, J. C. Woicik, W Wang, D. A. Fischer, J. Jordan-Sweet, and C. L. Chien, *Boron migration due to annealing in CoFeB/MgO/CoFeB interfaces: A combined hard x-ray photoelectron spectroscopy and x-ray absorption studies*, Appl. Phys. Lett. **99**, 222502 (2011).

4.19 Report on optical bridge MOKE detectors

P. Clausen, V. Kegel, B. Obry, and B. Hillebrands[1]

In this Report we present the latest developments of our MOKE detector system based on the optical bridge principle and the analog detector system originally introduced and developed by Martin Bauer [1]. The new detector system utilizes digital signal processing by means of microcontrollers and permits several advantages over the previous analog based system:

- Analog-to-digital conversion directly in the detector head reduces outside interferences
- TCP/IP over standard 10/100 MBit/s Ethernet is used for data transfer to PC
- Interactive menu allows for the observation of basic measurement data even without a PC

The magneto-optical Kerr effect (MOKE) is based on the fact, that the plane of polarization of linearly polarized laser light is rotated upon reflection on a magnetic surface Chapter 3.3, [2–4]. Typical Kerr rotation values for standard 3d ferromagnets are below 200 mdeg. So, the main goal is the detection of very small changes of the polarization of the reflected light.

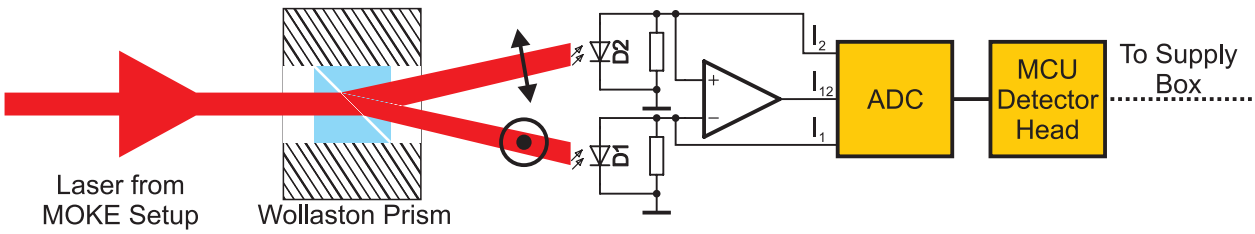

Fig. 1: Principle of an optical bridge: An incoming laser beam is split up by a Wollaston prism into two orthogonally polarized beams. Two photodiodes (D1&D2) measure the intensity of the beams. The difference signal is determined and amplified with the help of an instrumentation amplifier. The voltages of the difference signal and of the diodes are then digitized and sent from the detector head microcontroller unit (MCU) to the supply box.

One possible implementation of a MOKE detector is realized by means of an optical bridge. The principle of operation is shown in Fig. 1. An incoming laser beam is split up by a Wollaston prism into two orthogonally polarized beams. Two photodiodes (D1&D2) measure the intensity of the beams. The difference signal I_{12} is determined with the help of an instrumentation amplifier from the intensities I_1 and I_2 of the corresponding diodes. The best sensitivity and best signal-to-noise ratio is achieved by zeroing the difference signal I_{12} while choosing an amplification to match the operational range of the analog-to-digital conversion circuit. The voltages of the diodes and of the difference signal are then digitized. The normalization of the data by the formula $\frac{I_{12}}{I_1+I_2}$ is done with the measurement software on the PC. The normalized signal is directly proportional to the Kerr rotation angle Θ_{Kerr}. Due to the normalization the impact of laser intensity fluctuations or different reflectivities of the sample surface on the Kerr angle are reduced.

[1] V.K. is now at John Deere Werke Mannheim, 68163 Mannheim, Germany

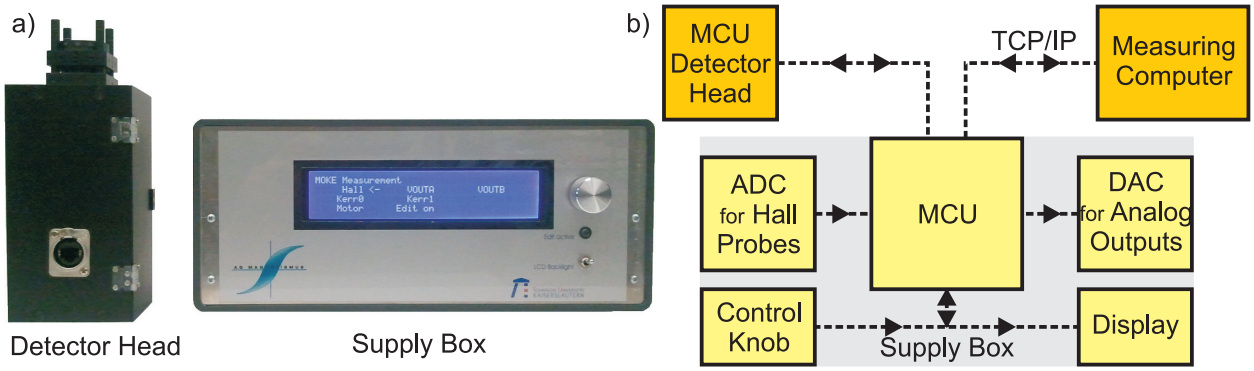

Fig. 2: a) Digital MOKE detector system with detector head (left) and supply box (right). b) Schematic circuit diagram with detector head microcontroller unit (MCU), measuring computer and supply box with MCU and MCU peripherals.

Our MOKE detector system consists of a detector head and a supply box as illustrated by Fig. 2a). The detector head encloses the optical bridge which consists of the Wollaston prism, two photodiodes and analog electronics. It further contains additional optics and the analog-to-digital conversion and signal processing electronics. With this design it is possible to keep the analog data transfer distance as short as possible and therefore reduce the outside interference on this signal.

The use of the analog-to-digital conversion in an early stage of the electronic signal processing is a key feature of this detector system. This results in a reduction of noise and an increase of the signal-to-noise ratio. For typical 3d metallic layers, noise levels below 2 mdeg for very fast measurement times (< 500 ms) are achieved. This noise level reduces below 0.5 mdeg for sampling times of a few seconds.

The supply box acts as an interface between several components. It is able to support up to two detector heads, offers two channels for Hall probes and eight digital-to-analog output channels. It houses the power supply and the low noise power supply for the analog electronics. Both hall probe channels can be independently adjusted to drive a Hall probe with $50 - 200$ mA. Each channel offers its own signal processing circuit and analog-to-digital conversion of Hall voltage and current of the corresponding channel.

The eight analog output channels operate in the voltage range of -10 V to 10 V with a resolution of 1 mV. They offer a wide area of application, e.g. they can be used to remotely control a magnet power supply or used as digital outputs.

The supply box also includes an interactive menu, which is navigated by a rotary knob. This menu allows reading and setting of basic system values even without a measuring computer. The most important parameters, which are accessible via the box menu, are the intensities from the detector head photodiodes as well as the difference signal and the analog amplification of the difference signal. Furthermore the Hall current and Hall voltage for both channels as well as the voltage of all eight analog output channels are accessible.

This detector system is commercially available from the University of Kaiserslautern. For further information or specifications about this system feel free to contact us at moke@physik.uni-kl.de.

References

[1] M. Bauer, *Grundlagen und Strategien für schnelles Schalten der Magnetisierung*, Ph.D. thesis, TU Kaiserslautern (2000).
[2] S. Visnovsky, *Magneto-optical ellipsometry*, Czech. J. Phys. B **36**, 625 (1986).
[3] S. Visnovsky, R. Lopusnik, M. Bauer, J. Bok, J. Fassbender, B. Hillebrands, *Magnetooptic ellipsometry in multilayers at arbitrary magnetization*, Opt. Express **9**, 121 (2001).
[4] Z.J. Yang, M.R. Scheinfein, *Combined three-axis surface magneto-optical of surface and ultrathin-film magnetism Kerr effects in the study*, J. Appl. Phys. **74**, 6810 (1993).

Chapter 5: Publications

Most publications can be downloaded from http://www.physik.uni-kl.de/hillebrands.

5.1 in press

1. *Spin-wave propagation and transformation in a thermal gradient*
   B. Obry, V.I. Vasyuchka, A.V. Chumak, A.A. Serga, B. Hillebrands
   Appl. Phys. Lett.

2. *Atom probe tomography of ion-irradiated ultra-thin Fe/Cr/Fe trilayers with sub-nm spatial resolution*
   H. Gnaser, R. Schiller, M. Wahl, B. Reuscher, A. Zeuner, M. Kopnarski, R. Neb, B. Hillebrands
   J. Phys. D: Appl. Phys.

5.2 published

1. *Brillouin light scattering spectroscopy of parametrically excited dipole-exchange magnons*
   A.A. Serga, C.W. Sandweg, V.I. Vasyuchka, M.B. Jungfleisch, B. Hillebrands, A. Kreisel, P. Kopietz, M.P. Kostylev
   Phys. Rev. B **86**, 134403 (2012)

2. *Fabricating high-density magnetic storage elements by low-dose ion beam irradiation*
   R. Neb, T. Sebastian, P. Pirro, B. Hillebrands, S. Pofahl, R. Schäfer, B. Reuscher
   Appl. Phys. Lett. **101**, 112406 (2012)

3. *Spin waves turning a corner*
   K. Vogt, H. Schultheiss, S. Jain, J.E. Pearson, A. Hoffmann, S.D. Bader, B. Hillebrands
   Appl. Phys. Lett. **101**, 042410 (2012)

4. *Storage-recovery phenomenon in magnonic crystal*
   A.V. Chumak, V.I. Vasyuchka, A.A. Serga, M.P. Kostylev, B. Hillebrands
   Phys. Rev. Lett. **108**, 257207 (2012)

5. *Oscillatory energy exchange between waves coupled by a dynamic artificial crystal*
   A.D. Karenowska, V.S. Tiberkevich, A.V. Chumak, A.A. Serga, J.F. Gregg, A.N. Slavin, B. Hillebrands
   Phys. Rev. Lett. **108**, 015505 (2012)

6. *Interplay of energy dissipation, ion-induced mixing, and crystal structure recovery, and surface effects in ion-irradiated Fe/Cr/Fe trilayers*
   A. Brodyanski, S. Blomeier, H. Gnaser, W. Bock, B. Hillebrands, M. Kopnarski, B. Reuscher
   Phys. Rev. B **84**, 214106 (2012)

7. *Direct detection of magnon spin transport by the inverse spin Hall effect*
   A.V. Chumak, A.A. Serga, M.B. Jungfleisch, R. Neb, D.A. Bozhko, V.S. Tiberkevich, B. Hillebrands
   Appl. Phys. Lett. **100**, 082405 (2012)

8. *Acoustic spin pumping: Direct generation of spin currents from sound waves in Pt/$Y_3Fe_5O_{12}$ hybrid structures*
   K. Uchida, A. Adachi, T. An, H. Nakayama, M. Toda, B. Hillebrands, S. Maekawa, E. Saitoh
   J. Appl. Phys. **111**, 053903 (2012)

9. *Low-damping spin-wave propagation in a micro-structured $Co_2Mn_{0.6}Fe_{0.4}Si$ Heusler waveguide*
   T. Sebastian, Y. Ohdaira, T. Kubota, P. Pirro, T. Brächer, K. Vogt, A.A. Serga, H. Naganuma, M. Oogane, Y. Ando, B. Hillebrands
   Appl. Phys. Lett. **100**, 112402 (2012)

10. *Magnonic band gap design by the edge modulation of micro-sized waveguides*
    F. Ciubotaru, A.V. Chumak, N. Yu. Grigoryeva, A.A. Serga, B. Hillebrands
    J. Phys. D: Appl. Phys. **34**, 255002 (2012)

11. *Storage recovery phenomenon in magnonic crystal*
    A.V. Chumak, V.I. Vasyuchka, A.A. Serga, M.P. Kostylev, B. Hillebrands
    Phys. Rev. Lett. **108**, 257207 (2012)

12. *Direct observation of nonlinear four-magnon scattering in spin-wave microconduits*
    H. Schultheiss, K. Vogt, B. Hillebrands
    Phys. Rev. B **86**, 054414 (2012)

13. *Probing dynamical magnetization pinning in circular dots as a function of the external magnetic field orientation*
    G.N. Kakazei, G.R. Aranda, S.A. Bunyaev, V.O. Golub, E.V. Tartakovskaya, A.V. Chumak, A.A. Serga, B. Hillebrands, K.Y. Guslienko
    Phys. Rev. B **86**, 054419 (2012)

5.3 Ph.D. theses

1. *Spin wave excitation by nano-sized antennas*
   Florin Ciubotaru, TU Kaiserslautern, April 2012.

2. *Optimierung von eingebetteten schnellen magnetischen Speicherzellen*
   Georg Martin Wolf, TU Kaiserslautern, December 2012.

Chapter 6: Conferences, Workshops, Schools, Seminars

(shown in chronological order; if not indicated otherwise the contributions were presented by the first author)

6.1 Conferences

6.1.1 Conference Organization

B. Hillebrands:
Conference Chair
IEEE International Conference on Microwave Magnetism (ICMM2012), TU Kaiserslautern, Germany, August 2012

A.A. Serga:
General Secretar
IEEE International Conference on Microwave Magnetism (ICMM2012), TU Kaiserslautern, Germany, August 2012

A.V. Chumak:
Publication Chair
IEEE International Conference on Microwave Magnetism (ICMM2012), TU Kaiserslautern, Germany, August 2012

6.1.2 Invited talks

A.A. Serga:
Time-resolved spin pumping by sub-micron wavelength magnons from a magnetic insulator
56th Annual Conference on Magnetism and Magnetic Materials, Scottsdale, USA, November 2011

B. Hillebrands:
Magnon spintronics
DPG-Frühjahrstagung Berlin, Germany, March 2012

B. Hillebrands:
Inverse spin Hall effect from spin waves over a large wavevector range
INTERMAG 2012, Vancouver, Canada, May 2012

A.V. Chumak:
Static and dynamic magnonic crystals
INTERMAG 2012, Vancouver, Canada, May 2012

B. Hillebrands:
Magnon Caloritronics
The 19th International Conference on Magnetism (ICM), Busan, Korea, July 2012

B. Hillebrands:
Spin-wave waveguides and magnonic crystals
Spin Dynamics in Nanomagnets Conference, Seoul, Korea, July 2012

6.1.3 Contributed talks and posters

G.N. Kakazei, M. Ilyn, O. Chubykalo-Fesenko, J.M. Gonzalez,A.A. Serga, A.V. Chumak, B. Hillebrands, K.Y. Guslienko:
Magnetization relaxation in circular magnetic dots near vortex state nucleation
56th Annual Conference on Magnetism and Magnetic Materials, Scottsdale, USA, November 2011

A.V. Chumak, M.B. Jungfleisch, A.A. Serga, R. Neb, B. Hillebrands:
Direct detection of magnon spin transport by the inverse spin Hall effect
56th Annual Conference on Magnetism and Magnetic Materials, Scottsdale, USA, November 2011

T. Meyer, B. Obry, P. Pirro, T. Brächer, R. Neb, J. Osten, T. Strache, J. Fassbender, B. Hillebrands:
Microscopic magnetic structuring of spin-wave wave-guides by ion implantation in a $Ni_{81}Fe_{19}$ layer
INTERMAG 2012, Vancouver, Canada, May 2012

B. Obry, V.I. Vasyuchka, A.V. Chumak, A.A. Serga, B. Hillebrands:
Spin-wave propagation and transformation in a thermal gradient
INTERMAG 2012, Vancouver, Canada, May 2012

V.I. Vasyuchka, M. Agrawal, A.A. Serga, A.V. Chumak, B. Hillebrands:
Optical measurement of magnon temperature in a magnetic insulator
INTERMAG 2012, Vancouver, Canada, May 2012

F. Ciubotaru, A.V. Chumak, B. Obry, A.A. Serga, B. Hillebrands:
Micromagnetic study of magnonic band gaps in waveguides with a periodic variation of the saturation magnetization
ICM 2012, Busan, South Korea, July 2012

T. Brächer, P. Pirro, B. Obry, A.A. Serga, B. Leven, B. Hillebrands:
Mode selective parametric excitation of spin waves in a $Ni_{81}Fe_{19}$ microstripe
IEEE International Conference on Microwave Magnetism (ICMM 2012), TU Kaiserslautern, Germany, August 2012

A.A. Serga, M. Agrawal, V.I. Vasyuchka, G.A. Melkov, B. Hillebrands:
Magnon temperature measurement in magnetic insulators
IEEE International Conference on Microwave Magnetism (ICMM2012), TU Kaiserslautern, Germany, August 2012

M. Agrawal, H. Idzuchi, Y. Fukuma, A.A. Serga, Y. Otani, B. Hillebrands:
Spin dynamics excitation in non-local spin valves
IEEE International Conference on Microwave Magnetism (ICMM2012), TU Kaiserslautern, Germany, August 2012

A. Chumak, V. Vasyuchka, A.A. Serga, M. Kostylev, V. Tiberkevich, B. Hillebrands:
Storage-recovery phenomenon in a magnonic crystal
IEEE International Conference on Microwave Magnetism (ICMM2012), TU Kaiserslautern, Germany, August 2012

D. Bozhko, O. Talalaevskij, G. Melkov, V. Malyshev, Y. Koblyanskij, A.V. Chumak, A.A. Serga, B. Hillebrands, A. Slavin:
Spin-Hall effect influence on ferromagnetic resonance in Pt-YIG structures
IEEE International Conference on Microwave Magnetism (ICMM2012), TU Kaiserslautern, Germany, August 2012

G. Rodriguez Aranda, G.N. Kakazei, S.A. Bunyaev, V.A. Golub, E.V. Tartakovskaya, A.V. Chumak, A.A. Serga, B. Hillebrands, K. Gusliyenko:
Field orientation dependence of dynamical magnetization pinning of the main ferromagnetic resonance mode in a circular dot
IEEE International Conference on Microwave Magnetism (ICMM2012), TU Kaiserslautern, Germany, August 2012

T. Langner, B. Obry, P. Pirro, T. Brächer, K. Vogt, A.A. Serga, B. Leven, B. Hillebrands:
Spin-wave resonance in $Ni_{81}Fe_{19}$ microstripes containing a mechanical gap
IEEE International Conference on Microwave Magnetism (ICMM2012), TU Kaiserslautern, Germany, August 2012

M.B. Jungfleisch, A.V. Chumak, A.A. Serga, R. Neb, D.A. Bozhko, V.S. Tiberkevich, B. Hillebrands:
Direct detection of magnon spin transport by the inverse spin Hall effect
IEEE International Conference on Microwave Magnetism (ICMM2012), TU Kaiserslautern, Germany, August 2012

T. Sebastian, P. Pirro, T. Brächer, T. Kubota, A.A. Serga, H. Naganuma, M. Oogane, Y. Ando, B. Hillebrands:
Nonlinear emission of spin-wave caustics from an edge mode of a micro-structured $Co_2Mn_{0.6}Fe_{o.4}Si$ waveguide
IEEE International Conference on Microwave Magnetism (ICMM2012), TU Kaiserslautern, Germany, August 2012

K. Vogt, H. Schultheiss, S. Jain, J.E. Pearson, A. Hoffmann, S.D. Bader, B. Hillebrands:
Bending spin waves around the corner
IEEE International Conference on Microwave Magnetism (ICMM2012), TU Kaiserslautern, Germany, August 2012

V.I. Vasyuchka, A.A. Serga, A.V. Chumak, B. Hillebrands:
Magnon mediated heat transport in a magnetic insulator
IEEE International Conference on Microwave Magnetism (ICMM2012), TU Kaiserslautern, Germany, August 2012

B. Obry, V.I. Vasyuchka, A.V. Chumak, A.A. Serga, B. Hillebrands:
Spin-wave propagation and transformation in a thermal gradient
IEEE International Conference on Microwave Magnetism (ICMM2012), TU Kaiserslautern, Germany, August 2012

P. Pirro, J. Westermann, T. Brächer, T. Sebastian, B. Obry, B. van de Wiele, A. Vansteenkiste, B. Hillebrands:
Phase sensitive spin-wave mode conversion in a two dimensional system
JEMS Conference, Parma, Italy, September 2012

A.V. Chumak, A.A. Serga, M.B. Jungfleisch, R. Neb, D.A. Bohzko, V.S. Tiberkevich, B. Hillebrands:
Inverse spin Hall effect detection of travelling magnons
JEMS Conference, Parma, Italy, September 2012

T. Brächer, P. Pirro, B. Obry, A.A. Serga, B. Leven, B. Hillebrands:
Mode selective parametric excitation of spin waves in a $Ni_{81}Fe_{19}$ microstripe
JEMS Conference, Parma, Italy, September 2012

6.1.4 Contributions to the DPG Frühjahrstagung

14 contributions: DPG Frühjahrstagung, Berlin, March 2012

6.2 Workshops and Schools

6.2.1 Invited lectures

V.I. Vasyuchka:
Magnon Seebeck effect and macron current transformation in thermal gradients
DFG Colloquium of SPP 1538 “Spin Caloric Transport”, Bad Honnef, Germany, January 2012

B. Hillebrands:
Magnon spintronics
Magnetic Single Nano-Object Workshop and School (M-SNOWS 2012, Les Houches, France, February 2012

B. Hillebrands:
Fundamentals of magnon spintronics
Student Workshop of DFG SPP 1538 ”Spin Caloric Transport“, Regensburg, Germany, April 2012

V.I. Vasyuchka:
Magnon caloritronics
3^{rd} Nordic Workshop on Spintronics and Nanomagnetism, NordicSpin 2012, Varberg, Sweden, April 2012

B. Hillebrands:
Magnons in spintronics
International Advanced School on Magnonics, Santa Margherita, Italy, September 2012

B. Hillebrands:
Magneto-optic techniques
International Scientific CNRS Fall School 2012 ”High Sensitivity Magnetometers: Sensors and Applications“, 4^{th} edition, Normandy, France, October 2012

6.2.2 Contributed talks and posters

T. Langner, V.I. Vasyuchka, M.B. Jungfleisch, A.V. Chumak, A.A. Serga, B. Hillebrands:
Interaction between coherent magnons and thermal magnon currents
DFG Colloquium of SPP 1538 "Spin Caloric Transport", Bad Honnef, Germany, January 2012

V.I. Vasyuchka, B. Obry, A.A. Serga, B. Hillebrands:
Magnon current transformation in thermal gradients
DFG Colloquium of SPP 1538 "Spin Caloric Transport", Bad Honnef, Germany, January 2012

T. Langner, V.I. Vasyuchka, M.B. Jungfleisch, A.V. Chumak, A.A. Serga, B. Hillebrands:
Interaction between coherent magnons and thermal magnon currents
PhD Student workshop of DFG SPP 1538 "Spin Caloric Transport", Regensburg, Germany, April 2012

P. Pirro, T. Brächer, T. Sebastian, B. Obry, B. Hillebrands:
Magnonic spintronics
Workshop of OPTIMAS Carl Zeiss Doctoral Program (OCZDP), Annweiler, Germany, April 2012

M.B. Jungfleisch, A.V. Chumak, A.A. Serga, R. Neb, D.A. Bozhko, V.S. Tiberkevich, B. Hillebrands:
Direct detection of magnon spin transport by the inverse spin Hall effect
4^{th} International Workshop on Spin Caloritronics, Sendai, Japan, June 2012

M.B. Jungfleisch, T. An, K. Ando, Y. Kajiwara, K. Uchida, T. Yoshino, H. Nakayama, B. Hillebrands, E. Saitoh:
Heat-induced spin-transfer torque in YIG/Pt bilayer structures
4^{th} International Workshop on Spin Caloritronics, Sendai, Japan, June 2012

T. Langner, V.I. Vasyuchka, M.B. Jungfleisch, A.V. Chumak, A.A. Serga, B. Hillebrands:
Interaction between coherent magnons and thermal magnon currents
4^{th} International Workshop on Spin Caloritronics, Sendai, Japan, June 2012

V.I. Vasyuchka, B. Obry, A.A. Serga, A.V. Chumak, B. Hillebrands:
Spin wave mediated heat transport in a magnetic insulator
4^{th} International Workshop on Spin Caloritronics, Sendai, Japan, June 2012

T. Sebastian, P. Pirro, A.A. Serga, B. Hillebrands:
Micromagnetic modeling of spin-torque nano-oscillators
Annual Meeting of ASPIMATT JST-DFG Research Unit, Sendai, Japan, July 2012

T. Sebastian, P. Pirro, T. Brächer, T. Kubota, A.A. Serga, H. Naganuma, M. Oogane, Y. Ando, B. Hillebrands:
Linear and nonlinear spin-wave propagation in a micro-structured Heusler $Co_2Mn_{0.6}Fe_{0.4}Si$ *waveguide*
Annual Meeting of ASPIMATT JST-DFG Research Unit, Sendai, Japan, July 2012

F. Ciubotaru, A.V. Chumak, B. Obry, A.A. Serga, N.Y. Grigoryeva, B. Hillebrands:
Micromagnetic analysis of spin wave propagation in nanostructrued magnonic crystals
Spin Dynamics in Nanomagnets, Seoul, South Korea, July 2012

K. Vogt, H. Schultheiss, S. Jain, J.E. Pearson, A. Hoffmann, S.D. Bader, B. Hillebrands:
Bending spin waves around the corner
IEEE Magnetics Society Summer School, Chennai, India, July 2012

T. Brächer, P. Pirro, B. Obry, A.A. Serga, B. Leven, B. Hillebrands:
Mode selective parametric excitation of spin waves in a $Ni_{81}Fe_{19}$ microstripe
IEEE Magnetics School, Chennai, India, July 2012

T. Brächer, P. Pirro, B. Obry, A.A. Serga, B. Leven, B. Hillebrands:
Mode selective parametric excitation of spin waves in a $Ni_{81}Fe_{19}$ microstripe
MAINZ Student Seminar, Cambridge, United Kingdom, August 2012

M. Agrawal, H. Idzuchi, Y. Fukuma, A.A. Serga, Y. Otani, B. Hillebrands:
Spin dynamics excitation in non-local spin valves
MAINZ Student Seminar, Cambridge, United Kingdom, August 2012

K. Vogt, H. Schultheiss, S. Jain, J.E. Pearson, A. Hoffmann, S.D. Bader, B. Hillebrands:
Bending spin waves around the corner
MAINZ Student Seminar, Cambridge, United Kingdom, August 2012

P. Pirro, J. Westermann, T. Brächer, T. Sebastian, B. Obry, B. van de Wiele, A. Vansteenkiste, B. Hillebrands:
Phase sensitive spin-wave mode conversion in a two dimensional system
International Advanced School on Magnonics, Santa Margherita, Italy, September 2012

T. Brächer, P. Pirro, B. Obry, A.A. Serga, B. Leven, B. Hillebrands:
Mode selective parametric excitation of spin waves in a $Ni_{81}Fe_{19}$ microstripe
International Advanced School on Magnonics, Santa Margherita, Italy, September 2012

B. Obry, V.I. Vasyuchka, A.V. Chumak, A.A. Serga, B. Hillebrands:
Spin wave propagation and transformation in a thermal gradient
International Advanced School on Magnonics, Santa Margherita, Italy, September 2012

P. Clausen, D.A. Bozhko, A.V. Chumak, A.A. Serga, G.A. Melkov, B. Hillebrands:
Phonon mediated Bose-Einstein magnon condensation
Annual Retreat of SFB/TRR49, Wiesbaden, Niedernhausen, Germany, September 2012

A.V. Chumak, A.A. Serga, V.I. Vasyuchka, B. Obry, B. Hillebrands:
Time evolution of Bose-Einstein condensate of magnons in q-space
Annual Retreat of SFB/TRR49, Wiesbaden, Niedernhausen, Germany, September 2012

B. Obry, V.I. Vasyuchka, A.V. Chumak, A.A. Serga, B. Hillebrands:
Spin wave propagation and transformation in a thermal gradient
Student Workshop of DFG SPP 1538 “Spin Caloric Transport”, Göttingen, Germany, October 2012

M. Agrawal, V.I. Vasyuchka, A.A. Serga, G.A. Melkov, B. Hillebrands:
Magnon temperature measurement in magnetic insulators
Student Workshop of DFG SPP 1538 “Spin Caloric Transport”, Göttingen, Germany, October 2012

6.3 Invited seminar talks and colloquia

V.I. Vasyuchka:
Spin caloric effects in a magnetic insulator
Faculdade de Ciencias da Universidade do Porto, Porto, Portugal, November 2011

B. Hillebrands:
Magnon spintronics
Physikalisches Kolloquium, Universität Bielefeld, Germany, December 2011

B. Hillebrands:
Nie mehr booten? Oder: eine Nobelpreisentdeckung verändert die Welt
Tag der Physik, TU Kaiserslautern, Germany, December 2011

B. Hillebrands:
Magnon-Spintronik
Physikalisches Kolloquium, Westfälische Wilhelms Universität Münster, Germany, January 2012

A.A. Serga:
Bose-Einstein condensate of magnons and evaporative cooling of a magnon gas
IFIMUP-IN, Universidade do Porto, Porto, Portugal, February 2012

B. Hillebrands:
Magnon gases
Oxford Physics Colloquium, Oxford, United Kingdom, April 2012

M.B. Jungfleisch:
Spin pumping/spin Hall effects in YIG/Pt bilayer structures
Tohoku University, IMR, Sendai, Japan, April 2012

T. Sebastian:
Introduction to Brillouin light scattering microscopy
Tohoku University, Sendai, Japan, April 2012

B. Hillebrands:
Magnon-Spintronik
Physikalisches Kolloquium, Universität Chemnitz, Germany, May 2012

B. Hillebrands:
Magnon gases
International Conference on Superconductivity and Magnetism (ICMN 2012), Istanbul, Turkey, May 2012

K. Vogt:
Optical detection of propagating spin waves in $Ni_{81}Fe_{19}$ microstructures
Forschungszentrum Rossendorf, Dresden, Germany, July 2012

B. Hillebrands:
Magnon caloritronics
4^{th} International Workshop on Spin Caloritronics IV, Sendai, Japan, June 2012

6.4 Seminars

P. Clausen:
Magnon gases and condensates
Student Seminar Summer Term of SFB/TRR, Riezlern, Austria, July 2011

6.5 Annual group retreat

In 2012 our group organized a three-day retreat at the Kurhaus am Trifels, Annweiler. We had two days of intense scientific discussion and 18 presentations by our group members. Prof. Dr. phil. Dipl.-Phys. Wolfgang Neuser from the University of Kaiserslautern gave a fascinating evening talk on *Logos and Mythos: the ultimate constitutives of science*. On the third day, the group members participated in a soft skill seminar on "Application Training" held by Robert Zaal.

6.6 Other meetings and trade fairs

A. Conca Parra, A. Ruiz Calaforra, B. Leven, B. Hillebrands:
Presentation of the Spintronic Technology Platform
Hannover Messe 2012, Hannover, Germany April 2012

A. Conca Parra, B. Leven, B. Hillebrands:
Presentation of the Spintronic Technology Platform
Bi-annual project meeting, Mainz, Germany, September 2012

A.A. Serga:
A phonon mediated Bose-Einstein magnon condensation
Annual Retreat of the SFB/TRR49, Niedernhausen, September 2012

Appendix: IEEE International Conference on Microwave Magnetics 2012

On August 26-29, 2012 our group hosted the IEEE International Conference on Microwave Magnetics 2012. After two conferences in the U.S. (Fort Collins in 2008 and Boston in 2010), the ICMM came to Europe for the first time. More than 120 participants discussed physical and technological aspects of magnetic phenomena in the microwave frequency range. The specific topics of the conference included:

- RF, microwave and millimeter wave devices,
- high frequency materials,
- magnetization dynamics and relaxation,
- nonlinear phenomena,
- magnon spintronics and caloritronics,
- spin-torque oscillators.

Professor Genadii Melkov (Ukraine) was awarded the conference's honorary award for his lifetime achievements in nonlinear spin-wave physics. This award was handed over during a festive conference banquet that took place at the famous Fritz-Walter Soccer Stadium. During the banquet we also enjoyed a magic show by Professor René Beigang from our Physics Department about "The Magic of Light, Spin and Matter".

The conference was chaired by Burkard Hillebrands, others member of our group involved in the Local Organizing Committee were Oleksandr Serha as Technical & Program Chair and Treasurer, and Andrii Chumak responsible for publications. Together with Alexy Karenowska (University of Oxford), Andrii is Guest Editor for the conference-related contributions in the IEEE Transactions on Magnetics March 2013 issue. In addition, Professor Martin Aeschlimann from our Department was kindly supporting us. All members of the AG Magnetismus helped very enthusiastically in the organization of the conference. Setting up the impressive and delightful scientific program that included more than 50 lectures and 60 poster presentations, would not have been possible without the International Advisory Committee of the conference.

Financial support for the conference was kindly provided by the State Research Center Optics and Material Sciences (OPTIMAS) and the University of Kaiserslautern. In addition we acknowledge sponsorship by Singulus Technologies AG (Kahl, Germany) and Sensitec GmbH (Lahnau, Germany).

Appendix: Impressions from 2012

Ph.D. defense Dr. Georg Wolf

Ph.D. defense Dr. Florin Ciubotaru